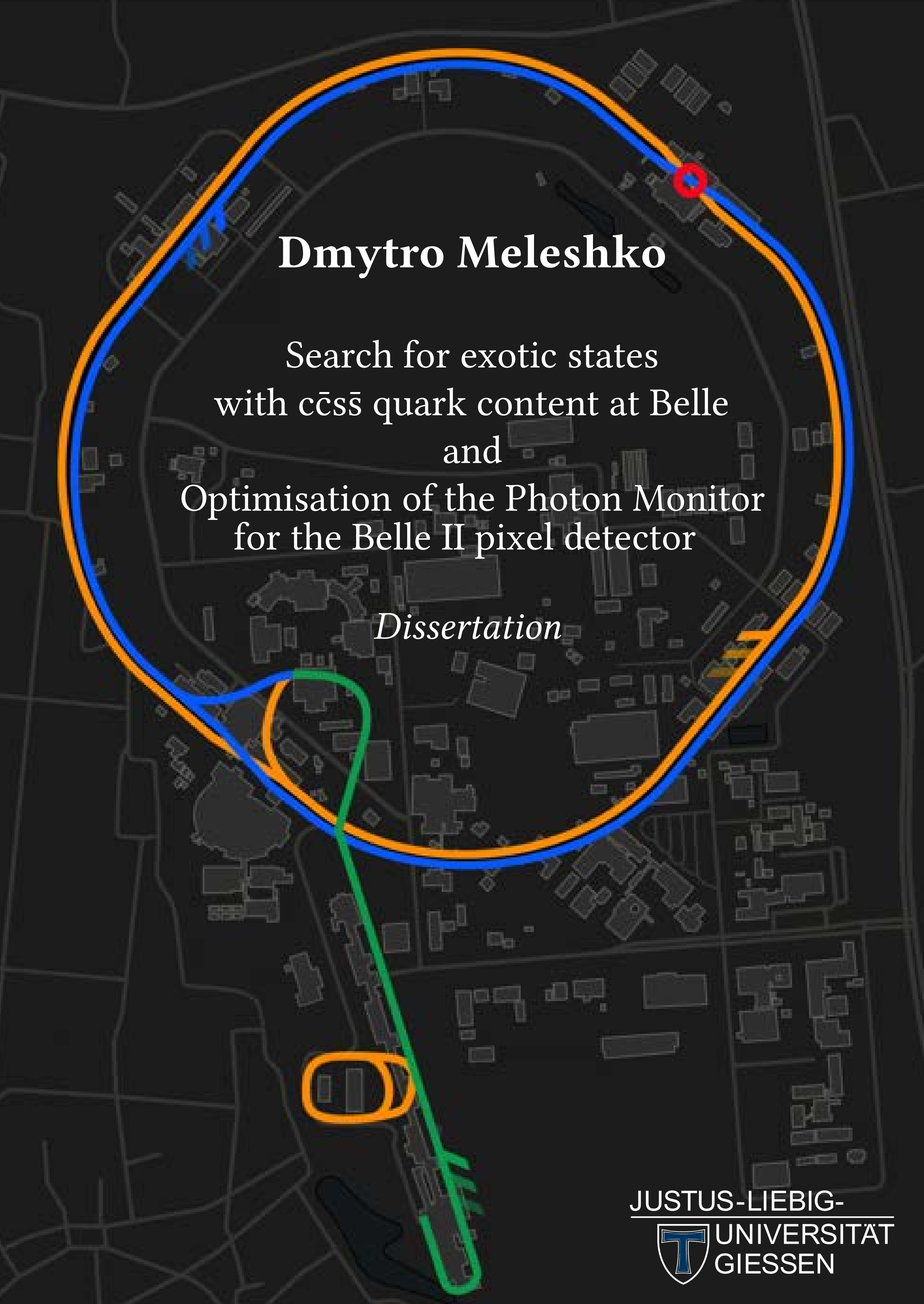

Dmytro Meleshko

Search for exotic states with $c\bar{c}s\bar{s}$ quark content at Belle and Optimisation of the Photon Monitor for the Belle II pixel detector

Dissertation

JUSTUS-LIEBIG-UNIVERSITÄT GIESSEN

Search for exotic states with $c\bar{c}s\bar{s}$ quark content at Belle and Optimisation of the Photon Monitor for the Belle II pixel detector

JUSTUS-LIEBIG-UNIVERSITÄT GIESSEN

Belle II

To science, a joyful sandbox that encourages
one's childhood passion to thrive ...

Suche nach exotischen Zuständen mit $c\bar{c}s\bar{s}$ Quarkinhalt am Belle und Optimierug des Photonmonitors für den Belle II Pixeldetektor

Dmytro Meleshko
geboren in Sumy, Ukraine

INAUGURALDISSERTATION
zur Erlangung des Doktorgrades

am
II. Physikalischen Institut
des
Fachbereich 07 — Mathematik und Informatik, Physik, Geographie
der
Justus-Liebig-Universität Gießen

(2026)

Dekan: Prof. Dr. Christian Heiliger
Gutachter: apl. Prof. Dr. Jens Sören Lange
Gutachter: Prof. Dr. Claudia Höhne

This document was typeset with LuaLaTeX 1.17 using the `memoir` class. The text is set in Libertine, Biolinum, and `LibertineMono`. Cover design by Tobias Blesgen, Bonn.

Versicherung der Eigenständigkeit

Ich erkläre: Ich habe die vorgelegte Dissertation selbstständig und ohne unerlaubte fremde Hilfe und nur mit den Hilfen angefertigt, die ich in der Dissertation angegeben habe. Alle Textstellen, die wörtlich oder sinngemäß aus veröffentlichten Schriften entnommen sind, und alle Angaben, die auf mündlichen Auskünften beruhen, sind als solche kenntlich gemacht. Ich stimme einer evtl. Überprüfung meiner Dissertation durch eine Antiplagiat-Software zu. Bei den von mir durchgeführten und in der Dissertation erwähnten Untersuchungen habe ich die Grundsätze guter wissenschaftlicher Praxis, wie sie in der „Satzung der Justus-Liebig-Universität Gießen zur Sicherung guter wissenschaftlicher Praxis" niedergelegt sind, eingehalten.

Angaben zu auf künstlicher Intelligenz (KI) basierender Hilfen wie ChatGPT oder SchulKI von OpenAI oder Gemini von Google zur Erstellung meiner Dissertation (Zutreffendes angekreuzt):

☐ Ich habe bei der Erstellung dieses Textes kein KI-Tool verwendet.

☐ Ich habe ein KI-Tool in den folgenden Bereichen eingesetz:

- ☐ Ideen finden, meine Kreativität anregen
- ☐ Verstehen von Konzepten, Recherche von Fakten und Definitionen
- ☐ Optimierung eines von mir verfassten Textes
- ☐ Erstellen ganzer Textpassagen nach meinen Vorgaben

Folgende KI-Tools habe ich verwendet, damit aufgeführte Teile meines Textes von dem Tool wie folgt profitiert haben: ChatGPT, Perplexity AI und Google Gemini.

Datum	*Unterschrift*

Acknowledgements

I would like to start my acknowledgements by thanking the whole SuperKEKB and Belle II team for immense efforts and full commitment to running the experiment, allowing hundreds of researchers to flex their curiosity in physics.

First and foremost, I would like to thank my supervisor, Sören Lange, for sharing expertise, mentoring and entrusting freedom along my PhD journey. The adoptable and human atmosphere in the working group has been a perfect environment for a well-balanced commitment to research.

I would also like to thank Elisabetta Prencipe for – along with the valuable experience earned over the years of work on the analysis – the continuous commitment to research, even when the career path took unpredictable turns. The insights I learned from you go far beyond physics.

Additionally, I would like to thank Simon Reiter, Björn Spruck, Maiko Takahashi and other collaborators for help on the service task, and to Andrii Dashko for advising on the theoretical overview provided in this thesis.

I sincerely thank my family for unconditional support and faith. I have discovered my passion to physics during early years of the high school, and my parents have been on the side of my dreams since. Thank you.

Lastly, from the bottom of my heart, I would like to thank my fiancé. You are the most important finding I made along the PhD journey. I am incredibly lucky, to have you on my side not only as a partner, but also as a remarkably bright physisist, supporting me in every possible way. Your love and care helped me to endure challenges and slumps in spirit. Thank you for helping me write this chapter. I am excited to start the next one.

Kurzdarstellung

Diese Dissertation fasst meinen Beitrag zu zwei Themen zusammen: der Suche nach vierquark-Zuständen in den Daten des Belle-Experiments sowie der Untergrundüberwachung für den Pixeldetektor (PXD).

Zum ersten Thema: Das Belle-Experiment war von 1999 bis 2010 am KEKB-Beschleuniger in Tsukuba, Japan, in Betrieb. Während dieser Laufzeit sammelte der Belle-Detektor knapp unter 1 ab^{-1} an Kollisionsdaten, größtenteils bei der Schwerpunktsenergie der $\Upsilon(4S)$-Resonanz, die überwiegend in ein Paar von B-Mesonen zerfällt. Der vollständige Datensatz umfasst etwa eine Milliarde B-Mesonenpaare und zählt damit zu den wertvollsten Datensatz für Messungen von seltenen Zerfällen in der B-Meson-Physik.

Im Jahr 2003 beobachtete Belle den sogenannten $X(3872)$, einen Zustand, der nicht in das konventionelle Charmonium-Spektrum passt und weithin als exotisch gilt. Zahlreiche weitere unkonventionelle $Q\bar{Q}$-ähnliche Zustände wurden anschließend von Belle und anderen Experimenten entdeckt. Ein weiteres aktiv beitragendes Experiment — LHCb am CERN in der Schweiz — berichtete 2017 und 2021 über mehrere exotische Kandidaten im Zerfallskanal $B^- \to J/\psi\phi K^-$. Trotz der beschränkten Quantenzahlen wurde die Beobachtung von sieben neutralen X-Kandidaten mit $c\bar{c}s\bar{s}$-Quarkinhalt gemeldet, viele davon erstmals. Da präzisere Messungen dieser Zustände entscheidend für das Verständnis ihrer Natur sind, wurde eine Suche nach $c\bar{c}s\bar{s}$-Kandidaten in einem alternativen Produktionsmechanismus vorgeschlagen.

In dieser Arbeit berichten wir über die Suche nach diesen und möglicherweise weiteren exotischen Zuständen mit $c\bar{c}s\bar{s}$-Quarkinhalt in den Prozessen $e^+e^- \to D_s^+ D_{s0}^*(2317)^-$ und $e^+e^- \to D_s^+ D_{s1}(2460)^-$ in der Kontinuumsproduktion unter Verwendung des vollständigen Belle-Datensatzes. Die Analyse ist im Vergleich zu früheren Studien empfindlich gegenüber einem breiteren Bereich von Quantenzahlen und untersucht einen bislang nicht betrachteten Produktionsmechanismus. Sie basiert auf Signal-Monte-Carlo-Daten, in denen die Ereignisrekonstruktion überprüft wird; auf generischen Monte-Carlo-Simulationen, in denen komplexe Cross-Feed-

Untergründe untersucht werden; sowie auf realen Daten, in denen eine blinde Suche nach exotischen Kandidaten durchgeführt wird.

Zum zweiten Thema dieser Dissertation: Das Belle-II-Experiment ist der Nachfolger des Belle-Experiments und zeichnet seit 2018 Kollisionsdaten am aufgerüsteten SuperKEKB-Beschleuniger auf, der am selben Standort betrieben wird. Die umfassende Aufrüstung umfasste wesentliche Verbesserungen des Beschleunigerdesigns, das nun höhere Schwerpunktsenergien, höhere momentane Luminosität und geringere Energieasymmetrie erreicht, was ein breiteres Physikprogramm ermöglicht. Die Modernisierung des Belle-II-Detektors beinhaltete Verbesserungen aller Teildetektoren sowie die Entwicklung eines neuen innersten Pixeldetektors, der eine Vertexauflösung in Strahlrichtung von 25 μm erreichen soll. Diese Aufrüstungen zielen auf eine momentane Luminosität von bis zu 6×10^{35} cm^{-2}s^{-1} (ein Faktor 30 höher als Belle) und ermöglichen eine Gesamtdatensammlung von bis zu 50 ab^{-1} über die Laufzeit des Experiments.

Die gesteigerte Luminosität, die Nähe des PXD zum Wechselwirkungspunkt und die Auslese über 7,68 Millionen Kanäle stellen hohe Anforderungen an das Datenerfassungssystem (DAQ). Bei der Designluminosität wird eine Ausleserate von über 18 Gb/s erwartet — ein Faktor 10 höher als bei allen anderen Teildetektoren zusammen. Daher wurde eine eigenständige DAQ-Lösung ausschließlich für den PXD entwickelt: das System *Online Selection Nodes* (ONSEN), entwickelt in Gießen in Zusammenarbeit mit dem IHEP Peking.

Eine Herausforderung für den PXD ist die erhöhte Unrergrundstrahlung. Verschiedene strahlinduzierte Quellen wurden untersucht und ihre Effekte minimiert. Eine dieser Quellen ist die indirekte Synchrotronstrahlung (SR), die durch Rückstreuung von der Innenwand des Beryllium-Strahlrohrs entsteht und vor allem die innere Lage des PXD betrifft. Um dies zu mindern, wurden während der ersten langen Abschaltphase 2021–2022 Gegenmaßnahmen im Strahlrohrdesign umgesetzt. Dadurch änderte sich das SR-Muster, was eine Aktualisierung des Echtzeit-Überwachungssystems *Photon Monitor* erforderlich machte. Diese Aktualisierung, im Rahmen dieser Arbeit durchgeführt, berücksichtigt die neuen SR-Bedingungen, bewertet die Untergrundkontamination in früheren Datennahmeperioden und liefert eine vorhersagebasierte Abschätzung der erwarteten SR-Belastung für zukünftige Messungen.

Abstract

This thesis summarises my contribution to two topics: search for quarkonium-like four-quark states in data of the Belle experiment and background monitoring for the pixel detector (PXD).

As for the first topic, the Belle experiment was operating from 1999 to 2010 at the KEKB accelerator in Tsukuba, Japan. During the running period, the Belle detector accumulated just under 1ab^{-1} of collision data, most of which was collected at the centre-of-mass energy of the $\Upsilon(4S)$ resonance, which predominantly decays into a pair of B mesons. The full Belle dataset includes around 1 billion of B meson pairs, making it one of the most valuable samples for rare decay measurements in B meson physics.

In 2003 Belle observed the so called $X(3872)$, a state which does not fit the conventional charmonium spectrum and is widely considered as an exotic candidate. Numerous discoveries of unconventional $Q\bar{Q}$-like candidates followed by Belle and other experiments. Another experiment actively contributing to the quarkonium field – LHCb at CERN, Switzerland – reported observation of multiple exotic candidates in the $B^- \to J/\psi\phi K^-$ decay channel in 2017 and 2021. Despite being constrained in the accessible quantum numbers, the analysis reported the observation of seven neutral X candidates with the $c\bar{c}s\bar{s}$ quark content, many of which had been observed for the first time. Since rediscoveries or refinements of the measurements of these X-states by other experiments are essential to elucidate their nature, a search for $c\bar{c}s\bar{s}$ candidates in an alternative production mechanism was suggested.

In this thesis, we report a search for these and potentially other yet undiscovered exotic states with a $c\bar{c}s\bar{s}$ quark content in $e^+e^- \to D_s^+ D_{s0}^*(2317)^-$ and $e^+e^- \to D_s^+ D_{s1}(2460)^-$ inclusive processes in the continuum, using the full Belle dataset. The proposed analysis, in comparison with earlier studies, is sensitive to a wider range of quantum numbers and probes a different production mechanism, which was not studied before. The analysis is performed using signal Monte-Carlo simulation, where event reconstruction is verified; generic Monte-Carlo, where complex cross-feed

background effects are studied; and data, where a blind search for exotic candidates is carried out.

As for the second topic of this thesis, the Belle II experiment is the successor of the Belle experiment, which began recording collision data in 2018. It operates at the upgraded SuperKEKB accelerator, which occupies the same site as its predecessor. The comprehensive on-site facility upgrade included major improvements to the accelerator design, which, among other enhancements, can now reach higher centre-of-mass energies, achieve higher instantaneous luminosity, and operates with a reduced energy asymmetry, enabling a broader physics programme. The upgrade of the Belle II detector involved, to varying extents, improvements to all individual sub-detectors and the development of a new innermost pixel detector, which is designed for reaching the vertex reconstruction resolution in beam direction of 25 μm. These hardware upgrades are aimed to set a new instantaneous luminosity record of up to 6×10^{35} $\text{cm}^{-2}\text{s}^{-1}$ (a factor of 30 higher than the record set by Belle), allowing the experiment to accumulate a total dataset of up to 50 ab^{-1} over the anticipated lifespan of the Belle II experiment.

The increased luminosity, the proximity of the PXD to the interaction point, and the readout via 7.68 million channels impose stringent requirements on the PXD data acquisition system (DAQ). At the design luminosity, the readout rate is expected to exceed 18 Gb/s, which is factor of 10 higher than the combined readout rate of all other sub-detectors. Therefore, a standalone DAQ solution was developed exclusively for the PXD. It includes, in particular, a data acquisition and data truncation system known as Online Selection Nodes (ONSEN), developed in Gießen in collaboration with the IHEP Beijing.

A challenge for the PXD is exposure to increased background radiation. Various beam-induced background sources were considered, and their effects had been mitigated or minimised. One such source is the indirect synchrotron radiation (SR), which originates from backscattering off the inner wall of the beryllium beam pipe and primarily affects the inner layer of the PXD. To mitigate this effect, countermeasures were implemented in the beam pipe design during the first long shutdown, which took place from mid-2021 to the end of 2022. As a result of these changes, the SR pattern has changed, necessitating an update to the real-time photon-radiation monitoring tool known as the Photon Monitor, which was accomplished as a part of this thesis. Consequently, this thesis also reports on the update to the Photon Monitor, which accounts for changes of the SR pattern, provides an assessment of background contamination in the previous data taking periods, and delivers a beam optics- and currents-aware prediction of the expected SR contamination for the future runs.

Contents

Chapter 1

Introduction

Experimental particle physics underwent a spectacular transformation from compact on-desk devices developed by individual enthusiasts to astonishing in scale international research facilities that include thousands of engineers and researchers working for years hand-to-hand to ensure stable operation, reliable data taking and unbiased data analysis. At each step of this evolution, scientific interest was frequently sparked by theoretical considerations that were developed alongside. Collaboration between experimental and theoretical physicists has been instrumental in generating new ideas and test cases for unresolved problems in modern physics.

After turning the page of successful predecessors, such as Belle, BaBar, Tevatron, HERA, etc., modern accelerators can be divided into two main sub-categories: electron-positron machines representing the *Intensity frontier*, where high luminosity is reached in relatively clean environment, allowing rare processes to be studied; and proton-proton colliders, which act on the side of the *Energy frontier*, where higher centre-of-mass energy allows producing heavier particles, while large pp cross-section generates thousands (per collision) light particles allowing to reach higher count of rare events. The most prominent lepton-lepton experiments are Belle II (Japan) – the next generation B-factory, and BESIII (China) – a charm-physics facility capable of operating at the tunable centre-of-mass energy. The zoo of pp-based experiments is mostly populated by LHC-based experiments (Switzerland/France), namely LHCb – an asymmetric spectrometer devoted to B-physics, CMS – a general-purpose detector that gained recognition through its role in the discovery of the Higgs boson, ATLAS – the largest LHC-based detector that is mostly recording Pb-Pb collisions data and is therefore focussed at the heavy-ion physics, and ALICE – an experiment mostly dedicated to the study of quark-gluon-plasma.

The Belle II experiment, which constitutes the main focus of this thesis, is set on a course of continuing the glorious legacy of the Belle experiment, which, in particular, earned its fame by observing CP-violation in B-decays[1] and discovering the first exotic $c\bar{c}$-like candidate – $X(3872)$. It is designed to reach the instantaneous luminosity that is 40 times higher than the one of Belle and accumulate up to 50 times more data. In order to achieve these goals, a brand-new detector was developed through a concerted international effort. In particular, to achieve higher vertexing precision with tolerance to increased background exposure, a state-of-the-art pixel detector (PXD) was developed by a collaboration of German universities. Due to extreme rate of data[2] it is designed to record via 7.6M channels, a standalone data acquisition system is utilised. Development of the PXD triggered countless number of task and challenges that had to be addressed, such as data buffering and truncation, slow control, calibration, background monitoring, etc. The latter is particularly critical for data quality and is touched upon in Chapter 4.

Even though Belle is the previous-generation experiment, Belle II has not yet accumulated a data sample comparable in size to that of Belle due to various challenges in establishing stable machine operation and data taking in recent years[3]. This elevates the relevance of the Belle data sample, making it feasible for analyses of yet unaddressed physics questions. In particular, Belle data have been utilised in numerous studies of heavy quarkonia, where not only the aforementioned $X(3872)$ exotic candidate was observed for the first time, but also many other $c\bar{c}$- and $b\bar{b}$-like candidates have been reported, as discussed in Chapter 5. This motivates us to revisit the charmonium-like spectroscopy by looking for $c\bar{c}s\bar{s}$ candidates in Belle, which is reported in Chapter 6.

[1] The achievement that was recognised with a Nobel Prize in 2008.
[2] up to 20 Gb/s at target luminosity
[3] It is, however, approaching the 1ab^{-1} milestone and is expected to surpass it by the summer of 2026.

Chapter 2

Theoretical overview

In this section, the fundamental principles and formalisms of the Standard Model of particle physics are reviewed. These principles, encoded in the Standard Model Lagrangian within the Quantum Field Theory (QFT) formalism, have been remarkably successful over the recent decades in describing a wide range of phenomena in particle physics. However, there are certain observations incompatible with the Standard Model framework. This motivates an extensive and multifaceted search for physics beyond the Standard Model, to which the Belle II experiment is expected to make significant contributions.

2.1 Particle physics in the Standard Model framework

Particle physics studies elementary particles and interactions between them. The most successful theoretical framework describing these phenomena, known as the *Standard Model of Particle Physics*, was developed in the mid-20$^{\text{th}}$ century based on non-Abelian gauge theories introduced by Yang and Mills [1], the *Electroweak Theory* formulated by Glashow [2], Weinberg, and Salam [3] and the Higgs mechanism proposed by Higgs, Englert and Brout [4, 5]. At the time of its formulation, the theory predicted several phenomena that were later confirmed experimentally, such as the weak neutral current discovered in 1973 [6] and the existence of the *Higgs Boson* first observed in 2012 [7]. The Standard Model (SM) is formulated within the *Quantum Field Theory* (QFT), a formalism that consistently combines classical field theory, quantum mechanics, and special relativity. Within this framework, the two central components of the SM are *Quantum Chromodynamics* (QCD) and the *Electroweak Theory*, which reduces to *Quantum Electrodynamics* (QED) after spontaneous symmetry breaking.

The SM describes fundamental interactions between elementary particles via the following forces:

- **Strong Force** — a short-range interaction governed by QCD, with a characteristic length scale[1] responsible for colour confinement and nuclear binding.
- **Weak Force** — an extremely short-range interaction[2] described by the electroweak $SU(2)_L \times U(1)_Y$ theory, which governs processes such as beta decay.
- **Electromagnetic Interaction** — an infinite-range interaction mediated by massless photons and acting between electrically charged particles.

Fig. 2.1 illustrates the particles introduced in the Standard Model: quarks (blue), leptons (red), and bosons (yellow and gray). Quarks and leptons are spin-$1/2$ fermionic particles composing matter observed in the visible universe. Massive leptons ($e^{\pm}$, $\mu^{\pm}$ and $\tau^{\pm}$) carry integer electric charge and distinct lepton flavours, while neutral leptons – known as neutrinos (ν_e, ν_μ and ν_τ) – are massless in the Standard Model framework. In contrast, quarks carry fractional electric charge and an additional colour charge, which confines them within hadrons. Quarks and leptons are arranged into three generations. Each generation contains a pair of quarks (up-type and down-type), a charged lepton, and a neutrino. The masses of particles generally increase with generation order[3], but occasionally violate the hierarchy within a generation.

Fundamental bosons are integer-spin particles that mediate the aforementioned forces. Gluons (g), photons (γ), and $W^{\pm}/Z$ bosons arise as excitations of the associated gauge fields and mediate the strong, electromagnetic, and weak forces, respectively. The only scalar boson – Higgs (H) – is responsible for the generation of mass for quarks, charged leptons and vector bosons via the Higgs mechanism.

The remaining fundamental interaction not mentioned above – gravity – is not described by the Standard Model. Although the existence of a particle mediating gravitational interactions is anticipated in the quantum theory of gravity, a consistent quantum description of General Relativity has not yet been established. Fortunately, unlike the other fundamental forces, gravitational interactions are suppressed by many orders of magnitude and are therefore generally negligible within the SM framework.

[1] $r \sim \Lambda_{\text{QCD}}^{-1} \sim 10^{-15}\,\text{m}$
[2] $r \sim m_W^{-1} \sim 10^{-18}\,\text{m}$
[3] including estimated upper limits on neutrino masses

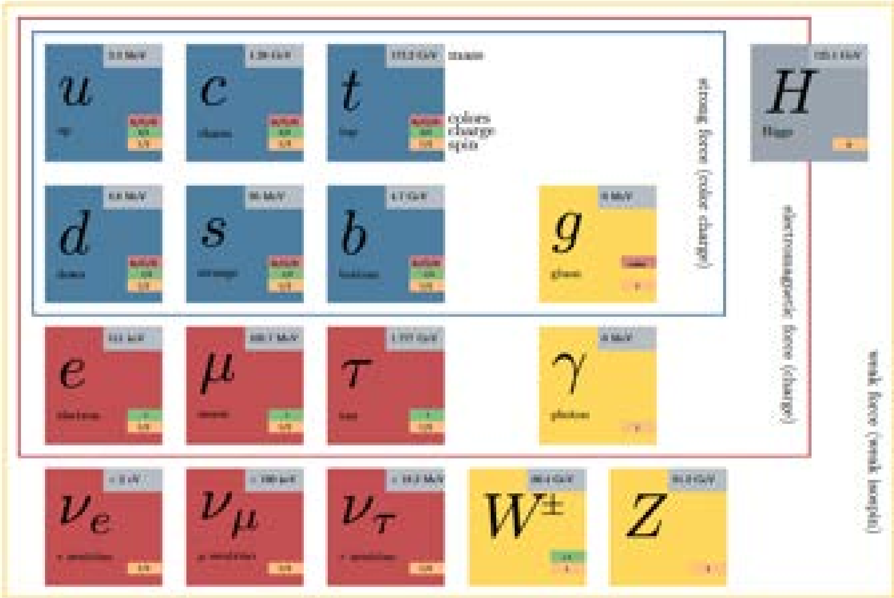

Figure 2.1: Fundamental particles of the Standard Model.

2.2 The Standard Model Lagrangian

The Standard Model is based on the following gauge group

$$G = SU(3)_c \times SU(2)_L \times U(1)_Y, \tag{2.1}$$

where the subscript c refers to colour, subscript L indicates the left-chiral nature of the $SU(2)$ coupling, and Y stands for the *weak hypercharge* quantum number related to the electric charge as

$$Y = Q - T_L^3, \tag{2.2}$$

where T_L^3 is the third component of the $SU(2)_L$ weak isospin and Q is the electric charge.

The $SU(3)_c$ factor is a non-chiral QCD component that has 8 gauge bosons (gluons) and gauge coupling g_s. It acts on colour indices, α ($\alpha = 1, 2, 3$), of the left (L) and right (R) chiral quarks. In contrast, the electroweak $SU(2)_L \times U(1)_Y$ factor is chiral. The $SU(2)_L$ group has gauge coupling g, gauge bosons $W^i, i = 1, 2, 3$, and acts only on the $L-$chiral fermions, leading to charged (associated with $W^{\pm}$)

and neutral (associated with Z^0) current interactions. The abelian $U(1)_Y$ factor is described with a coupling constant g' and a gauge boson B. It is chiral and acts both on L- and R-handed fermions with different charges. The spontaneous symmetry breaking (SSB) of $SU(2)_L \times U(1)_Y$ results in a single unbroken $U(1)_Q$, which results in a massless photon, a massive Z^0 – linear combination of W^0 and B bosons – as well as charged $W^{\pm}$.

The Standard Model Lagrangian density, stemming from the gauge symmetry group introduced above, can be written as

$$\mathcal{L} = \mathcal{L}_{\text{gauge}} + \mathcal{L}_f + \mathcal{L}_H + \mathcal{L}_{\text{Yuk}}, \tag{2.3}$$

where subscripts mark individual terms referring to gauge, fermion, Higgs and Yukawa sectors of the SM theory, respectively.

• The gauge term is expressed as

$$\mathcal{L}_{\text{gauge}} = -\frac{1}{4}G^a_{\mu\nu}G^{\mu\nu,a} - \frac{1}{4}W^i_{\mu\nu}W^{\mu\nu,i} - \frac{1}{4}B_{\mu\nu}B^{\mu\nu}, \tag{2.4}$$

where the respective field strength tensors for $SU(3)_c$, $SU(2)_L$ and $U(1)_Y$ are

$$\begin{aligned} G^a_{\mu\nu} &= \partial_\mu G^a_\nu - \partial_\nu G^a_\mu - g_s f_{abc} G^b_\mu G^c_\nu, \quad a,b,c = 1 \cdots 8 \\ W^i_{\mu\nu} &= \partial_\mu W^i_\nu - \partial_\nu W^i_\mu - g\epsilon_{ijk} W^j_\mu W^k_\nu, \quad i,j,k = 1 \cdots 3 \\ B_{\mu\nu} &= \partial_\mu B_\nu - \partial_\nu B_\mu. \end{aligned} \tag{2.5}$$

Due to the non-abelian nature of $SU(3)_c$ and $SU(2)_L$, gluons (g) feature three- and four-point self-interactions, unlike B bosons.

• The fermion part of the Standard Model involves $F = 3$ families of quarks and leptons, each consisting of

$$\begin{aligned} L-\text{doublets:} \quad & q^0_{mL} = \begin{pmatrix} u^0_m \\ d^0_m \end{pmatrix}_L, \quad \ell^0_{mL} = \begin{pmatrix} \nu^0_m \\ e^0_m \end{pmatrix}_L, \\ R-\text{singlets:} \quad & u^0_{mR},\ d^0_{mR},\ e^0_{mR}. \end{aligned} \tag{2.6}$$

where, the superscript ^{0} marks *weak eigenstates*[4]. The fermions' features touched upon in the previous section are reflected in the Eq. 2.6 notation. Namely, u^0 and

[4] *i.e.* properties of field gauge transformations are defined as such that transform elements of each doublet into each other under $SU(2)$

d^0 are up- and down-type quarks, which after SBB acquire electric charges $2/3$ and $-1/3$, respectively. Each quark also carries a colour index, which is dropped in the notation above for the sake of simplicity. The e^0 and ν^0 leptons are colour singlets with electric charge -1 and 0, respectively. The inclusion of right-handed neutrino singlets (ν^0_{mR}) is tentative, as they are required by many models for neutrino mass generation[5], but they are dropped in the notation above due to their absence in nature. Since $U(1)_Y$ commutes with $SU(3)_c$ and $SU(2)_L$, the hypercharge values (see Eq. 2.2) are identical for all members of the $SU(3)_c \times SU(2)_L$ multiplets: $\frac{1}{6}$, $\frac{2}{3}$ and $-\frac{1}{3}$ for q^0_{mL}, u^0_{mR} and d^0_{mR}; and $-\frac{1}{2}$, 0 and -1 for ℓ^0_{mL}, ν^0_{mR} and e^0_{mR}, respectively.

The chiral representations of the $SU(2)_L \times U(1)_Y$ gauge group forbids fermion mass terms in $\mathcal{L}_f$. As a consequence, $\mathcal{L}_f$ consists solely of kinetic terms and gauge interactions, and is invariant under a global $U(3)^6$ flavour symmetry. This invariance implies that the Lagrangian is insensitive to independent unitary rotations among the three families. Moreover, since the QCD gauge group $SU(3)_c$ is flavour-blind and commutes with the flavour symmetry, strong interactions preserve this invariance. As a consequence, the number of independent fermion flavour structures in the fermionic term of the Lagrangian is significantly reduced

$$\begin{aligned}\mathcal{L}_f = \sum_{m=1}^{F} &\left(\bar{q}^0_{mL} i\not{D} q^0_{mL} + \bar{\ell}^0_{mL} i\not{D} \ell^0_{mL}\right. \\ &\left.+\bar{u}^0_{mR} i\not{D} u^0_{mR} + \bar{d}^0_{mR} i\not{D} d^0_{mR} + \bar{e}^0_{mR} i\not{D} e^0_{mR} + \bar{\nu}^0_{mR} i\not{D} \nu^0_{mR}\right).\end{aligned} \tag{2.7}$$

Here, the first term can be expanded as

$$\begin{aligned}\bar{q}^0_{mL} i\not{D} q^0_{mL} = i &\sum_{\alpha,\beta=1}^{3} \left(\bar{u}^{0\alpha}_{mL}\ \bar{d}^{0\alpha}_{mL}\right) \gamma^\mu \\ \times &\left[\left(\partial_\mu I + \frac{ig}{2}\vec{\tau}\cdot\vec{W}_\mu + ig' Y_{qL} I B_\mu\right)\delta_{\alpha\beta} + \frac{ig_s}{2}\vec{\lambda}_{\alpha\beta}\cdot\vec{G}_\mu I\right] \begin{pmatrix} u^0_{mL\beta} \\ d^0_{mL\beta}\end{pmatrix},\end{aligned} \tag{2.8}$$

where I is the $SU(2)$ identity matrix. The latter terms in Eq. 2.6 follow this expansion pattern. The Eq. 2.8 clearly illustrates that $SU(3)_c$ and $SU(2)_L \times U(1)_Y$ groups

[5]However, there are alternative ways to incorporate observed non-zero neutrino masses.

commute. Then, the gauge covariant derivatives for fermions can be expanded as

$$\begin{aligned}
D_\mu q^0_{mL} &= \left(\partial_\mu + \frac{ig}{2}\vec{\tau}\cdot\vec{W}_\mu + \frac{ig'}{6}B_\mu\right) q^0_{mL},\\
D_\mu \ell^0_{mL} &= \left(\partial_\mu + \frac{ig}{2}\vec{\tau}\cdot\vec{W}_\mu - \frac{ig'}{2}B_\mu\right) \ell^0_{mL},\\
D_\mu u^0_{mR} &= \left(\partial_\mu + \frac{2ig'}{3}B_\mu\right) u^0_{mR},\\
D_\mu d^0_{mR} &= \left(\partial_\mu - \frac{ig'}{3}B_\mu\right) d^0_{mR},\\
D_\mu e^0_{mR} &= \left(\partial_\mu - ig'B_\mu\right) e^0_{mR}.
\end{aligned} \tag{2.9}$$

where gluon couplings for the q^0_{mL}, u^0_{mR} and d^0_{mR} are prominent.

• The Higgs term of the SM Lagrangian density is expressed as

$$\mathcal{L}_\phi = \left(D^\mu\phi\right)^\dagger D_\mu\phi - V(\phi), \tag{2.10}$$

where $\phi = \begin{pmatrix}\phi^+\\ \phi^0\end{pmatrix}$ is the complex Higgs scalar doublet. The gauge covariance derivative is

$$D_\mu\phi = \left(\partial_\mu + \frac{ig}{2}\vec{\tau}\cdot\vec{W}_\mu + \frac{ig'}{2}B_\mu\right)\phi. \tag{2.11}$$

The term $V(\phi)$ entering the Eq. 2.10 is the Higgs potential, which is restricted by the $SU(2)_L \times U(1)_Y$ gauge invariance and renormalizability to

$$V(\phi) = +\mu^2\phi^\dagger\phi + \lambda\left(\phi^\dagger\phi\right)^2. \tag{2.12}$$

Negative μ^2 and positive λ values allow for non-zero vacuum expectation values (VEV), which spontaneously breaks electroweak symmetry and generates masses for $W^\pm$ and Z bosons.

• The Yukawa term ($\mathcal{L}_{\text{Yuk}}$) describes the interaction between the Higgs doublet and fermions, which generates mass of the latter by non-zero VEV of the Higgs field. For a generic number of fermion families F, it can be expressed as

$$\begin{aligned}
\mathcal{L}_{\text{Yuk}} = -\sum_{m,n=1}^{F} &\Big[\Gamma^u_{mn}\bar{q}^0_{mL}\tilde{\phi}u^0_{nR} + \Gamma^d_{mn}\bar{q}^0_{mL}\phi d^0_{nR}\\
&+\Gamma^e_{mn}\bar{\ell}^0_{mL}\phi e^0_{nR} + \Gamma^\nu_{mn}\bar{\ell}^0_{mL}\tilde{\phi}\nu^0_{nR}\Big] + h.c.,
\end{aligned} \tag{2.13}$$

where

$$\tilde{\phi} \equiv i\tau^2 \phi^\dagger = \begin{pmatrix} \phi^{0\dagger} \\ -\phi^- \end{pmatrix} \tag{2.14}$$

is a conjugate form of the Higgs doublet. Γ^u, Γ^d, Γ^e and Γ^ν are arbitrary $F \times F$ matrices determining fermion masses and mixings. Since no additional constraints are imposed on them[6], these matrices introduce most of the free parameters in the SM and break most of the $U(F)^6$ symmetries that are otherwise preserved for the rest of $\mathcal{L}$.

For example, the mn term of Γ^d and its Hermitian conjugate are

$$\begin{aligned} \Gamma^d_{mn} \bar{q}^0_{mL} \phi d^0_{nR} &= \Gamma^d_{mn} \left[\bar{u}^0_{mL} \phi^+ d^0_{nR} + \bar{d}^0_{mL} \phi^0 d^0_{nR} \right], \\ \Gamma^{d\dagger}_{nm} \bar{d}^0_{nR} \phi^\dagger q^0_{mL} &= \Gamma^{d*}_{mn} \left[\bar{d}^0_{nR} \phi^- u^0_{mL} + \bar{d}^0_{nR} \phi^{0\dagger} d^0_{mL} \right], \end{aligned} \tag{2.15}$$

which can be interpreted as interaction vertices depicted in Fig. 2.2. Yukawa interactions flip the chirality, but conserve the electric charge. Non-diagonal $m \neq n$ Yukawa terms are responsible for mixing between fermion families.

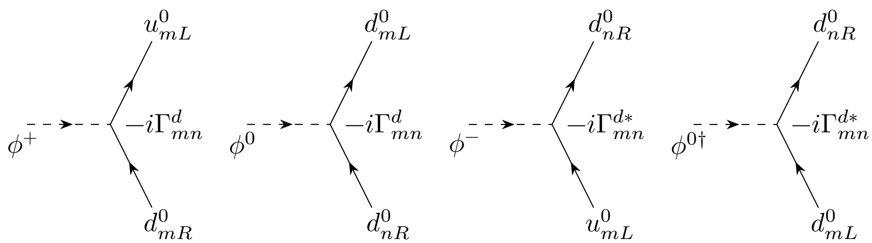

Figure 2.2: Yukawa couplings associated with $\Gamma^d_{mn} \bar{q}^0_{mL} \phi d^0_{nR} +$ h.c.

If one explicitly expands gauge and fermionic terms given in Eqs. (2.4) and (2.7) using the respective covariant derivatives defined in Eqs. (2.5) and (2.9), the summands can be regrouped in a phenomenology-oriented manner, where the kinetic, QCD and electroweak parts of the Lagrangian are isolated. Namely, terms quadratic in fermionic fields are identified as kinetic, contributions involving the $SU(3)_c$ gauge fields as QCD, and those involving the $SU(2)_L$ and $U(1)_Y$ gauge fields as electroweak. Upon performing this regrouping, the Lagrangian originally written as in Eq. 2.3 can be rewritten as

$$\mathcal{L} = \mathcal{L}^f_{\text{Kinetic}} + \mathcal{L}_{QCD} + \mathcal{L}_{EW} + \mathcal{L}_H + \mathcal{L}_{\text{Yuk}}. \tag{2.16}$$

[6] $i.e.$ they are not necessarily required to be Hermitian, symmetric, diagonal or real

This decomposition is purely notational and introduces no additional assumptions beyond those already contained in the original formulation.

The QCD term $\mathcal{L}_{QCD}$ describes the strong interaction associated with the non-Abelian gauge $SU(3)_c$ color symmetry. Its fundamental degrees of freedom are quarks, which carry color charge, and gluons – gauge bosons mediating the interaction. Due to the non-Abelian structure of the gauge group, gluons also carry color charge and therefore interact among themselves.

A key property of QCD is asymptotic freedom: the strong coupling decreases at high energies, allowing perturbative calculations, while it becomes large at low energies. This behavior introduces the characteristic scale $\Lambda_{\mathrm{QCD}} \sim 200\,\mathrm{MeV}$, below which the theory enters a strongly coupled regime. In this regime, the phenomenon of confinement arises, implying that colored particles cannot exist as free asymptotic states. Instead, the observable low-energy spectrum consists of color-singlet bound states – hadrons, the simplest of which are mesons, composed of a quark-antiquark pair, and baryons, consisting of three quarks.

The electroweak interaction term of the Standard Model Lagrangian $\mathcal{L}$ can be written in terms of fermionic currents as

$$\mathcal{L}_{\mathrm{EW}} = -\frac{g}{\sqrt{2}}\left(W_\mu^+ J_W^{\mu+} + W_\mu^- J_W^{\mu-}\right) - \sqrt{g^2 + g'^2}\, Z_\mu J_Z^\mu - e A_\mu J_Q^\mu, \tag{2.17}$$

where $J_W^{\mu\pm}$, J_Z^μ, and J_Q^μ denote the charged, neutral, and electromagnetic fermionic currents, respectively. After electroweak symmetry breaking, the L-handed fermion fields are rotated from the weak interaction basis to the mass basis by unitary matrices A_L^f, defined as

$$f_L^0 = A_L^f\, f_L, \tag{2.18}$$

where $f_L = u_L, d_L, e_L, \nu_L$ and the fields on the right-hand side correspond to the fermion mass eigenstates.

In the mass basis, the charged current then takes the form

$$J_W^{\mu+} = 2\bar{\nu}_L \gamma^\mu A_L^{\nu\dagger} A_L^e e_L + 2\bar{u}_L \gamma^\mu A_L^{u\dagger} A_L^d d_L. \tag{2.19}$$

This defines the lepton and quark $F \times F$ unitary mixing matrices

$$V_\ell \equiv A_L^{\nu\dagger} A_L^e \qquad \text{and} \qquad V_q \equiv A_L^{u\dagger} A_L^d, \tag{2.20}$$

respectively, where u_L, d_L, e_L, and ν_L are F-component vectors. The matrix V_q describes the likelihood of transitions between up- and down-type quarks. An analogous A_ℓ matrix is defined for the leptonic sector.

A complex unitary matrix V_q can be defined[7] by $(F-1)^2$ parameters, which include $F(F-1)/2$ *angles* and $(F-1)(F-2)/2$ *phases*. For the nature-motivated case of $F=3$ families, the quark mixing matrix is commonly dubbed as V_{CKM}

$$V_{CKM} = \begin{pmatrix} V_{ud} & V_{us} & V_{ub} \\ V_{cd} & V_{cs} & V_{cb} \\ V_{td} & V_{ts} & V_{tb} \end{pmatrix} \tag{2.21}$$

It is defined by three mixing angles and an observable CP-violation phase. The latter one is in charge of the discrepancy between V_{CKM} and V^*_{CKM} matrix elements. The strength of up-down transitions is illustrated in Fig. 2.3. It clearly illustrates that transitions within a family are strongly favoured.

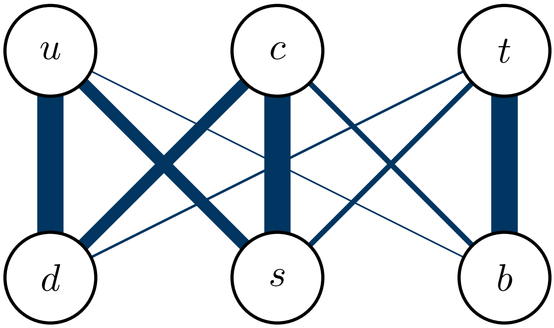

Figure 2.3: V_{CKM} matrix elements visualized as intensity lines for transitions between up- and down-type quarks. Square root scaling of V_{ij} elements is applied to improve visibility.

Several V_{CKM} matrix parametrisations exist. The one widely adopted in the Belle community includes α, β and γ mixing angles defined as following

$$\alpha = \arg\left(-\frac{V_{td}V^*_{tb}}{V_{ud}V^*_{ub}}\right), \quad \beta = \arg\left(-\frac{V_{cd}V^*_{cb}}{V_{td}V^*_{tb}}\right), \quad \gamma = \arg\left(-\frac{V_{ud}V^*_{ub}}{V_{cd}V^*_{cb}}\right). \tag{2.22}$$

They form a so-called unitarity triangle illustrated in Fig. 2.4, in which the unitarity of the CKM matrix implies the $\alpha+\beta+\gamma=\pi$ constraint.

The unitarity and relations between CKM-matrix elements have been subjected to thorough experimental testing in various decays and scattering processes ($e.g.$ those illustrated in Fig. 2.4). However, the magnitude of the CP-violation measured within the CKM matrix alone is insufficient to account for *baryogenesis* as a whole, meaning an additional – yet unknown – source of CP breaking is required.

[7]when rotational invariance is accounted for quark fields

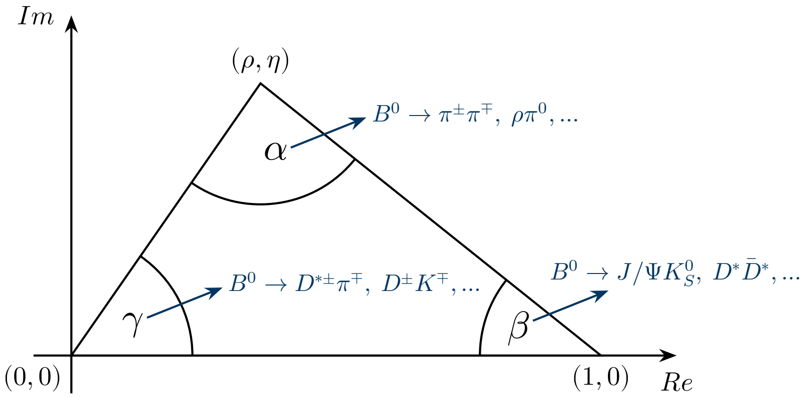

Figure 2.4: Illustration of the unitarity triangle in the notation commonly used in the Belle II community. Blue arrows indicate processes, in which the respective mixing angles can be measured.

2.3 Open problems of the Standard Model

Despite the tremendous success of the Standard Model, there is a plethora of problems that so far could not be resolved in the developed framework. They include, but are not limited to:

The Fermion Problem
The composition of terrestrial matter includes solely the fermions of the first family. Meanwhile, the existance of the other two, which appear as heavier copies of the first one, is justified by the role they played in the early universe. Both the number of families F and the mass hierarchy that spreads across 5 orders of magnitude between the lightest ($e^{\pm}$) and the heaviest (t) fermion are not justified within the SM. Furthermore, non-diagonal elements of the *CKM* and the *PMNS* mixing matrices differ by several orders of magnitude and are both nearly diagonal, which could hint at another, yet undisclosed, flavour symmetry. Several beyond SM (BSM) models attempt to describe these phenomena [8–12], but adequate experimental signatures are essential to favour one.

The Strong CP Problem
The magnitude of the CP violation remains orders of magnitude below the rate required to explain the matter-antimatter asymmetry observed in the visible universe. In contrast to the CP-violation mechanism incorporated in the Yukawa and Electroweak sectors of the SM, the strong interaction mysteriously seems to feature CP conservation. While this phenomenon is not explained within the SM framework,

some models suggest that parity might be violated spontaneously [13]. However, such models usually lead to difficult phenomenological and cosmological problems. Another possibility is the Peccei-Quinn mechanism [14], which imposes an extra global $U(1)$ symmetry, making θ_{QCD} dynamically variable. Spontaneous breaking of the suggested symmetry introduces an additional very light pseudo-Goldstone boson known as the *axion* [15, 16]. Experimental efforts probe this hypothesis by searching for *invisible axion-like particles* (ALPs) in processes involving electromagnetic coupling to $F_{\mu\nu}\tilde{F}^{\mu\nu}$, as a "shining through the wall" effect[8], etc.

The Higgs Problem

The Higgs field is responsible for generating the masses of the $W^{\pm}$ and Z bosons as well as those of charged fermions through the mechanism of electroweak SSB. The physical Higgs boson corresponds to the quantum excitation of this field and has been observed with the mass of approximately $M_H \simeq 125\,\text{GeV}/c^2$, close to the electroweak scale. However, the bare mass parameter of the Higgs field receives quadratically divergent radiative corrections, implying that an extreme degree of fine-tuning is required in order to obtain the physical Higgs boson mass at the electroweak scale. Given that it creates tension with the *naturalness* principle[9], multiple SM extensions have been proposed to stabilize the Higgs mass, including supersymmetry [17], composite or pseudo-Goldstone Higgs models [18], models with extra dimensions [19], etc. The current precision of electroweak measurements and flavour studies constrain most of these models. The possibility remains that the observed scalar is part of a richer Higgs sector, as predicted in most of the aforementioned extensions of the Standard Model.

The Gravity

Since general relativity is not a quantum theory, it can not be consistently unified with the QFT description of the SM. Therefore, drastically alternative perspectives exist, such as *loop quantum gravity* [20], *Kaluza-Klein theory* [21], supergravity [22–24] and, of course, string theories. The latter appear to be the most promising, but they struggle with infinite possibilities of string vacua, without an obvious selection principle. Potentially, they might become prominent at the higher energy scale, which is not reachable at the site of modern experiments.

The Gauge Symmetry Problem

The SM is built around the gauge symmetry G (see Eq. 2.1). However, only its electroweak term is chiral and parity-violating. Similarly, the *quantisation of charge*, which is essential to make charge neutrality possible, is not explained within the SM. The complicated gauge structure might presume a certain interaction unification either via a superstring of a kind [25–28], or via grand unification [29]. In either way,

[8] $i.e.$ photon-axion-photon conversion producing a signal on the other side of an opaque barrier

[9] $i.e.$ fundamental parameters should not depend on delicate cancellations

it would explain both phenomena though embedding of hypercharge values Y, some of which would be forbidden due to higher symmetries.

2.4 Belle II experiment physics programme

The activity in individual Belle II working groups (WGs) gives a good snapshot of the Belle II physics programme and outlines the ongoing experimental efforts aimed at the search for answers to the open questions of the SM and beyond discussed above. Its brief summary is provided below.

The Semileptonic and Leptonic B-Decays WG focuses on semileptonic $b \to c$ and $b \to u$ transitions to measure the CKM matrix elements $|V_{ub}|$ and $|V_{cb}|$, probing for new physics in both inclusive and exclusive processes. Charged and radiative leptonic decays, $e.g.$ $B^+ \to e/\mu/\tau$ or $B^+ \to \ell\gamma\nu$, are also attributed to this WG.

The Radiative and Electroweak Penguins (EWP) WG gathers under its umbrella

- Inclusive $b \to s\gamma$ radiative decays via inclusive, partial and full reconstruction tagging;
- Inclusive $b \to s\gamma$ and $b \to d\gamma$ radiative decays via exclusive methods;
- Exclusive $b \to s\gamma$ and $b \to d\gamma$ radiative decays relevant in the context of polarisation or asymmetry studies, $e.g.$ $B \to K_1\gamma, K^*\gamma$ or $B \to \rho\gamma, \omega\gamma, a_1\gamma$;
- EWP with neutrinos, $e.g.$ $B \to K\nu\bar{\nu}$ or $B \to \nu\bar{\nu}$;
- Inclusive dilepton decays, $e.g.$ $B \to X_s\ell^+\ell^-$;
- Rare and forbidden decays, $e.g.$ $B_s \to \gamma\gamma$, neutral leptonic $B^0_{(s)} \to \tau\tau$, or lepton or/and flavour violating $B \to \ell\tau$ decays.

The Time-Dependent CP Violation (TDCPV) WG revisits measurement of unitarity triangle parameters. Namely, the α angle is measured in processes like $B \to \rho\rho, \rho\pi, a_1\pi$; precision of the β angle can be improved in various $b \to c\bar{c}q$ processes, while search for new phases is carried out in $b \to s\bar{q}q$ transitions. Lastly, the γ angle is revisited with the GLW method in processes like $B \to D(KK, \pi\pi, K_S\pi^0)K$; the ADS method in doubly Cabbibo-suppressed decays, $e.g.$ $B \to D(K\pi)K$; the GGSZ Dalitz method in three body decays, such as $B \to D(K_SKK)K$ or $B \to D(K_S\pi\pi)K$; or the combined GLW+ADS method in processes like $B \to DK, D^*K, DK^*$.

The Charmless Hadronic B-decays WG manages efforts in direct CP violation measurements, in particular angular analyses for $B \to VV$. It also studies 2 body $B \to hh'$ and Dalitz-motivated 3 body processes; as well as hadronic B_s decays, QCD factorisation and flavour symmetry breaking.

The Charm WG has an elaborate physics programme that includes study of D^0 mixing, direct CPV in the charm sector, radiative decays, signs of NP via rare/forbidden decays ($e.g.$ $D \to \gamma\gamma$, $D \to e^+e^-$) and (semi-) leptonic decays.

The Quarkonium WG focuses at inclusive baryon and meson production in $\Upsilon(nS)$ decays, energy scan studies, production of exotic charmonium-like states below and above the open-charm threshold and (potentially) b-hadron production at $\Upsilon(5S)$.

The Tau WG governs efforts in studying lepton flavour violating (LFV) τ decays, τ properties, lepton universality, CP violation in leptonic sector and precision measurements of SM decays.

The Dark Sector and Low-multiplicity WG includes two-photon and precision electroweak physics, as well as the search for dark photon[10], ALPs, BSM scalar bosons ($e.g.$ the dark Higgs), etc.

[10]in direct production (via exotic mixing) and exotic final states

Chapter 3

The Belle II experiment

The Belle II experiment is a successor of the Belle experiment, which was successfully running from 1999 to 2010. It is located on the flatlands of the Ibaraki prefecture, Japan, near the city of Tsukuba. For a decade, together with the BaBar experiment, Belle held leadership in B-physics and beyond. It accumulated a large sample (1 ab^{-1}) of electron-positron collision data that was utilised in hundreds of analyses to study B-decays, discover exotic quarkonium-like states, search for physics beyond the SM, etc. The most prominent experimental result delivered by Belle collaboration, the discovery of CP violation in B-decays, was honoured with a Nobel Prize in 2008. Belle II experiment aimed to follow-up on the physics programme of its predecessor by looking into yet unaddressed mysteries with the improved machinery and data analysis techniques.

3.1 The SuperKEKB accelerator

SuperKEKB represents an upgraded version of the former KEKB collider. The primary goal of the Belle II experiment is to accumulate a data sample approximately 50 times larger than that of Belle ($\approx$50 ab^{-1}). Achieving this requires a substantial increase in the instantaneous luminosity by a design factor of 40. This section highlights key SuperKEKB upgrade features, while a more comprehensive accelerator overview is provided in Ref. [30].

Fig. 3.1 schematically illustrates the layout of the SuperKEKB facility. The existing KEKB tunnels gave room for the upgraded low- and high-energy rings (LER and HER, respectively), each around 3 km in circumference. The HER stores bunches of electrons accelerated to 7 GeV, while 4 GeV positrons are stored in the LER. The energy asymmetry quantified as $\beta\gamma$ has been decreased from 0.48 to 0.28 to allow for reaching higher beam currents, while an improved spatial resolution of the newly developed vertex detector (VTX) balances it out.

A reconfigured radio frequency (RF) gun fires short laser pulses onto a photo cathode to produce electrons, which are accelerated up to 7 GeV in LINAC before being dumped into the HER. At the same time, a thermionic electron gun inherited from KEKB generates 3.3 GeV electrons that strike a new tungsten target, producing bremsstrahlung photons which, in turn, generate electron-positron pairs. To enhance positron production, flux concentrators and large-aperture accelerating structures are installed around the tungsten target. To meet the injection requirement on positron emittance, an additional damping ring is employed to reduce it by a factor of two. A combination of the new tungsten target and the newly constructed dumping ring decreases horizontal positron emittance by a factor of 5-10 [30].

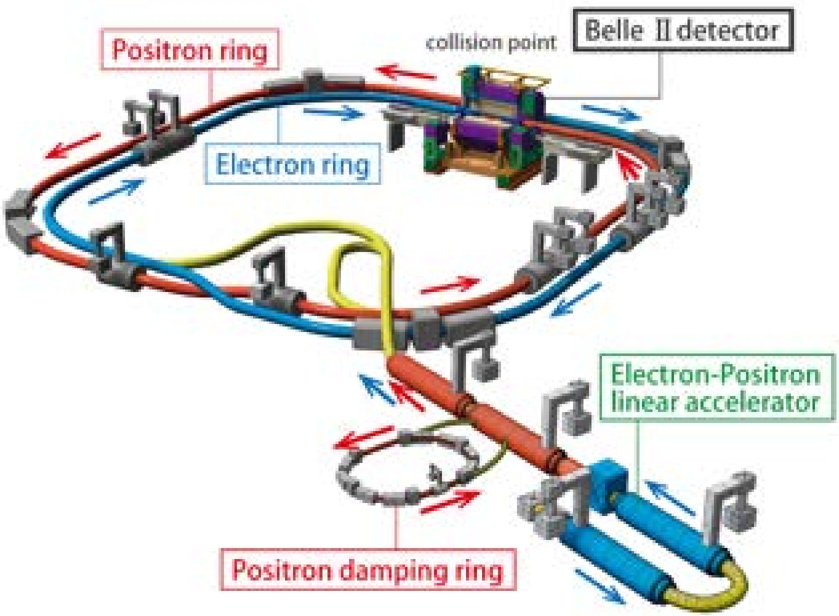

Figure 3.1: Schematic of the SuperKEKB facility. The positron storage ring (LER) is shown in red and the electron storage ring (HER) in blue. Other key components—the LINAC, damping ring, and Belle II detector centred at the interaction point where collisions occur—are labelled accordingly.

A key design change aimed to ramp up instantaneous luminosity is the so-called *nano-beams scheme*, which is illustrated in Fig. 3.2. It pursues the idea of minimising the longitudinal size of the overlap region for colliding bunches (d) to reduce the vertical beta function (β_y^*) in the interaction region (IR), which is generally limited by the *hourglass effect*. In the case of head-to-head collisions, the hard limit introduced by the hourglass effect is defined by the longitudinal bunch size: $\beta_y^* > \sigma_z$, where $\sigma_z \approx 5$ mm. This is why a collision scheme at a finite crossing angle has been adopted. In this case, the hard limit on the beta function is expressed as:

$$\beta_y^* > d \cong \frac{\sigma_x^*}{\phi}, \tag{3.1}$$

where σ_x^* is the transverse bunch size and ϕ is the crossing angle, which is set to 41.5 mrad. The feasibility of collisions at a large crossing angle was tested during late stages of the Belle experiment using crab cavities[1]. This allowed reaching record luminosity reported in Table 3.1 and proved the design concept that was later implemented in Belle II. A secondary hourglass effect emerges for collisions at a large crossing angle due to the vertical displacement of colliding particles in a non-uniform betatron function field. It has been addressed with a crab-waist scheme, which uses sextuple magnets to correct the trajectory of displaced "waist" particles and prevent the beam performance degradation and the ξ_y blow-up.

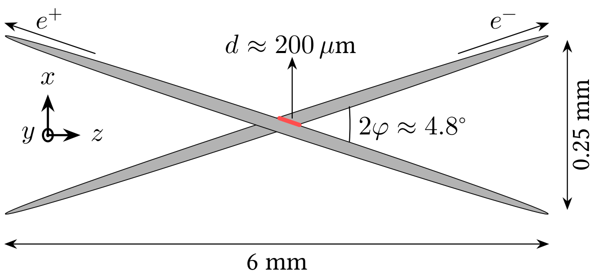

Figure 3.2: Illustration of the nano-beams scheme for colliding beams.

For a collision of two flat bunches of the same size, the luminosity is quantified as:

$$L = \frac{\gamma_\pm}{2er_e}\left(\frac{I_\pm \xi_{y\pm}}{\beta_{y\pm}^*}\right)\left(\frac{R_L}{R_{\xi_y}}\right), \tag{3.2}$$

where γ, e and r_e are the Lorentz factor, the elementary charge and the electron classical radius, respectively; the $\pm$ subscript denotes association of parameters to

[1]KEKB originally employed an (almost) head-to-head collision scheme with 22 mrad crossing angle

positrons (+) or electrons (−). The reduction factors R_L and R_{ξ_y} arise from the crossing angle and the hourglass effect and are of the same order of magnitude. Tunable parameters that fundamentally define the luminosity are the total beam current (I), the vertical beam-beam parameter (ξ_y) and the vertical betatron function at the IP (β_y^*). Achieved and designed values of these parameters for KEKB and SuperKEKB, respectively, are provided in Table 3.1. A reader can point out that the adoption of the nano-beam technique allowed reducing the vertical beta function by a factor of 20, which in combination with the doubled target currents facilitates a factor of 40 luminosity increase.

Parameter (LER/HER)	KEKB (achieved)	SuperKEKB (designed)	Units
Energy	3.5/8.0	4.0/7.0	GeV
ξ_y	0.129/0.090	0.090/0.088	
β_y^*	5.9/5.9	0.27/0.41	mm
I	1.64/1.19	3.60/2.62	A
Luminosity	2.11	80	$\times 10^{34}$ cm^{-2} s^{-1}

Table 3.1: Summary of achieved and designed beam parameters for KEKB and SuperKEKB, respectively.

To maintain beam focusing at the interaction point, a new magnet assembly known as the QCS system was installed in its vicinity. The system comprises eight quadrupole magnets—five superconducting and three permanent—along with 43 corrector magnets and four compensation solenoids designed to counteract the magnetic field of the Belle II solenoid. This field compensation effectively minimises the vertical beam emittance near the interaction point.

The SuperKEKB accelerator performed the first collisions in April 2018. Since then, the instantaneous luminosity record that was earlier set by KEKB was updated several times. It currently stands at 5.1×10^{34} cm^{-2}s^{-1} [2].

The machine has a certain degree of the energy tuning flexibility, which allows operating at different centre-of-mass (CM) energies (E_{CM}). The accessible E_{CM} range includes Υ(nS) resonances ($n = \overline{1,6}$) and intermediate off-resonance points. The maximum achievable centre-of-mass energy is limited to 11.24 GeV due to the limited injection power of LINAC. Although, even if this limit is circumvented, the performance of magnets would only allow ramping the energy up to 12 GeV. The majority of the Belle data sample ($\approx 70\%$) was accumulated at the centre-of-mass energy that corresponds to the Υ(4S) resonance (E_{CM}=10.58 GeV), while the

[2] As for the time of delivering this letter, set in December 2025

remaining data sample is shared between other Υ(nS) resonances and continuum collisions. The latter, in particular, includes several energy scan campaigns, when the machine was operated at off-resonance E_{CM} points to accumulate a data sample useful for studies beyond B-physics. A similar campaign has been carried out during the early Phase 2 of Belle II experiment (Nov 2021). E_{CM} scan points have been chosen in between those of Belle to cover a wider physics programme (see Fig. 3.3).

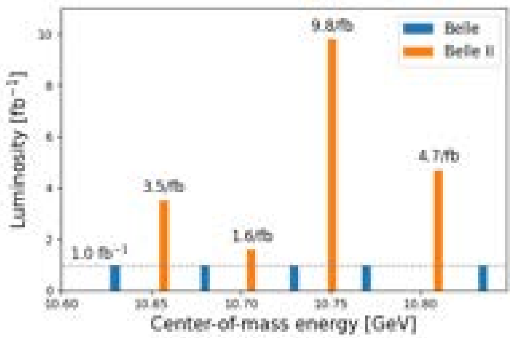

Figure 3.3: E_{CM} points KEKB and SuperKEKB accelerators were operating at during the respective energy scan campaigns.

3.2 The Belle II detector

The Belle II detector is positioned around the interaction point, where the electron and positron beams collide. It consists of multiple sub-detectors, each with a unique design and specific functions (see Fig. 3.4). The detector features an asymmetric geometry to account for the centre-of-mass boost in the Oho direction. The superconducting solenoid, which encloses the magnetic spectrometer and electromagnetic calorimeter, generates a 1.5 T magnetic field parallel to the beam axis. It is made of a niobium–titanium alloy and is cooled to superconducting temperatures using a liquid-helium cryogenic system. The coordinate system commonly used for discussing the detector geometry is defined as follows: the z-axis is parallel to the beam axis and points in the direction of the energy boost, with the origin ($z = 0$) set at the IP. The x and y axes lie in the plane perpendicular to the z-axis, where the x-axis is oriented horizontally outward from the collider centre, and the y-axis is defined vertically upward. An alternative, spherical coordinate space, employs commonly-defined polar (θ) and azimuthal (ϕ) angles.

In this section, we briefly outline the main sub-detectors constituting the Belle II detector and the readout system utilised to process recorded data. For curious readers, an actual picture of the Belle II detector is given in Fig. A.2 of the App. A. It has been taken in the Tsukuba Hall in February 2023, when the detector was partially disassembled due to the undergoing first long shutdown (LS1). Many accelerator and detector components have been upgraded during the LS1. In particular, the single-layer PXD1 that was in operation during Phase 2 has been replaced with the complete two-layer PXD2.

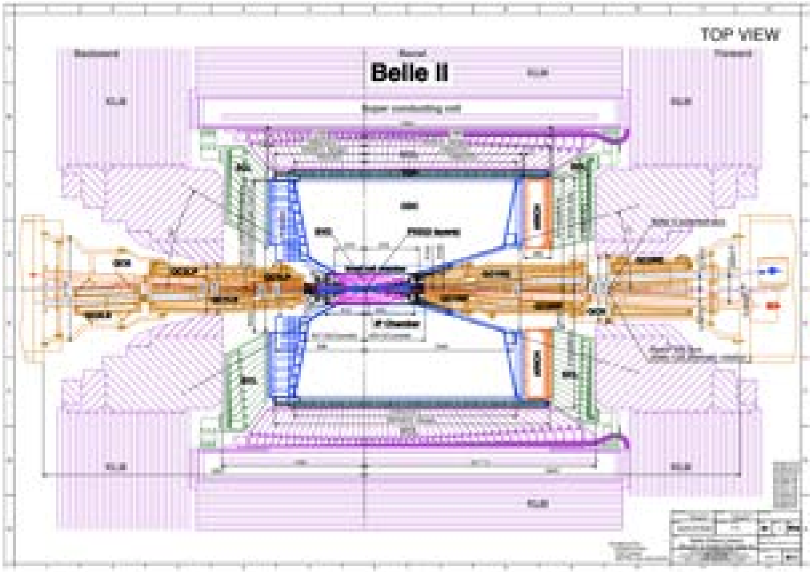

Figure 3.4: Schematic top-view of the Belle II detector [30].

3.2.1 The Vertex Detector (VXD)

The innermost sub-detector, VXD, performs precise tracking and vertex measurements. It comprises two constituent parts: the Pixel Detector (PXD) and the Silicon Vertex Detector (SVD). In tandem, they provide a polar angular coverage of $17^\circ < \theta < 150^\circ$, while resolution of the impact parameters and the lifetime[3] is around 12 μm and 65 fs, respectively [31]. A more compact design of the Belle II interaction region (IR)[4] allows the VXD to be placed closer to the IP. This results

[3]Estimated for the D-meson decay.
[4]w.r.t. the Belle SVD

in an increase in beam-induced background abd necessitates an exceptionally high trigger rate (30 kHz) for teh readout system.

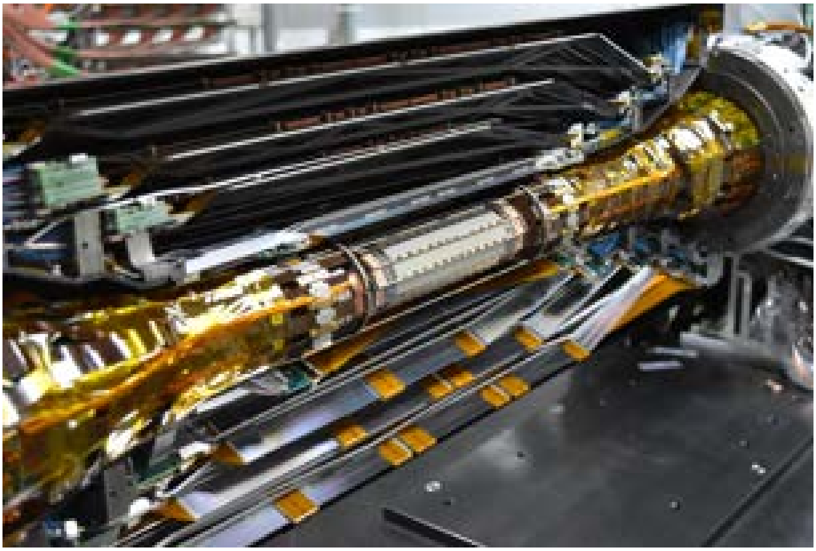

Figure 3.5: Picture of the VXD taken in the clean room with PXD and SVD assembly in progress (credit: Koji Hara and Katsuro Nakamura, KEK).

The Pixel Detector (PXD)

The pixel detector [32] is the innermost component of the VXD. It consists of 40 modules (half-ladders) arranged in two layers, each displaced for 14 mm and 22 mm from the beam axis respectively see (Fig. 3.6). Since one of the focal points of this thesis is the background monitoring in the PXD (see Chapter 4), this sub-detector is described below more elaborately than others.

Detection mechanism

The PXD utilises depleted field-effect transistors (DEPFET) for signal detection. The underlying concept of the DEPFET was developed Josef Kemmer and Gerhard Lutz in the MPI for Physics [34] in 1987. It performs signal detection and amplification within a single device. The PXD is the first “field” application of this technology in a particle physics experiment. Thickness of the sensitive area is of high importance for vertex detectors, as a particle passing through a detector layer undergoes multiple scattering, which degrades the vertex resolution. These considerations motivate the

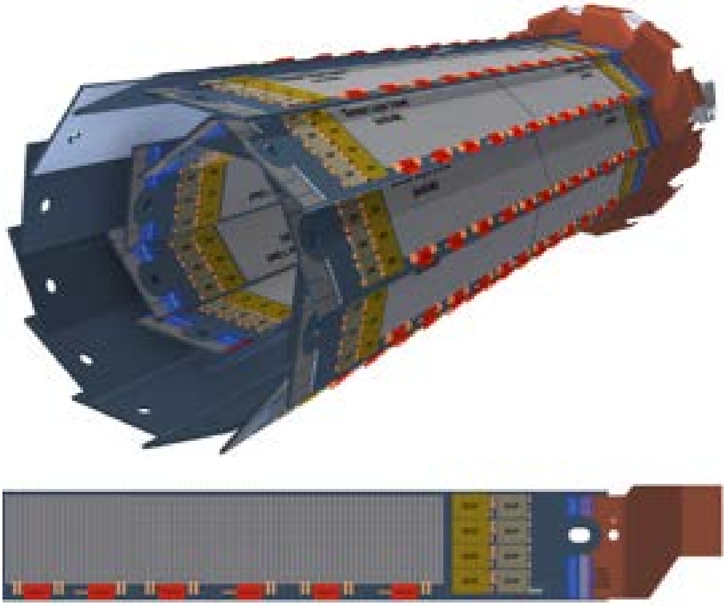

Figure 3.6: Rendering of: [left] complete PXD design, [right] a PXD module (forward direction, outer layer) by the DEPFET collaboration [33].

choice of DEPFET technology for the PXD, as it allows reaching the thickness of a sensitive area as small as 75 μm.

A DEPFET pixel consists of a silicon bulk that is grounded to a positive contact and capped by a p-channel Metal Oxide Semiconductor Field Effect Transistor (MOSFET). The positive grounding plate depletes the bulk region of free charge carriers, leaving it fully depleted, while the p-doped ground plate acquires a negative potential. When a charged particle traverses the silicon bulk, it ionises the material, producing electron–hole pairs. The "positively charged" holes drift toward the ground plate, whereas the electrons are collected in a potential minimum just beneath the FET gate forming the "internal gate", which compensates the potential of the FET gate. Once the gate is active, the drain current, which is proportional to the count of generated charge carriers, can be measured. After the amplified signal is sent down the data acquisition sequence, the drift charge is cleared by applying a positive potential to the clear gate. This forces electrons to drift towards the original location clearing the internal gate and allowing the next measurement to be performed.

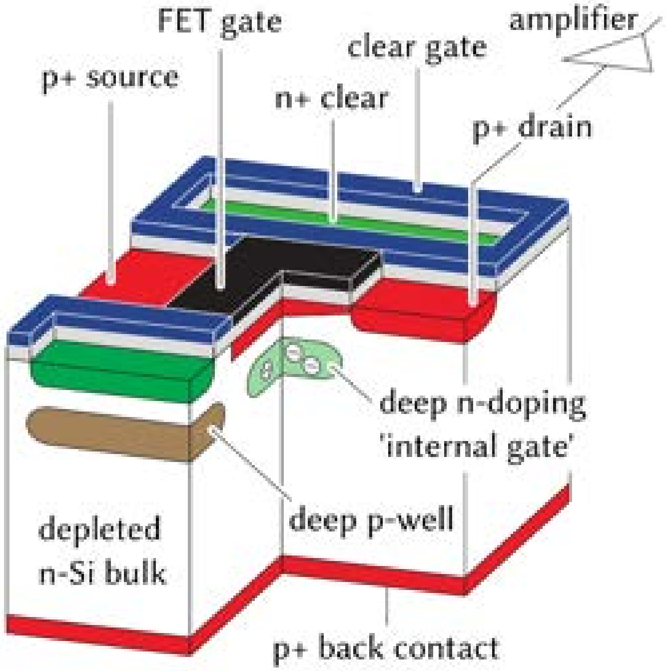

Figure 3.7: Schematic Illustration of a DEPFET pixel [33].

Module design and readout

Each pixel measures $50\times(55–60)$ μm^2 in the inner layer and $50\times(70–85)$ μm^2 in the outer layer. The pixels form sensitive areas of 768×250 units each, corresponding to widths of 12.5 mm for modules in both layers, and lengths of 44.8 mm and 61.44 mm for modules in the inner and outer layers, respectively. Each sensitive area is mounted on a 420 μm-thick silicon support frame, defining the dimensions of each half-ladder as 15.4×68 mm^2 for the inner modules and 15.4×85 mm^2 for the outer modules. The supporting structure of a PXD module ensures mechanical stability and provides space for application-specific integrated circuits (ASICs) essential for control, read-out and voltage supply. The latter is provided by a flexible printed circuit (Kapton), which establishes the connection to external control systems and power supplies.

The pixel matrix of each sensitive area consists of 250 long columns and 768 short rows. Electrically, pixels are connected in a way that combines four physical rows into a row group, giving 1000 pixels in total per group. This rearrangement defines

1000 logical columns, called *drain lines*, and 192 logical rows, known as *gates*. This modified logical structure enables a higher readout speed. The voltage is applied to each DEPFET pixel in a way that allows the accumulated charge to flow along the drain line it towards the Analog-to-Digital Converter (ADC). The readout is performed from all logical columns simultaneously, while the signal from individual drain lines is sampled in sequence to ensure stable readout and complete discharge.

The readout of a module utilises ASICs of three different types that are placed directly on the supporting structure of a half-ladder:

Switchers

Six switchers [35] hosted by each module frame provide fast voltage pulses of up to 20 V in amplitude to activate gate rows and clear the internal DEPFET gates[5]. When no voltage is applied, drain charge is accumulated in the sensor. Application of the gate voltage kick-starts the readout via an ADC. After a delay, sufficient for readout to be completed, the clear voltage is added to neutralize the collected charge. The complete readout cycle takes about 100 ns before a switcher continues with the next row. With almost 200 rows, the complete readout cycle of a module takes around 20 μs.

DCDs

Each of the four Drain Current Digitizers (DCD) [36] mounted for each module converts analog drain currents from the DEPFET matrix into digital signals with 8-bit resolution across 256 channels. Implemented in 0.18 μm CMOS technology with radiation-hard design, the DCD achieves noise levels below 100 nA and operates reliably up to doses of 7 MRad. The analog input stage keeps the column line potential constant, which is necessary for fast readout. It also performs pixel-to-pixel offset correction (pedestal compensation) and provides adjustable gain and bandwidth, allowing noise optimisation for each pixel individually.

DHPs

Four data handling processors (DHPs) [37], each handling output from one of four DCDs, reduce data volume from the DCDs through zero suppression and selective readout of triggered events. Before suppression, the data are corrected for common-mode noise and pixel pedestal fluctuations, with offsets continuously updated to account for slow drifts. The processed hit data are stored in buffers and read out upon receiving a trigger signal (the buffer size is chosen to store the data of an entire module twice, ensuring that the previous readout remains available after a trigger signal). Each DHP transmits the selected data via high-speed optical links

[5]All pixels within a logical row receive the same voltage.

(1.25 Gbit/s), providing a total bandwidth of 5 Gbit/s per module. In addition, the DHP controls synchronisation of the DCDs and switchers and provides configuration access through a JTAG interface.

The Silicon Vertex Detector (SVD)

As discussed in Sec. 3.2, the primary goal of the silicon vertex detector is to precisely measure the position of the primary decay vertex without significantly distorting kinematic properties of decay products. This requires the SVD to have low mass, high resolution and radiation tolerance. The latter is motivated by its proximity to the IP, which subjects the sub-detector to high radiation and requires its efficient cooling.

To fulfil the above requirements, the SVD design is similar to that of the PXD. It consists of 49 ladders arranged in four layers (see Fig. 3.8). The innermost layer is positioned 38 mm from the interaction point, while the outermost layer is located 140 mm away from it. Most of the ladders are rectangular, except for those mounted in layers 2-4 toward the forward endcap, which are trapezoidal[6]. The polar angular acceptance ranges from 17°to 160°. The asymmetry of the acceptance region accounts for the forward boost in the centre-of-mass frame. The total of 187 double-sided sensors is connected via manifolds across the ladders following the Origami concept [30]. Each sensor consists of a set of highly p-doped strips oriented along the beam direction and highly n-doped strips arranged perpendicular to it. The strips are separated by an n-type bulk region that becomes ionised when traversed by charged particles. This ionisation produces electron-hole pairs, with the electrons and holes drifting toward the nearest oppositely charged strips. The size of DSSD sensors varies from 36×123 mm^2 to 58×123 mm^2. Rectangular sensors mounted on rectangular ladders are arranged such that the long strips on the p-side run parallel to the beam axis, while the short n-side strips are oriented along the $r-\phi$ plane. Slanted DSSDs are utilised for trapezoidal ladders.

When ionising radiation passes through the silicon strips, it generates free electrons and holes that, within the solenoid's magnetic field, experience the Lorentz force, causing a transverse spread. In order to minimise it, all modules are tilted. According to Ramo's theorem [38], the motion of both carrier types induces same currents on p- and n-sides, but die to higher mobility: the Hall angle (and thus the deflection) is three times higher for electrons than for holes. Consequently, the tilt angle of the sensor plane reduces the electron spread at the cost of increased hole spread (see Fig. 3.9). The overlap between adjacent ladders accounts for 8 to 10% of

[6]The change of shape is motivated by the limited design volume.

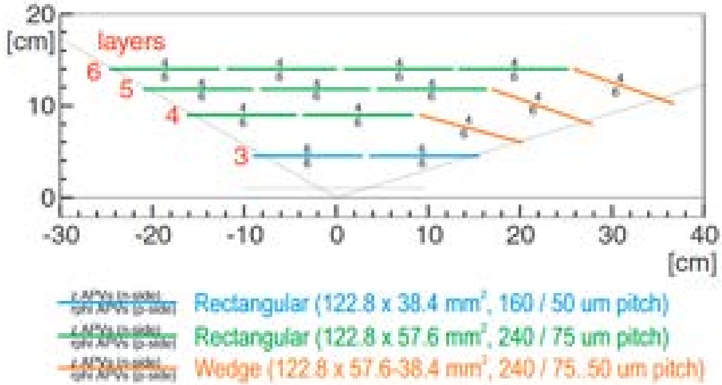

Figure 3.8: Schematic design of the SVD geometry. Black integers mark the number of APV25 readout chips for each side of a ladder [30].

the total sensor area. A relatively large overlap facilitates precise module alignment, which is difficult to achieve with alternative methods, *e.g.* using cosmic muons.

The primary readout system of the SVD involves 1902 APV25 chips [39] (each reading 128 strips), an Flash Analog-to-Digital Converter (FADC) and a Processing module (PROC). Extrapolation of dosimetric measurements performed in the area, where DOCK boxes of the SVD2 were installed, yielded the expected radiation doze of 250 kRad, which is deadly for most on-shelf components. This is why the conversion and processing block is placed away from the IR and connected to APV25 chips with some 12 m-long copper cables.

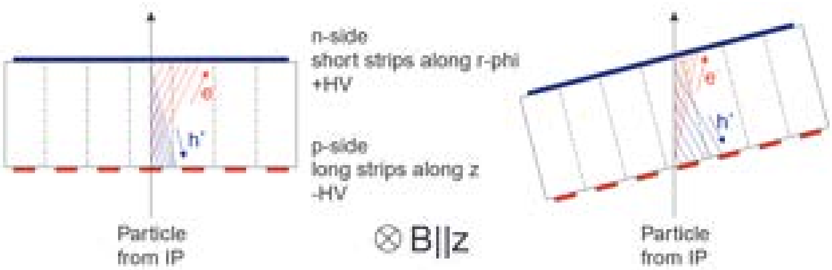

Figure 3.9: Sensor orientation in the magnetic field: [left] electrons and holes deflected by Lorenz force in the magnetic field passing through an untilted module; [right] the minimised spread of charge carriers in a tilted module [30].

3.2.2 Central Drift Chamber (CDC)

The Central Drift Chamber (CDC) is the third innermost sub-detector, which plays a key role in tracking and particle momentum measurements [40]. It also provides energy loss measurements (dE/dx) that are crucial for particle identification. Low-energy tracks that do not leave the CDC volume can be identified using the dE/dx measurements alone. Finally, it provides efficient and reliable trigger signals for charged particles.

The CDC has a radius of 160−1130 mm from the beam axis and extends for 2.4 m along it. The total of 14366 sensor wires is arranged within its fiducial volume, which is filled with a 50:50 mixture of He and C_2H_6 gasses. An ionising particle passing through the CDC volume generates free electrons, which are accelerated in the strong electric field before reaching the sensor wires. An avalanche created by the chain reaction amplifies the signal to increase its detection efficiency. The spacial resolution of the CDC wire grid is 120 μm [41], while the maximum drift time is 350ns.

Thin (30 μm) CDC sensor wires are arranged in eight alternating super layers. Each super layer is composed of 6 layers[7] (in contrast with 3 or 4 layers in the Belle CDC design). The innermost and outermost super layers have an axial layout[8] ("A"), which mimics the shape of adjacent sub-detectors (see Fig. 3.10). The intermediate super layers are arranged in the alternating sequence of stereo ("U" or "V") and axial layers. The wires in stereo layers are tilted for an angle that varies between 70 and 74 mrad. The stereo design provides spacial information in the $x - y$ plane, while

[7]Except for the innermost layer, which has 2 additional layers containing guard wires.
[8]Parallel to the solenoid field.

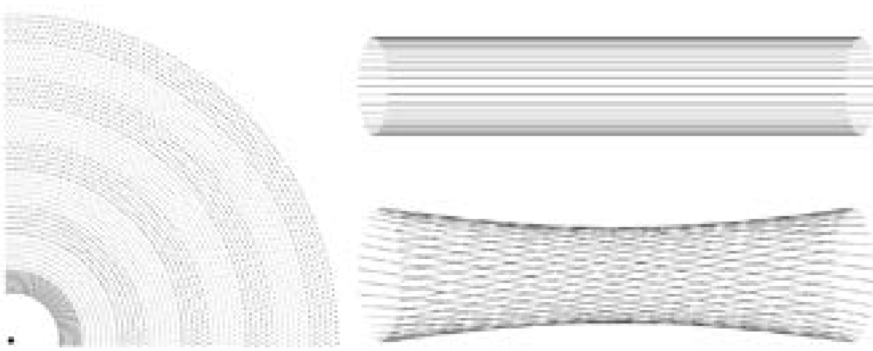

Figure 3.10: Left: the layout of CDC wires in $x - y$ plane. Right: the arrangement of CDC wired in an axial [top] and a stereo [bottom] layer [41].

the z coordinate is measure by axial layers. In tandem, they facilitate a complete three-dimensional reconstruction of track helices. The complete arrangement of CDC super layers is expressed as: *AUAVAUAVA*.

The new readout electronics system has been developed to handle higher trigger rates with less deadtime. A new ASIC chip that incorporates an amplifier, a shaper and a discriminator processes the readout signal, while a time-to-digital converter (TDC) implemented on a field-programmable gate array (FPGA) measures the drift time. The signal charge is measured by a slow ($\sim$ 30 MHz) FADC. The components of the frontend electronics mentioned above are mounted on a single board located near endcaps. It sends signals to the electronics hut (E-hut) via optical fibres.

3.2.3 Particle Identification

The role of the particle identification (PID) at Belle II is devoted to two sub-detectors: the Time of Propagation Counter (TOP) surrounding the barrel region and the Aerogel Ring-Imaging Cherenkov detector (ARICH) covering the forward and backward endcap regions. Both sub-detectors make use of the Cherenkov effect, which suggests that a particle propagating in a medium with a refraction index $n > 1$ radiates light. The angular distribution of the emitted light is expressed as:

$$\Theta = \text{arccos}\frac{1}{\beta n}, \tag{3.3}$$

where $\beta = v/c$ – is the particle velocity expressed in units of the speed of light in vacuum. The angle Θ shapes the conical wavefront, known as *Cherenkov cone* (see Fig. 3.11). eq. 3.3 relates a particle's velocity to its Cherenkov angle. Combined with momentum measurements from other subdetectors, this permits mass inference.

The combined performance of the TOP and ARICH sub-detectors provides excellent kaon–pion separation across the full kinematic range, while electron–muon discrimination is achievable for particles with momenta below 1 GeV/c^2. The current TOP hardware and software configuration achieves a kaon identification efficiency of 85% with a 10% pion misidentification rate [42], while the ARICH attains a 93% kaon identification efficiency at the same pion misidentification rate [43].

Time of Propagation Counter (TOP)

The Time of Propagation Counter (TOP) [44] consists of 16 quartz bars, each measuring 270×45×2 cm^3, arranged around the outer surface of the CDC. Five out of six facets of each bar are coated to fully reflect Cherenkov photons produced by traversing charged particles. The remaining backward end is transparent. It extends into a 51 mm-wide prism, to which an array of 32 microchannel-plate photomultiplier

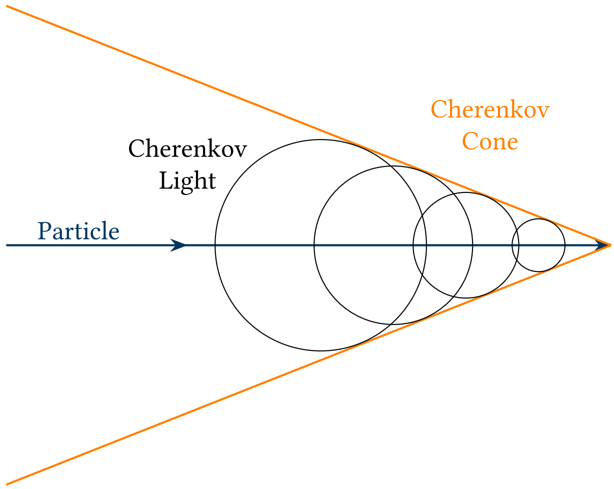

Figure 3.11: Schematic illustration of Cherenkov radiation showing the cone formed by overlapping wavefronts.

tubes (MCP-PMTs) is attached (see Fig. 3.12). A focusing system that disperses the ring image according to wavelength is employed to reduce the chromatic smearing of the Cherenkov light [45], which limits the PID performance. To implement it, a focusing spherical mirror ($r = 7$ m) is mounted to the forward side of each quartz bar.

The schematic path of photons propagating through the quartz medium is shown in Fig. 3.12. Photons with different Θ focus onto different PMT channels. The

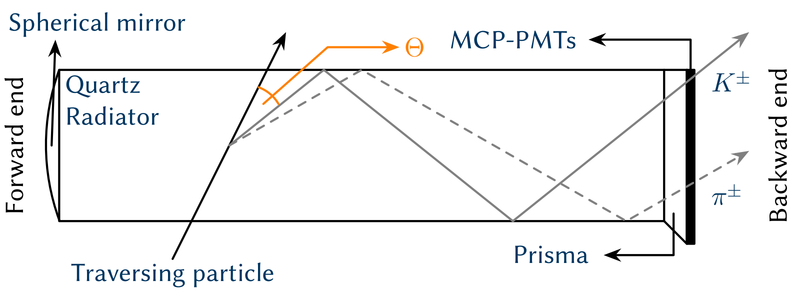

Figure 3.12: Schematic illustration of the Cherenkov light propagation in the TOP detector.

Cherenkov image is reconstructed from three-dimensional information – the (x, y) coordinates and precise timing – both provided by the MCP-PMTs. Each module contains four board stacks, each equipped with 16 custom-built 8-channel ASICs responsible for waveform sampling readout [30]. The timing information is subsequently extracted using Standard Control Readout Data (SCROD) boards [46].

Aerogel Ring-Imaging Cherenkov Detector (ARICH)

The proximity-focusing Aerogel Ring-Imaging Cherenkov detector (ARICH) [47] is installed in the forward endcap region. The ARICH system consists of an aerogel *radiator*, where Cherenkov photons are generated; an *expansion volume*; an array of *position sensitive photon detectors*; and a *readout system* (see Fig. 3.13).

The two-layer silica aerogel radiator comprises 2×248 individual tiles with high optical transparency ($\Lambda > 40$ mm for $\lambda = 400$ nm [30]), each measuring $16 \times 16 \times 2$ cm^3. The tiles are made from two types of aerogel with refractive indexes of 1.045 and 1.055.

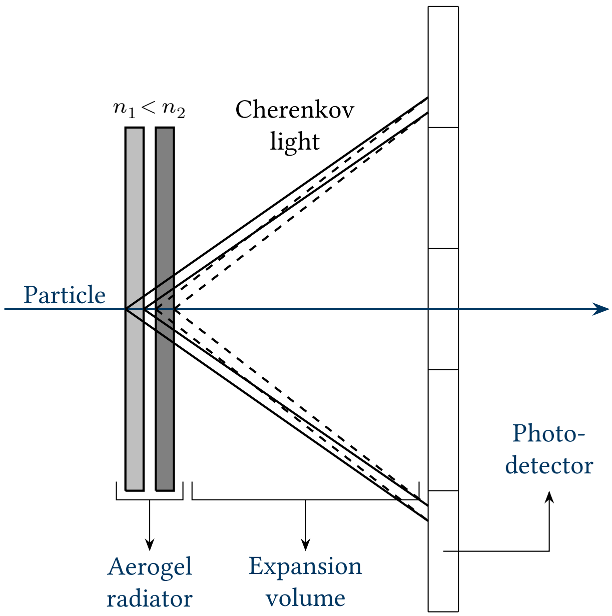

Figure 3.13: Schematic illustration of the Cherenkov light propagation in the ARICH. The focusing radiator is composed of materials with gradually increasing refraction indexes for better photon detection efficiency.

The refractive indices are selected to ensure that the Cherenkov rings generated in the two aerogel layers coincide on the photon detector plane (see Fig. 3.13). Separated from the radiator by a 20 cm-wide expansion volume, the photodetector consists of 540 hybrid avalanche photon detectors (HAPD) arranged in 9 concentric rings in the radial direction. The HAPD modules are produced by Hamamatsu Photonics. Each module measures 73×73 mm^2 in cross-section and contains a 12×12 array of pixels, 4.9×4.9 mm^2 each. They serve as baseline photon detectors, offering high single-photon detection efficiency and excellent spatial resolution. A dedicated ASIC-based readout system is employed to pass the 80k-channel output of the photodetector to FPGAs for the feature extraction [30]. The ASIC and the FPGA chips are encapsulated in a printed circuit board directly attached to the HAPD output pins.

3.2.4 Electromagnetic Calorimeter (ECL)

The Electromagnetic Calorimeter (ECL) is mainly responsible for photon detection and the precise measurement of photon energy and angular coordinates. It also assists with electron identification, online and offline luminosity measurement and generation of trigger signal (more in Sec. 3.3) [30]. Since roughly a third of B-decays involve π^0's and/or other neutral particles in wide a kinematic range from 20 MeV to 4 GeV, a high resolution calorimeter is utilised by Belle II. The energy-dependent resolution of the ECL is expressed by Eq. 3.4. This, for example, gives a 2 MeV energy resolution for a photon with the energy of 100 MeV.

$$\frac{\sigma_E}{E} = \sqrt{\left(\frac{0.066\%}{E}\right)^2 + \left(\frac{0.81\%}{\sqrt[4]{E}}\right)^2 + (1.34\%)^2} \tag{3.4}$$

The ECL consists of a barrel and two endcap regions (forward and backward), which together provide a polar angle coverage of $12.4^\circ < \theta < 155.1^\circ$[9]. The barrel section is 3 m long and 1.25 m in radius, while the forward and backward endcaps are located at $z = 1.96$ m and $z = -1.02$ m respectively. Each section is composed of thallium-doped caesium iodide CsI(Tl) crystals, with 6624 in the barrel and 2112 in the endcaps. Altogether, the calorimeter contains 8736 crystals with a total mass of roughly 43 tons. Each crystal is covered with a 200 μm thick of Gore-Tex porous teflon followed by two 25 μm thick layers of aluminium and mylar. The crystals composing the barrel region are shaped as truncated pyramids with an average size of about 6×6 cm^2 in cross-section and 30 cm in length, while the crystals in endcap regions have 69 different shapes. Two 20×10 mm^2 Hamamatsu Photonics S2744-08 photodiodes are mounted to each crystal through a 1 mm thick acrylite plate.

[9] except for two $\sim 1^\circ$ wide gaps between the barrel and endcaps

Two independent pre-amplified signals are read out from each crystal and digitised at external Shaper Digital Signal Processor (ShaperDSP) boards, which are placed in 52 crates around the Belle II detector. Waveform fits are done to the digitised signals using FGPAs to extract amplitude and timing information from the original light pulses [30].

3.2.5 The K_L^0 and Muon Detector (KLM)

The outermost detector, KLM, is responsible for the detection of long-living particles, mainly K_L^0 and muons, and serves as the magnetic flux return for the solenoid. It is located outside the superconducting solenoid, but inside the magnetic yoke. Similarly to the ECL, it is composed of an octagonal barrel covering the polar angle range from 45° to 125° and two endcaps extending the nominal acceptance coverage to the range 20°–155°. The barrel consists of 15 detector layers interleaved with 14 iron plates, whereas each endcap contains 14 detector layers and 14 iron plates.

Each detector layer in the barrel section consists of glass electrode resistive plate chambers (RPCs) [48] which range from 2.2$\times$1.5 m^2 to 2.2$\times$2.7 m^2 in size, the exception being the modules in the vicinity of the helium chimney, where each plate is 63 cm shorter (see Fig. 3.14). Each side of a symmetric RPC module consists of two 3 mm thick dielectric glass layers with a narrow gap filled with air in between (see Fig. 3.15). A mylar spacer separates two symmetric sides. While being technically insulating, glass electrodes do conduct electricity with extremely high resistivity. When a high voltage is applied to both electrodes, a particle passing through the material generates ions, which are accelerated by the strong electric field and ignite a chain reaction resulting in a streamer serving as a conducting channel allowing charge to flow between plates. The aforementioned air gaps help with the initial streamer formation and prevent afterpulsing in the surrounding area. The high resistance of glass limits transverse spread of the discharge allowing to precisely map it on external pickup strips, each 5 cm in width. There are 48 pickup strips attached to each module, which are arranged in two orthogonal layers and compose a pickup superlayer capable of two-dimensional positioning of the discharge. The dielectric foam separating pickup strips from an outer conducting ground plate serve as a transmission line. The signals from both readout planes are transmitted via twisted-pair cables to discriminators and serializers mounted on the periphery of the iron yoke. Long recotime of the electric field in RPCs leads to an extended dead time, thereby reducing signal detection efficiency under high-background conditions. Although, even when operating at the SuperKEKB design currents, the beam-induced background is expected to remain comparable to the level of the cosmic radiation.

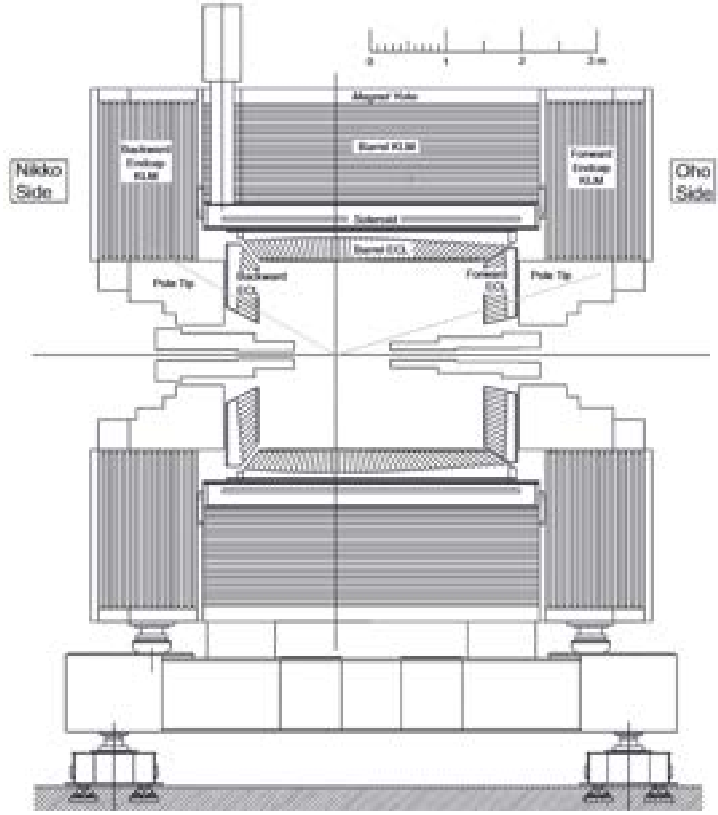

Figure 3.14: Schematic side-view of the KLM detector. Gray lines mark the nominal polar angular acceptance [30].

In contrast, endcap regions of the KLM are strongly affected by the high flux of neutrons produced upstream in the beam pipe and reaching the detector due to the limited shielding along the beam line. RPCs are therefore not suitable for endcap sections of the KLM, where scintillators are employed. Due to the limited hardware space and the strong magnetic field, photomultipliers are also not suitable for signal amplification. Instead, organic scintillation strips, each measuring on 8.5×40 mm^2 in cross-section and from 885 to 2820 mm in length, each embedded with a wavelength-shifting fibre, are utilised to collect the produced scintillation light. The signal of each fibre is read out by a silicon sensor attached to the end of a strip. The total of 16800 strips are arranged into 28 superlayers. The readout of the signal from organic

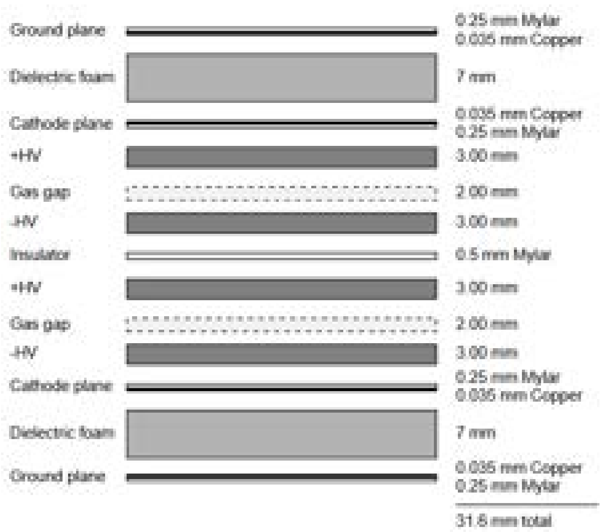

Figure 3.15: Exploded cross-section of an RPC superlayer [30].

sensors is performed by a 16-channel ASIC chip, which passes it to an FPGA for digitisation.

Muons and non-showering charged hadrons–those that either decay in flight or do not undergo hadronic interactions–traverse the KLM until they either escape (for momenta above approximately 1.5 GeV/c) or range out due to electromagnetic energy loss. As they propagate through the KLM volume along nearly straight trajectories, their track identification is challenging. In order to distinguish muons from charged hadrons, the KLM signal is combined with the CDC readout to construct the identification likelihood. The muon identification efficiency is 89% for candidates with the momentum above 1 GeV/c, while the efficiency of K_L^0 reaches a maximum of 80% for a momentum of 3 GeV/c. The majority of false positive muon candidates are in fact charged pions. On contrary, K_L^0 candidates do not leave hits in the CDC and therefore follow a different identification algorithm, which involves clusters reconstructed in the ECL. It requires at least two aligned clusters projecting roughly to the interaction point: either both belonging to two different KLM layers for KLM-only K_L candidates, or each belonging to their respective sub-detector for ECL+KLM candidates. Following this approach, the K_L detection efficiency rises nearly linearly with momentum, reaching its plateau of 80% at 3 GeV/c^2. The resolution is approximately 1.5° and 3° for K_L candidates reconstructed with KLM-only and ECL+KLM algorithms, respectively.

3.3 The Belle II Data Acquisition (DAQ)

3.3.1 Trigger System (TRG)

The Belle II Trigger System (TRG) is employed to isolate individual events in the continuous flow of data recorded by the detector and to discard those that are not interesting from physics perspective, helping to reduce disc occupancy. It performs a trivial analysis of data acquired from outer sub-detectors to classify the shape of events into one of predefined categories. In this way – using the charge and track direction determined by the CDC and ECL, the timing information provided by the ARICH and TOP, the energy deposition integrated by the ECL and the presence of muons reconstructed by the KLM – the Belle II trigger has the classification efficiency for events that include B-mesons above 99%. In order to cope with the target luminosity of 8×10^{35} cm^{-2}s^{-1}, the trigger is designed for a maximum average trigger rate of 30 kHz, a fixed latency of 5 μs, the timing precision below 10 ns and a minimum two-event separation of 200 ns [49]. The trigger rate expected for relevant physics events is summarised in Table 3.2.

Physics process	Cross section (nb)	Rate (Hz)
$\Upsilon(4S) \to B\bar{B}$	1.2	960
Hadron production from continuum	2.8	2200
$\mu^+\mu^-$	0.8	640
$\tau^+\tau^-$	0.8	640
Bhabha ($\theta_{\text{lab}} \geq 17^\circ$)	44	350^*
$\gamma\gamma\,(\theta_{\text{lab}} \geq 17^\circ)$	2.4	19^*
2γ processes ($\theta_{\text{lab}} \geq 17^\circ, p_t \geq 0.1\text{GeV}/c$)	~ 80	~ 15000
Total	~ 130	~ 20000

Table 3.2: Total cross-section and trigger rates at the design luminosity from various physics processes at Υ(4S) CM energy [30]. For the entries marked with a *, the rate is pre-scaled by a factor of 1/100.

All readout channels of individual sub-detectors send data to the *global decision logic* (GDL) [50], which summarises available signals to create the final trigger decision signal. Flexible configuration of the GDL allows masking or emphasising particular channels, if tuning adjustments are required. The trigger decision is sent out to frontend timing switches (FTSW) [51]. Multiple FTSWs arranged in a tree-like structure ensure simultaneous readout of the most recent data by the frontend digitalisation boards. If the final decision of the L1 trigger is positive, a signal that includes an automatically incremented event number and a 64-bit trigger type is passed to the *high level trigger* (HLT).

3.3.2 Data Flow

All Belle II sub-detectors, excluding the PXD, have a similar readout scheme. Raw data are promptly read out and digitised by individual fast FPGA- or ASIC-based Front End Electronics (FEE). Each FEE module then sends data via the *Belle2link* using a unified data transfer protocol [52] to several Common Pipeline Platform for Electronics readout (COPPER) boards [53] located in the E-hut. Each COPPER module additionally receives a trigger signal and current calibration constants, which allow building a sub-event fragment. Up to 16 individual sub-event fragments corresponding to a single trigger signal are sent to the sub-detector readout PC (ROPC) via Gigabit Ethernet (GbE) links, where they are combined into a single sub-event (Event builder 0).

Event fragments received from individual sub-detectors are transmitted from ROPCs to the Event builder 1 (EB1). A round-robin scheme is used to merge them into a single event, which is then forwarded to the HLT located in the computer room via 10 GbE preserving the original event order (see Fig. 3.16).

The HLT is a software-based server-farm responsible for online reconstruction of triggered events in the *basf2* environment [54]. It consists of 20 individual units, each including a distributor node, multiple worker nodes and a collector node. The HLT uses data from all sub-detectors except for the PXD to perform the complete real-time event reconstruction and decide whether an event should be saved for later physics analysis or discarded. The processing time of a single event varies from few milliseconds to 5 seconds, depending on the event topology, with an average of 1 s. All events are processed in parallel across 20 HLT units, sending preserved events as soon as possible, without maintaining the original event order. There are two HLT modes used for detector operation: *filtering* – all events are classified, but only events of interest are kept; and *monitoring* – all events are classified and and saved on the disc with a respective tag. The latter mode is only used to verify HLT performance, but not for the regular data taking. The HLT event filtering is expected to perform a factor 3 data reduction, but the actual reduction factor depends on background conditions and parameters set.

As mentioned earlier, PXD data is not included in the HLT decision-making mechanism. Instead, so-called *regions of interest* (ROIs) are reconstructed by the HLT and passed to the standalone PXD DAQ to truncate PXD data (see Sec. 3.3.5). Truncated PXD sub-events that satisfy the HLT filtering are merged with the rest of sub-events reconstructed by HLT at the *event builder 2*. The resulting complete

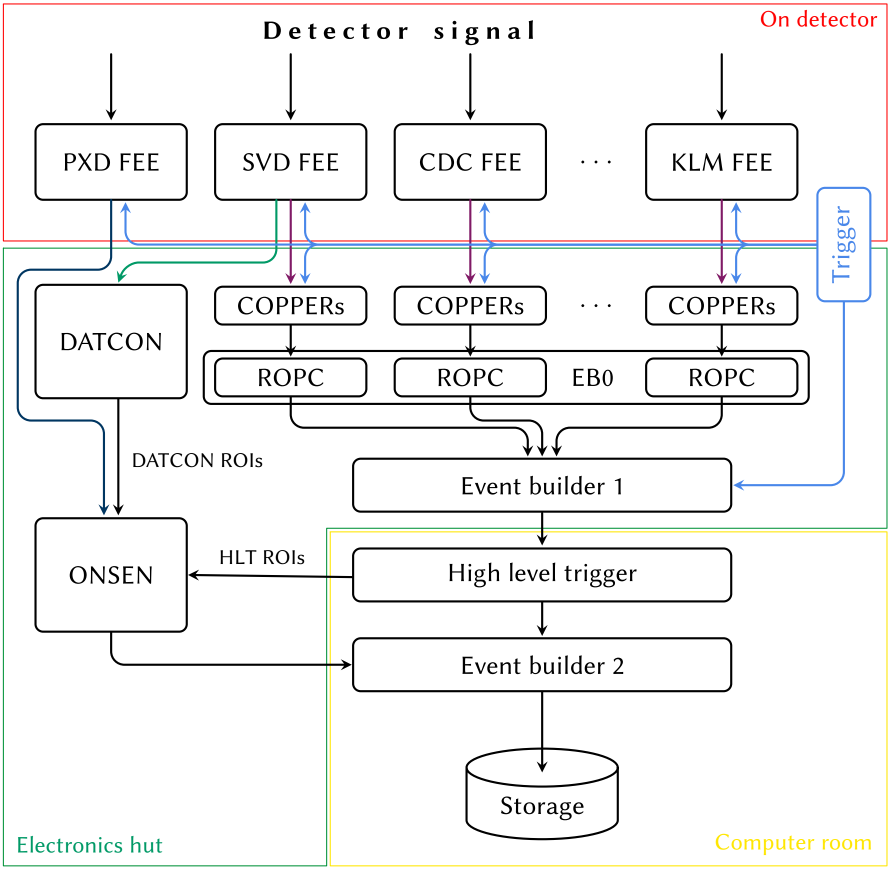

Figure 3.16: Schematic view of the Belle II DAQ sequence. Components constrained within the area with the red edge ( ) are located directly on individual sub-detectors, with the emerald edge ( ) – in the E-hut and with the golden ( ) – in the computer room. The arrows illustrated in purple (↗) are Belle2links [52], in dark blue (↗) are the ONSEN AURORA-based links, in green (↗) are DATCON optical links, in light blue (↗) are trigger timing links and in black are GbE cables.

events that contain data from **all** sub-detectors are temporarily stored on a disc in the SROOT format [55], which protects previously written data from corruption in the event of a failure. These files are later converted into the standard ROOT format used for physics analysis [56], which are saved to the permanent storage.

3.3.3 PXD DAQ

The proximity of the PXD to the IP subjects it to a remarkably high radiation, which imposes high requirements on its data readout system. As discussed above, the maximum average PXD occupancy is limited to 3%. With 7.68 million pixels in two PXD layers, this corresponds to a projected data rate of 17.3 GB/s at the design trigger rate of 30 kHz. As data propagates down the DAQ stream, it is being reformatted and augmented with metadata that includes checksums, module IDs, etc. Altogether, a conservative estimate of the data rate reaches $\sim$20 GB/s. To give a perspective, PXD data flow rate is $\sim$10 times higher than the data rate from all other sub-detectors **combined**. These rough estimates highlight why the standard readout scheme is not feasible for the PXD data. Instead, a different readout concept, which is described in this section, is employed.

The *data handling hub* (DHH) [57, 58] is a dedicated system designed to receive raw data from the PXD FEE, discriminate it into individual events using the trigger signal and build a PXD sub-event that is passed further to the Online Selection Nodes (ONSEN) system for data reduction. It consists of 5 *data handling concentrators* (DHCs), 8 *data handling insulators* (DHI) and 40 *data handling engines* (DHE) organised into 8 individual DHH carrier cards (DHHCC). Each DHHCC is based on an Advanced Telecommunications Computing Architecture (ATCA) board. It hosts one DHC, one DHI and 5 DHEs. Fig. 3.17 illustrates the connectivity scheme of a single DHHCC unit, which there are 8 of. All DHH modules are implemented on FPGAs equipped with 4 GB of memory, supporting an internal bandwidth of up to 5 Gbps and capable of streaming data at 6.125 Gbps.

PXD raw data is transmitted from the FEE to individual DHEs via individual 1.5 Gbps optical links routed through the patch panel. Accurate timing information is crucial to ensure the integrity of PXD images. Another module, DHI, distributes the trigger signal and timing information to DHPs via CameraLink cables, allowing to isolate data corresponding to an individual sub-event. It also communicates the DHH status to the slow control (JTAG commands). The DHE readout begins right after a trigger signal arrives. Due to the long image readout time of 20 μs, the next trigger signal might arrive before the integration is completed. In this case, two images must be received simultaneously. Only for this scenario is it permitted for the average occupancy rate to exceed 5% for a short time to prevent data loss. To

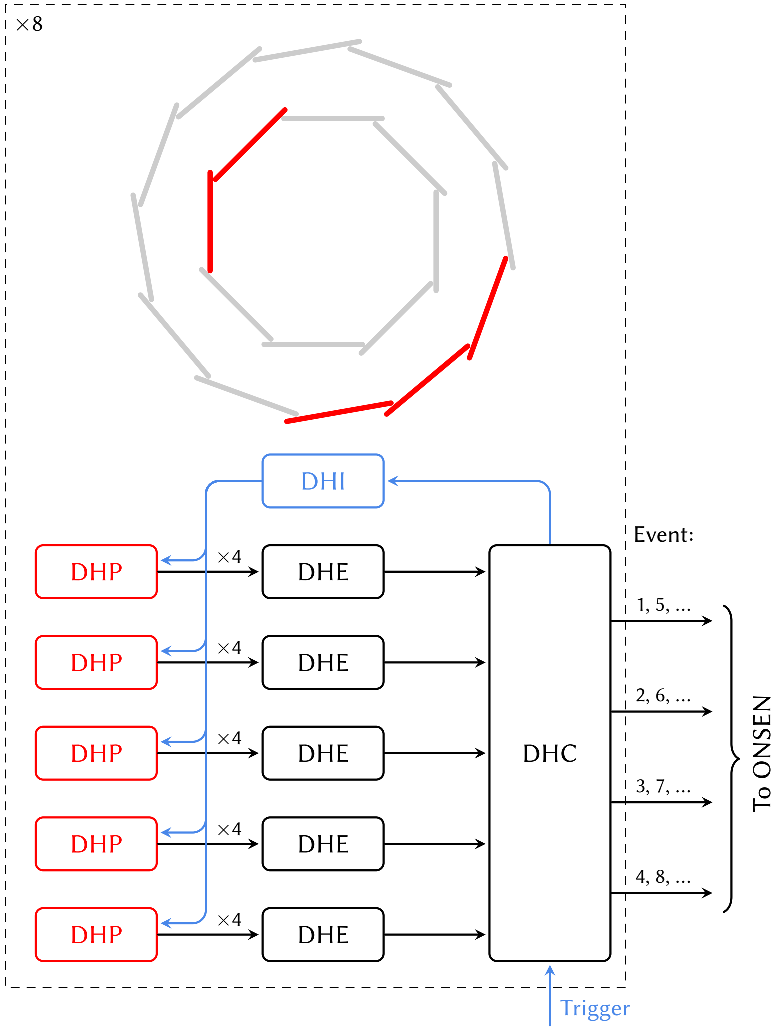

Figure 3.17: DHH connectivity scheme. The DHE receives PXD data from the FEE and passes it to the DHC for sub-event building. The trigger signal received by the DHC is passed further to the DHI to be distributed to the readout electronics for precise timing synchronisation. Each DHC streams out individual sub-events to four ONSEN nodes using the round-robin scheme.

achieve this, the DHP behaviour is mimicked in the DHE. After receiving a complete PXD image, the DHE augments it with the start and end frames, time stamp, DHE ID, etc., and passes it further to the DHC via 5×6.125 Gbps links using the Xilinx AURORA protocol [59].

Since the maximum average occupancy of inner PXD modules is three times higher than that of outer modules, the bandwidth usage of the DHP–DHE links is uneven. To mitigate this effect, each DHC receives data from two adjacent inner modules and three neighbouring outer half-ladders that are diametrically opposite to the first two. This connectivity scheme ensures *load balancing* and allows reducing the number of DHC output channels down to 4 for each DHC without data truncation. All PXD sub-events isolated by DHEs and DHCs are transmitted to ONSEN via 32 optical links following the round-robin scheme. A fraction of data processed by the DHH is used for module monitoring and other local studies. For this purpose, the first four optical links additionally pass data to the local DAQ system, where its quality is assessed independently of the central Bell II data quality monitor (DQM). As will be discussed in Chapter 4, raw PXD data available in the local DAQ system proved useful for studying photon radiation in the PXD.

3.3.4 PXD data reduction

Raw PXD data is highly contaminated with background events originating from sources that are later discussed in Sec. 4.1. Although, it is challenging, if not impossible, to determine whether a particular event stems from a signal cascade or from a background process using PXD data only. To figure it out, the response from other sub-detectors, especially the tracking information provided by the SVD and CDC, is required. These sub-detectors operate at much lower background levels, which allow efficient reconstruction of charged tracks without the shattering dominance of fake tracks. If these tracks are complemented with PXD clusters that are close to the IP, vertex resolution is improved greatly (see Fig. 3.18).

The concept illustrated in Fig. 3.18 can be naturally extended with an effective data reduction mechanism: PXD clusters that are **not** associated with tracks promptly reconstructed by the HLT are discarded, as they are unlikely to originate from signal events. To realise this approach, the exact position at which an extrapolated track intercepts a PXD layer–referred to as the Most Probable Hit (MPH)–is determined. The area centred around an MPH defines a Region of Interest (ROI). PXD hits that belong to established ROIs are preserved, while all others are discarded. This set of ROIs is referred to as **HLT ROIs**, as they are determined in the sequence of prompt reconstruction performed by the HLT. HLT ROIs are received by the PXD DAQ system with a delay comparable to that of the classifier output, $i.e.$ up to 5 s.

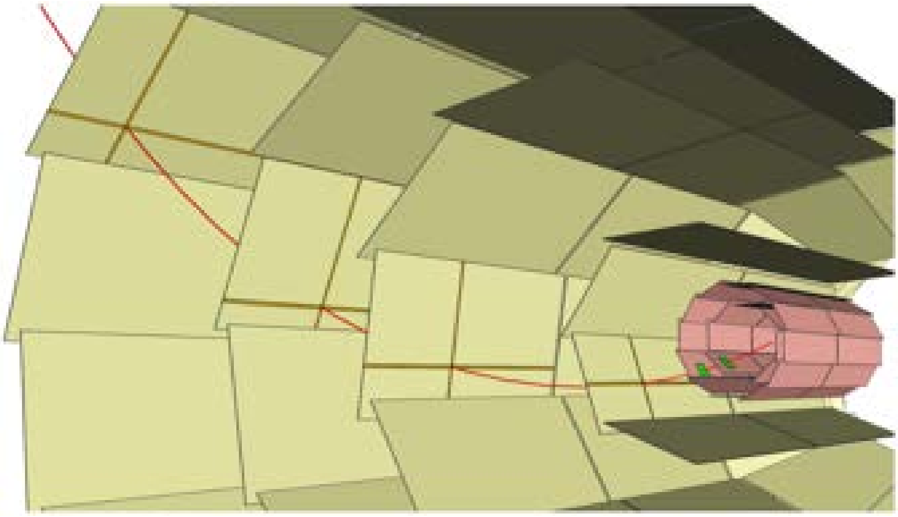

Figure 3.18: Illustration of the ROI finding technique. A track reconstructed using the response of the SVD and CDC is extrapolated in the IP direction to locate a ROI in two PXD layers. The area around the interception points is referred to as an HLT ROI.

The second set of ROIs is built for PXD sub-events by the Data Acquisition Tracking and Concentrator Online Node (DATCON) [60]. In contrast to the computationally demanding track reconstruction performed by the HLT using raw data from all outer sub-detectors, DATCON is an FPGA-based system capable of fast ($\sim$100 μs) reconstruction of SVD data to acquire so-called **SVD ROIs**. The sequence implemented in the DATCON firmware first performs the hit clustering using the next-neighbour search enhanced with Centre of Gravity (CoG) and η-corrections to precisely determine strip-hit positions. Resulting hit coordinates are then processed by the Fast Hough Transform, which performs pattern recognition in the $r - \phi$ and $r - z$ planes to identify track candidates. These 3D track candidates are subsequently extrapolated toward PXD layers to define SVD ROIs. This additional set of ROIs, thanks to a more advanced reconstruction algorithm implemented in embedded circuits, tends to have higher reconstruction efficiency and lower rate of fake candidates for tracks left by charged particles with low p_T, as they do not leave hits in outer sub-detectors.

Finally, two sets of ROIs are meant to be combined into a single set, which is used to truncate data for events that pass HLT classification. Although, as for the moment of delivering this thesis, the DATCON concept has not been implemented in hardware yet. Therefore, the data truncation is performed using HLT ROIs only.

The sequence described above forms the basis of the PXD sub-event filtering procedure. It is expected to reject the majority of PXD hits at the negligible cost of discarded signal events. In reality, the reduction factor strongly depends on beam conditions, which affect tracking efficiency. Early simulations suggest a reduction factor of $\sim$10 with HLT ROIs only [61], which, when combined with HLT filtering, results in an overall factor of 30 data reduction. This translates into the reduction of the 18 GB/s incoming data rate transmitted by the DHH down to 600 MB/s of data passed to EB2. A system dedicated to the data reduction, known as Online Selector Nodes (ONSEN) is discussed in the next section.

3.3.5 Online Selection Nodes (ONSEN) system

Due to the standalone PXD DAQ stream, the HLT filtering discussed above is applied to PXD sub-events following an alternative sequence. With a classifier latency of up to 5 s, a substantial PXD data volume must be buffered during the continuous readout cycle before an HLT signal is received. Therefore, a dedicated system, known as ONSEN had to be developed. It is capable of meeting the 30 kHz rate of the L1 trigger, integrates sufficient low-latency memory necessary to delay a retain/reject decision execution and is compatible with the 6.125 Gbps DHH output. As mentioned earlier, the mean decision-making time required for the HLT is 1 s. If double of that is assumed to calculate the required buffer size and bandwidth for a data reduction system, it translates into 36 GB of the total memory capacity and 6.125 Gbps per DHH link. Only after HLT filtering is applied to PXD sub-events, preserved candidates are passed to the EB2, where they are merged with HLT-filtered event fragments reconstructed in other sub-detectors.

The ONSEN system [62–64] has been developed considering the data buffering and truncation requirements discussed above. It is capable of buffering PXD data corresponding to 2.5 s of continuous readout at design luminosity, combining ROIs from two independent sources, performing event-level filtering and data truncation and streaming the resulting data to the EB2.

These features are achieved by using field-programmable gate arrays – reconfigurable integrated circuits that consist of programmable logic blocks, memory elements, and high-speed interconnects. They can implement complex data-flow architectures with nanosecond-level latency, making them ideal for front-end and trigger applications in the high-energy physics. In contrast to application-specific integrated circuits, they feature flexible firmware updates, while compared to CPU- or GPU-based systems, they achieve substantially lower latency and higher I/O bandwidth through direct serial link connections. This flexibility enables the ONSEN system to sustain the full PXD data throughput within a self-contained hardware infrastructure.

System architecture

The complete ONSEN system consists of 9 *compute node carrier boards* (CNCBs) and 33 *xTCA-based FPGA Processor* (xFP) developed by the Trigger Lab at IHEP (Beijing) in collaboration with Gießen [65, 66]. It is hosted inside an *Advanced Telecommunications Computing Architecture* (ATCA) shelf [67], which features full-mesh topology allowing high-speed (3.125 Gbps) communication between individual boards (see Fig. 3.19). Each shelf is controlled by the Shelf Manager, which communicates with *Intelligent Platform Management Controllers* (IPMCs) on individual boards via the *Intelligent Platform Management Interface* (IPMI) [68], supporting hot-swappable modules and redundancy. Communication between the Shelf Manager and the slow control system allows remote access and monitoring of power consumption, temperature, and other system health indicators.

Each CNCB installed in 9 of the 14 ATCA shelf slots is equipped with a Xilinx Virtex-4 FPGA and a 2 GB DDR2 SDRAM module, and can host up to four full-size xFP daughter cards [69, 70]. It provides multi-gigabit connections to the full-mesh backplane, which can be extended with a *Rear Transition Module* (RTM) that offers Ethernet, USB, and JTAG ports for slow control, debugging, and firmware programming. The automatic configuration of FPGAs is achieved via an onboard *Complex Programmable Logic Device* (CPLD) and Flash memory, which store the carrier bitstream and a compressed Linux image executed by an embedded PowerPC CPU to manage board operation and slow control. Additional components, such as IPMCs, enable integration with the shelf manager allowing remote monitoring through the slow control.

xFP daughter cards hosted by CNCBs are equipped with a Xilinx Virtex-5 FPGA [71, 72] and a 2 GB DDR2 SDRAM module. Each board connects to the CNCB via six *Multi Gigabit Transceivers* (MGT) and twelve two-directional *Low Voltage Differential Signal* (LVDS) links located at the end of the docking bay. The external optical connection for high rate data transfer (up to 6.125 Gbps) is realised through two SFP+ cages located at the front side of each xFP card. Additionally, it hosts an extra Ethernet port that provides an interface to external monitoring and *universal asynchronous receiver/transmitter* (UART) connections providing debugging functionality. The readout is achieved via an add-on *Module Management Controller* (MMC) developed by the Belle II group at the University of Mainz.

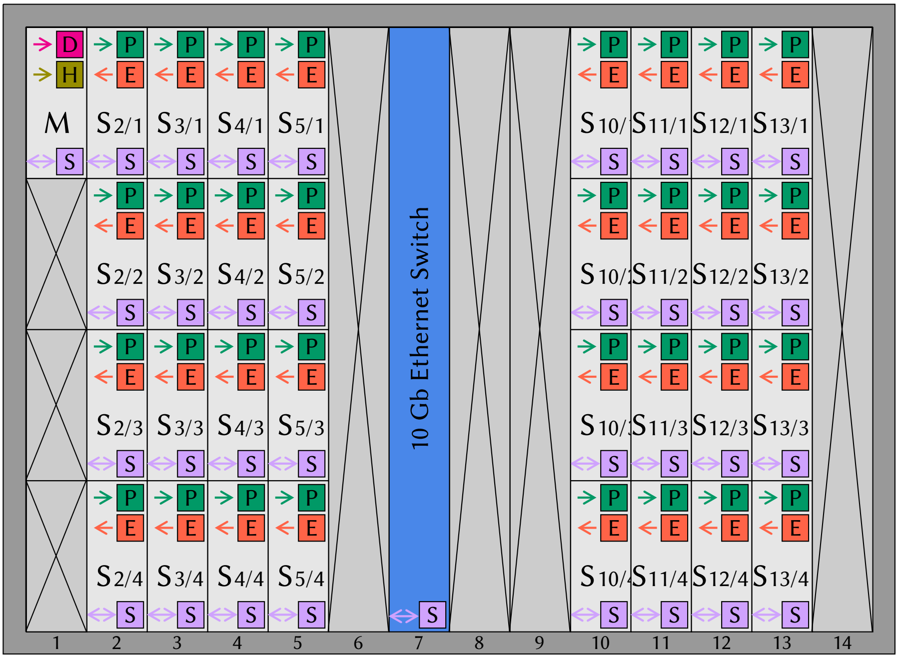

Figure 3.19: Schematic illustration of the ONSEN system. Light-gray ( ) rectangles indicate individual xFPs programmed with the selector (S) or merger (M) bitstreams. Each xFP has an Ethernet port for the communication with the slow control (S). Each selector xFP is labelled following the S_{ij} scheme, where i is the xFP order in a CNCB (counting from top to bottom) and j is the number of an ATCA slot a CNCB it belongs to is inserted in. Each selector xFP has two optical connection: one for receiving data from the DHH (P) and one for passing truncated data to the EB2 (E). Optical ports of the Merger xFP serve different purposes: one passing SVR ROIs from the DATCON (D) and the other passing HLT ROIs and the classifier output (H). Empty xFP and CNCB slots are marked with crosses. The blue ATCA slot hosts a base-channel GbE switch.

ONSEN firmware

The firmware of the ONSEN system is implemented through four main projects. Two of these, called *Merger* and *Selector*, run on xFP FPGAs, while the other two, *Merger Switch* and *Selector Switch*, run on CNCB FPGAs [62, 63]. The current arrangement of xFPs and CNCBs programmed in either way is depicted in Fig. 3.19, while an actual picture of the ONSEN system is provided in App. A in Fig. A.3.

The Merger xFP receives ROI data from the DATCON via 3.125 Gbps AURORA links and stores it in the local memory. The trigger number and the memory address of each ROI are recorded in a Look-Up Table (LUT). HLT ROIs, which arrive later due to the higher processing time of the HLT, are matched to the stored DATCON ROIs using the trigger number. The merger-core then combines both ROI streams, sorting the merged ROIs by ascending DHE-ID, and transmits the result via the AURORA interface to the Merger Switch on the CNCB.

The Merger Switch distributes merged ROI packets to Selector Switch units on other CNCBs according to the load-balancing scheme of the DHH system. Each Selector xFP receives pixel data corresponding to the assigned DHE-ID and the trigger number, and buffers it in local memory until the associated ROI packet arrives. The pixel-filter core then selects only those hits within the ROI, effectively reducing the data volume. Filtered pixel data are transmitted to the EB2, where they are merged with other sub-detector data streams. The flow of PXD data truncation algorithm is schematically illustrated in Fig. 3.20.

The control and monitoring of the firmware is handled by the embedded PowerPC

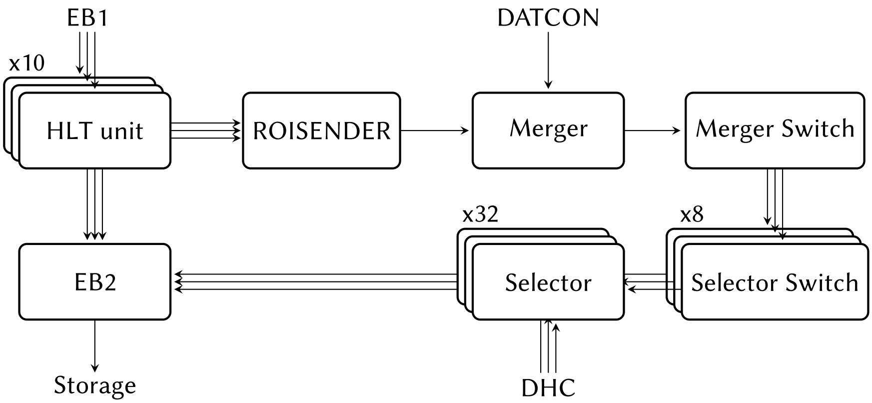

Figure 3.20: Schematic illustration of data reduction algorithm. HLT units receive raw data from outer sub-detectors to calculate HLT ROIs, which are sent via ROISENDER to the Merger AMC, where HLT ROIs are merged with DATCON ROIs. Combined ROIs are communicated via Merger and Selector Switches to individual Selector AMCs, where they are used to truncate PXD data passed by DHC modules. Truncated PXD data is passed to the EB2, where it is combined with sub-events reconstructed by the HLT using data from other sub-detectors. Fully reconstructed events with truncated PXD data are passed to storage units.

CPUs within FPGAs. Intellectual property cores implement the data-path logic and expose 32-bit registers and interrupt interfaces accessible via a local bus. Software running on embedded CPUs, including the EPICS-based slow control, can configure, monitor, and debug the FPGA logic. Automatic programming of both xFP and CNCB FPGAs is supported via CPLDs and onboard the flash memory, ensuring correct initialisation and allowing on-demand reprogramming during operation.

Chapter 4

Beam-induced background in the PXD

The performance of the Belle II detector is steadily improved, as various hardware upgrades and software updates are carried out. The rejection of background events originating from diverse sources has critical importance for the longevity of hardware components, quality of accumulated data and maximum luminosity reached. Being the innermost detector, the pixel detector is most heavily exposed to the radiation in the interaction region. Isolating sources of the background contamination, mitigating their impact, and continuously monitoring them are essential for the stable PXD operation. In this section, we review measures taken to limit the impact of background events on the PXD and report on efforts taken to improve its online monitoring.

The upgrade of KEKB allowed setting a new instantaneous luminosity record, which currently stands at 5.1×10^{34} cm^{-2}s^{-1} and was reached with the vertical betatron function (β^*_Y) of 1.0 mm at the interaction point. The current target peak luminosity for the decade ahead is 6×10^{35} cm^{-2}s^{-1} and is projected to be reached at β^*_Y = 0.3 mm. Higher luminosity is reached by increasing beam currents, utilising low-emittance colliding beams and reducing transverse dimensions of individual bunches using the so-called nano-beams scheme. These measures come at the cost of higher background, as larger number of beam particles deviate from the designed trajectory and are eventually absorbed by the inner surface of the beam pipe. If this happens in the vicinity of the Belle II detector, interaction of high-energy electrons and positrons with the material of the beam pipe inner wall generates showers of secondary particles, which are registered by the detector. The increase of the detected hit rate and the larger radiation exposure associated with these events are referred to as "beam (induced) background", which is by far the most significant source of the background in Belle II. It is projected that some sub-detectors, $e.g.$ TOP and CDC, will be subjected to near-limit radiation levels, when target luminosity is reached. In this view, mitigation of the beam-induced background emerges as one of the most critical challenges for the SuperKEKB team [73].

The SuperKEKB design, in comparison with the original design of KEKB, includes several major modifications, which are intended to reflect changes of beam energies, ensure stable machine operation at higher luminosity and mitigate the consequential rise of the beam background rate. They include, but are not limited to, the following measures: i) LER dipole magnets were exchanged with longer ones to accommodate the increased energy of the positron beam, ii) the IR has been redesigned to integrate QCS final focusing magnets, iii) beam pipes with titanium nitride (TiN) inner coating have been installed in the LER to mitigate higher density of the synchrotron radiation, iv) a damping ring has been constructed to reduce the emittance of injected positrons, v) the radio-frequency (RF) system has been modified to enable higher beam currents, vi) movable beam collimators have been installed to filter out particles with large transverse deviation from the nominal beam orbit before they reach the IR.

4.1 Beam background sources

Critical hit rates induced by background showers pose the danger to individual sub-detectors, as they can degrade the performance or even cause the irreversible damage. Mitigation efforts generally depend on the underlying mechanisms of the background radiation production. In this section, we break down the most common sourced of the beam induced background and the respective counter-measures taken.

Touschek background. The Touschek background arises from Coulomb scattering between particles in a beam bunch. As a result of such interactions, energy is transferred between particles, which smears the energy distribution for particles in a bunch and increases the beam emittance. The magnitude of this effect is proportional to the beam current squared and inversely proportional to both the number of bunches in a ring and the beam size. Due to the nano-beams scheme employed at SuperKEKB, the small beam size elevates the Touschek scattering rates. While horizontal collimators installed near the interaction region have significantly suppressed the associated particle loss within the detector, Touschek scattering remains one of the dominant sources of background in Belle II.

Beam-gas background. Interactions between beam particles and residual gas atoms in the beam pipe represent another major source of background in SuperKEKB. The beam-gas Coulomb scattering alters particle trajectories, while the beam-gas bremsstrahlung leads to the energy loss. The scattering rate is proportional to both the residual gas pressure and the beam current. A high beam-gas loss rate within the detector region is expected due to the narrow diameter of the beam pipe near the IP and the exceptionally large vertical betatron function of the QCS. Although vertical collimators have significantly reduced this background, further suppression requires narrowing the collimator aperture by decreasing the gap between jaws — a measure that may induce beam instability at higher currents. [74].

Luminosity background. The beam-beam interaction in the IR induces the luminosity background, which – as the name suggests – is proportional to the instantaneous luminosity. It is expected to dominate at the target luminosity of SuperKEKB.

The primary mechanism responsible for the background generation in beam-beam interactions is the radiative Bhabha scattering ($e^+e^- \to e^+e^-\gamma$). Its cross-section is approximately 300 times higher than that of the key physics process – $\Upsilon(4S)$ production – at the design centre-of-mass energy. The emission of bremsstrahlung photons causes beam particles to deviate from the nominal orbit and smears their energy distribution. Thanks to the upgraded quadrupole magnets system at SuperKEKB, which is no longer shared between the in- and outgoing beams, the loss rate of these off-momentum particles inside the detector has been significantly reduced. However, due to various reasons [73, 75], a small fraction of low-energy beam particles can still be lost inside the detector. The radiative Bhabha scattering can also induce neutron backgrounds, which originate from the interaction of bremsstrahlung photons that propagate along the beam pipe with accelerator components (primarily magnets) located 10−20 meters downstream from the IP. These interactions, through the giant photo-nuclear resonance, produce neutrons that may be backscattered into the detector, increasing the occupancy of the KLM [76].

Additionally, low-momentum electron-positron pairs can be produced in the interaction region via two-photon process, $i.e.$ $e^+e^- \to e^+e^-e^+e^-$. These soft charged particles are particularly problematic: if their transverse momentum is sufficient, they can curl in the Belle II solenoidal field and leave multiple hits in the inner detector, significantly contributing to the total background.

Synchrotron radiation background. The synchrotron radiation (SR) is another well-established source of the beam induced background. Its intensity scales with the beam energy and magnetic field strength squared. Therefore, the HER beam is primarily responsible for the contamination of the SVD and PXD with the SR-induced photons that feature the energy spread from a few to several tens of keV. A more elaborate discussion of the SR-induced radiation will is provided in Sec. 4.3.

Injection background. Due to the limited beam lifetime at SuperKEKB, regular top-up injections using the betatron injection scheme [77] are required to maintain stable beam currents. When the total beam current drops below the predefined threshold (currently around 99% of the nominal value), additional electrons or positrons are injected at the rate of 1–25 Hz. Newly injected particles feature a relatively large transverse momentum, leading to betatron oscillations in the horizontal plane around the main stored beam. These oscillations generate elevated background rates in Belle II whenever a “refuelled” bunch passes through the interaction region. This effect typically lasts for a few milliseconds until kinematic properties of all particles in a bunch become uniform. To prevent saturation of the readout system during this period, dedicated trigger vetoes are applied [54]. However, these vetoes introduce dead time in the data acquisition, effectively reducing the recorded luminosity. The intensity and time evolution of the injection-related background are continuously monitored online to optimise injection parameters, refine veto schemes, and ensure that background remains within acceptable limits. Maintaining stable injection background levels over long operational periods remains one of the key challenges of the SuperKEKB operation.

Large beam loss accidents. An unintended firing of one of the injection kicker magnets can perturb a stored beam during its 2-μs-long pulse, potentially steering a beam toward a horizontal collimator and causing severe damage to collimator jaws. In addition, for reasons that are not yet fully understood, events known as *sudden beam losses (SBL)* can occur. In an even of a SBL, a beam becomes increasingly unstable up to the point of directly hitting components of SuperKEKB. If this happens in the vicinity of the IR, a single SBL may cause irreversible catastrophic damage to the detector. Multiple incidents of this kind led to quenches of the QCS or damage to sensitive Belle II hardware components. In less severe cases, jaws of impacted collimators can be heavily damaged, requiring their replacement, a process that typically results in the loss of 1–2 weeks of the beam time. Notably, the frequency of SBL events tends to increase when beam currents exceed 0.5 A. These disruptions have caused multiple delays and significantly hindered the progress toward the target integrated luminosity.

The SuperKEKB team conducted (and continues conducting) extensive analyses dedicated to the search of underlying causes of these instabilities. During the 2023 run campaign, after two consecutive SBL events caused severe damage to the PXD, the sub-detector was excluded from the global data taking to stay protected from further damage. Currently, the leading hypothesis explaining beam instabilities puts blame on dust particles accumulated inside the beam pipe. It is believed that fine dust adhering to the inner wall of the pipe, possibly originating from damaged collimator jaws, can become detached from the wall surface at high beam currents. These particles may then interact with the beam in what is referred to as a “fireball” event. As clearing electrodes mounted on the upper side of the beam pipe inner wall were identified as a likely site of dust accumulation, they were flipped during the 2023–2024 campaign to mitigate the problem. Later in 2024, another promising hypothesis emerged. It supposes the improper use of vacuum sealant, which led to contamination of the beam pipe. This contamination is now considered another potential trigger for SBL events, and therefore the work on removing the vacuum sealant is ongoing, as well as other mitigation efforts. As a precautionary measure, the PXD will remain excluded from the physics data taking at least until mid-2026. This measure might be reconsidered, if the problem of severe beam instability is resolved and the safety of the PXD operation is ensured. However, while several plausible hypotheses have been proposed for SBL events happening in the LER, the origin of similar events in the HER, which account for roughly 10% of all SBLs, remains unknown.

4.2 Beam background mitigation efforts and online monitoring

A reader can mention that collimators play a key role in preventing damage to the detector by off-orbit beam particles, independently on the mechanism of the trajectory deviation or energy loss. Therefore, as a part of the KEKB upgrade, movable collimator have been installed around SuperKEKB rings to filter out beam particles with the large transverse deviation from the nominal beam trajectory before they reach the IR. They are also instrumental in preventing colossal damage to Belle II and the QCS in an event of a SBL [78]. There are currently two types of collimators installed around SuperKEKB rings: asymmetric *KEKB-type* that have only one jaw and symmetric *SuperKEKB-type* with jaws on both sides. Horizontal collimators are targeted to stopping Touschek scattered particles, while vertical collimators are mainly used to filter out beam-gas Coulomb scattered particles [79].

While collimators effectively protect the detector from the impact by scattered beam particles, the detector shielding is essential for protecting against other background sources. Therefore, a thin layer of tungsten is installed outside the beam pipe and inside the vertex detector (beyond the physics acceptance region) to shield from single-beam losses and the luminosity background, while thick tungsten plates are covering QCS magnets to protect Belle II components from frequent beam losses happening in the QCS due to a large betatron function.

The IP beam pipe has been meticulously engineered to minimise the impact of the SR in the IR [80]. Its central beryllium section is shielded from the upstream SR by the tapered part of the incoming pipe, ensuring the IR is fully protected from the direct radiation. The indirect (secondary) radiation is effectively suppressed by the rigid structure on the tapered surface of the incoming beam pipe. Although some backscattering contamination ma persist, its intensity has been significantly reduced thanks to the redesigned geometry of the QCS. This effect and corresponding mitigation efforts will be discussed in more details in Secs. 4.3 and 4.4

The beam quality and the level of background it induces are monitored online to ensure the detector safety and the data taking quality. There are multiple online monitors and sensors taking online measurements to control them in the real time. They include, but are not limited to, the following:

Beam quality monitors

- X-ray beam profile monitors (XRMs) are used to measure transverse dimensions of the beam [81];
- The Luminosity Online Monitor (LOM) is employed for the online measurement of the instantaneous and integrated luminosity [82].

Vacuum system monitors

- A system of 300 cold cathode gauges (CCGs) is used to measure the residual gas pressure in a ring [83];
- Residual gas analysers (RGAs) are utilised to measure the molecular composition of residual gases in a beam pipe.

Background monitors

- Diamond sensor-based detectors (Diamonds) [84] are used for measurement of the radiation dose in the IR;
- The sCintillation Light And Waveform Sensors (CLAWS) detector system [85] monitors beam-induced backgrounds associated with the SuperKEKB injection;
- The BEAST TPC system is utilised to provide directional and spectral measurements of the fast neutron flux [86];
- ^{3}He tube detectors [87] are in charge of counting thermal neutrons with kinetic energy below 0.025 eV;

- PIN photo-diodes [88] are installed next to each collimator to measure the localized radiation caused by beam losses;
- 5-m-long ion chambers [88] mounted along the accelerator tunnel to measure cumulative and distributed beam losses, helping to identify regions with persistent losses and radiation buildup;
- New loss monitors, based on photomultiplier tubes (PMTs) and electron-multiplier tubes (EMTs) are used in tandem to pin down the location of sudden beam losses around both rings.

Beam abort system

- A dedicated beam abort system that combines readings from Diamonds, PIN photo-diodes, ionisation chambers and eight closest to the IP CLAWS detectors is utilised to dump unstable beams and avoid severe damage to Belle II and SuperKEKB components. It is capable of triggering a beam abort $\sim$10 μs earlier than Diamonds alone.

The global online monitoring systems listed above requires a dedicated hardware to perform measurements, while dozens of other monitors are based on the real-time analysis of data recorded by individual sub-detectors. Given that each Belle II detector component has individual vulnerabilities, dedicated background monitoring systems are employed. In the context of the PXD, while SBLs pose the most significant threat of irreversible damage to the PXD hardware, irreducible two-photon processes and the injection background are the main sources of beam background in the PXD. It is also particularly sensitive to the backscattered SR of low energy photons. The nature of this contamination and the online monitoring system dedicated to it are subjects of particular attention in this thesis and will be elaborately discussed in later sections.

4.3 Backscattered synchrotron radiation (BSR)

As outlined in the previous section, a thoughtful design of the beam pipe shields the IR both from the primary and secondary SR. The SR generated by most of the mechanisms discussed above propagates parallel to the beam pipe orientation, and therefore is filtered out by the tapered section implemented in the new beam pipe design (see Fig. 4.1). On contrary, the SR emitted by injected beam particles, which have larger transverse momentum, is non-parallel to the orientation of the beam pipe. Therefore, after propagating through the IR, it can hit the start of the chamfer and get scattered back into the acceptance region leaving hits in the PXD. The propagation

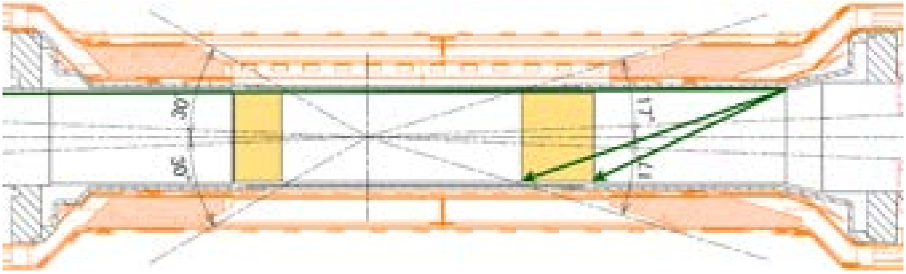

Figure 4.1: Schematic design of the upgraded beam pipe installed prior to the Run II. The area limited by dot-dashed lines, which are offset by specified angles, is the physics acceptance region. Green arrows show the propagation of non-parallel X-rays responsible for the backscattered radiation. The yellow-filled region represents the gold coating on the outer surface of the beam pipe's inner wall (credit: Shuji Tanaka, KEK).

path of the non-parallel X-rays is illustrated by green arrows in Fig. 4.1. In order to mitigate it, an additional thin layer of gold coating has been added to the outer wall of the inner beryllium beam pipe outside the acceptance region, as highlighted in the design scheme depicted in Fig. 4.1 and photograph shown in Fig. 4.2.

Figure 4.2: An image of the inner beryllium beam pipe with additional fragments of gold coating added (credit: Shuji Tanaka, KEK).

The impact of the BSR can be observed by looking into collision data recorded by the PXD. A particle penetrating a layer of the pixel detector deposits energy in one or multiple pixel in the area of interaction. A dedicated clustering mechanism developed and integrated in the Belle II software is utilised to allocate pixels that were 'lit' in a collision event and group pixels activated in the same region into a cluster. Each pixel cluster corresponds to a single instance of a particle penetrating a PXD layer. Based on the cluster shape and the total energy deposited in a cluster, it is possible to distinguish the type of a particle that has been recorded. Charged particles tend to generate clusters that consist of multiple pixels (MPC) and deposit a larger amount of energy (>30keV). On contrary, photon clusters usually consist of a single pixel (SPC) and deposit less than 30 keV of energy. Fig. 4.3 shows examples of clusters lit up in the PXD by a photon and a positron.

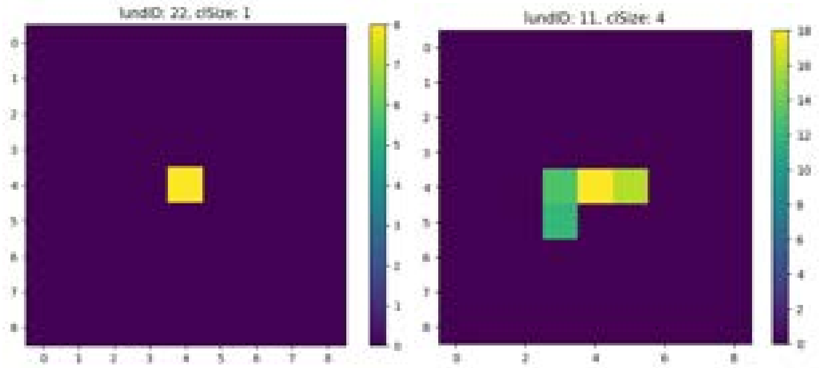

Figure 4.3: An image of clusters reconstructed in the PXD that were left by a [left] photon and a [right] positron.

In order to demonstrate correlation between the injection timing and the intensity of the photon radiation in the PXD, we perform an analysis of data collected with the PXD in Run I and Run II. Event reconstruction with the *basf2* software allows combining response from all Belle II sub-systems. In particular, the timing information provided by the trigger and raw hits recorded by the PXD are relevant in this context. When a hit is recorded by the PXD, the drift charge gained by individual pixels is mapped as described in Sec. 3.2.1. After clustering is performed, the charge is summed up over all pixels in an individual cluster to determine the *cluster charge*. In order to account for the non-uniform collection of the drain current by gates of individual DEPFET pixels across a given row, gain calibration is performed. As a part of the Conditions Database, a dedicated *basf2* module, *PXDGainCalibrator*, stores the pixel-to-pixel gain map, which corrects the *cluster charge* value measured in individual pixels for the respective charge gain performance. By renormalising it to the keV scale, the *cluster energy* is acquired. Fig. 4.4 illustrates distributions of the cluster charge and cluster energy for single-pixel clusters (SPC) and multiple-pixel clusters (MPC) in the Experiment 30 Run 2486 with PXD2. The comparison of both plots shows that these distributions are fairly similar, which is why some exclusive to the PXD data analyses, which do not the response of other sub-detectors or the Belle II -wide software, make use of the cluster charge data within the internal PXD software, such as *lab framework*, without converting it to the cluster energy. It is also noticeable that the cluster energy distribution exhibits repetitive bins with abnormally high counts. This happens due multiplication of a discrete cluster charge value by a float gain calibration factor, which results into a repetitive saw-like structure in the cluster energy distribution, when finite binning is applied.

To continue the discussion of cluster the charge/energy distribution, there are two distinctive peaks contributing to the distribution of SPCs. A narrow peak around 15 keV is formed by SR-induced fluorescence photons emitted perpendicular to the beam pipe surface during the interaction with the gold coating of the inner wall. These photons can penetrate the beryllium beam pipe and leave hits in the PXD. On contrary, the broad distribution peaking at the larger energy of 35 keV is produced by SR photons, which penetrate the beam pipe directly. This peak is less visible in the measured energy spectra, as it is shadowed by the component generated by charged particles that can be described by a Landau distribution with the maximum around 50keV.

The cluster energy distribution depicted in Fig. 4.4 supports a common way to discriminate particle and photon clusters in the PXD. Single-pixel clusters with low energy, more precisely from 8 to 30 keV, are considered to be photon clusters

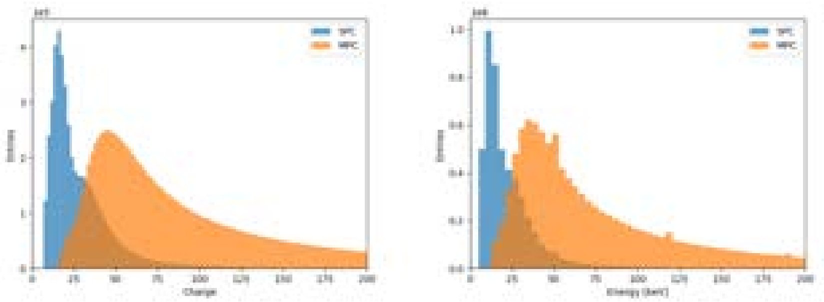

Figure 4.4: Distribution of the [left] cluster charge and [right] cluster energy for SPCs and MPCs in the Experiment 30 Run 2486 with PXD2.

(LE SPCs), while multiple-pixel clusters with energy above 30keV (HE MPCs) are treated as particle clusters. For clusters discriminated in this way, we determine the corresponding time stamp since the last HER injection to map the dependency depicted in Fig. 4.5. The zoomed-in distribution in the top plot in Fig. 4.5 clearly shows a periodic feature in the photon radiation intensity at a frequency of about 7 kHz, matching the expected frequency of betatron oscillations. The increased photon rate fades out entirely after around 10ms since the last HER injection, as the bottom plot in Fig. 4.5 illustrates. The periodic structure is less pronounced for particle clusters, but can be still observed in runs with various beam optics and currents (see Fig. B.1 in App. B).

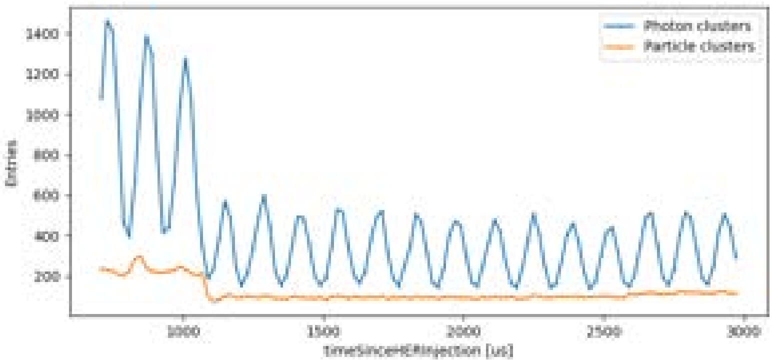

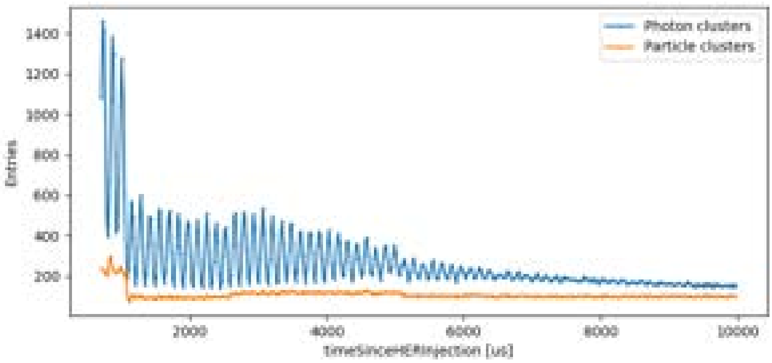

Figure 4.5: Number of photon and particle clusters versus the time since the last HER injection in the Experiment 30 Run 1957 with PXD2.

4.4 Evolution of the BSR in the PXD

In this section, we provide a brief overview of the BSR evolution in the PXD1 during the Run II, along with the mitigation steps taken to address it. An increased photon radiation during the injection period with the characteristic footprint in backward (BWD) PXD modules was first observed in the Experiment 8. The newly observed radiation was fully alleviated by adjusting the vertical HER tune.

The BSR reappeared in Experiment 10, when beam optics were changed. As briefly described in Sec. 3.1, the focusing strength of QCS magnets is defined by horizontal and vertical betatron functions – β^*_X and β^*_Y, respectively. In pursuit of the higher instantaneous luminosity, beta functions are reduced to achieve a denser focused beam in the IR. After the Experiment 10 Run 5401, the horizontal betatron function of final focusing magnets was reduced from 80 mm to 60 mm, leading to increased radiation in the PXD due to the BSR. The previously effective vertical adjustment of the HER orbit in the IR no longer alleviated the BSR. Instead, a rotation of the orbit by 0.42 mrad was applied. This reduced the localized radiation in BWD modules but led to a more uniform exposure in other modules.

To demonstrate the pattern of the BSR in early runs of Run I, we perform a reconstruction of PXD clusters in raw data stored by the *pxdlocaldaq* machine. We choose to directly processes raw PXD data using lab framework, as the response from other sub-detectors is not relevant for the current analysis. This approach requires less CPU time and memory, allowing to process more events and runs.

We consider the background knowledge mentioned above for an educated pick of runs with PXD1 to perform analysis of:

- **Exp.10 Run 5401** – $I^{\text{avg}}_{\text{HER/LER}}$=365/444 mA, $\beta^*_{X/Y}$=80/1 mm – the last run before beam optics change (see Fig. 4.6);
- **Exp.10 Run 5451** – $I^{\text{avg}}_{\text{HER/LER}}$=303/435 mA, $\beta^*_{X/Y}$=60/1 mm – the first long run with the horizontal betatron function reduced to 60 mm (see Fig. 4.7 [top]);
- **Exp.10 Run 5611** – $I^{\text{avg}}_{\text{HER/LER}}$=338/475 mA, $\beta^*_{X/Y}$=60/1 mm – the first “good” run after the rotation of the HER orbit to mitigate the increased photon radiation (see Fig. 4.7 [bottom]).

Given the strong dependency of the photon radiation in the PXD on beam currents and optics, these values are provided above for each run under study. For the chosen runs, we reconstruct PXD hits accumulated in a sample of arbitrarily selected 100k events. After clustering is performed, reconstructed clusters are discriminated into LE SPCs and HE MPCs, as described in the previous section. Eventually, to demonstrate the pattern of the photon radiation, a 2D map is plotted for photon clusters in the first PXD layer (L1) in each run (see Figs. 4.6 and 4.7). The maximum bin count is set to each map individually at 120% from the 90th percentile value to exclude sparse misfiring pixels. The module H1032 is missing in each map, as it was excluded from PXD1 data taking due to the poor performance.

Figs. 4.6 and 4.7 clearly illustrate features of the photon contamination described above. The photon radiation for the Experiment 10 Run 5401, which is the last run before beam optics were changed, illustrates relatively low contamination with LE SPCs (see Fig. 4.6). The BSR observed in this run, despite being dominant in the central region of the map, is still relatively uniform across all modules, if the total number of LE SPCs is compared (see Fig. 4.8). This changes dramatically in the Run 5451, which is the first stable run with new beam parameters, where the value of the horizontal betatron function was changed from 80 to 60 mm (see Fig. 4.7 [top]). The photon radiation map plotted for this run illustrates emergence of the intense fan localized in BWD modules, which is caused by the BSR generated by the HER beam. The change of this pattern can be observed in the map of the Run 5611 (see Fig. 4.7 [bottom]), before which the orbit of the HER beam had been rotated by 0.42 mrad. The photon hit distribution plotted for this run exhibits more homogeneous photon

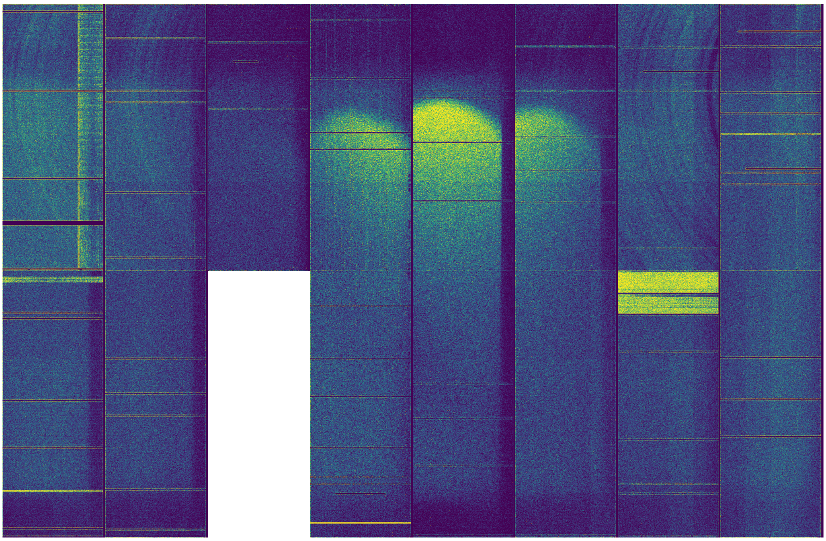

Figure 4.6: Photon radiation map in the Exp.10 Run 5401 with PXD1.

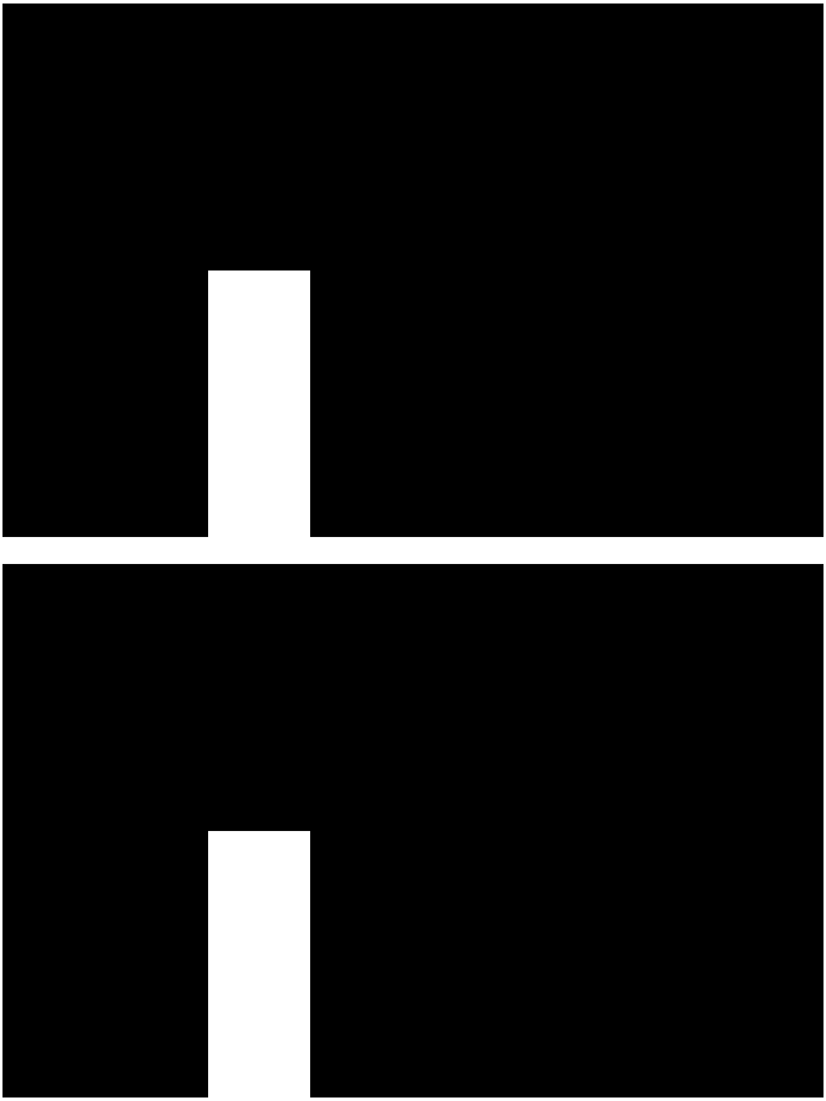

Figure 4.7: Photon radiation maps in [top] the Exp.10 Run 5451 and [bottom] the Exp.10 Run 5611 with PXD1.

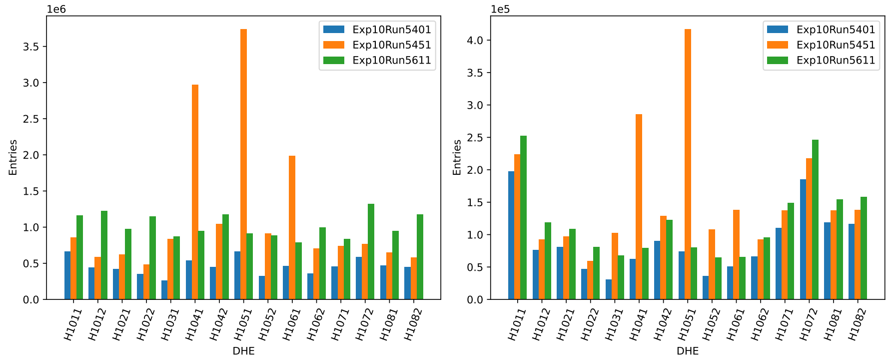

Figure 4.8: Intensity of [left] photon and [particle] hits in L1 modules of the PXD1 in selected runs of the Experiment 10.

radiation, which is less dominant in the central region.

It is worth mentioning that the localized photon radiation is particularly problematic for the PXD. As discussed in Sec. 3.2.1, data from each PXD module sensor is read out by 6 switchers and 4 ASICs. The voltage applied to each of them can be adjusted individually to control sensitivity. Therefore, if flux of the homogeneous radiation changes, switchers' currents can be adjusted accordingly to ensure safety of a module without harming the data taking quality. On contrary, if a localized radiation is observed, there is no way to decrease sensitivity exclusively in an arbitrarily shaped sensor area. In addition, areas subjected to higher photon radiation tend to degrade at higher rate, which additionally contributed to the efficiency loss.

It is useful to compare the total number of LE SPCs and HE MPCs in the considered runs (see Fig. 4.8). Given that the average HER currents for each run lies within 10% of the average of the three, the increase in the photon radiation intensity observed in individual modules must be caused by the beam optics change. This distribution confirms the drastic increase in the photon radiation in modules H1041, H1051 and H1061, which was later uniformly smeared across all the modules with the HER orbit rotation applied.

To study the SR evolution for PXD2 during Run II, we perform a similar exercise for the following runs with relatively long duration and stable beam currents:

- **Exp.30 Run 1463** – $I^{\text{avg}}_{\text{HER/LER}}$=358/448 mA, $\beta^*_{X/Y}$=200/8 mm (see Fig. 4.9 [top]);
- **Exp.30 Run 1731** – $I^{\text{avg}}_{\text{HER/LER}}$=378/518 mA, $\beta^*_{X/Y}$=100/3 mm (see Fig. 4.9 [bottom]);

- **Exp.30 Run 2486** – $I^{\text{avg}}_{\text{HER/LER}}$=639/780 mA, $\beta^{*}_{X/Y}$=60/1 mm (see Fig. 4.10 [top]);
- **Exp.31 Run 138** – $I^{\text{avg}}_{\text{HER/LER}}$=799/997 mA, $\beta^{*}_{X/Y}$=60/1 mm (see Fig. 4.10 [bottom]).

Comparison of photon hit maps for the selected runs in Experiments 30 and 31 illustrates radiation density increase in the central area, as the beam is being squeezed (see Figs. 4.9 and 4.10). Additional gold shielding applied prior to Run II helps to create a photon radiation shade outside the central area and to limit the area of the high photon radiation in problematic BWD modules, $i.e.$ H1041, H1051 and H1061. As beam operation was resumed after LS1, parameters of the designed HER beam trajectory were reset, reverting the aforementioned HER orbit rotation. This, in combination with gradually ramped up beam currents and consistently decreased betatron functions of the final focusing magnets, escalated intensification of the local photon radiation. To give a timeline perspective of the photon radiation evolution in the PXD2, we also perform reconstruction of photon clusters in the Experiment 31 Run 138 – one of the last runs before the PXD2 was excluded from the data taking due to safety concerns. This run features same optics, as the Exp. 30 Run 2486, but also further ramped up beam currents. In the corresponding map (see Fig. 4.10 [bottom]), where multiple switchers killed by frequent SBLs are visible, the characteristic SR "paw" appears to be the most intense so far recorded by the PXD2.

Similarly to the analysis of the Experiment 10 data with PXD1, we plot distributions of the numbers of LE SPCs and HE MPCs in L1 modules of the PXD2, but with a couple of important modifications. Firstly, some of the switchers and isolated pixels of the PXD2 have been irreversibly damaged by frequent sudden beam losses that took place over the course of Run II. These pixels, after being corrupted by large radiation doses, no longer record genuine hits, but generate frequent *misfires* that are recorded by the PXD DAQ. In order to filter out the data provided by compromised pixels, we calculate occupancy of L1 pixels to discard those with occupancy above 0.2% – a value selected by looking into occupancy plots for individual $PXD2$ modules in the Experiment 30 runs listed above. As an example, in Figs. B.2 and B.3 in App. B we provide occupancy distributions plotted for L1 ladders in the Run 2486. Secondly, photon maps shown in Fig. 4.9 illustrate noisy regions observed in modules H1041 and H1042. These areas have been fixed in later runs by adjusting voltages for the corresponding switchers. Although, data recorder by these areas in affected runs can not be recovered. We therefore exclude modules H1041 and H1042 in Run 1463 and the module H1042 in Run 1731 from the histograms shown in Fig. 4.11 to prevent misleading hit rates.

Histograms shown in Fig. 4.11 illustrate the increasing concern of the localized photon radiation in the PXD caused by the backscattered SR. The overall intensity of

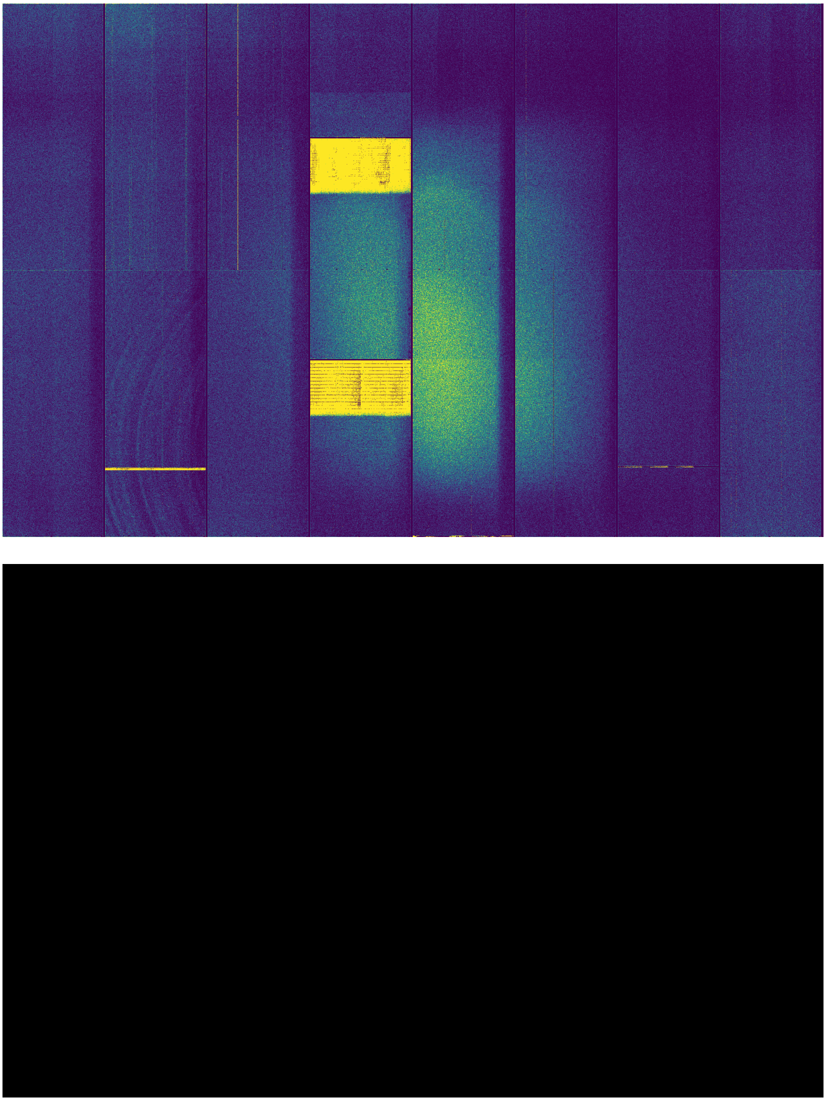

Figure 4.9: Photon radiation maps in: [top] Exp.30 Run 1463 and [bottom] Exp.30 Run 1731 with PXD2.

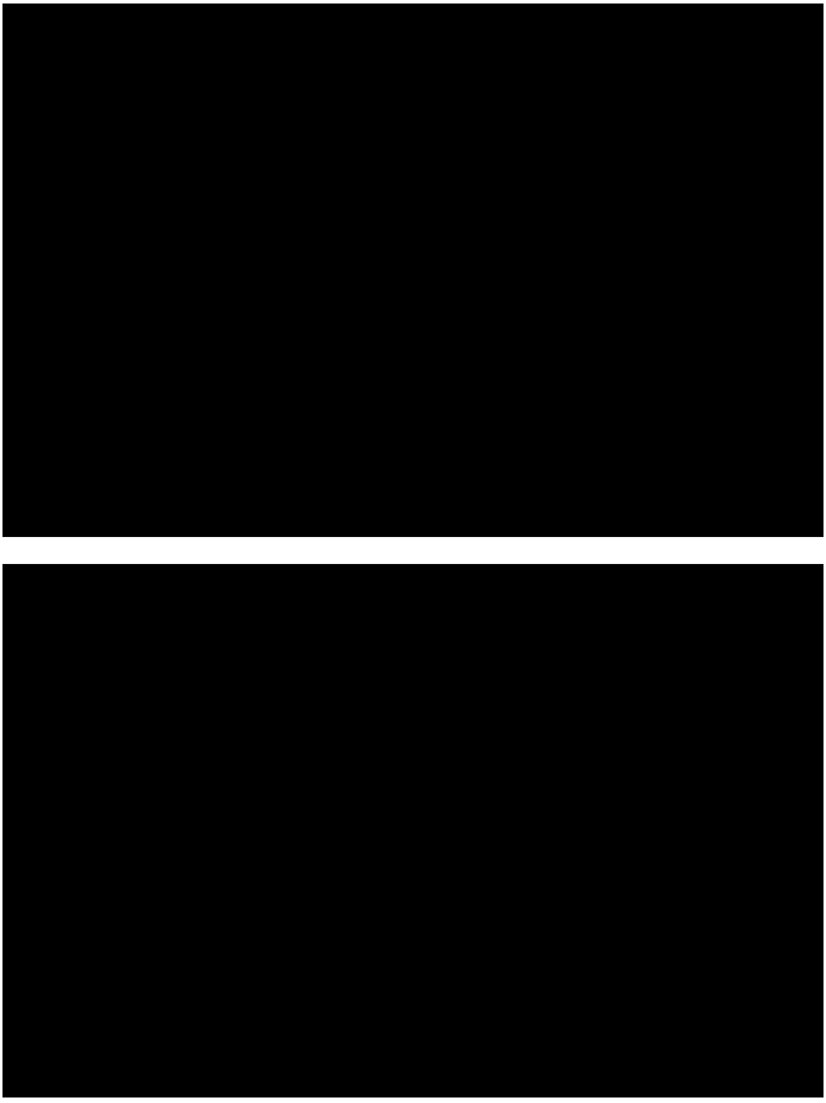

Figure 4.10: Photon radiation maps in: [top] Exp.30 Run 2486 and [bottom] Exp.30 Run 138 with PXD2.

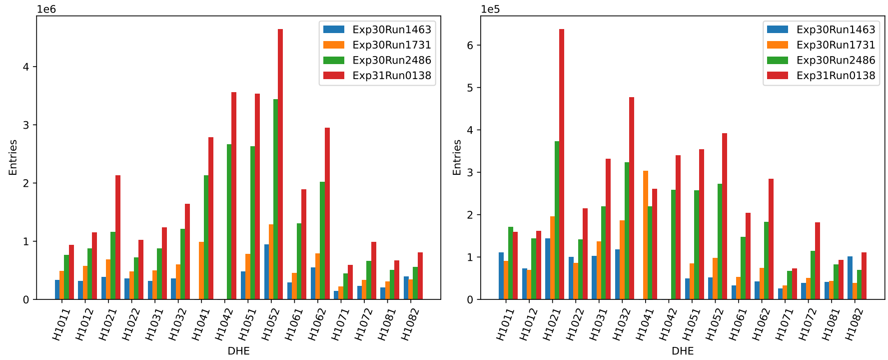

Figure 4.11: Intensity of [left] photon and [particle] hits in L1 modules of the PXD2 in selected runs of the Experiments 30 and 31 with PXD2.

the SR increases with higher HER currents, while consistent decrease of transverse and longitudinal dimensions of beam bunches localize radiation in modules H1041-H1062.

For the sake of completeness, we would like to elaborate on additional studies of clusters' distributions in Run I. Looking beyond the conservative discrimination of clusters into LE SPCs and HE MPCs, it was observed in the reconstruction of Experiment 12 data that distributions of HE SPCs and HE double-pixel clusters (DPC) feature higher density in several FWD modules affected by the backscattered radiation generated by the LER beam, namely H1012 and H1022 (see Fig. B.4 in App. B). While the concentrated intensity of HE SPCs can be explained by events falling in the right tail of the wide peak in the cluster charge distribution, as explained in the beginning of this section and illustrated in Fig. 4.4, the localized feature of the HE DPCs distribution was a new phenomenon to observe. Later in Run I, as beam parameters evolved, localized features of the HE DPCs distribution faded away and the intensity of the HE SPCs distribution decreased by the Experiment 26 (see Fig. B.5 in App. B). The same distributions in the Run II show that the intensity of localizes HE SPCs continues to vanish (see Fig. B.6 in App. B plotted for the Experiment 30 Run 2486). This evolution effectively excludes HE SPCs and HE DPCs from the area of interest in the context of SR study. Distributions of other clusters, $e.g.$ LE DPCs, have also been studied, but no significant localized contamination is observed (see Fig. B.7 in App. B). We therefore preserve the original scheme of interpretation of LE SPCs and HE MPCs as photon and particle clusters, respectively.

4.5 Photon Monitor

In order to monitor the photon radiation in the PXD, the Photon Monitor (PM) is employed. Implemented as a part of the *lab framework*, it is performing the real-time analysis of data acquired with the PXD. The calculation is performed on the *pxdlocaldaq* machine. During the SuperKEKB and Belle II operation, the PV monitored by the PM is communicated to the BCG shifter to monitor the level of the SR in the PXD.

The Photon Monitor utilises the cluster discrimination scheme described in previous sections, in which LE SPCs are treated as photon hits and HE MPCs are identified as particle hits. Monitoring of cluster densities of each kind is performed in *reference* and *signal* areas defined in modules that are affected by the localized photon radiation the most. Reference regions are typically defined in parts of individual modules that are not affected by the BSR, while signal regions are defined to cover areas with the highest density of the localized photon radiation.

For each i-th region defined within a given module (data from which is handled by a given DHE), the total number of LE SPCs and HE MPCs, as well as the total area size, are calculated as follows:

$$\begin{aligned} N_i^{\mathrm{DHE}} &= N_i \cdot \omega_i \cdot \mathrm{hF}_i, \\ S_i^{\mathrm{DHE}} &= \mathrm{pxl\_size}^{\mathrm{DHE}} \cdot N_i^{\mathrm{pxl}} \cdot \omega_i, \end{aligned} \tag{4.1}$$

where N_i is the total number of reconstructed clusters in an area, ω_i is the area weight factor, hF is the area hit factor, pxl_size is the physical size of DEPFET pixels in a given ladder in $\mu\mathrm{m}^2$ and N_i^{pxl} is the total number of pixels in an area.

Counted rates (N_i^{DHE}) and areas sizes (S_i^{DHE}) estimated in individual regions are then separately summed over all reference and signal regions across all modules to determine the hit rate intensity:

$$I = \frac{N^{\mathrm{sig}}/S^{\mathrm{sig}}}{\mathrm{rF} \cdot N^{\mathrm{ref}}/S^{\mathrm{ref}}} = \frac{\sum\limits_{\mathrm{DHE},i}^{\mathrm{sig}} N_i^{\mathrm{DHE}} / \sum\limits_{\mathrm{DHE},i}^{\mathrm{sig}} S_i^{\mathrm{DHE}}}{\mathrm{rF} \cdot \sum\limits_{\mathrm{DHE}}^{\mathrm{ref}} N^{\mathrm{DHE}} / \sum\limits_{\mathrm{DHE}}^{\mathrm{ref}} S^{\mathrm{DHE}}}, \tag{4.2}$$

where rF is the reference area factor. Each ladder, in which measurement regions are introduced, has a single reference area, but might have several signal areas, depending on the shape of the field affected by the photon radiation. This explains the i summing index in the nominator.

Following the Eq. 4.2, intensities of LE SPCs ($I_{\mathrm{SPC}}^{\mathrm{LE}}$) and HE MPCs ($I_{\mathrm{MPC}}^{\mathrm{HE}}$) are calculated. The ratio of two is used to estimate the resulting PV of the PM, which is used to assess the contamination of the PXD with the photon radiation:

$$\text{res} = \frac{I^{\text{LE}}_{\text{SPC}}}{I^{\text{HE}}_{\text{MPC}}} - 1 \tag{4.3}$$

If the value monitored in the real time is fluctuating around 0, the data collected with the PXD is considered to be *good*, $i.e.$ clear from the SR. If the PV is higher than 3, the PXD is considered to be highly affected by the SR and the alarm is issued to the BCG shifter.

Measurement regions of the Photon Monitor were established during Run I with PXD1, based on the photon radiation map that was valid at the time. Figs. 4.6, 4.7, 4.9 and 4.10 clearly illustrate changes in the photon radiation pattern for PXD2, which need to be reflected in the updated definition of Photon Monitor regions to improve its efficiency. The old definition of the photon monitor includes the following DHEs: H1011, H1012, H1022, H1031, H1041, H1051 and H1061. As discussed in the previous section and illustrated by Figs. 4.7 and 4.9, the SR monitoring in the BWD modules in the central region of the map remains a relevant challenge, but the location of areas needs to be reconsidered. Meanwhile, modules H1011, H1012 and H1022, which were previously affected by theBSR generated by the LER beam (as also observed in distributions of HE S- and DPCs), no longer show this effect in later runs, reducing the relevance of continued monitoring in these modules.

In order to reconsider definition of signal and reference areas, we plot distributions of LE SPCs in the ladders that historically used to be (see Sec. 4.4) or are (in latest physics runs with the PXD included) the most affected by the BSR. For these plots, we overlay boundaries of measurement areas using the following colour scheme:

- red – old reference areas;
- green – old signal areas;
- magenta – new reference areas;
- orange – new signal areas.

The event reconstruction and mapping of photon hits in individual modules are performed on raw data of the Experiment 30 Run 2486, using the same procedure described in the previous section. Fig. 4.12 illustrates the photon hit map in the modules that used to be affected by the SR in the early Run I. Given that the localized SR is no longer observed in these modules, these areas have been removed.

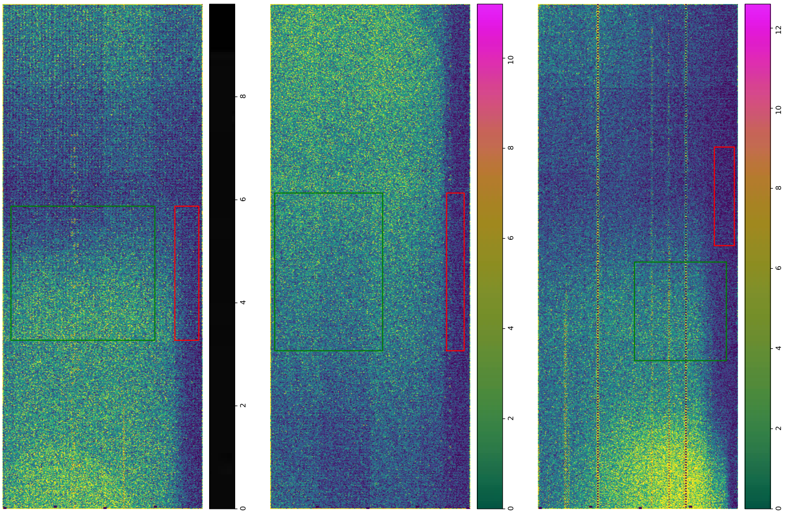

Figure 4.12: Distribution of photon clusters in modules [left] H1011, [center] H1012 and [right] H1031. Red boxes indicate boundaries of reference areas defined in the previous version of the Photon Monitor, while green boxes mark signal regions.

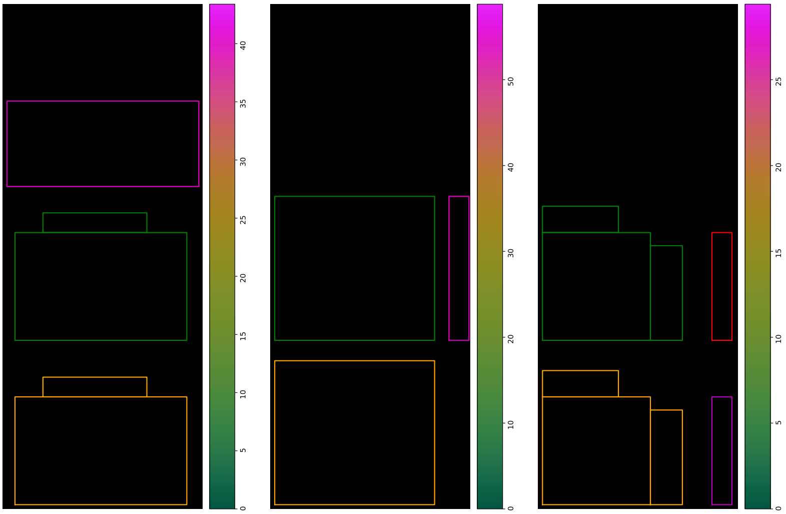

Figure 4.13: Distribution of photon clusters in modules [left] H1041, [center] H1051 and [right] H1061. Red boxes indicate boundaries of reference areas defined in the previous version of the Photon Monitor, while green boxes mark signal regions. Similarly, magenta boxes indicate boundaries of reference areas defined in the new version of the Photon Monitor, while orange boxes mark signal regions. Reference areas in the new and old definitions overlap in the left and central plots.

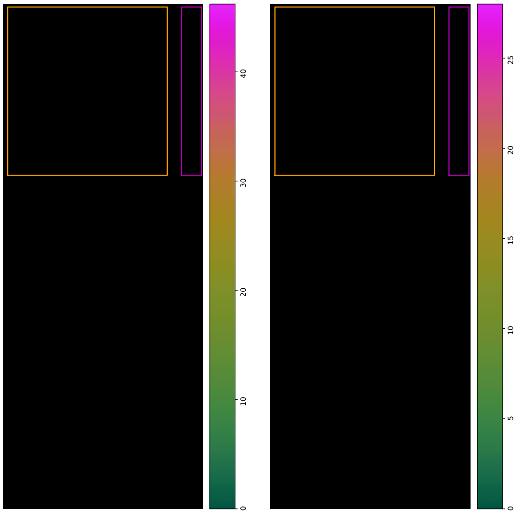

Figure 4.14: Distribution of photon clusters in modules [left] H1052 and [right] H1062. Magenta boxes indicate boundaries of newly introduced reference areas, while orange boxes mark signal regions.

The highly contaminated region in the BWD modules – which are most affected by BSR generated by the HER beam – has significantly shifted due to the additional gold shielding. We therefore redefine reference and signal areas in modules H1041, H1051 and H1061 as illustrated in Fig. 4.13. This effect extends into FWD modules, in which a dense SR fan is also observed. We therefore introduce new areas in modules H1052 and H062 (see Fig. 4.14).

Newly reconsidered measurement areas have been implemented in the PM source code. The old version of the photon monitor performs calculation of the photon rate and photon fraction only in BWD modules. We therefore introduce additional PVs to monitor photon contamination in FWD modules and in all modules combined. To test the new implementation, we run the PM over raw data of the Experiment 30 Run 2486 and plot PVs calculated in real time. The photon rate and photon fraction distributions for BWD modules illustrate clear improvement of the Photon Monitor's performance of capturing the photon radiation, as both values increase by factor $\sim$7 (see Fig. 4.15). Similar distributions for FWD modules and for all modules combined shown in Figs. B.8 and B.9 in App. B illustrate a similar behaviour.

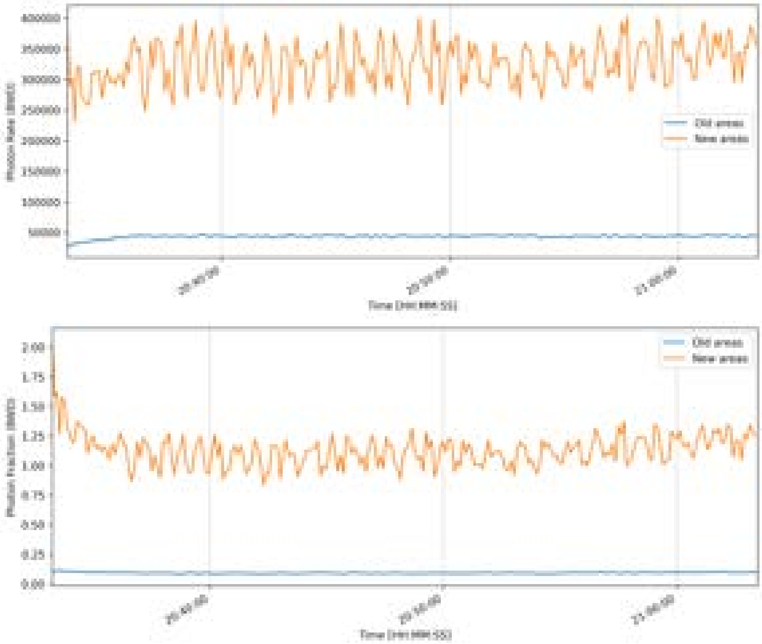

Figure 4.15: [top] The photon rate and [bottom] photon fraction calculated by the Photon Monitor using the old versus new area definitions in the BWD modules.

4.6 Extrapolation of the BSR and possible mitigation steps

To study the output of the revisited Photon Monitor and to try to extrapolate it into future runs, we apply the new PM to the list of selected "good" runs in the Run II. These runs are required to have all sub-detectors included, last longer than 30 minutes and to have stable HER beam currents, $i.e.$ the maximum deviation of any minute-averaged value from the mean value over the run should not exceed 5%. We select the total of 212 runs in Experiments 30 and 31 that satisfy these requirements, but the raw data of only 210 of them is available at the KEKCC for analysis.

As the PM is running over selected raw data, it writes out values of the photon rate and photon fraction with the refresh rate of 5000 frames. The average value of the photon rate and photon fraction is estimated for each run. Both values are calculated for areas defined in FWD, BWD and all modules. In Fig. 4.16, we show distributions of photon rates and fractions in selected runs, plotted against the HER beam current. The trend is clear and expected: higher beam currents induce higher

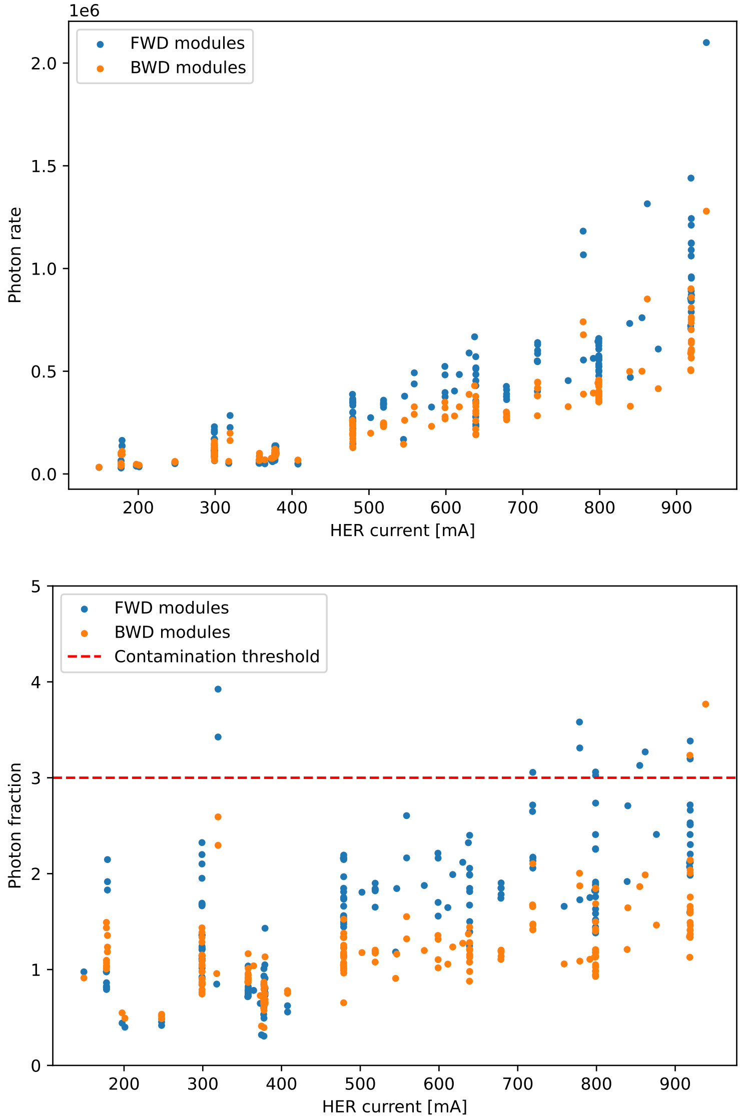

Figure 4.16: [top] The photon rate and [bottom] photon fraction estimated by the Photon Monitor in FWD and BWD modules across selected "good" runs in Experiments 30 and 31.

photon contamination, which, if we look at the photon fraction, is reaching and sometimes even exceeding the alarming limit. In the current implementation of the Photon Monitor, only the photon fraction calculated in BWD PXD modules is communicated to the BCG shifter, and, if the threshold is exceeded, an alarm is issued. Although, as Fig. 4.16 illustrates, the intensity of the photon radiation dominated in FWD modules, which might incentivise redefinition of the communicated PV in the future. For now, we stick to the existing PV definition to preserve consistency with earlier measurements.

Mitigation of the photon radiation is an evolving and intensifying challenge for the PXD. Photon radiation patterns depicted in Figs. 4.6 and 4.7 illustrate the emergence of the localized photon radiation and how it evolves with beam optics changes. Various steps, including beam orbit adjustment and beam pipe modification, have been taken in the past to reduce its strength. At the current experiment stage, when stability of the beam has the highest priority for the collaboration, possibilities of beam orbit adjustment are limited, while the hardware changes are not possible until the LS2. Therefore, effective monitoring is essential to ensure safety of the PXD and the quality of data taking.

Evolution of the photon radiation in the PXD, has now been reflected in the new definition of the Photon Monitor. Tests described above have confirmed its improved capability to monitor the intensity of the photon radiation. Current levels of the SR fan, even though are approaching alarming rates, do not pose the threat to the PXD yet. Though, the effect of localized photon radiation on the PXD can intensify in the future, as betatron oscillation functions are decreased and beam currents are ramped up. Therefore, an insight into this topic in later runs, when the PXD is included in the global data taking again, is required to work on future mitigation efforts.

Chapter 5

Introduction to the spectroscopy of exotic states

Despite the remarkable success of the Constituent Quark Model in describing the spectrum of most known hadrons, recent experimental studies of heavy quarkonium systems revealed growing tensions between QCD-motivated predictions and experimental observations. While the interpretation of these discrepancies remains ambiguous, such results provide a unique testing ground for our current understanding of the QCD and fuel the interest in various possibilities of more exotic hadron configurations beyond conventional mesons and baryons. In this section we summarise the status of the heavy quarkonium spectroscopy in the context of the search for structures with the $c\bar{c}s\bar{s}$ quark content to motivate the analysis reported in the next chapter of this thesis.

5.1 Constituent Quark Model

The Gell-Mann Zweig idea, currently known as the *Constituent Quark Model* (CQM), remains an effective scheme for classifying all known hadrons. It was developed half a century ago, when only light quarks, $i.e.$ up (u), down (d) and strange (s), had been discovered. Although, it could be successfully expanded to accommodate heavier quarks: charm (c), bottom (b) and top (t). The CQM explains the structure of conventional hadrons – mesons and baryons – to be composited of a quark-antiquark pair and a quark-triplet, respectively. In order to avoid the violation of the Pauli principle in cases, when a baryon is composed by several identical quarks, $e.g.$ sss, the *strong charge* was introduced by M. Y. Han and Y. Nambu in 1965 [89]. The

Han-Nambu idea suggests that each quark represents an $SU(3)$ triplet in the flavour-space with a *strong charge* in another $SU(3)$ triplet. Then, each hadron represents a singlet in this space of an additional $SU(3)$ symmetry group. Due to the similarity of these rules to the human perception of colour, the *strong charge* was later dubbed as the *colour charge*, which takes values of red, green and blue. Following this analogy, all free particles can only exist in a colourless composition, such as, for the case of conventional hadrons, colour-anticolour for a meson or a complete colour-triplet for a baryon.

As discussed in Chapter 2, forces binding individual quarks into hadrons are described by the QCD. Due to the self-interacting nature of gluons, the beta function of the strong coupling receives an extra summand, which changes the coupling constant evolution[1]. As a result, the strong interaction strength *decreases* at short distances, reaching values as low as $\alpha_s = 0.1185 \pm 0.0006$ at $r \backsimeq 0.002$ fm, resulting in a phenomenon known as *asymptotic freedom*. At long distances, the α_s value scales up, facilitating the effect known as *confinement*, which explains why free quarks can never be observed in nature. These features of the strong interaction potential elevate the feasibility of perturbative expansions for first-principle calculation at short distances, which can be probed in the high-p_T environment of collider experiments, such as LHC-based LHCb or CMS. However, as the perturbative calculation example shows for quark-quark scattering at high momentum transfer, long-distance effects, which can not be described with the perturbative expansion, significantly impact the momentum distribution of quarks within protons and must be approximated in some other way. This example indicates significant limitations of the pure perturbative QCD expansion even for a golden test case.

The CQM leaves room for hadronic configurations more complex than conventional mesons and baryons, as long as the requirement of the total color neutrality is maintained. Exotic states are in particular predicted in the light meson spectrum, but earlier experimental efforts suggest that light sector suffers from dense background of conventional states, which makes unambiguous isolation of exotic candidates challenging. For example, several pentaquark candidates, dubbed as Z_0 and Z_1 were included in the PDG review in 1976 [90]. But after no observations of these states by other experiments followed in almost two decades and alternative theoretical interpretations for the observed enhancements were suggested [91], these states were eventually removed from the PDG listing by 1994 [92]. The same happened to the resonance formerly known as Θ^+. Its sharp peak ($\Gamma < 25$ MeV) was originally observed in the K^+n invariant mass distribution near $M = 1.64 \pm 0.01$ GeV in the $\gamma n \to K^+K^-n$ inelastic scattering [93]. This observation sparked a heated discussion, as the newly observed resonance matched an earlier prediction of an

[1] in comparison to the QED

open-strange ($\mathcal{S} = +1$) pentaquark [94]. Alas, by 2006, the Θ^+ resonance had been removed from the PDG listing [95], when more comprehensive experimental results became available [96–98].

Meanwhile, an approach alternative to the perturbative QCD expansion gained attention after the first $c\bar{c}$ states had been discovered: J/ψ [99], ψ' [100] and χ_{cJ} [101]. Due to the large mass of the c quark ($m_c \backsimeq 1.3$ GeV), its motion in the $c\bar{c}$ system is nearly non-relativistic. Therefore, it can be described reasonably well by the Cornell potential [102], which includes a Colomb-like component resembling the asymptotic freedom at short distances and a linear component reflecting the confinement at large distances (see Eq. 5.1). The feasibility of the potential model constructed within this approximation has been confirmed over time, as nearly all observed charmonium states were found to be consistent with corresponding predictions (see Fig. 5.1 [top]).

$$V(r) = -\frac{4}{3}\frac{\alpha_s}{r} + \sigma r \tag{5.1}$$

The spectrum of conventional bottomonium underwent a similar story of the potential model success, as the same non-relativistic approximation is even more feasible for it[2]. Namely, most of narrow $\Upsilon^{(\prime/\prime\prime)}$ resonances discovered in the 9.4–10.4 GeV mass region matched respective non-perturbative calculations (see Fig. 5.1 [bottom]). Due to their notorious similarity, the c and b quarks are usually referred to as *heavy quarks* (denoted as Q, in contrast to the q notation for light quarks). Likewise, the *quarkonium* umbrella term collectively describes charmonium and bottomonium states, denoted as $Q\bar{Q}$.

The large mass of heavy quarks suppresses its production in a fragmentation process. Hence, if a $Q\bar{q}$ meson is observed, a heavy quark is likely to be constituent to the mother particle. This advantage of heavy-quarkonium allows searching for exotic candidates in a cleaner environment than the one of the light sector. In addition to it, $Q\bar{Q}$ candidates tend to have narrower width, making their identification less ambiguous due to the limited overlap with adjacent conventional quarkonium states. These arguments introduce heavy-quarkonium as a prospective field for search for unconventional hadronic states. Until recent years, there were few quarkonium(-like) candidates without a viable conventional interpretation. This status-quo changed in late 2000' – early 2010', when a boom of discoveries reporting observation of unconventional candidates happened, mostly in the charmonium-like spectrum. Pentaquark and charmonium-like candidates observed in this era point to a possible extensive exotic hadronic spectrum, which goes beyond predictions of the yet successful potential model.

[2]due to yet larger mass of the b quark

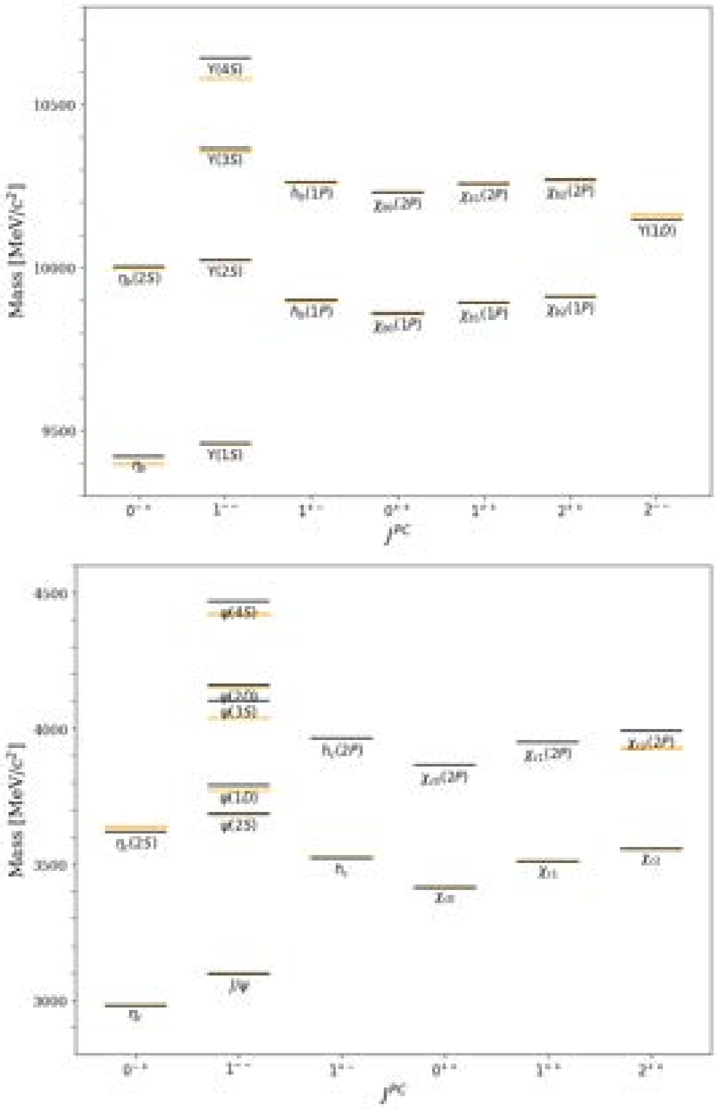

Figure 5.1: Spectrum of conventional quarkonium: [top] charmonium and [bottom] bottomonium. Black bars show potential model predictions calculated in the non-perturbative approximation [103], while yellow boxes indicate experimental measurements listed in the PDG2024 [104].

In the next section, a general classification of theoretical models describing the structure of unconventional states is provided. While in the section that follows it, the summary of latest experimental results reported by B-factories (Belle/Belle II, BaBar), LHC- (LHCb, ATLAS, CMS) and Tevatron-based experiments (DØ, CDF) is given to assess feasibility of the aforementioned theoretical models and to highlight yet unresolved matters of the charmonium spectrum relevant in the context of this thesis.

5.2 Theoretical models for unconventional hadrons

Unlike conventional hadrons, which have a limited number of *valence* quarks and therefore can only take certain J^{PC} quantum numbers[3], unconventional states have more degrees of freedom and therefore can access J^{PC} combinations that are forbidden for conventional hadrons[4]. As discussed above, the first-principle approach features limited feasibility. Therefore, various simplified models step-up for predicting unconventional states allowed by the CQM.

Across these models, the concept of a diquark appears in the role of a "building block" for different configurations. Originally introduced by Jaffe [105], $[qq]$ diquarks and $[\bar{q}\bar{q}]$ antidiquarks naturally carry a colour charge and therefore are bounded by the strong force. It was originally articulated that considering the Pauli principle, diquarks can either form a "good" spin-zero combination with the attractive potential, or a "bad" spin-one coalescence subjected to repulsive forces. Although, these considerations were later revised by Maiani [106] and Teraski [107], who independently concluded that "badness" of $S = 1$ diquarks is significantly weakened for (anti-)diquarks containing a heavy (anti-)quark due to the factor m_q/m_Q suppression of spin-spin interactions, allowing them to play an important role in constituting exotic hadrons [108].

Existing models of exotic quarkonium-like states can be divided into two large families: QCD-motivated compact models and loosely bound hadronic molecules. Compact models include (but are not limited to) tetraquarks, hadro-quarkonium, hybrids and glueballs. We now provide a brief overview of concepts underlying the listed models and include a simplified illustration of respective inner structures in Fig. 5.2.

a) Compact tetraquarks

These tightly bound diquark–antidiquark configurations were introduced to account for exotic charmonium-like states that cannot be accommodated within the con-

[3] $\vec{J} = \vec{L} + \vec{S}$, $P = (-1)^{L+1}$ and $C = (-1)^{L+S}$

[4] such as 0^{--}, 0^{+-}, 1^{-+}, 2^{+-}, etc.

ventional $Q\bar{Q}$ spectrum. Theoretical calculations using the color–spin Hamiltonian predict a rich spectrum of such compact states, as all constituent quarks significantly contribute to the structure of the full state. The compact tetraquark model provides a natural explanation for unconventional 1^{++} charmonium-like exotics and offers a reasonable description of the full 1^{--} sector [109]. The internal diquark–antidiquark also structure helps to account for the observed preference of many of these states to decay into open-flavour mesons rather than conventional quarkonia.

In the nearly-static approximation of the Hamiltonian treatment, the concept of a *dynamic tetraquark*—in which diquark–antidiquark pairs are produced with large relative momentum—plays a key role. It prevents the system from reorganizing into a more loosely bound open-flavour state and naturally explains why many exotics exhibit relatively small widths[5]. As a result, compact tetraquarks can appear as narrow resonances, even above open-flavour thresholds, making them experimentally accessible and phenomenologically distinct from meson-meson molecular states [110].

b) Hadroquarkonium

The underlying idea for the hadro-quarkonium model stems from the fact that decays of conventional charmonium states located above open-charm thresholds into respective open-charm modes are favoured over transitions into lower-laying charmonium states by 2–3 orders of magnitude, while for unconventional candidates this favouring factor is 10 or less [111]. The hadro-quarkonium model accounts for this discrepancy by embedding a compact $Q\bar{Q}$ "core" into a "cloud" of light quarks and antiquarks. Driven by a QCD version of the Van der Vaals potential, mutual forces between the "core" and the "cloud" are strong enough to form a compact object, while favouring transitions into hidden-quarkonium in comparison with branching fractions of "fall-apart" decays predicted by loosely bound configurations [112].

c) Hybrids

In contrast to the QED, the linear term of the strong field confines colour field-lines within a compact *flux tube* that runs between valence quarks (antiquarks) of a hadron [113]. In a ground state, J^{PC} quantum numbers of a hadron are defined exclusively by the relative orbital momentum of quarks and the alignment of their spins. Although, if a flux tube is excited, its non-zero orbital momentum and/or spin can contribute to the total J^{PC} quantum numbers of a state, leading it to take values that are otherwise forbidden for a conventional hadron [114]. Some hybrid models suggest that their decay into a pair of S- and a P-wave states is favoured over a decay into a pair of S-states (just like for the conventional quarkonium) [115, 116]. Therefore,

[5]Decay can only occur via the long-distance tails of meson wave functions connecting the quarks and antiquarks.

searches for hybrid candidates are mostly focused on decays into $D^{**}\bar{D}^{(*)}$ or $B^{**}\bar{B}^{(*)}$.

d) Glueballs

Due to the self-interacting nature of the strong field, compact bound states composed exclusively of gluons, known as glueballs, are predicted. Like hybrids, these states can take J^{PC} quantum numbers inaccessible for conventional hadrons. Lattice QCD predicts the lightest scalar glueball around 1.5–1.7 GeV, as well as tensor and pseudoscalar states at higher masses. Experimental efforts are mostly focussed on production mechanisms that include light mesons with $J^{PC} = 0^{++}$, 0^{-+}, and 2^{++}. So far, only indirect evidences exist for a scalar glueball mixed with nearby conventional mesons, while searches for tensor and pseudoscalar glueballs remain inconclusive. Even though glueballs are generally not considered viable explanations for quarkonium-like exotic states, they may contribute to states with unusually broad or flavour-diverse decays. A more complete discussion can be found in Ref. [117].

e) Hadronic molecules

The concept of a shallow hadronic state bound by a Yukawa-like meson exchange was introduced several decades ago [118–120]. Such "molecular" states are expected to lie near the threshold defined by masses of their constituent mesons and to adopt J^{PC} values corresponding to their S-wave combination. In 1994, Törnqvist predicted the existence of $B\bar{B}^*$ and $B^*\bar{B}^*$ states predominantly bound by the pion exchange [121]. Due to the similarity of the binding mechanism to that of the deuteron, this model was imaginatively dubbed a "deuson." Within this framework, if a molecular state is formed by a pair of open-flavour mesons, the heavy quark and antiquark are spatially well separated, resulting in minimal overlap. This configuration favours decays into a pair of open-flavour mesons rather than coalescence into a hidden-quarkonium plus a residual light meson. Moreover, because pseudoscalar couplings such as $D\bar{D}\pi$ or $B\bar{B}\pi$ are forbidden by rotation–parity invariance, the formation of shallow states composed of $D\bar{D}$ or $B\bar{B}$ meson pairs is disfavoured. This argument justifies extensive experimental efforts in searching for exotic candidates fitting the molecular picture in systems like $D^{(*)}\bar{D}^{(*)}\pi$, $D_s^{(*)}\bar{D}_s^{(*)}\pi$ or $B^{(*)}\bar{B}^{(*)}\pi$.

In addition to models describing unconventional four-quark structures, hexaquark states have been introduced. Dyson [122] and Jaffe [105] envisaged the possible existence of non-trivial six quark configurations. Once formed, dibaryons are predicted to be fairly stable. A search for hexaquark candidates holds potential to shed the light on the possible existence of even more exotic structures than what we have seen up to now. Gaining an understanding of the mass spectrum of these exotic candidates, as well as precise branching fraction, width and spin parity measurements are critical for their interpretation. The latter – when possible – can be accessed by an angular analysis approach.

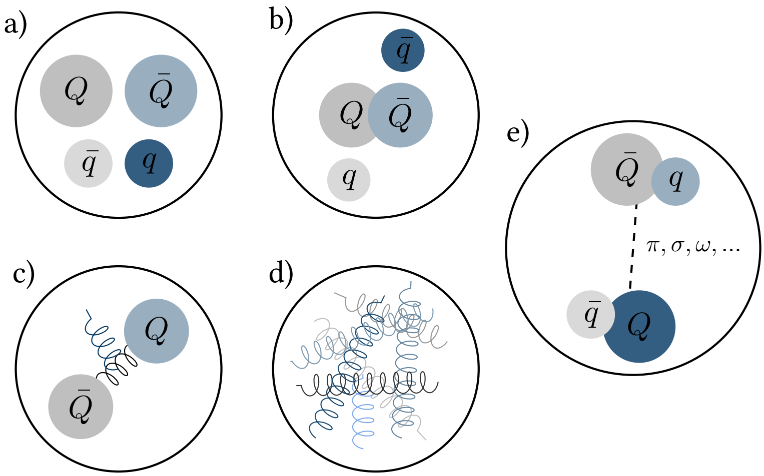

Figure 5.2: Illustration of a a) compact tetraquark, b) hadro-quarkonium, c) hybrid, d) glueball and e) hadronic molecule

5.3 All that peaks is not resonance

An experimental search for exotic hadrons naturally presumes looking for enhancements in invariant mass distributions of interest. Although, not always can these enhancements be associated with genuine resonances, as some kinematically induced effects must be considered, mainly *threshold cusps* and *anomalous triangle singularity*.

Threshold cusp is a kinematic effect appearing at the opening of an S-wave threshold [123]. It stems from the steep rise of the imaginary part of the scattering amplitude at the threshold [124–126]:

$$\operatorname{Im} T(s) \propto g^2 \rho(s), \tag{5.2}$$

where g is the coupling constant and $\rho(s)$ is the phase-space factor. An abrupt growth of the imaginary part is eventually terminated by the hadronic form-factor $F(s)$:

$$\rho(s) = \frac{2k}{\sqrt{s}} F(s), \tag{5.3}$$

where k is the momentum in the two-body rest frame.

The real part of the scattering amplitude is expressed as:

$$\operatorname{Re} T(s) = \frac{1}{\pi} P \int_{s_{\text{thresh}}}^{\infty} \frac{ds' g^2 (s') \rho (s')}{s' - s}, \tag{5.4}$$

where P is the principal value integral and s_{thresh} is the squared mass of the threshold. The resulting $|T|$ features a sharp resonance-like peak at the S-wave opening, $e.g.$ as demonstrates in Fig. 5.3 [left] for the case of the $D\bar{D}^*$ threshold.

Some authors doubt the pure kinematic cusp production [127], questioning non-analytic form-factors in the definition of the coupling constant g. On contrary, it is suggested that the presence of a nearby pole is always required to see the kink as pronounced. Therefore, in case of an observation of a near-threshold enhancement in an experiment, it is always advised to perform an analysis of the Argand diagram, when the sample size allows. However, this approach is not always accessible, especially in cases when a very rare process is studied.

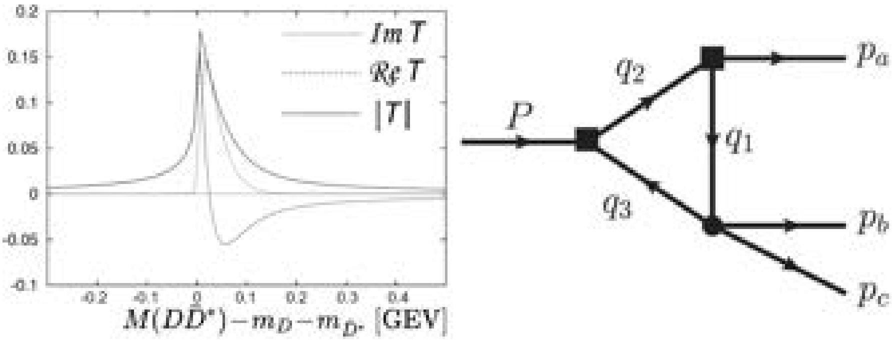

Figure 5.3: [left] The scattering amplitude near the $D\bar{D}^*$ threshold. The dotted line represents the imaginary part of the scattering amplitude, while the dashed line – the real part. The solid curve is $|T|$. [right] A three-body decay with an internal triangle.

Three-body decays can configure diagrams with internal triangles, as illustrated in Fig. 5.3 [right]. According to Landau [128], a diagram of this type becomes singular, when all three virtual particles are simultaneously on-shell. This leads to an effect called the *anomalous triangle singularity* (ATS). If kinematic conditions are satisfied [129], the ATS can produce resonance-like peaking structures that have nothing to do with true particle resonances. This effect does not yield misleading enhancements in elastic scattering, as shown by Schmidt [130]. But in the presence of many coupled channels, the sum of amplitudes can produce a Dalitz plot, which in projection to individual channels can produce narrow resonance-like peaks [131]. A more detailed description of the ATS can be found in Ref. [132–134].

5.4 Overview of the exotic charmonium-like spectroscopy

The field of the charmonium-like spectroscopy is dominated by 3 main categories of players: B-factories (Belle/Belle II and BaBar), LHC-based experiments (LHCb, ALICE and CMS) and specifically BESIII. Each of the listed experiments features unique advantages that amplify its potential in some areas of the exotic spectroscopy and weakening in others.

LHC-based experiments are recording data of pp collisions and enjoy the production rate of $q\bar{q}$ pairs that is 5–6 orders of magnitude larger than in e^+e^- collisions. Even after correcting this for the lower reconstruction efficiency and the shorter accumulated beam time, the production rate of hidden charmonium is still approximately 1000 times larger compared to B-factories. To give a vivid perspective, the data sample of B decays to J/ψ and light hadrons that was accumulated during the three-year-long Run-I of the LHCb experiment ($\sim 3fb^{-1}$) is roughly one order of magnitude larger than that of the Belle experiment accumulated over a decade-long operation. Meanwhile, by the time of delivering this thesis, the data sample accumulated by LHCb is approaching the mark of 20fb^{-1}, strengthening the importance of the experiment in the area of flavour physics even more. Another advantage of LHCb is the exceptional spacial resolution thanks to a large boost, which results into a better signal purity than in BaBar or Belle for analyses targeting long-living open-bottom hadrons. The notorious downside of experiments operating at hadron-hadron collisions is their low sensitivity to channels including neutrals, $e.g.$ γ or π^0. This being said, does not entirely veto this type of analyses, as the recent LHCb analysis of $X(3872)$ decays into $\gamma J/\psi$ and $\gamma\psi'$ shows [135], but significantly limits the minimal energy of neutrals that can be detected and the reconstruction efficiency due to the missing decay vertex information.

Meanwhile, B-factories benefit from the clean environment of lepton-lepton collisions. Their almost 4π-geometry detectors allow recording data at the instantaneous luminosity that is higher than that of pp experiments. Light material budget of electromagnetic calorimeters employed by Belle/Belle II and BaBar allows detecting soft photons with energies as low as 25 MeV[6], while precise vertexing, event topology classification and flavour tagging techniques significantly improve the reconstruction efficiency, signal clarity and expand the range of decay modes accessible for reconstruction.

The BESIII experiment features key advantages of e^+e^- B-factories, but in addition has some crucial design advantages putting it a unique position in the field of the charmonium spectroscopy. In particular, it records collision data of the BEPCII collider, which is capable of operating at the tunable centre-of-mass energy from

[6]for the case of Belle II [30]

2.0 to 4.6 GeV. The ability of BEPCII to adjust the collision energy allows BESIII accumulating datasets targeting individual charmonium(-like) resonances. While B-factories have to resort to leptonic decays of conventional charmonium, which feature distinct event topology and tolerable background levels, BESIII is capable of reconstructing J/ψ and ψ' decays into multiple hadrons, which usually have larger branching fractions. Another advantage of diverse BESIII datasets is the ability to profile energy-dependent cross-sections of individual processes to look for enhancement in production rates at different energy points. This type of analyses is usually not accessible for other experiments, as they are operating at a fixed E_{CM} most of the run time[7].

In the context of B-factories, these are the main processes, in which $c\bar{c}$ pairs are produced and therefore charmonium(-like) states can be searched for:

- *B-mesons decays*

  A $\Upsilon(4S)$ resonance predominantly ($> 96\%$) decays into a $B\bar{B}$ meson pair. A b quark constituting a B meson may transition into a c quark by emitting a W boson, which with 15% probability converts into a $\bar{c}s$ quark-antiquark pair. The obtained c and $\bar{c}$ quarks materializes into a 0^{-+}, 1^{--} or 1^{++} charmonium state, while the s quark and a spectator quark coalesce into a kaon.

- *Two-photon processes*

  Fusion of two photons radiated by beam leptons can produce a quark-antiquark pair with the probability that is proportional to e_q^4. Given the charge of a c quark, $c\bar{c}$ production is favoured. These mostly "untagged" events feature low p_T, which serves as an important experimental signature. Quantum numbers accessible for a charmonium created in this process are $0^{\pm+}$ and $2^{\pm+}$.

- *Double charmonium production in the continuum*

  The QCD-motivated effective field theory predicts the $J/\psi c\bar{c}$ production rate of around 10% at the E_{CM} of 10 GeV [136]. This former prediction was contradicted with the observations of B-factories, which reported that prompt J/ψ production accounts for almost 69% [137]. Due to the unexpectedly high $c\bar{c}$ production rate in the recoil of J/ψ, several conventional (η_c, χ_{c0} and η_c') and unconventional states have been studied in the inclusive $e^+e^- \to J/\psi X$ precesses [138].

- *Initial state radiation (ISR)*

  The spontaneous radiation of a photon by the initial state e^+ or e^- can reduce

[7] with the exception of several energy scan campaigns carried-out by B-factories

the effective centre-of-mass energy, bringing it closer to threshold energies of the charmonium production. This higher-order process, known as *initial state radiation* (ISR), is suppressed by QED and can only generate resonances with 1^{--} quantum numbers[8].

Unconventional charmonium-like candidates are collectively called XYZ states. In the commonly used naming scheme, X states denote neutral states with unconventional or not yet established quantum numbers, Y states designate neutral candidates with $J^{PC} = 1^{--}$ and Z states mark *charged* charmonium-like states.

The discovery of $X(3872)$ by the Belle collaboration in 2003 [139] introduced the experiment as on of the key players in the field of charmonium-like spectroscopy[9]. Observation of a narrow resonance in the $J/\psi\pi^+\pi^-$ invariant mass distribution, later established by LHCb to have 1^{++} quantum numbers [141], kick-started a heated discussion on its nature, which boils until now. Its measured invariant mass falls behind the expectation for the missing χ'_{c1} by almost 80 MeV [103], which would reflect in the inverted $\delta M_{2-1}(1P)$ vs. $\delta M_{2-1}(2P)$ mass splitting hierarchy. It is also reported to favour isospin violating decays, measured as $\mathcal{B}(X \to \omega J/\psi)/\mathcal{B}(X \to \pi^+\pi^- J/\psi) = 0.8 \pm 0.3$ [104], by the rate that exceeds expectation for a pure charmonium for at least one order of magnitude and can not be explained by the pure suppression of the $X \to \omega J/\psi$ kinematic phase space[10]. These arguments, in addition to the narrow width [104][11], disfavour interpretation of $X(3872)$ as a pure charmonium.

Observation of the $X(3872) \to D^0\bar{D}^0\pi^0$ decay channel with the rate that dominates over the $\pi^+\pi^- J/\psi$ mode by the factor $9.4^{+3.3}_{-4.3}$ [142] strengthened the hypothesis of its coupling to the $D^0\bar{D}^{*0}$ channel, which by the time of the discovery was speculated about due to the proximity of the $X(3872)$ invariant mass to the respective threshold. The latest measurement of the splitting is expressed as:

$$\delta M = M_{X(3872)} - M_{\bar{D}^{*0}} - M_{D^0} = -0.08 \pm 0.09 \text{ MeV/c}^2, \tag{5.5}$$

which is consistent with zero within the uncertainty [104]. Arguments listed above support identification of $X(3872)$ as a molecular state. This interpretation is able to accommodate most of attributed abnormalities and the lack of observed partners, which should arise, if an alternative interpretation, $e.g.$ a compact tetraquark,

[8] as the produced resonance couples to the virtual ISR photon

[9] This publication stands out as the most cited Belle paper, even more cited than the one reporting the discovery of CP-violation that earned a Nobel Prize in 2008 [140]

[10] Charged pions in the $\pi^+\pi^- J/\psi$ mode originate from ρ decays, as confirmed by the shape of di-pion distribution [142].

[11] in comparison with the $\Gamma = 0.84 \pm 0.04$ MeV width of χ_{c1}, even though it has fewer allowed decay channels as an S-wave state

is assumed. Although, this model confronts with the enormous scattering length $a_{00} > 9$ fm[12], which comes from the resonance location precisely at the $D^0\bar{D}^{*0}$ threshold [143]. Another argument disfavouring the molecular interpretation of $X(3872)$ comes from its prompt production in pp collisions [143], where the dependence of the differential cross-section on the transverse momentum clearly resembles the pattern of ψ', rather than the one of a genuinely composite object, such as deutron, hypertriton or helium. Due to existing counter-arguments, pure molecular interpretation of $X(3872)$ lures to be challenging, which is why a mixed hypothesis stands out as the most complete one. It is described by Eq. 5.6, which contains coherent charmonium and molecular components, with the former constituting $(28-44)\%$ [143].

$$|X\rangle = \sqrt{Z_{c\bar{c}}}|\chi_{c1}(2P)\rangle + \sqrt{Z_{\text{mol}}}|D^0\bar{D}^{*0}\rangle \tag{5.6}$$

The latest efforts in better understanding of $X(3872)$ paradoxes are focussed on the study of its lineshape [144–146] and mostly struggle with the sensitivity of the Flatté model, which is aimed to describe it [147]. Pole positions that are derived from the Flatté fit can disclose whether $X(3872)$ is a genuine resonance or a virtual state. Although, uncertainties derived by these calculations do not allow claiming the position of at least one pole on a physical Riemann sheet. Qualitative improvement of these measurements require significantly larger data samples, especially those from e^+e^- experiments, as they are sensitive to the $X(3872) \to D^0\bar{D}^0\pi^0$ decay channel.

Shortly after the discovery of $X(3872)$, observation of another narrow structure, this time in the $\omega J/\psi$ invariant mass system, was reported by Belle [148]. Formerly observed in B-decays, the enhancement dubbed as $X(3915)$ was later confirmed by BaBar in the same process [149, 150]. In parallel, a resonance decaying into the same final state was also observed by Belle and BaBar in two-photon processes [151, 152]. Due to the similarity in measured properties, both observations were attributed to the same resonance with the following fitted average mass and width [153]:

$$\begin{aligned} M &= 3918.4 \pm 1.9 \text{ MeV/c}^2 \\ \Gamma &= 20.0 \pm 5.0 \text{ MeV} \end{aligned} \tag{5.7}$$

Similarly to $X(3872)$, despite having the matching 0^{++} quantum numbers [152], $X(3915)$ can not be identified as a conventional $c\bar{c}$ state [154–156]. This conclusion is supported by the anomalously small $\delta M_{2-0}(2P)$ mass splitting [156–158], the observation of the OZI-suppressed $\omega J/\psi$ decay mode [159–161] and the absence of

[12] twice the value of the deutron's scattering length

evidence for the expected dominant decays into $D\bar{D}$. Therefore, its interpretation as an exotic charmonium-like candidate, both in the form of a molecular state [162] and a compact tetraquark [163], is considered. The molecular interpretation is supported by the proximity of the measured mass to the $2D_s$ threshold ($\delta M = 18.2$ MeV/c^2). It can account for the suppression of the $X(3915) \to D\bar{D}$ decay via the OZI mechanism, as well as for the enhancement of decays into $\omega J/\psi$ due to the presence of an $s\bar{s}$ component in the former. A recent LHCb publication reported results of an amplitude analysis of the $B^+ \to D^- D^+ K^+$ decay [164], which established the presence of two resonances, $\chi_{c0}(3930)$ and $\chi_{c2}(3930)$, with spin-0 and spin-2, respectively. The former was identified as the $X(3915)$ state, but due to the contradiction with the earlier measurements and poor signal purity, authors claim that a substantially larger data sample is required to eliminate ambiguity. The same is relevant for the observation of a resonant structure near the $D_s^+ D_s^-$ threshold by LHCb [165]. Despite the significance of 12σ, the Flaté fit to the near-threshold enhancement yields an invariant mass value, which is almost 40 MeV/c^2 larger than the world average for $X(3915)$. This result, along with the confident (9σ) establishment of its quantum numbers as 0^{++}, can either be interpreted as the strong coupling of the hypothetical $[c\bar{s}][\bar{c}s]$ molecular component of $X(3915)$ to the $D_s^+ D_s^-$ channel, which manifests in its larger width, or as a sign that the newly observed state is different to the $X(3915)$ known before.

The LHCb study of $B^+ \to J/\psi \phi K^+$ [166], which reported observation of 4 new neutral X resonances in the $J/\psi\phi$ invariant mass distribution, shook the field of charmonium-like spectroscopy in 2017. This full amplitude analysis resolving seven coherent $K^* \to \phi K$ resonances and possible $X \to J/\psi\phi$ states yielded confirmation of $X(4140)$ and $X(4274)$ states that were earlier reported by CDF [167][13], and reported the first observation of two other neutral states, dubbed as $X(4500)$ and $X(4700)$. An improved amplitude analysis performed in 2021, exploiting the Run-II data set ($6fb^{-1}$), revisited the same decay channel. In addition to confirming the states reported in the earlier study, it reported the observation of three additional neutral X states and two charged Z states that had not been seen previously [168].

Within the states reported in LHCb publications [166, 168], the $X(4140)$ state has been previously studied the most by other experiments. It was first observed by CDF [167] and rediscovered by CMS in B-decays [169]. Shortly after the rediscovery, it was observed in prompt production by DØ [170]. In view of consistent experimental results and inability to incorporate $X(4140)$ in the spectrum of conventional charmonium, various theoretical interpretations have been suggested, including a compact tetraquark [163, 171–174], $D_s^{*-} D_s^{*+}$ molecule [175–184], 1^{-+} hybrid [183, 185] or kinematic cusp [186, 187]. A large fraction of hypotheses was ruled out,

[13] each with significance below 5σ

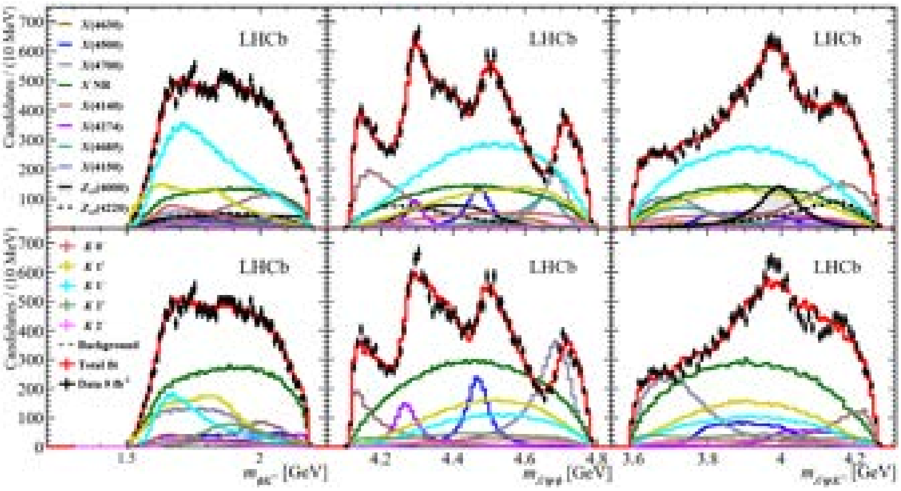

Figure 5.4: Distribution of the [left] ϕK^+, [middle] $J/\psi\phi$ and [right] $J/\psi K^+$ invariant mass distributions for $B^+ \to J/\psi\phi K^+$ candidates (black points) approximated (red curve) either with the [top row] default or [bottom row] Run-I model.

when $J^{PC} = 1^{++}$ quantum numbers were assigned to $X(4140)$ by LHCb. Within the remaining interpretations, the tetraquark model proposed by Stancu stands out the most [173], as not only it correctly predicts quantum numbers of the $X(4140)$ state, but also anticipates the existence of a second 1^{++} tetraquark with a mass close to that of the observed $X(4274)$ resonance. Another viable interpretation proposed by LHCb [188] explains $X(4140)$ as a possible $D_s D_s^*$ *cusp* effect below the $J/\psi\phi$ threshold. According to the 2024 PDG [104], the world average width of $X(4140)$ is based on earlier CDF, CMS and DØ results and excludes latest LHCb measurements. This exclusion persists due to the pronounced discrepancy between widths reported by LHCb ($\Gamma = 83 \pm 21^{+21}_{-14}$ and $162 \pm 21^{+24}_{-49}$ MeV [166, 168]) and those from previous studies ($e.g.$ $\Gamma = 28^{+15}_{-11} \pm 19$ and $16.3 \pm 5.6 \pm 11.4$ MeV [169, 170]), despite the substantially larger event sample derived by LHCb[14]. The reason for this drastic deviation lacks clear explanation.

An evidence for the second X state confirmed by LHCb, $X(4274)$, was reported by CDF. Due to the large statistical error of the measured width ($\Gamma = 32.3^{+21.9}_{-15.3} \pm 7.6$ MeV), the $X(4274)$ width measured by LHCb is consistent with the former result ($\Gamma = 53 \pm 5 \pm 5$ MeV). The most prominent models describing the existance of

[14]LHCb isolated approximately 4.2k events in 2017 [166] and 24k in 2021 [168], compared to 14–616 events reported by other analyses [167, 169, 170, 189, 190].

$X(4274)$ suggest its interpretation as a hybrid or a compact tetraquark. Further studies are required to favour a particular interpretation.

The initial rejection of the conventional $c\bar{c}$ interpretation of $X(4140)$ was based on its narrow width measured by CDF: $\Gamma = 11.3^{+8.3}_{-5.0} \pm 3.7$ MeV [167]. Although, in view of the latest LHCb results, these conclusions might be reconsidered. Several potential models predict conventional $c\bar{c}$ states with masses and widths in the range of values reported by LHCb. For example, $X(4140)$ and $X(4274)$ states can be considered as candidates for the missing $\chi_{c1}(3P)$ state, as they lay within considerable theoretical uncertainties for its predicted mass and width [115, 191–195]. Similarly, $X(4500)$ and $X(4700)$ states have been suggested as candidates for the $\chi_{c0}(4P)$ and $\chi_{c0}(5P)$ resonances, respectively [194, 195]. If these interpretations are correct, the aforementioned X states should manifest in fall-apart decays into $D^{(*)}_{(s)}\bar{D}^{(*)}_{(s)}$, which are expected to be pronounced for conventional charmonium resonances. The lack of experimental searches for these states in decays involving charmed-strange mesons contribute to the motivation for the search reported this thesis.

Its feasibility is additionally highlighted by another recent Belle result, which reported observation (5.9σ) of a narrow resonance in the $D_s^+ D_{s1}(2536)^-$ invariant mass distribution [196] and the evidence (3.4σ) for an enhancement in the $D_s^+ D_{s1}(2573)^-$ system [197] in ISR processes. Measured mass and width of both enhancements are consistent with those of the narrow $Y(4660)$ resonance that was earlier seen in $e^+e^- \to \pi^+\pi^-\psi'$ by BaBar [198] and Belle [199]. In a suggested model [200], $Y(4660)$ is interpreted as a shallow $D_s^+ D_{s1}(2536)^-$ molecular state bounded by the $f_0(980)$ exchange. In this regard, the reported observation of fall-apart open-charm decays supports this interpretation, but further studies are required to make reliable conclusions.

Experimental results summarises in this section list various candidates for charmonium-like state, including those with $c\bar{c}s\bar{s}$ quark content. Decays into open-charm final states are OZI-favoured for these states, if conventional or molecular interpretations are assumed. The clear lack of experimental efforts in searching for decays into various charmed-strange mesons form the comprehensive motivation for the analysis described in the following chapter.

Chapter 6

Search for $c\bar{c}s\bar{s}$ exotic states

In this section, we present an analysis focussed on a study of decay channels, where structures with $c\bar{c}s\bar{s}$ quark content can be revealed using the full Belle data set. As such, we study the $e^+e^- \to D_s^+ D_{sJ}^{(*)-}$ *+ anything* inclusive process, where $D_{sJ}^{(*)-}$ denotes either the $D_{s0}^*(2317)^-$, or the $D_{s1}(2460)^-$ meson, and look for resonances in the $D_s^+ D_{sJ}^{(*)-}$ invariant mass distributions. Along with cross-section upper limit estimates for the process under study, we look into other matters, such as mass splitting and width estimates for the $D_{s0}^*(2317)^-$ and $D_{s1}(2460)^-$ meson, which give insight into reasons behind their deviation from potential model predictions.

The central idea of the proposed analysis is based on the search for $c\bar{c}s\bar{s}$ exotic resonances in continuum, *i.e.* in the $e^+e^- \to c\bar{c}$ process. This approach ensures the access to a larger variety of quantum numbers that a potential exotic state can take and allows utilising the full Belle dataset, rather than Υ(4S) resonance data only. The primary goal of the analysis is the search for resonances in $D_s^+ D_{sJ}^{(*)-}$ invariant mass systems. In addition to it, we look into adjacent topics, such as precise mass-splitting measurements and the measurement of the $D_{s0}^*(2317)^-$ width, which can shed light on open questions of the $c\bar{s}$ spectrum and the ambiguous nature of the $D_{s0}^*(2317)^-$ and $D_{s1}(2460)^-$ mesons.

Earlier studies of decay channels including $D_{s0}^*(2317)^-$ and $D_{s1}(2460)^-$ indicated significant cross-feed affects caused by kinematic similarity of their decay products [201–203]. These effects will be elaborately discussed in later chapters (see Sec. 6.3.5), but for the current context, it justifies the motivation to study the $e^+e^- \to D_s^+ D_{s0}^*(2317)^-$ *+ anything* and $e^+e^- \to D_s^+ D_{s1}(2460)^-$ *+ anything* decay channels in parallel – to correctly interpret observed events. Here, and throughout the text, an inclusive process with the *+ anything* component is presumed for the decay channels under study. We therefore are dropping the *+ anything* notation from now on. Charge conjugated modes are also considered by default throughout the entire text for mesons present in the decay cascade.

This work is strongly connected with the search for exotic states in the $B \to J/\psi\phi K$ process that was performed in the working group of E. Prencipe[1] . It, just like the analysis reported in this document, is focussed on the search for non-constituent resonances with $c\bar{c}s\bar{s}$ quark content, but makes use of a different production mechanism, $i.e.$ through B decays.

6.1 Search feasibility

As discussed in Chapter 5, recent results reported by LHCb reignited the interest to the field of exotic charmonium-like states, when the rediscovery of $X(4140)$ and $X(4274)$ and the first observation of $X(4500)$ and $X(4700)$ was published. As the list of newly observed X states was shortly extended with $X(4150)$, $X(4630)$ and $X(4685)$ reported by the follow-up study [168], the need for confirmation of numerous exotic candidates with $c\bar{c}s\bar{s}$ quark content in other processes got underlined. Given that the $D_s^+ D_{sJ}^{(*)-}$ and $J/\psi\phi$ invariant mass ranges partially overlap, as reported in Table 6.1, this analysis offers a unique opportunity for a cross-check of resonant states reported by LHCb [166, 168, 188] in both different systems and different decay modes, and eventually a look for yet unseen exotic states.

With the present analysis in the continuum, we are looking for a possible confirmation of X-resonant states observed by LHCb in a new production mechanism. If resonant state(s) compatible with those are found, this would constitute the first observation by a non-LHC experiment. Such a finding would be of critical importance, as $e.g.$ if a state compatible with $X(4274)$ is observed, it would further support $X(4274)$ interpretation as a genuine particle, rather than a reflection of the controversial $X(4140)$ peak, as proposed by CMS.

From an experimental point of view, the best method to verify, if a molecular or a cusp hypothesis is feasible for an exotic candidate, is to look for it in elastic scattering. The average measured mass of $X(4140)$ is (4146.5 ± 3.0) MeV/c^2 [104], while the threshold of $D_s^+ D_s^{*-}$ is ≈ 4080 MeV/c^2. Consequently, $X(4140)$ is located more than 60 MeV/c^2 above the $D_s^+ D_s^{*-}$ threshold, which makes its interpretation

[1]DFG project n. 389090153 (2017), *Search for four- and six- quark states with c- and -s quarks*

Invariant mass system	Decay from	Range [GeV/c^2]
$D_s^- D_s^+$	B_s^0	[3.936—5.367]
$D_s^- D_s^+ \pi^0$	B_s^0	[4.071—5.567]
$D_s^- D_s^{*+}$	B_s^0	[4.080—5.567]
$D_s^- D_{s0}^*(2317)^+$	B_s^0	[4.285—5.567]
$D_s^- D_{s1}(2460)^+$	B_s^0	[4.428—5.567]
$J/\psi\phi$	B^0	[4.118—5.280]
$J/\psi\phi$	$B^\pm$	[4.116—5.279]
$J/\psi\phi$	continuum	[4.116—E_{cm}]
$D_s^- D_{s0}^*(2317)^+$	continuum	[4.285—E_{cm}]
$D_s^- D_{s1}(2460)^+$	continuum	[4.428—E_{cm}]

Table 6.1: Physics processes, where a search for resonances with $c\bar{c}s\bar{s}$ quark content is feasible.

proposed by LHCb [188] as a $D_s^+ D_s^{*-}$ cusp not ideally suited, though still possible. Therefore, the $D_s^+ D_s^{*-}$ elastic scattering is a viable test case for the $X(4140)$ puzzle.

This applies even more prominently to $X(4274)$: its average measured mass of 4286^{+8}_{-9} MeV/c^2 is located exactly at the $D_s^+ D_{s0}^*(2317)^-$ threshold (≈ 4285 MeV/c^2). Therefore, the hypothesis of $X(4274)$ being a $D_s^+ D_{s0}^*(2317)^-$ cusp effect below the $J/\psi\phi$ threshold is feasible. The latest LHCb results report comprehensive establishment of quantum numbers (J^{PC}) for $X(4140)$ and $X(4274)$ as 1^{++}. This important result favours looking for $X(4140)$ in the $D_s^+ D_s^{*-}$ invariant mass system, but is against the cusp interpretation of $X(4274)$, for which other possibilities could be considered [163, 173, 200, 204]. As a reminder, Belle showed an evidence for a state dubbed as $X(4350)$ by analysing the $J/\psi\phi$ invariant mass via $\gamma\gamma$ interaction, with still unclear interpretation of its nature [205]. Lebed and Polosa [163] propose a model, where quantum numbers of $X(4140)$ coincide with those reported by LHCb (1^{++}). The same model claims for a state compatible with $X(4274)$ on the mass scale and with quantum numbers compatible with those of the $D_s^+ D_{s0}^*(2317)^-$ system – 0^{-+}[2], though contradicting with 1^{++} found by LHCb. A more recent theoretical paper from Maiani, Polosa and Riquer [206] explains $X(4274)$ in a tetraquark model as a possible overlap of 2 nearby states with J^{PC} = 0^{++} and 2^{++}.

In this view, search for $X_{c\bar{c}s\bar{s}}$ states as from Ref. [168] in elastic scattering by analysing $e^+e^- \to D_s^+ D_{sJ}^{(*)-}$ processes gains significant importance. In case of observation, cusp hypothesis for the aforementioned $X_{c\bar{c}s\bar{s}}$ states could be excluded.

[2] $0^- \otimes 0^+ = 0^-$

X decays into	Thresholds	J^P product	Compatible with
$D_s^+ D_s^{*-}$	4081 MeV/c^2	$0^- \otimes 1^-$	$X(4140)$: possible cusp
$D_s^+ D_{s0}^*(2317)^-$	4286 MeV/c^2	$0^- \otimes 0^+$	$X(4274)$: possible P-wave cusp
$D_s^+ D_{s1}(2460)^-$	4428 MeV/c^2	$0^- \otimes 1^+$	None reported in Ref. [168]
$D_s^+ D_{s1}(2536)^-$	4504 MeV/c^2	$0^- \otimes 1^+$	$X(4500)$: possible cusp
$D_s^+ D_{s2}(2573)^-$	4537 MeV/c^2	$0^- \otimes 2^+$	$X(4500)$
$D_s^+ D_{s2}(2700)^-$	4682 MeV/c^2	$0^- \otimes 2^-$	$X(4500)$: not a cusp
$D_s^+ D_{s1}(2860)^-$	4827 MeV/c^2	$0^- \otimes 1^-$	$X(4700)$
$D_s^+ D_{s3}(2860)^-$	4828 MeV/c^2	$0^- \otimes 3^-$	None reported in Ref. [168]

Table 6.2: Possible $X_{c\bar{c}s\bar{s}}$ decays, as from Ref. [207]. A possible interpretation of $X_{c\bar{c}s\bar{s}}$ states observed in Refs. [166, 168], if any will be found in the continuum, is given in the last column of this table. Some of those $X_{c\bar{c}s\bar{s}}$ states are eligible to be interpreted as cusps since their mass is very close to the indicated threshold.

Table 6.2 shows several newly observed resonances that appear near thresholds, for which this check is compulsory.

The considerations outlined above form the analysis proposal: study of the $e^+e^- \to D_s^+ D_{s0}^*(2317)^-$ and the $e^+e^- \to D_s^+ D_{s1}(2460)^-$ decay channels. These decay channels open a possibility to perform first cross-section measurements of the $e^+e^- \to X(\to D_s^+ D_{s0}^*(2317)^-)$ and $e^+e^- \to X(\to D_s^+ D_{s1}(2460)^-)$ inclusive processes to, in particular, look for $X_{c\bar{c}s\bar{s}}$ exotic candidates reported by LHCb. The D_s^+ and $D_{s0}^*(2317)^-$ mesons carry 0^- and 0^+ quantum numbers respectively. Hence, the $D_s^+ D_{s0}^*(2317)^-$ system carries 0^- quantum numbers in S-waves, and 1^+ in P-waves. After discarding the $X(4140)$ resonance, which lays below the $D_s^+ D_{s0}^*(2317)^-$ invariant mass threshold, only the $X(4274)$ and $X(4685)$ states appear to be feasible candidates within those reported by LHCb [197] for a decay into the $D_s^+ D_{s0}^*(2317)^-$. Repeating this exercise for the system of D_s^+ and $D_{s1}(2460)^-$, 1^- quantum numbers are allowed for X states in S-wave, while 0^+, 1^+, and 2^+ in P-wave. This means that only $X(4500)$ and $X(4700)$ (both 0^+), as well as $X(4630)$ (1^-), are allowed (see Table 6.2).

Still, we should not limit the spotlight of this analysis to rediscovery of resonances observed in the $J/\psi\phi K$ system, as we cannot rule out a possibility that other previously unobserved resonant states may appear in this study. For example, a possible 0^- particle decaying to $D_s^+ D_{s0}^*(2317)^-$ predicted by Rosner and Karliner is supposed to peak at the mass value of 4286.0 GeV/c^2 (the exact threshold)[3]. In addition, as reviewed in Sec. 5.4, two recent papers published by Belle [196, 197] reporting analyses of $e^+e^- \to D_s^+ D_{s1}(2536)^-$ and $e^+e^- \to D_s^+ D_{s2}^*(2575)^-$ via ISR show an interesting enhancement at the mass of 4626 MeV/c^2. The observed enhancements are compatible in mass, width, quantum numbers and cross-section with the $Y(4660)$ vector state. These results additionally indicate that the proposed analysis of $e^+e^- \to D_s^+ D_{sJ}^{(*)-}$ processes carries high discovery potential that can be realised with a bit of luck.

Invariant mass ranges, in which the $D_s^+ D_{s0}^*(2317)^-$ ($D_s^+ D_{s1}(2460)^-$) system can be studied with available Belle datasets are:

- [4.286(4.428) – 9.460] GeV/c^2 with the $\Upsilon(1\text{S})$ sample;
- [4.286(4.428) – 10.023] GeV/c^2 with the $\Upsilon(2\text{S})$ sample;
- [4.286(4.428) – 10.355] GeV/c^2 with the $\Upsilon(3\text{S})$ sample;
- [4.286(4.428) – 10.580] GeV/c^2 with the $\Upsilon(4\text{S})$ sample;
- [4.286(4.428) – 10.885] GeV/c^2 with the $\Upsilon(5\text{S})$ sample.

Additionally, this analysis may make use of a plethora of off-peak samples recorded by the Belle detector.

To further motivate the analysis of decay channels involving the $D_{s0}^*(2317)^-$ and $D_{s1}(2460)^-$ mesons, it is beneficial to review the history of their discovery. A rich spectrum of heavy-light ($Q\bar{q}$) mesons was originally anticipated. Unlike for the quarkonium, for which masses of constituent quarks are comparable and their interaction can be well described by the total angular momentum, spin interactions are suppressed for heavy-light mesonic systems due the large mass of a heavy quark (c). There are two possible $Q\bar{q}$ meson combinations in S-wave: 0^- and 1^-, which correspond to parallel and antiparallel orientations of the total angular momentum ($\vec{j_q}$) and spin angular momentum of a heavy quark ($\vec{s_Q}$), respectively. Meanwhile, in P-wave, the j_q value can be equal to 1/2 and 3/2, which opens a possibility for two doublets of mesons: 0^+ and 1^+ for $j_q = 1/2$; and 1^+ and 2^+ for $j_q = 3/2$.

In the case of non-strange charmed mesons ($Q = c, q = u/d$), a pseudoscalar D and vector D^* form a well-established isospin doublet. The same is valid for the spectrum of charmed-strange mesons, where the D_s^+ and D_s^{*+} isospin singlets are observed (see Fig. 6.1). This gives nearly equal hyperfine mass splitting for both meson pairs: $m_{1^-} - m_{0^-} = 140\text{MeV/c}^2$. On contrary, P-wave charmed mesons are

[3] It is expected to be an η-bound state

either difficult to produce or study. For example, the non-strange 0^+ resonance, $i.e.$ the $D_0^*(2300)^-$, was discovered relatively recently, in 2004 [208]. Its relatively late discovery is mainly attributed to the extremely large width of 229±16 MeV, which made its observation complicated. Meanwhile, the spectrum of $c\bar{s}$ states appeared to be even more puzzling. Its narrow $j_q = 3/2$ states, $i.e.$ the $D_s(2536)^+$ and the $D_s(2573)^+$ (see Fig. 6.1), were discovered by CLEO in 1993 [209], but the $j_q = 1/2$ scalar and vector mesons remained undiscovered for another decade. They were predicted to feature the invariant mass above the $m_{D^{(*)}} + m_K$ threshold, where intensive experimental efforts were concentrated to search for their decays into DK and D^*K. However, these efforts did not yield the anticipated observation.

Later, in 2003, a BaBar discovery shed the light on this puzzle, when an extremely narrow state decaying into $D_s^+\pi^0$ was observed in the $e^+e^- \to D_s^+\pi^0$ inclusive interaction [201]. The newly-observed state was named $D_{sJ}^*(2317)^+$, as per its measured mass. It was shortly confirmed by CLEO [203] in the analysis, which in addition reported observation of another previously unseen state with the mass near 2460 MeV, dubbed as $D_{sJ}(2460)^-$. The same study assigned 0^+ and 1^+ quantum numbers to the newly observed mesons, leading to their current naming as $D_{s0}^*(2317)^-$ and $D_{s1}(2460)^-$, respectively. Later the same year results of BaBar and CLEO were complemented by the Belle study, which established the inclusive production of both states. The $D_{s1}(2460)^-$ state was confirmed to decay into $D_s^*\gamma$ and to have 1^{++} quantum numbers.

Eventually, the two newly discovered mesons were recognised as the missing P-wave $c\bar{s}$ states, as their measured quantum numbers and the mass splitting of 141.8 ± 0.8 MeV/c^2 matched initial predictions. However, their masses were much lower than expected and, more importantly, below the DK and D^*K thresholds (see Fig. 6.1). This fact leaves these states with the only opportunity to decay via an isospin violating process, which causes their extremely small widths.

The measurement of the mass difference, defined as $\Delta M = M(D_{sJ}^{(*)-}\pi^0) - M(D_s^{(*)-})$, is crucial for better understanding of the $D_{s0}^*(2317)^-$ and $D_{s1}(2460)^-$ resonant states. The background knowledge suggests that strong interactions involve three light flavours (*u, d, s*) and three heavy flavours (*c, b, t*) with respect to the QCD infrared scale. The spontaneous breaking of chiral symmetry characterizes the light sector, while the heavy sector exhibits heavy-quark symmetry. There are theoretical works [210] pointing to the question of the form of the heavy-light effective action in the limit, where light flavours are massless, while the heavy flavours are infinitely massive. The spontaneous chiral symmetry breaking yields the mass splitting between the chiral doublet of about 345 MeV/c^2, when the pion coupling to the doublet is half its coupling to a free quark.

The $D_{s0}^*(2317)^-$ and $D_{s1}(2460)^-$ mesons can be interpreted as the first chiral partners of hadrons that are theoretically built of light (*s*) and heavy (*c*) quarks. As such, they represent a pattern of spontaneous breakdown of chiral symmetry rather than isolated events. This motivates elevation of the (0^+,1^+) doublet over the (0^-,1^-) doublet by the aforementioned value of 345 MeV/c^2. Although, judging on the latest mass splitting measurements, it is not necessarily the case. Former mass difference measurements for the $D_{s0}^*(2317)^-$ and $D_{s1}(2460)^-$ mesons have large statistical and systematic errors because of the limited data sample available and large deviation of the central mass value from the PDG average [104]. Despite the world-average mass splitting for the $D_{s0}^*(2317)^-$ and $D_{s1}(2460)^-$ mesons coincide within 1σ, individual measurements, especially for $D_{s1}(2460)^-$, do not necessarily support the chiral symmetry hypothesis. The lack of precision in experimental measurements did not allow disclosing the nature of $D_{s0}^*(2317)^-$ and $D_{s1}(2460)^-$, which still remains unknown. Consequently, their precision study could potentially offer a unique possibility to perform a tests of chiral symmetry breaking in heavy-light systems. This provides an additional motivation for this analysis, as we expect, thanks to improved analysis techniques and the full Belle dataset currently available, to measure the $D_{s0}^*(2317)^-$ and $D_{s1}(2460)^-$ mass splittings with higher precision to test the chiral symmetry hypothesis in a heavy-light systems.

The discrepancy of the measured massed of the $D_{s0}^*(2317)^-$ and $D_{s1}(2460)^-$ mesons with respect to former predictions and the potential chiral symmetry breaking laid the ground for various speculation on the structure of these resonances. It was pronounced that $D_{s0}^*(2317)^-$ and $D_{s1}(2460)^-$ could potentially be four-quark structures implemented either in the form of a $[cq][\bar{s}\bar{q}]$ tetraquark (a group of charged and doubly charged is expected to exist in this case), or a $D^{(*)}K$ molecule [212]. There are arguments that favour the molecular hypothesis [163, 173, 200, 204, 206], though it has not been proven so far due to the difficulty of measuring the extremely narrow width. Some other theories beyond the quark model are also reluctant to explain these resonances as compact states. In particular, exotic molecular states with negative parity were predicted [200]: a possible molecular interpretation of states with $J^P = 0^-$ and $J^P = 2^-$ is enhanced, as they could be bound by η exchange. On contrary, some lattice QCD calculations explained $D_{s0}^*(2317)^-$ as a canonical $c\bar{s}$ state [213]. However, they are rather scarce and outdated.

The best way to distinguish, if $D_{s0}^*(2317)^-$ is a pure $c\bar{s}$ state, a molecule or something else, it is to measure its width. As reported in several theoretical papers [214–221], width predictions are strongly dependent on the assumption of the quark content and the inner structure of the $D_{s0}^*(2317)^-$ resonance (see Table 6.3 and Fig. 6.2), making it a unique discriminant that can disclose the nature of $D_{s0}^*(2317)^-$. A reader can spot that width predictions reported in Table 6.3 are all extremely narrow. This

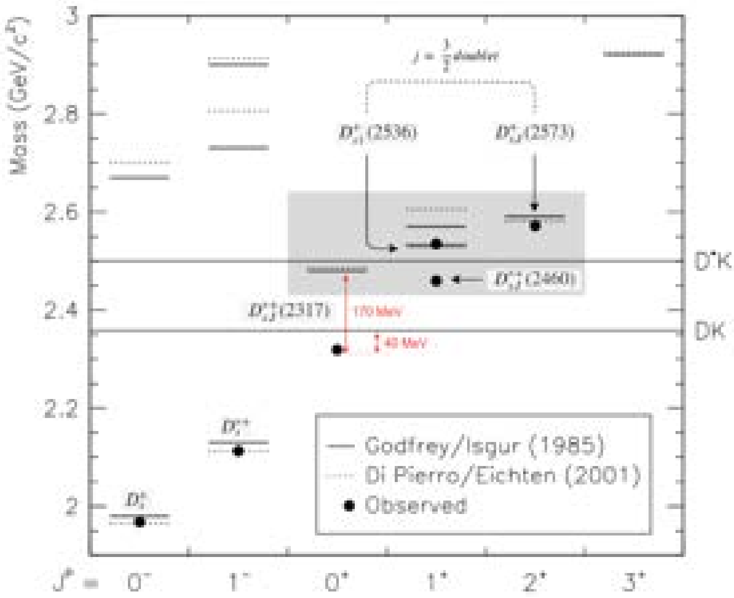

Figure 6.1: The $c\bar{s}$ meson spectrum, as predicted by Godfrey and Isgur [115] (solid lines) and Di Pierro and Eichten [211] (dashed lines) and as observed by experiment (points). The DK and $D^{*}K$ mass thresholds are indicated by the horizontal lines spanning the width of the plot.

makes the direct measurement of the intrinsic width impossible due to the detector smearing. However, the width upper limit (UL) measurement is still possible and can be used to reject some of theoretical interpretations.

The latest $D^{*}_{s0}(2317)^{-}$ width UL measurement was performed by BaBar in 2006 [223]. The idea was to describe the $D^{*}_{s0}(2317)$ line shape with a convolution of a modified Lorentzian and relativistic Breit-Wigner functions, where the width parameter (Γ) is fixed to a constant value. By varying this constant in the interval of interest, a likelihood scan has been performed. The width value ($\Gamma^{95\%}$) that demarcates 95% of the total likelihood curve integral was then taken as the width UL at 95% confidence level (CL). The $D^{*}_{s0}(2317)^{-}$ width UL value of 3.8 MeV that was acquired with this technique, still stands as the world-best measurement. It is worth mentioning, there are different approaches to the width UL measurement, which can deliver better results. Although, they are based on likelihood studies of

Reference	$D^*_{s0}(2317)^-$ width prediction (keV)	Interpretation
[214]	6 ± 2	pure cs-state
[215]	7 ± 1	pure cs-state
[216]	10	pure cs-state
[217]	10—100	tetraquark
[218]	79.3 ± 39.6	DK-molecule
[219]	140	Dynamically-generated resonance
[220, 221]	133 ± 22	DK-molecule

Table 6.3: Summary of the main theoretical prediction of the $D^*_{s0}(2317)^-$ width.

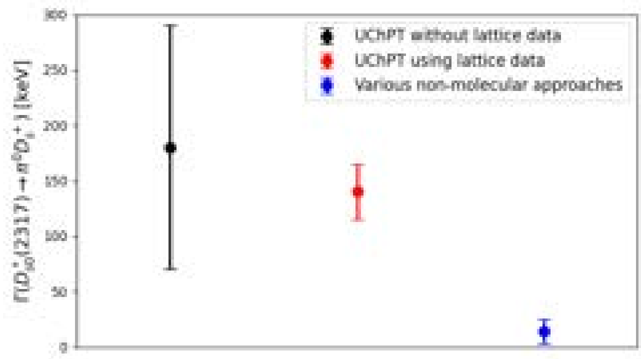

Figure 6.2: Prediction of the $D^*_{s0}(2317)^-$ width, using different theoretical approaches, as indicated in Ref. [222]

multidimensional distributions, which can be composed in B decays. For example, in 2011 the $X(3872)$ width UL study reported the following: $\Gamma < 1.2$ MeV at 90% CL [224]. However, the suggested analysis offers a search for $D^*_{s0}(2317)$ candidates in off-resonant interactions, and therefore multidimensional techniques are inapplicable in its context.

To conclude this section, searching for either earlier observed or yet unseen resonances in the $D_s^+ D_{sJ}^{(*)-}$ system is a topic of very high impact, as it would open a way for two scenarios:

- If $D_{sJ}^{(*)-}$ is a pure $c\bar{s}$ state, the newly found resonance in this invariant mass system can be interpreted as a molecule or as a compact tetraquark;

- If $D_{sJ}^{(*)-}$ is a tetraquark or a molecular state, the newly found resonant state might contain *six* constituent quarks.

The goal of the hereby proposed analysis is then not only looking for exotic candidates in the $D_s^+ D_{sJ}^{(*)-}$ system, but also, if the analysis conditions allow, to probe the nature of $D_{s0}^*(2317)^-$ by performing the most precise $D_{s0}^*(2317)^-$ width UL and mass-splitting measurements. The high ability of the Belle calorimeter to reconstruct photons, then π^0, and the high statistics collected over the past years, make this analysis feasible. Known restrictions due to the trigger cuts and limitation in reconstructing low momentum photons at LHCb favour the use of the Belle data set for such investigation. On the other hand, in competition with earlier $D_{sJ}^{(*)-}$ measurements, introduction of 3 additional tracks to reconstruct an additional primary D_s^+ meson will significantly decrease the reconstruction efficiency, which is expected to be below 1%.

6.2 Analysis goals and strategy

In this section we summarise goals of the proposed analysis and suggest a strategy for achieving them.

The main goals are:

- Search for resonances in the $D_s^+ D_{s0}^*(2317)^-$ and $D_s^+ D_{s1}(2460)^-$ invariant mass systems in the continuum;
- Cross-section measurements of the $e^+e^- \to X(\to D_s^+ D_{s0}^*(2317)^-)$ and $e^+e^- \to X(\to D_s^+ D_{s1}(2460)^-)$ inclusive processes, where X denotes accessible states reported by Ref. [168] and, as discussed in the previous chapter, are accessible in the proposed process;
- Precise mass-splitting measurements;
- $D_{s0}^*(2317)^-$ and $D_{s1}(2460)^-$ width upper limit measurements.

Achieving the last two goals is only possible if analysis conditions allow, $i.e.$ if the reconstructed yield is high enough to perform a reliable fit of the $D_{sJ}^{(*)-}$ line shape. For the example of $D_{s0}^*(2317)^-$, the most optimal channel to perform these measurements would be an inclusive $e^+e^- \to D_s^- \pi^0$ decay, being $D_{s0}^*(2317)^- \to D_s^- \pi^0$ – the only channel where the $D_{s0}^*(2317)^-$ meson has ever been observed. In principle, the width measurement can also be performed in $e^+e^- \rightarrow D_s^+ D_{s0}^*(2317)^-$, as we intend to. However, limited yield and poor reconstruction efficiency significantly reduce the sensitivity of such measurement. The Belle analysis of the $e^+e^- \rightarrow D_s^- \pi^0$ inclusive channel reported 761 $D_{s0}^*(2317)^-$ candidates in 87 fb^{-1}, suggesting approximately 8700 candidates from the complete dataset. However, reconstructing an additional primary D_s^+ meson will decrease the yield by at least one order of magnitude, constraining the achievable precision for $D_{s0}^*(2317)^-$ measurements. The same logic applied to the decay channel that includes the $D_{s1}(2460)^-$ meson.

Our strategy for the proposed analysis consists of the following steps:

1. A dedicated reconstruction of the $e^+e^- \rightarrow D_s^+ D_{s0}^*(2317)^-$ decay channel that mostly relies on selection criteria reported in former analyses [201–203, 223] is developed for initial Monte-Carlo (MC) studies;

2. Various approaches in MC generation of signal events with $EvtGen$ framework are studied. The best performing $EvtGen$ model is selected to generate a sufficiently large (1M events) signal MC sample and simulate its evolution and interaction with Belle detector components;

3. The validated approach to generation, simulation and reconstruction of signal events is then applied to the second channel of interest, $i.e.$ the $e^+e^- \rightarrow D_s^+ D_{s1}(2460)^-$. Reconstruction results of both decay channels are studied in parallel to confirm cross-feed background components that are expected in this analysis;

4. Selection criteria are optimised in generic MC sample. The optimised event reconstruction and selection is performed in Belle data;

5. A more sophisticated MVA technique is employed to maximise reconstruction efficiency in generic MC and data;

6. $D_s^+ D_{sJ}^{(*)-}$ invariant mass systems are studied to validate resonances, if any observed. Cross-section calculations are performed, or, depending on the yield, ULs are set;

7. Precise mass-splitting and width UL measurements are performed, if competitiveness is confirmed.

6.3 Signal Monte-Carlo study

6.3.1 Simulation model

We study $e^+e^- \to D_s^+ D_{s0}^*(2317)^-$ inclusively, without imposing any requirements on the rest of event. The inclusive component of the decay channel is not reconstructed explicitly, while primary mesons, $i.e.$ D_s^+ and $D_{s0}^*(2317)^-$, are reconstructed exclusively following their respective decay modes.

An educated choice of the $EvtGen$ model is critical for reliable simulation of signal events. As the text that follows will explain, different models have characteristic pros and cons, as well as innate limitations. Their immanent features can distort kinematic properties of decay products and lineshapes of intermediate resonances in comparison with real data.

The following two approaches suitable for simulation of continuum $c\bar{c}$ events were considered:

- **CASE (A)**. Simulation of $e^+e^- \to D_s^+ D_{s0}^*(2317)^-$ events, assuming no resonant state $X \to D_s^+ D_{s0}^*(2317)^-$ exists;

- **CASE (B)**. Introduction of an artificial intermediate resonance ($Dsprt$) in the particles' library to allow it to decay into $D_s^+ D_{s0}^*(2317)^-$.

One million events were studied in order to validate both approaches. Simulation of signal events was performed using $EvtGen$ MC generator, while the detector penetration was simulated with $GEANT4$. The standard $basf$ revision was employed to perform reconstruction of signal events. The cascade of secondary decays defined for events generation is schematically shown in Fig. 6.3.

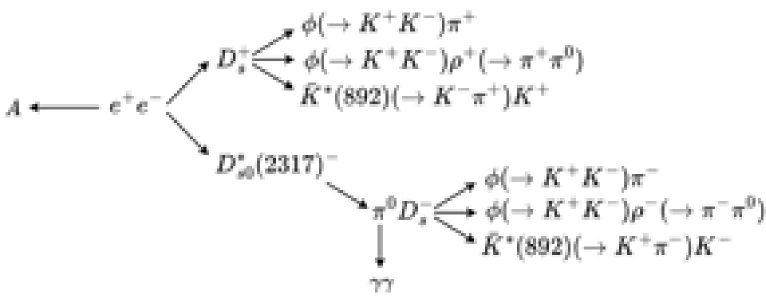

Figure 6.3: The $e^+e^- \to D_s^+ D_{s0}^*(2317)^-$ decay scheme, where A (*anything else*) denotes the generic rest of event.

The result of case (A) is show in Fig. 6.4 [top-left]: clearly this is not the correct way to proceed in this analysis. We then decide to follow the approach reported in case (B). The hypothetical $Dsprt$ is initially defined as a scalar ($J = 0$) with the threshold invariant mass, $i.e.$ equal to the sum of the masses of the D_s^+, and the $D_{s0}^*(2317)^-$ meson and a zero intrinsic width ($\Gamma = 0$ GeV). We further vary parameters of the $Dsprt$ particle to study how their definition affects the distribution of signal events. Here below we provide the summary of the $Dsprt$ parameters that were studied (see Fig. 6.4):

- **Case B1** $m = 4.286$ GeV/c^2, $\Gamma = 0$ GeV, $J = 0$ (Fig. 6.4 [top-central]);
- **Case B2** $m = 4.3$ GeV/c^2, $\Gamma = 0$ GeV, $J = 0$ (Fig. 6.4 [top-right]);
- **Case B3** $m = 4.5$ GeV/c^2, $\Gamma = 0$ GeV, $J = 0$ (Fig. 6.4 [central-left]);
- **Case B4** $m = 4.7$ GeV/c^2, $\Gamma = 0$ GeV, $J = 0$ (Fig. 6.4 [central-central]);
- **Case B5** $m = 5.0$ GeV/c^2, $\Gamma = 2$ GeV, $J = 0$ (Fig. 6.4 [central-right]);
- **Case B6** $m = 6.0$ GeV/c^2, $\Gamma = 4$ GeV, $J = 0$ (Fig. 6.4 [bottom-left]);
- **Case B7** $m = 6.0$ GeV/c^2, $\Gamma = 4$ GeV, $J = 1$ (Fig. 6.4 [bottom-central]);

This sequence of simulations is developed to create a pull of bias-dependent invariant mass distributions, which will come handy for the comparison to results on data. This may allow tracing back intrinsic features of a resonance, if any observed. Cases **B5-B7** are studied to create invariant mass distributions of signal events following the shape of the phase space (PHSP). A similar shape of the distribution is expected, if no resonant state is observed in the $D_s^+ D_{s0}^*(2317)^-$ system. We also notice that changing spin, $J = 0$ or $J = 1$, has no significant effect in our simulated PHPS-like distributed events. Each signal MC sample is generated at $\Upsilon(nS)$ ($n = \overline{1,5}$) center-of-mass energies, with each subset proportional to the luminosity of the corresponding energy in the full Belle data sample.

It is worth mentioning that additional studies have been performed by using different decay models, but those appeared to be vastly unsatisfactory. In particular, the $PYCONT$ model, which is often used for running inclusive analyses in continuum, has been tested. However, it leads to nonphysical results, if a state with the invariant mass greater than that of the lightest $c\bar{c}$ state is included in the decay cascade. In our case, the mother particle is an artificial particle with the invariant mass of 4.287 GeV/c^2 – greater than the mass of η_c. Hence, the model used for former $D_{s0}^*(2317)^-$ studies cannot be used in our case.

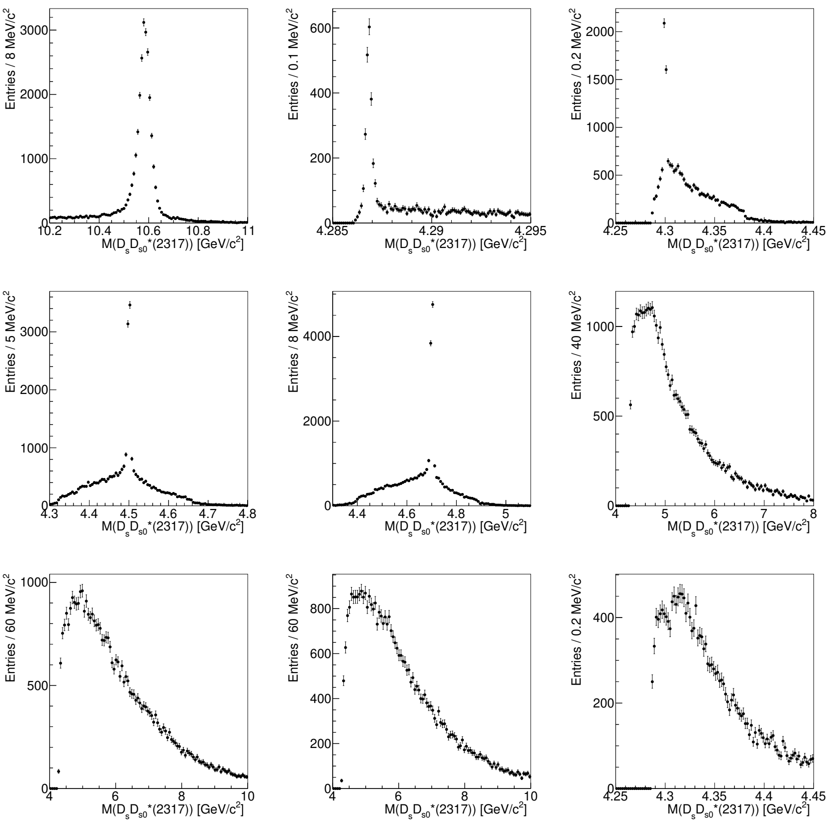

Figure 6.4: Invariant mass distribution of the $D_s^+ D_{s0}^*(2317)^-$ system reconstructed in a signal MC sample. For each MC sample, the simulation of the $e^+e^- \rightarrow D_s^+ D_{s0}^*(2317)^-$ process is performed following the cases described in the text: A [upper-left], B1 [upper-central], B2 [upper-right], B3 [central-left], B4 [central-central], B5 [central-right], B6 [bottom-left], B7 [bottom-central] and B8 [bottom-right].

Our final choice of the model that is used for all further MC studies falls on the case **B1**, as it aligns with theoretical hypotheses and experimental results that we intend to cross-check, as introduced in Sec. 6.1. The model we finally choose for simulation of signal events is a compromise, as it is able to correctly reproduce invariant mass distribution of intermediate resonances, but distorts their kinematic properties. This, in turn, leads to challenges in the event selection and calculation of the reconstruction efficiency in signal MC. This is best illustrated by an example of $D^*_{s0}(2317)^-$ candidates reconstructed in a generated sample. While the invariant mass distribution is reasonable, some distributions of kinematic variables exhibits unphysical behaviour and hence cannot be included in the event selection due to limitations of the MC model (see Fig. C.2 in App. C.2). Looking ahead, the irrelevance of kinematic distributions becomes even more prominent, if one compares them to similar plots acquired in the generic MC study (see Fig. C.3 in Sec. 6.4). This motivates us to adopt event selection criteria from Refs. [201–203] as reference in the early analysis stages.

Additionally, we report in Fig. 6.4 [bottom-right] a case, where parameters of the artificial $Dsprt$ state are set in accordance with those of the $X(4274)$ resonance reported in Ref. [188]: $m = 4274$ MeV/c^2 and $\Gamma = 56$ MeV. Despite its invariant mass is located below the $D_s^+ D^*_{s0}(2317)^-$ threshold, which makes the decay into $D_s^+ D^*_{s0}(2317)^-$ kinematically forbidden, its close location to the threshold and the large width opens a possibility of its off-shell generation. This may create possible interference effects, which might need to be accounted for in this analysis. At the same time, given that the mass resolution for $X(4274)$ at LHCb is not very high, the reported resonance may also end up being above the $D_s^+ D^*_{s0}(2317)^-$ threshold.

Former analyses involving the $D^*_{s0}(2317)^-$ and $D_{s1}(2460)^-$ mesons confirm their strong interdependence and suggest that it is essential to study the $e^+e^- \to D_s^+ D^*_{s0}(2317)^-$ and $e^+e^- \to D_s^+ D_{s1}(2460)^-$ processes in parallel to account for complicated mutual reflections. Decay products of these two particles are kinematically similar, which leads to cross-feed background that can not be reliably modelled without analysing both channels simultaneously. Therefore, we additionally perform MC simulation of the decay channel involving the $D_{s1}(2460)^-$ meson by following the same approach that has been selected for the $e^+e^- \to D_s^+ D^*_{s0}(2317)^-$ process and the decay cascade depicted in Fig. 6.5. Both decay files used for generation of signal MC events are provided in App. C.4 and App. C.4.

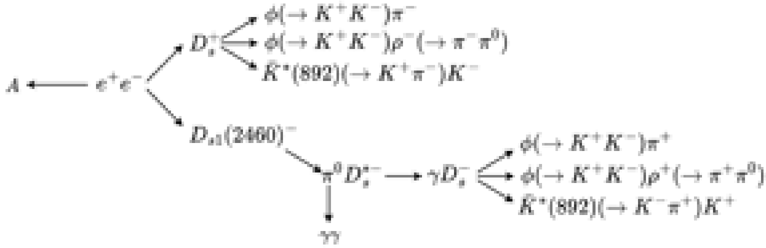

Figure 6.5: The $e^+e^- \to D_s^+ D_{s1}(2460)^-$ decay scheme, where A (*anything else*) denotes the generic rest of event.

6.3.2 Event pre-selection

We apply the initial loose selection (pre-selection) to events reconstructed online to discard obviously misidentified tracks, misfired photon clusters and incorrectly combined composite particles. This allows to vastly reduce the size of the $ntuples$ at a negligible cost of correctly reconstructed candidates.

Each of the reconstructed decay channels includes two D_s^- mesons of the opposite charge: the primary one coming from the artificial $Dsprt$ particle, and the secondary one originating from the $D_{s0}^*(2317)^-$ or $D_{s1}(2460)^-$ decay. We therefore require at least 6 tracks to be detected – 3 tracks for each D_s^- meson – and at least 2 neutrals essential for composition of a π^0 candidate. All charged tracks are required to meet spacial conditions that are considered standard for a Belle analysis. As such, all tracks must have the impact parameter $dr < 1.5$ cm in the $r - \phi$ plane with respect to the interaction point and the displacement $|dz| < 3$ cm in the $r - z$ plane (see App. C.1 for a more elaborate definition). In order to identify a track and distinguish kaons from pions, we use a likelihood criterion, which makes use of response properties of each track in various sub-detectors. The binary ratio $P(K/\pi) = \mathcal{L}(K/\pi)/(\mathcal{L}(K)+\mathcal{L}(\pi))$ estimates the likelihood of a tack to be a kaon or a pion. In our study, for each pair of kaons combined to form a D_s^- candidate, we apply a tight selection on one the kaon candidates by requiring $P(K) > 0.6$, and a loose selection on the second kaon candidate – $P(K) > 0.2$. Meanwhile, all pion candidates must meet the requirement $P(\pi) > 0.1$.

We reconstruct ϕ and K^* candidates in their respective decay channels into K^-K^+ and $K^-\pi^+$. For ϕ meson candidates, we combine pairs of oppositely charged kaons originating from the same vertex. The width of the K^-K^+ invariant mass distribution is dominated by the intrinsic width of ≈ 4 MeV. We therefore define the signal region for ψ candidates within 10 MeV/c^2 ($\sim 2.5\sigma$) from the ϕ nominal value: $1010 < M(K^-K^+) < 1030$ MeV/c^2. In order to verify the goodness of the ϕ

reconstruction, their residual distribution is plotted (see Fig. C.10 in App. C.3). A fit to the residual distribution performed with a Crystal Ball proves the absence of the reconstruction bias: $\mu = (7.20 \pm 1.59) \times 10^{-5}$ MeV/c^2, while the fitted width of 0.55 ± 0.19 MeV implies good detector resolution. The width of the $K^-\pi^+$ invariant mass distribution is also primarily determined by the large natural width of K^*: 51.4 ± 0.8 MeV. Accordingly, prioritising the signal purity, a narrow signal region of $845 < M(K^-\pi^+) < 945$ MeV/c^2 is defined for K^* candidates. Charge conjugated with respect to $K^*(892)$, $\bar{K}^*(892)$ candidates, are selected the same way.

In order to combine π^0 candidates, we select photons with energy larger than 100 MeV. A tight selection applied on photon candidates helps with suppression of high combinatorial background coming from numerous fake photon clusters in the low energy region. The FWHM of the $\gamma\gamma$ invariant mass distribution is dominated by the detector resolution, which is estimated to be ≈ 4.5 MeV/c^2. Therefore, we define the signal region for π^0 candidates as: $122 < |M(\gamma\gamma)| < 148$ MeV/c^2 – $\pm 3\sigma$ from the nominal π^0 invariant mass. We also require π^0 candidates to have momentum greater than 150 MeV/c. After applying the complete π^0 selection, we proceed to perform the mass-constrained fit to π^0 candidates. All fits to invariant mass distributions of intermediate resonances and the summary of corresponding fit parameters are provided in App. C.3 (see Figs. C.9 to C.12).

From the study of the invariant mass distributions of secondary D_s^- in different decay modes (see Figs. C.13 and C.15 in App. C.3), we learn that its resolution and reconstruction efficiency varies significantly, depending on a specific decay mode. As such, the two decay modes that are combining only charged tracks, $i.e.$ $\phi\pi^-$ and K^*K^-, tend to have higher reconstruction efficiency, which is indicated by fitted yields of $3,106 \pm 57$ and $2,616 \pm 53$, respectively. They also have compatible detector resolutions of 3.6 ± 0.20 and 4.0 ± 0.21 MeV, respectively. On contrary, the decay mode that includes an additional π^0 into a combination of a D_s^- candidate, as expected, has lower reconstruction efficiency (the fitted yield is 134 ± 12) and exhibits the detector resolution of 7.88 ± 0.62 MeV, which is twice as large as the width of the invariant mass distributions for the modes that do not include neutrals. Although, due to the low yield of the $\phi\pi^-\pi^0$ mode, the standard fitting procedure that employs a double Gaussian to describe the signal component performs well for the D_s^- invariant mass distribution that includes events reconstructed in all 3 decay modes. The total resolution of 3.94 ± 0.15 MeV established as a weighted sum of two Gaussian components, motivates us to define the signal region for D_s^- candidates as: $1.955 < |M(D_s^-)| < 1.979$ MeV/c^2 ($\pm 3\sigma$). The D_s^- invariant mass hypothesis is then applied to all selected D_s^- candidates: both primary and secondary.

We reconstruct D_s^{*-} candidates by combining a selected D_s^- candidate with a photon that is required to have energy larger than 100 MeV. The D_s^{*-} invariant mass distribution includes two peaking components: the matched signal and the broken signal (BS) (see Fig. C.17 in App. C.3). The so-called broken signal component is originating from $D_s^-\gamma$ combinations, in which a correctly reconstructed D_s^- candidate is paired with an arbitrary photon detected in the calorimeter. This leads to emergence of the peaking background that can be described with a Gaussian with relatively large fitted width (17.95 ± 2.92 MeV). Meanwhile, the width of the matched signal component is almost 4 times as little: ≈ 5 MeV. A $\pm 3\sigma$ signal region is then assigned to D_s^{*-} candidates: $2.097 < M(D_s^-\gamma) < 2.127$ MeV/c^2. The mass constraint fit is later applied to all D_s^{*-} candidates that have passed this selection.

$D_{s0}^*(2317)^-$ and $D_{s1}(2460)^-$ candidates are reconstructing by combining a π^0 candidate with D_s^{*-} and D_s^{*-}, respectively. No extra selection criteria are applied on the $D_{s0}^*(2317)^-$ and the $D_{s1}(2460)^-$ candidates at this level.

6.3.3 Event post-selection

In this section, we make a list of selection criteria that are applied offline. Since there are two D_s^- mesons in each decay channels (see Fig. 6.3 and Fig. 6.5), they can be matched in a wrong way, which leads to existence of an artificial peak in the $D_{s0}^*(2317)^-$ and $D_{s1}(2460)^-$ invariant mass distributions. A truth-matching criterion is employed to avoid it. In signal MC, it is imposed by requiring that the mother of the primary D_s^+ is $Dprt$, and the mother of the secondary D_s^- is $D_{s0}^*(2317)^-$ or the $D_{s1}(2460)^-$, depending on the decay channel.

We implement the second Fox-Wolfram momentum variable, R_2 (see App. C.1 for an elaborate definition), to test its separation power between $B\bar{B}$ and continuum events. Following the example of the former Belle analysis [201], the $R_2 < 0.4$ criterion is tested. Although, the study of the R_2 selection in combination with other selection criteria, especially the $p^*(D_{sJ}^{(*)-})$ selection that is first introduced in generic MC (see Sec. 6.4), has indicated its redundancy. The p^* selection criterion, defined as the momentum of a particle in the CM rest frame, had been proven to be the most powerful criterion capable of rejecting a vast majority of $B\bar{B}$ events. We therefore do not include the R_2 selection in the final list of selection criteria.

To further enhance signal purity, we apply a selection on the helicity angle (θ_H) for ϕ and K^* candidates. It is defined as the angle between their first daughter – K^- – and the mother particle – D_s^- – in the rest frame of ϕ or K^*, depending on the D_s^- decay channel (see Fig. 6.6). As suggested by Ref. [225], scalar states are expected to have a uniform $cos\theta_H$ distribution, while the same distribution for vector states take a parabolic shape. Since both ϕ and K^* are vector mesons, they are expected to have similar $cos\theta_H$ distributions (see Fig. 6.6). The asymmetry of the depicted $cos\theta_H$ distribution can be explained by the asymmetric kaon identification (see K/π

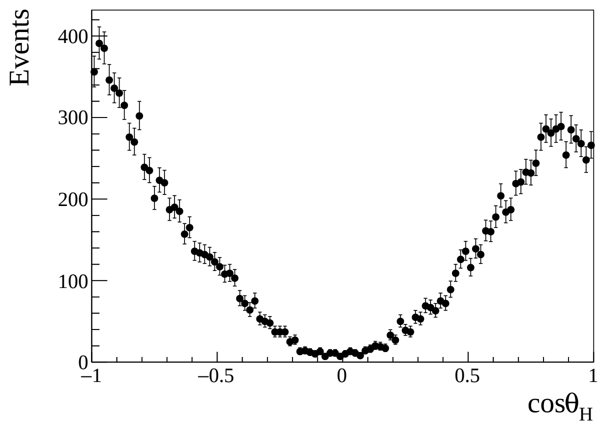

Figure 6.6: The $cos\theta_H$ distribution for matched ϕ and K^* candidates in the signal MC.

PID described above). We preliminarily require $|cos\theta_H| > 0.35$ for all ϕ and K^* candidates, as suggested by Ref. [202]. This selection criterion, along with the others used in post-selection, will later be optimised using generic MC, where a realistic background overlay is introduced.

The so-called χ^2 probability (P_{χ^2}) is another criterion used for the post-selection. It is calculated for each vertex present in a decay scheme to which vertex fit is applied and is based on two parameters: χ^2 and ndf. Effectively, it quantifies the vertex fit goodness. While it may appear that χ^2 plays the same role as P_{χ^2}, χ^2 can reach high

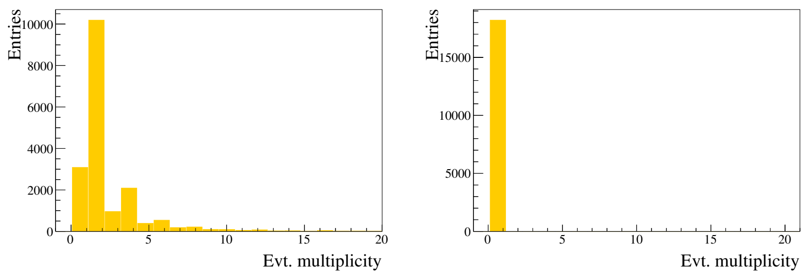

Figure 6.7: Multiplicity of reconstructed $D_s^+ D_{sJ}^{(*)-}$ candidates before [left] and after [right] BCS.

values, *e.g.* 200, which is inconvenient for selection standardisation. On contrary, the value of P_{χ^2} is mathematically constrained in the [0,1] range, which is more convenient in use than the χ^2 variable. Values of P_{χ^2} are usually communicated in percent, *e.g.* $P_{\chi^2} = 0.01$ is 1%. As such, we require $P_{\chi^2} > 0.1\%$ for ϕ, $K^*(892)$, D_s^- and $D_{sJ}^{(*)-}$ vertexes and $P_{\chi^2} > 1\%$ for π^0 candidates.

Additionally, we address the issue of multiple candidates per event, which may occasionally be combined. Fig. 6.7 [left] indicates that the majority of events offer more than one candidate per event. We therefore apply a dedicated best candidate selection (BCS), which is based on the χ^2 value of the $D_s^+ D_{sJ}^{(*)-}$ vertex fit. As such, we preserve a candidate with the lowest χ^2, while all the other candidates combined in a single event are discarded. Fig. 6.7 [right] proves that only one candidate per event is preserved after BCS.

6.3.4 Fit to $\Delta M(D_s^{(*)-}\pi^0)$ distributions

Following the event selection procedure described above, we isolate $D_{s0}^*(2317)^-$ and $D_{s1}(2460)^-$ candidates and illustrate $\Delta M(D_s^{(*)-}\pi^0)$ distributions defined as: $\Delta M(D_s^{(*)-}\pi^0) = M(D_s^{(*)-}\pi^0) - M(D_s^{(*)-})$ (see Fig. 6.8). A fit to each of these

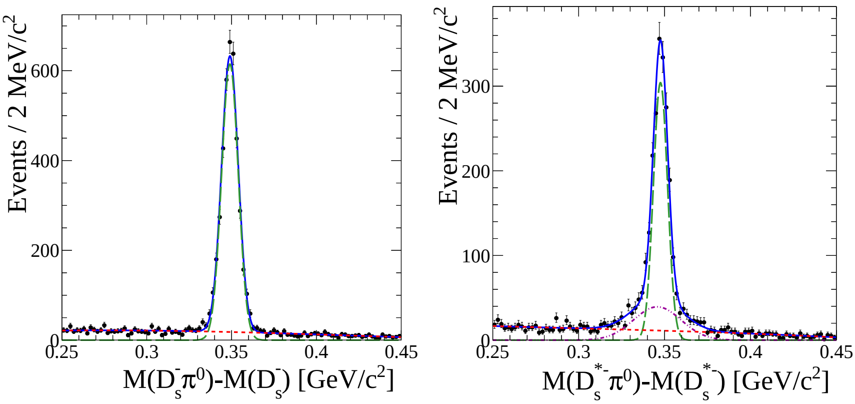

Figure 6.8: The [left] $\Delta M(D_s^-\pi^0)$ and [right] $\Delta M(D_s^{*-}\pi^0)$ distributions in signal MC. In each figure, the solid blue curve represents the fit, where signal (dashed green) and broken signal (dashed purple) components are described with a Gaussian, while track combinations are fitted with the first-order Chebychev polynomial (dashed red).

distributions is performed to separate signal components, which can be described with a Gaussian. We report the fitted yield of $3,805\pm64$ reconstructed events and the fitted width of 4.95 ± 0.07 MeV for the $\Delta M(D_s^-\pi^0)$ distribution, while for the $\Delta M(D_s^{*-}\pi^0)$ distribution these values are $1,577 \pm 76$ and 4.12 ± 0.16 MeV, respectively. The mean value of the broken signal peaking component in the $\Delta M(D_s^{*-}\pi^0)$ distribution coincides with the position of the signal $D_{s1}(2460)^-$ component within the error and is estimated to have a fitted width of 14.3 ± 1.3 MeV. The total of 690 ± 67 events fall into this category.

6.3.5 Track combination study

The $D_{s0}^*(2317)^-$ and $D_{s1}(2460)^-$ decay chains are kinematically similar, which is the reason why cross-feed effects are present and strongly affect this analysis. Using the generator-level information, misreconstructed combinations can be identified and their distributions can be modelled in signal MC. We therefore will refer to these misreconstructed signal events as “background”, even though the use of this term in signal MC simulations may be misleading.

Accordingly, we identify the following peaking background sources that are expected in this analysis:

- **Feed-down background**

  $D_{s1}(2460)^-$ decays into D_s^- and 3 neutrals. When its decay products are combined in a reconstruction process, a single photon can be omitted to create an incomplete $D_s^-\pi^0$ combination. As a result of the kinematic similarity, this $D_s^-\pi^0$ system can be identified as a fake $D_{s0}^*(2317)^-$ candidate, which is effectively combined from the $D_{s1}(2460)^-$ decay products. Since it was reported that the mean value of the corresponding reflection peak is located 4 MeV lower than the central value of the genuine $D_{s0}^*(2317)^-$ peak, this contribution is referred to as the “feed-down background” [202].

- **Feed-up background**

  Similarly, $D_{s0}^*(2317)^-$ decays into a D_s^- meson and 2 neutral particles. Hence, when tracks are combined to form the D_s^- vertex, a random photon caught in the detector can be added to the combination. This will create a fake D_s^{*-} candidate, which is consequently combined with a π^0 to create a fake $D_{s1}(2460)^-$ candidate. It leads to the existence of the so-called “feed-up background”, analogously called in such a way due to its location 8 MeV higher than the true $D_{s1}(2460)^-$ peak [202].

- **Broken signal (BS)**

  The last peaking background component present in the $D_{s1}(2460)^-$ invariant mass region that has already been shortly mentioned in the text above is called "broken signal". It originates from $D_{s1}(2460)^-$ decay products, when combining a D_s^- meson with a random photon, rather than the one genuinely radiated in the decay of D_s^{*-}. In this way, a misreconstructed D_s^{*-} candidate is created and a fake $D_{s1}(2460)^-$ is seen, as a consequence.

In order to study the aforementioned sources of background that are induced by decay products of signal modes, a cross-feed reconstruction, $i.e.$ reconstruction of the $e^+e^- \to D_s^+ D_{s0}^*(2317)^-$ mode over the $e^+e^- \to D_s^+ D_{s1}(2460)^-$ signal MC sample and vice versa, has been performed. The result of such approach is shown in Fig. 6.9. In particular, Fig. 6.9 [left] shows the result of $D_{s0}^*(2317)^-$ reconstruction over the $D_{s1}(2460)^-$ signal sample. A clear reflection peak can be seen. The same was acquired by running the $D_{s1}(2460)^-$ reconstruction macro over the $D_{s0}^*(2317)^-$ signal sample (Fig. 6.9 [right]). The component of the "broken signal" has been observed earlier in Fig. 6.8, where the $D_{s1}(2460)^-$ reconstruction over its signal sample had been performed (see Fig. 6.8 [right]). A wider distribution in the plot

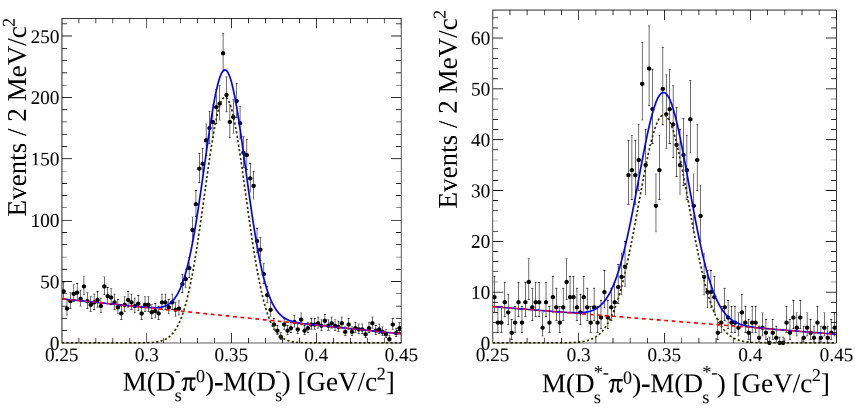

Figure 6.9: [left] The $\Delta M(D_s^-\pi^0)$ distribution acquired by reconstructing $D_{s0}^*(2317)^-$ over the $D_{s1}(2460)^-$ signal sample. [right] The $\Delta M(D_s^{*-}\pi^0)$ distribution acquired by reconstructing $D_{s1}(2460)^-$ over the $D_{s0}^*(2317)^-$ signal sample. In each figure, the solid blue curve represents the fit, where cross-feed peaking background components are described with a Gaussian (dashed yellow), while track combinations are fitted with the first-order Chebychev polynomial (dashed red).

clearly shows this effect.

Following this procedure, parameters of various peaking contributions are determined. In particular, the feed-down background appears to be shifted slightly less than what is reported by the reference analysis – for ≈ 3 MeV/c^2 (Table 6.4). The central value of the Gaussian describing the aforementioned "broken signal" is shifted by ≈ 1.7 MeV/c^2 with respect to the $D_{s1}(2460)^-$ signal peak – 2σ away from the central value it is expected to coincide with within the error. The biggest discrepancy with the reference analysis is observed for the feed-up background. It is shifted for only ≈ 2 MeV/c^2, while an 8 MeV/c^2 shift has been reported in the former research [202]. It was emphasised in Ref. [202] that cross-feed effects are very sensitive to the model and particles' parametrisation in simulation of signal events. Hence, we believe that the discrepancy we observe here can be explained by the different model that was used for generation of signal MC. No information is provided in the reference regarding the model, which could allow us to make the proper comparison or reproduce the results from the simulations in Ref. [202].

Impact type	σ [MeV]	μ [MeV/c^2]	N
True $D_{s0}^*(2317)^-$ signal	4.95 ± 0.07	349.0 ± 0.1	$3{,}805 \pm 64$
Feed-down background	12.1 ± 0.2	346.2 ± 0.3	$3{,}034 \pm 64$
True $D_{s1}(2460)^-$ signal	4.12 ± 0.16	347.6 ± 0.1	1577 ± 76
Feed-up background	14.6 ± 0.5	349.5 ± 0.6	823 ± 33
"Broken signal"	14.3 ± 1.3	345.9 ± 0.9	690 ± 67

Table 6.4: Fit parameters for peaking components observed in the $\Delta M(D_s^-\pi^0)$ and $\Delta M(D_s^{*-}\pi^0)$ distributions in signal MC (see Fig. 6.8 and Fig. 6.9).

6.3.6 Simultaneous fit test

At the level of signal MC, $D_{s0}^*(2317)^-$ and $D_{s1}(2460)^-$ signal events are not mixed in the same sample, which allows studying background effects separately by relying on a stable fitting procedure. Although, it is not the case in generic MC and real data, where a trivial fit with multiple floating parameters might be incapable of correct identification of reconstructed events in distributions with multiple peaking components. This motivates the development of a more sophisticated fitting approach that can be tested in signal MC and later applied in generic MC and data.

A simultaneous fit can be employed here. By fitting separately two distributions in signal MC samples, we have 3 floating parameters for each peak present in the mass distribution: mean value (μ), width (σ) and the number of entries (N). These floating parameters are extrapolated by fit for each peaking topology. In total, with 5 peaks expected in two mass distributions, a trivial fitting model procedure would include 15 floating parameters. This might lead to fit instability and divergence. In order to prevent it, we follow the simultaneous fit approach. It applies the knowledge of the peaking background parameters estimated above to fix them to the respective values in the new fitting model, while leaving the parameters of true peaks floating. In this way the total number of floating parameters is reduced down to 6, ensuring higher stability of the fitting procedure.

Apart from mean values and fitted widths of the peaking topologies reported in Table 6.4, we also fix the ratios of fitted events. Each of them is estimated as the ratio of the fitted number of peaking background events to the number of fitted true signal events that induce a given topology:

$$\begin{aligned} f^{\text{feed-down}} &= N^{\text{feed-down}}/N^{\text{true}}_{D_{s1}(2460)^-} = 1.924 \\ f^{\text{feed-up}} &= N^{\text{feed-up}}/N^{\text{true}}_{D^*_{s0}(2317)^-} = 0.216 \\ f^{\text{BS}} &= N^{\text{BS}}/N^{\text{true}}_{D_{s1}(2460)^-} = 0.437 \end{aligned} \tag{6.1}$$

The suggested parametrisation of the $\Delta M(D_s^-\pi^0)$ and $\Delta M(D_s^{*-}\pi^0)$ mass difference can then be expressed as:

$$\begin{aligned} \Delta M(D_s^-\pi^0) &= N_1 G(\mu_1, \sigma_1) \\ \Delta M(D_s^{*-}\pi^0) &= N_2 G(\mu_2, \sigma_2) + f^{\text{BS}} N_2 G(\mu^{\text{BS}}, \sigma^{\text{BS}}) \end{aligned} \tag{6.2}$$

where parameters with the upper script, $e.g.$ μ^{BS}, denote fixed parameters, while parameters with the lower script are floating.

Eq. 6.2 includes only 3 topologies: two true peaks and a broken signal. There are no cross-feed components because $D^*_{s0}(2317)^-$ and $D_{s1}(2460)^-$ signal events are not mixed on reconstructed samples. This provides a trivial fitting model that is available for testing in signal MC, where it expected to be highly stable, as it includes only 3 topologies. Cross-feed peaking backgrounds will be later included in the model for a fit in generic MC and data.

Following this approach, plots displayed in Fig. 6.10 are acquired. The fitted number of matched $D^*_{s0}(2317)^-$ and $D_{s1}(2460)^-$ signal events in these two plots are $3,806 \pm 64$ and $1,615 \pm 36$ respectively, while the number of "broken signal" events is 708 ± 8. These results are consistent with values reported in Table 6.4 within 1σ, which proves feasibility of this approach. The complete list of fit parameters is reported in Table C.10 in App. C.3.

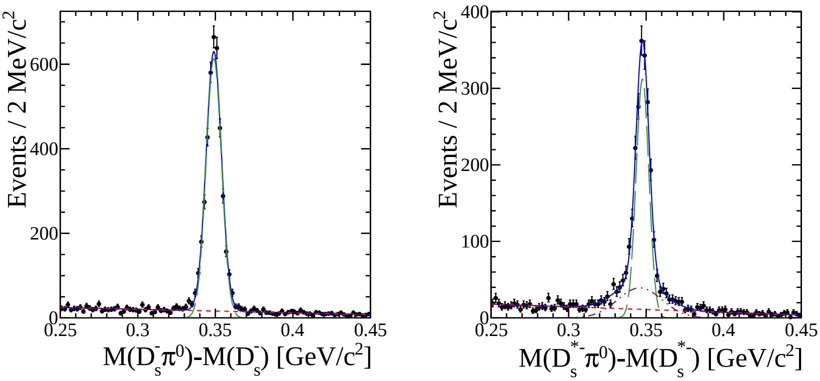

Figure 6.10: The [left] $\Delta M(D_s^- \pi^0)$ and [right] $\Delta M(D_s^{*-}\pi^0)$ distributions in signal MC fitted with the simplified simultaneous fit model (see Eq. 6.2). In each figure, the solid blue curve represents the total fit model, where signal (dashed green) and broken signal (dashed purple) components are described with a Gaussian, while track combinations are fitted with the first-order Chebychev polynomial (dashed red).

6.3.7 Fit to the $\mathbf{D_s^+ D_{sJ}^{(*)-}}$ invariant mass in signal MC

As the final step of the present signal MC study, an attempt to fit the $D_s^+ D_{s0}^*(2317)^-$ and $D_s^+ D_{s1}(2460)^-$ invariant mass distributions has been performed. We define signal regions for primary mesons as follows: for the prompt D_s^+ candidate – $1.955 < M(D_s^+) < 1.979$ GeV/c^2; for $D_{s0}^*(2317)^-$ – $2.305 < M(D_s^- \pi^0) < 2.329$ GeV/c^2; and for $D_{s1}(2460)^-$ – $2.448 < M(D_s^{*-}\pi^0) < 2.472$ GeV/c^2. These mass ranges rely on the resolution measured for respective invariant distributions and reflect 2–3σ mass windows. We then apply mass constraint fits to all primary mesons to compensate the detector smearing. Fits to the $D_s^+ D_{s0}^*(2317)^-$ and $D_s^+ D_{s1}(2460)^-$ invariant mass distributions for reconstructed and selected events in signal MC, with the initial parameter of the hypothetical $Dprt$ state set in accordance to the **B1** case (see Sec. 6.3.1), are depicted in Fig. 6.11. In the reconstruction of 1M signal events, we report following fitted yields: $3,131 \pm 63$ events for $D_s^+ D_{s0}^*(2317)^-$ and $1,580 \pm 83$ for $D_s^+ D_{s1}(2460)^-$ (see complete fits' results in Table C.11 in App. C.3).

With the dedicated selection explained above, the reconstruction efficiency of the $D_s^+ D_{s0}^*(2317)^-$ and $D_s^+ D_{s1}(2460)^-$ invariant masses are $(0.313 \pm 0.006)\%$ and $(0.158{\pm}0.008)\%$, respectively. Although, if we calculate reconstruction efficiency for

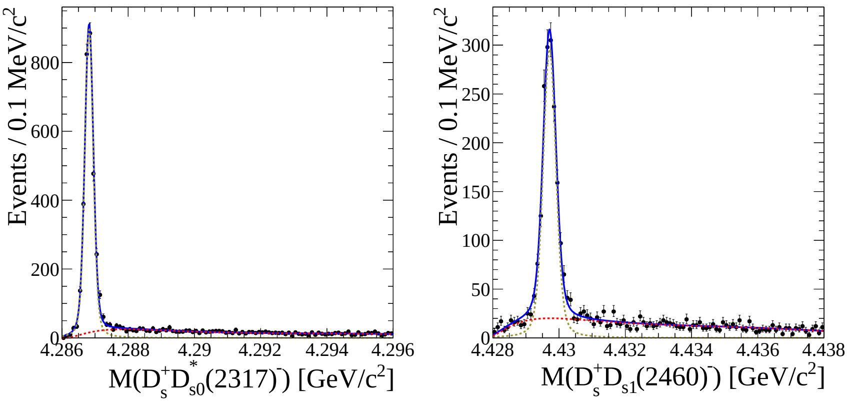

Figure 6.11: The $D_s^+ D_{s0}^*(2317)^-$ invariant mass distribution reconstructed on a signal MC sample that follows the B1 case. The signal contribution is fitted with the Voigt function, while the non-resonant background is approximated with a threshold function.

different individual D_s^- decay channels, these values vary a lot. For example, let ε_{ij} be the $D_s^+ D_{s0}^*(2317)^-$ reconstruction efficiency for a decay mode, where the secondary D_s^- meson decays into i-mode and the primary D_s^+ meson – into j-mode. With this nomenclature, we report the following reconstruction efficiencies: $\varepsilon_{11} = 1.05\%$, $\varepsilon_{22} = 0.01\%$ and $\varepsilon_{33} = 0.81\%$. This illustrates the fact that the reconstruction efficiency of the D_s^- meson decaying into $\phi\pi\pi^0$ is, as expected, significantly lower than for the other two decay modes. Since all D_s^- decay modes are evenly weighted in our signal MC simulation, reweighting of the reconstruction efficiency will be required for the final ε calculation.

6.4 Study on generic Monte-Carlo sample

6.4.1 Selection optimisation and summary

One of the main issues of the proposed analysis is the model used for simulating signal MC events. It, as discussed in Sec. 6.3.1, is incapable of properly describing the physics of the signal decay in the continuum. However, as the following section will illustrate, reconstruction results on data and on the generic MC sample match pretty well, including distributions of kinematic variables. We therefore decide to perform the selection optimisation on the generic MC sample, where, just like in signal MC, truth matching can be made use of to discriminate events. We then define a metric that is commonly used for optimisation of selection criteria:

$$\text{FoM} = \frac{S}{\sqrt{S+B}}, \tag{6.3}$$

where S is the number of signal events estimated by imposing MC truth matching and $S+B$ is the total number of reconstructed events. Using this metric, the following selection criteria have been optimised: $p^*(D_{sJ}^{(*)-})$ and $|cos\theta_H|$ (see Fig. C.4 in App. C.2).

Here is the summary of the optimised selection criteria for a $D_{s0}^*(2317)^-/D_{s1}(2460)^-$ decay chain:

- $|cos\theta_H| > 0.42/0.44$
- $p^*(D_{s0}^*(2317)) > 2.79$ GeV/c^2
- $p^*(D_{s1}(2460)) > 3.05$ GeV/c^2

With these criteria, we finalise the selection, which is summarised in Table 6.6.

For the sake of completeness, using the defined figure of merit, we additionally test other selection criteria that can be considered as an alternative to $p^*(D_{sJ}^{(*)-})$ for rejecting $B\bar{B}$ events. As those, we consider the second Fox-Wolfram momentum R_2, $p^*(D_s^+ D_{sJ}^{(*)-})$ and the scaled momentum x_p (see Eq. C.3 in App. C.1), which we compare side-by-side to find out, if any alternative selection criterion features a better background suppression. After each selection criterion had been optimised, the highest FoM has been reached with the $p^*(D_{sJ}^{(*)-})$-based selection (see Table 6.5). We therefore conclude that the best method to reject background and preserve the highest reconstruction efficiency is the selection over $p^*(D_{sJ}^{(*)-})$.

Optimised criterion	Yield (S)	FoM
N/A	6,476	5.384
$x_P > 0.205$	4,157	6.231
$R_2 > 0.225$	5,285	5.578
$p^*(D_{s0}(2317)) > 2.79$ GeV/c	4,538	9.813
$p^*(D_s D_{s0}(2317)) > 1.79$ GeV/c	4,018	5.721

Table 6.5: Comparison of the R_2, x_p, $p^*(D_{sJ}^{(*)-})$ and $p^*(D_s^+ D_{s0}(2317)^-)$ selection criteria. The optimal FoM value is evaluated using the metric defined in Eq. 6.3.

We verify the consistency of the optimised event selection by looking into invariant mass distributions of intermediate mesons, such as π^0 and secondary D_s^- (see Figs. C.18 and C.19 in App. C.3). No abnormalities are observed. The detector resolution for the reconstruction of D_s^- mesons in generic MC is described by a weighted width of a double Gaussian used to perform the fit in Fig. C.19 in App. C.3. We report this value to be 5.11 ± 0.25 MeV/c^2.

Particle	Selection criterion
Tracks	$dr < 0.5$ cm $dz < 3$ cm $P_{K_1}(K/\pi) > 0.5$ $P_{K_2}(K/\pi) > 0.2$ $P_{\pi^-}(K/\pi) < 0.9$
π^0	$E(\gamma) > 100$ MeV $p(\gamma\gamma) > 150$ MeV/c $122 < M(\gamma\gamma) < 148$ MeV/c^2 $P_{\chi^2}(\gamma\gamma) > 1\%$
ϕ	$1.010 < M(KK) < 1.030$ GeV/c^2 $P_{\chi^2}(K^-K^+) > 0.1\%$
$K^*(892)$	$842 < M(K^-\pi^+) < 942$ MeV/c^2 $P_{\chi^2}(K^-\pi^+) > 0.1\%$
$\phi/K^*(892)$	$\|cos\theta_H\| > 0.42/0.44$
D_s^-	$1.9585 < M(D_s^-) < 1.9785$ GeV/c^2 $P_{\chi^2}(D_s^-) > 0.1\%$
γ_*	$E(\gamma_*) > 100$ MeV
D_s^{-*}	$2.097 < M(D_s^-\gamma) < 2.127$ GeV/c^2 $P_{\chi^2}(D_s^-\gamma) > 0.1\%$
$D_{s0}^*(2317)^-$	$p^*(D_s^-\pi^0) > 2.79$ GeV/c $P_{\chi^2}(D_s^-\pi^0) > 0.1\%$ $2.305 < M(D_s^-\pi^0) < 2.329$ GeV/c^2
$D_{s1}(2460)^-$	$p^*(D_s^{*-}\pi^0) > 3.05$ GeV/c $P_{\chi^2}(D_s^{*-}\pi^0) > 0.1\%$ $2.448 < M(D_s^{*-}\pi^0) < 2.472$ GeV/c^2

Table 6.6: Selection summary for $D_s^+ D_{s0}^*(2317)^-/D_s^+ D_{s1}(2460)^-$ candidates reconstructed in generic MC and data. γ_* denotes the photon combined with D_s^- to create a D_s^{*-} candidate.

6.4.2 Background parametrisation and simultaneous fit

Distributions of events reconstructed in on- and off-peak generic MC samples share general features with those from signal MC. However, parameters of peaking background contributions are sensitive to the Monte-Carlo parametrisation. Since generic MC typically reproduces data more accurately than signal MC, we must re-evaluate the background parametrisation in generic MC for later use for data. This task is complicated by the fact that $D^*_{s0}(2317)^-$ and $D_{s1}(2460)^-$ events are mixed in the generic sample. However, we can exploit the MC truth matching to disentangle the origin of evens. We therefore propose the following approach to discriminate events in each peak:

1. **In the $\mathbf{\Delta M(D_s^- \pi^0)}$ distribution:**

   a) **True $\mathbf{D^*_{s0}(2317)^-}$ signal peak**
   MC truth matching is applied to isolate correctly reconstructed $D^*_{s0}(2317)^-$ candidates;

   b) **$\mathbf{D_{s1}(2460)^-}$ reflection peak (feed-down background)**
   Remaining mismatched $D^*_{s0}(2317)^-$ candidates include $D_{s1}(2460)^-$ reflection background and the flat combinatorial background component.

2. **In the $\mathbf{\Delta M(D_s^{*-} \pi^0)}$ distribution:**

   a) **True $\mathbf{D_{s1}(2460)^-}$ signal peak**
   MC truth matching is applied to isolate correctly reconstructed $D_{s1}(2460)^-$ candidates;

   b) **$\mathbf{D^*_{s0}(2317)^-}$ reflection peak (feed-up background)**
   We select mismatched $D_s^{*-}\pi^0$ combinations, where a D_s^{*-} meson is not originating from a $D_{s1}(2460)^-$ meson (using the mother ID). This allows isolating $D_{s1}(2460)^-$ candidates that are mistakenly combined from $D^*_{s0}(2317)^-$ decay products.

   c) **$\mathbf{D_{s1}(2460)^-}$ "broken signal" background**
   Here we also select mismatched $D_s^{*-}\pi^0$ combinations, but require a D_s^{*-} meson to indeed originate from a $D_{s1}(2460)^-$ meson. These conditions preserve only $D_{s1}(2460)^-$ "broken signal" events and combinatorial background.

Following this approach, we perform individual fits to each invariant mass distribution for events partitioned in the categories described above (see Figs. C.20 to C.24

in App. C.3). From each fit, we extract parameters of peaking components to fix their lineshapes for later use in the simultaneous fit. The results summarised in Table 6.7 confirm the shift of cross-feed topologies with respect to their true signal peaks, which is in better agreement with the reference analysis [202] than the results obtained in signal MC. The feed-down background is shifted by 3.7 ± 0.8 MeV/c^2 and features the 13.9 ± 0.8 MeV width, while the feed-up background is shifted by 4.4 ± 1.3 MeV/c^2 and has the width of 17.1 ± 1.5 MeV. On contrary, parameters of the broken signal topology show more tension with the reference analysis. While the mean value coincides with the one of the true $D_{s1}(2460)^-$ peak due to the large statistical uncertainty, its width estimated as 27.0 ± 6.6 MeV is 2.5σ away from the reference value. To reliably estimate parameters of the broken signal peak (2c), we use parametrisation of the combinatorial background in the $D_{s1}(2460)^-$ invariant mass distribution containing reflected $D^*_{s0}(2317)^-$ events (2b) to fix its shape in the distribution containing broken signal events. This approach ensured stability of the fit to the BS peaking topology. Lastly, based on the extracted fitted yield, we update fractions of numbers of events fitted in each peaking background component:

$$\begin{aligned} f^{\text{feed-down}} &= 2.870 \\ f^{\text{feed-up}} &= 0.163 \\ f^{\text{BS}} &= 0.579 \end{aligned} \tag{6.4}$$

We profit from the study of the simultaneous fit (SF) performed in signal MC, presented in Sec. 6.3.6, and apply the complete model to the generic MC sample. The following parametrisation is used to describe both distributions simultaneously:

$$\begin{aligned} \Delta M(D_s^-\pi^0) &= N_1 G(\mu_1, \sigma_1) + f^{\text{feed-down}} N_2 G(\mu^{\text{feed-down}}, \sigma^{\text{feed-down}}) \\ \Delta M(D_s^{*-}\pi^0) &= N_2 G(\mu_2, \sigma_2) + f^{\text{feed-up}} N_1 G(\mu^{\text{feed-up}}, \sigma^{\text{feed-up}}) \\ &\quad + f^{\text{BS}} N_2 G(\mu^{\text{BS}}, \sigma^{\text{BS}}) \end{aligned} \tag{6.5}$$

Here, variables with the upper script describing peaking background contributions are fixed to the values reported in Table 6.7 and Eq. 6.5, while the six parameters with the subscript defining “true” peaks are left floating. This fitting procedure proves being stable in generic MC, deriving parameters reported in Table 6.7. As expected, fixing parameters to the values estimated in generic MC makes SF results more reliable in comparison with the use of fit parameters determined in signal MC, as it eliminates the component of model imperfection.

Comparison of the simultaneous fit results to the values acquired by applying various MC-level conditions is summarised in Table 6.7. These results indicate that the chosen SF approach is moderately effective, as it is capable to correctly estimate

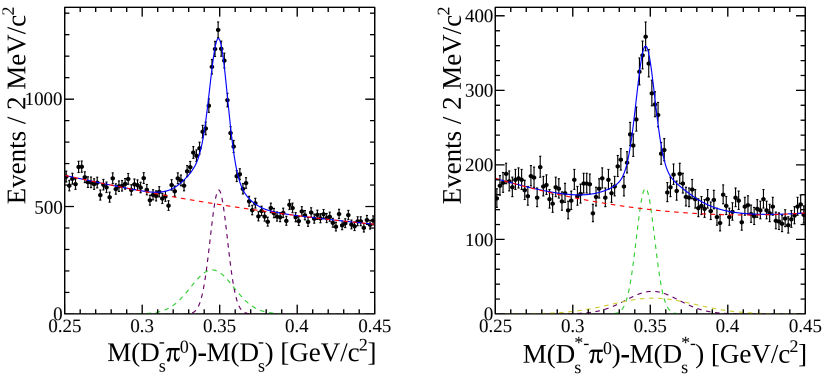

Figure 6.12: Simultaneous fit to the [left] $\Delta M(D_s\pi^0)$ and [right] $\Delta M(D_s^*\pi^0)$ distributions. In the left plot, the purple line represents the true $D_{s0}^*(2317)^-$ contribution, the green line - $D_{s1}(2460)^-$ reflection. In the right plot the green line represents the true $D_{s1}(2460)^-$ contribution, the purple line - the $D_{s0}^*(2317)$ reflection and the yellow line - the $D_{s1}(2460)^-$ broken signal. True peaks and the corresponding reflection peaks are marked in these plots with the same color to visualise cross-feed effects. Fit output parameters are summarised in Table 6.7.

mean values and widths of 'true' peaks. Meanwhile, fitted yields are only in 2σ agreement with the values acquired by applying truth-matching. This discrepancy can be explained by the compromise we made in the definition of the SF model. Distributions depicted in Fig. C.20 and Fig. C.22 in App. C.3 both feature a heavy left tail that can not be perfectly described with a single Gaussian. Potentially, a more complicated P.D.F., $e.g.$ Crystal-Ball or Johnson, would have been able to describe 'true' peaks better, but they would have also introduced additional fit parameters that could consequently make SF procedure unstable. This motivated us to describe matched $D_{sJ}^{(*)-}$ topologies with trivial Gaussians and keep SF model as simple as possible. As a drawback of this compromise, 'true' events present in left tails drift into peaking background topologies, which slightly distorts the $D_{s0}^*(2317)$ and $D_{s1}(2460)^-$ fitted yields. But despite this minor inconsistency, we conclude that the SF procedure is stable and is capable of delivering trustworthy interpretation of events contributing to $\Delta M(D_s\pi^0)$ and $\Delta M(D_s^*\pi^0)$ distributions

We additionally emphasise that the width of the $D_{s0}^*(2317)^-$ parametrisation given in Table 6.7 it is equal to 6.21 ± 0.09 MeV, which is 1.39 MeV less compared to the result published in Ref. [202]. It proves the possibility to improve the results of

Topology type	μ [MeV/c^2]	σ [MeV]	N
	Simultaneous fit		
True $D^*_{s0}(2317)$ signal	349.4 ± 0.2	5.55 ± 0.26	$4,010 \pm 202$
Feed-down background	345.2 (fixed)	13.9 (fixed)	$2.870 \cdot N_2$
True $D_{s1}(2460)$ signal	346.9 ± 0.4	5.86 ± 0.38	$1,241 \pm 71$
Feed-up background	351.5 (fixed)	13.9 (fixed)	$0.163 \cdot N_1$
$D_{s1}(2460)$ broken signal	351.8 (fixed)	27.0 (fixed)	$0.579 \cdot N_2$
	Results estimated by applying truth-matching requirements		
True $D^*_{s0}(2317)$ signal	348.9 ± 0.1	6.21 ± 0.09	$4,509 \pm 70$
Feed-down background	345.2 ± 0.8	13.9 ± 0.8	$3,117 \pm 235$
True $D_{s1}(2460)$ signal	346.9 ± 0.2	5.99 ± 0.18	$1,086 \pm 35$
Feed-up background	351.3 ± 1.3	17.1 ± 1.5	734 ± 91
$D_{s1}(2460)$ broken signal	351.8 ± 5.1	27.0 ± 6.6	628 ± 184

Table 6.7: Simultaneous fit results and results estimated by truth-matching requirements in generic MC.

former $D^*_{s0}(2317)^-$ and $D_{s1}(2460)^-$ studies published more than two decades ago.

As mentioned earlier, we assume that the background behaves similarly in generic MC and data. Therefore, it is meaningful to use parameters of background topologies estimated in generic MC for a simultaneous fit on data, where truth-matching is not available.

6.4.3 Fit to the $\mathbf{D_s^+ D^*_{s0}(2317)^-}$ mass

As the final step of our preliminary generic MC study, we show the $D_s^+ D^*_{s0}(2317)^-$ invariant mass distribution (see Fig. 6.13). Signal regions for $D^*_{s0}(2317)^-$ and primary D_s^+ candidates are defined identically to those applied in the signal MC selection. The invariant mass distribution depicted in Fig. 6.13 clearly differs from the one in the signal MC sample (see Fig. 6.11), where a fake $Dsprt$ particle with zero width peaking at the $D_s^+ D^*_{s0}(2317)^-$ threshold is introduced. Since no such resonances are present in the generic MC sample, PHSP-like distribution of $D_s^+ D^*_{s0}(2317)^-$ events depicted in Fig. 6.13 is approximated with the 7$^{\text{th}}$ order Bernstein polynomial. The choice of the Bernstein polynomial over $e.g.$ Chebychev polynomial is motivated by its robustness for fits with low event count and faster minimisation flow, which might be particularly important for a potential

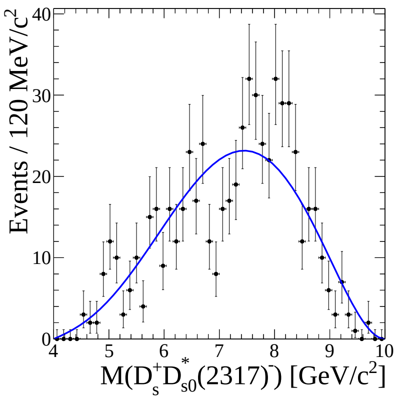

Figure 6.13: The $D_s^+ D_{s0}^*(2317)^-$ invariant mass distribution in generic MC sample. The fit is performed with Bernstein polynomial of 7$^{\text{th}}$ order.

toy MC study[4]. The observed background shape is an important result, which will be later compared to the result on data.

6.5 First study of $\mathbf{D_s^+ D_{sJ}^{(*)-}}$ events on data

6.6 Analysis of data

Finally, we apply the developed procedure over on- and off-resonance data sets to verify regularity of mass distributions and the validity of event selection. After performing reconstruction of both decay modes following the exact same procedure as in generic MC, we check the consistency of invariant mass distributions for all intermediate mesons, *e.g.* secondary D_s^- (see Fig. C.25 in App. C.2). We report a detector resolution of 6.24 ± 0.94 MeV for reconstructed D_s^- mesons on data, which agrees within 1σ with the value estimated from generic MC. We verify the ordinance of the D_s^{*-} invariant mass distribution, but do not perform a fit to it to avoid misidentification of correctly reconstructed candidates and broken signal events (see Fig. C.5 in App. C.2).

In both decay channels, we observe clear peaks, which correspond to the $D_{s0}^*(2317)^-$ and $D_{s1}(2460)^-$ resonant states. When more photons are involved in a decay chain, *i.e.* the $D_{s1}(2460)^-$ case, a higher background level is shown

[4]The latter might be necessitated, if an enhancement above the depicted phase-space-like distribution is observed on data.

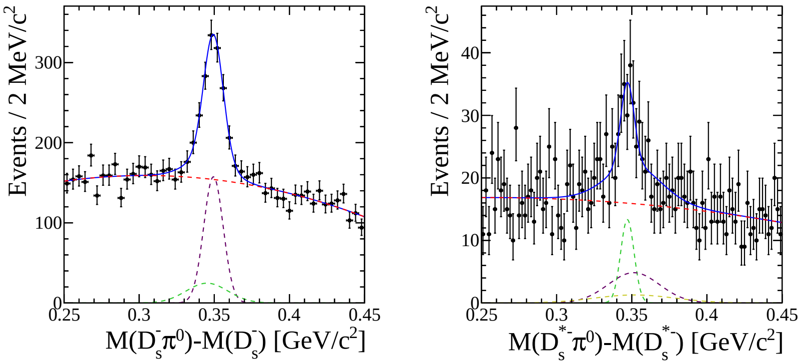

Figure 6.14: Simultaneous fit to the [left] $\Delta M(D_s^-\pi^0)$ and [right] $\Delta M(D_s^{*-}\pi^0)$ distributions on data. In the left plot, the purple line represents the true $D_{s0}^*(2317)^-$ contribution, the green line - $D_{s1}(2460)^-$ reflection. In the right plot, the green line represents the true $D_{s1}(2460)^-$ contribution, the purple line - the $D_{s0}^*(2317)$ reflection and the yellow line - the $D_{s1}(2460)^-$ broken signal. True peaks and the corresponding reflection peaks are marked in these plots with the same color to visualise cross-feed effects.

on data, as expected. We follow the simultaneous fit procedure to perform a fit to these distributions. Parameters of the peaking background are fixed to the values obtained in generic MC. The SF result is shown in Fig. 6.14, while final values of floating parameters are listed in Table 6.8. This, in particular, allows evaluating the $D_{s0}^*(2317)^-$ and $D_{s1}(2460)^-$ yields achieved with the cut-based event selection: 639 ± 71 and 75 ± 20, respectively. The reported yield highlights the lack of statistics in this analysis, which motivates the use of a multi-variable analysis approach for event classification, as described in the next section.

Topology type	μ [MeV/c^2]	σ [MeV]	Yield
True $D_{s0}^*(2317)^-$ signal	349.4 ± 0.6	6.48 ± 0.61	639 ± 71
Feed-down background	345.1 (fixed)	13.5 (fixed)	$2.870 \cdot N_2$
True $D_{s1}(2460)^-$ signal	347.1 ± 1.3	4.48 ± 1.29	75 ± 20
Feed-up background	352.0 (fixed)	13.9 (fixed)	$0.163 \cdot N_1$
$D_{s1}(2460)^-$ broad state	346.7 (fixed)	22.7 (fixed)	$0.579 \cdot N_2$

Table 6.8: Summary of the simultaneous fit result for the cut-based analysis on data.

6.7 Event classification using multi-variable analysis

The final result acquired on data, as explained in the previous section, clearly indicates the lack of statistics in this analysis. To increase the yield, an attempt to use a multi-variable analysis (MVA) approach for event classification has been employed.

Various sets of input parameters were tested for classification of $D^*_{s0}(2317)^-$ events. The information given by the correlation matrix highlights variables in the input set with strong correlations (see Fig. 6.15). These variables were studied to eliminate strongly correlating variables with negligible positive effect on the selection efficiency. The final set of input variables used for MVA selection predominantly consists of the variable employed for the cut-based selection and includes the following 9 variables:

- p^*, P_{χ^2} and χ^2 of $D^*_{s0}(2317)^-$ candidates;
- P_{χ^2} and χ^2 of secondary D^-_s candidates;
- p, P_{χ^2} and χ^2 of π^0 candidates combined into $D^*_{s0}(2317)^-$;
- $|cos\theta_H|$ of ϕ or K^* candidates;

Within the standard models implemented in TMVA, the following approaches were tested in the described configurations for the classification task:

1. Boosted decision trees (BDT):
    - 850 trees;

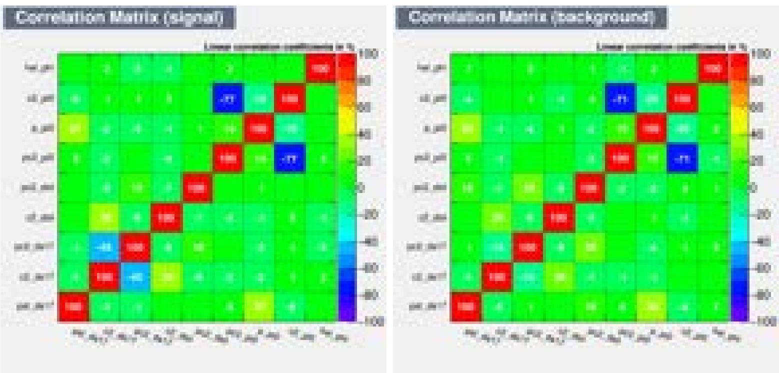

Figure 6.15: Correlation matrix for the [left] signal and [right] background events.

- The minimal percentage of training events required in a leaf node is 2%;
- Maximum depth of a decision tree is set to 3;
- *AdaBoost* boost is employed;
- Learning rate for the *AdaBoost* algorithm is set to 0.5;
- *Bagged boost* is enabled;
- Relative size of the bagged event sample to the original size of the data sample is set to 0.5;
- Gini Index separation criterion for node splitting is chosen;
- Number of grid points in the variable range used for finding the optimal selection criterion in node splitting is 20;

2. Multi-layer perceptron (MLP):
   - *tanh* neuron activation function is used;
   - Input variables are normalized to the [-1,1] interval;
   - 600 training cycles are repeated;
   - 6 nodes are used in the one-and-only hidden layer;
   - Test rate is set to 5;

3. Fisher classifier:
   - PDFs for classifier outputs are created;
   - Two-degrees spline interpolation method is used to for reference histograms;
   - The number of bins is set to 50;
   - The number of PDFs smoothing iterations is set to 10;

4. Likelihood classifier:
   - Likelihood output is transformed by the inverse sigmoid function;
   - Two-degrees spline interpolation method is used to for reference histograms;
   - The number of smoothing iterations for input histograms is set to 10;
   - The average number of events per bin is set to 50;
   - PCA input variable transformation is used.

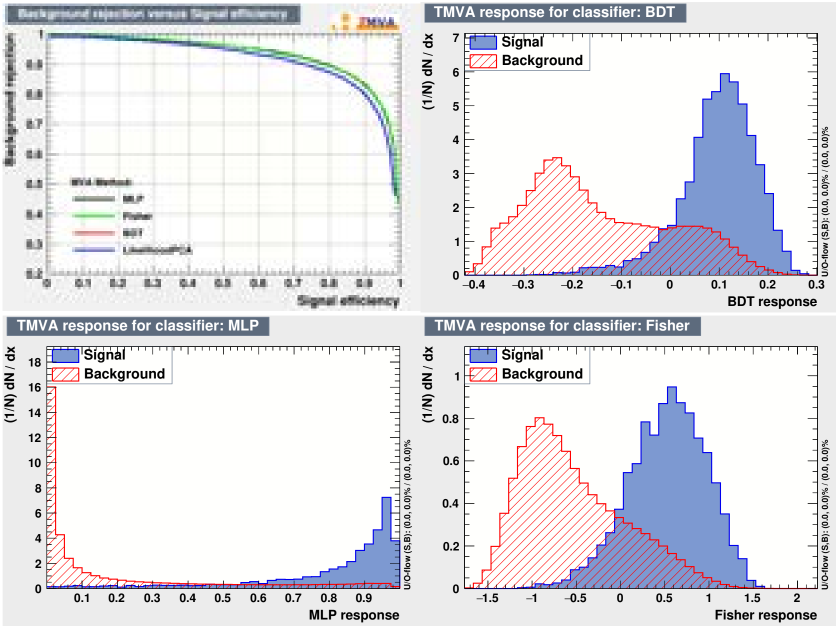

Figure 6.16: [top-left] ROC curve for BDT, MLP and Fisher architectures. The distribution of classifier responses for the[top-right] BDT, [bottom-left] MLP and [bottom-right] Fisher classifier.

The ROC curve shown in Fig. 6.16 illustrates the performance of different MVA implementations. In particular, the efficiency of the Fisher, BDT and MLP methods are similar, while the performance of the Likelihood selection is not as good as for other methods. Classifier response distributions for best-performing models are also given in Fig. 6.16. Given the comparable background rejection performance for the compared MVA approaches, we decided to proceed with the MLP architecture for the classification task, as it shows the best separation power of the response variable and features relative simplicity, stability, and flexibility of implementation.

Several reasons were considered, when choosing the MLP architecture. The number of hidden layers for the MLP is selected following the Weierstrass theorem for neural networks, which advises proceeding with a single-hidden-layer architecture for relatively simple classification tasks. The number of nodes is calculated according to a widely-used "rule of a thumb": $N^{\text{nodes}} = (N^{\text{in}} + N^{\text{out}}) \times 2/3$, where N^{in} and N^{out} denote the numbers of variables in the input and output layers – 9 and 1 for the case discussed, respectively. These guidelines define the hidden MLP architecture as

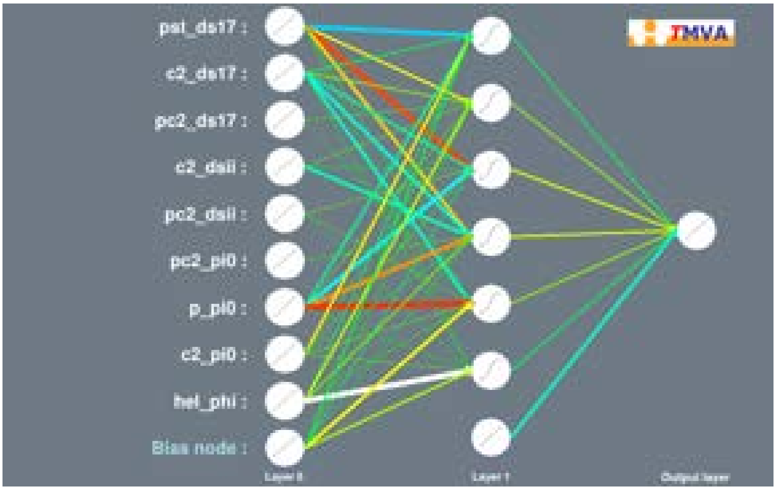

Figure 6.17: MLP architecture. The width of lines connecting nodes is proportional to the weight of each input variable in the response function.

one layer with 6 nodes. A schematic representation of this architecture is shown in Fig. 6.17. Here, lines connecting nodes tend to have different widths. This represents weights of each input parameter present in the input layer. In this way Fig. 6.17 indicates critical importance of $p^*(D^*_{s0}(2317)^-)$, $p(\pi^0)$ and $|cos\theta_H|$ parameters for the classification task, as they tend to have the largest weight in the response function.

Training and validation of the model are performed on events reconstructed from generic MC samples, where signal and background events can be distinguished on the true level. We use approximately 80% of the total number of signal events, which is 7000, and the equal number of background events for the network training. All remaining events are used for validation. The MLP training and validation flows are stable, which can be illustrated by the convergence test (see Fig. 6.18 [left]). The network provides a scalar output value of the classifier, which can be used to discriminate events. We optimise the selection criterion on it by searching for the maximum of the figure of merit defined in Eq. 6.3, which is reached for the minimum classifier output of 0.8825.

Several intermediate conclusions can be drawn at this point about the performance of the event selection with the developed MVA approach. Firstly, the highest FoM reached with the MLP selection is 24.7, while the best signal clarity that can be reached with the standard cut-based analysis is 19.1. This result clearly indicates better background rejection capability of the MLP. Secondly, the number of

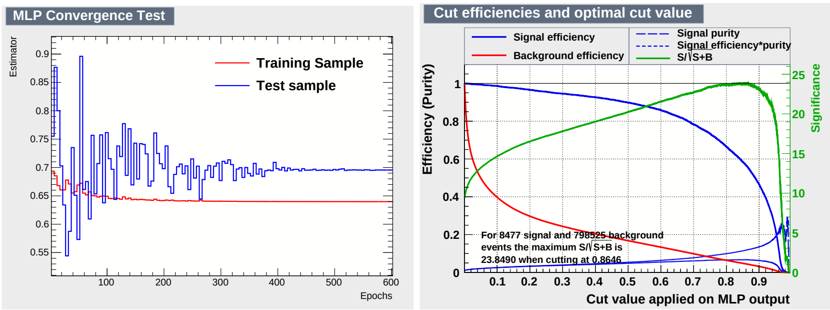

Figure 6.18: [left] The MLP convergence test. [right] The MLP classifier cut efficiency.

true $D^*_{s0}(2317)^-$ events selected using the simple cut-based selection is 4,509 $\pm$ 70, while the MVA approach preserves 4,185 $\pm$ 68 true $D^*_{s0}(2317)^-$ events. This slightly lower signal yield, though is an important intermediate result, should be treated with caution because the performance of the event classification with the MLP on data – which is the most important, after all – may differ. Lastly, we confirm that $D^*_{s0}(2317)^-$ candidates that pass MLP selection, as intended, originate from continuum events, not from $B\bar{B}$ processes. This can be illustrated by plotting the p^* distribution for selected $D^*_{s0}(2317)^-$ candidates (see Fig. C.5 in App. C.2).

We repeat a similar classification of $D_{s1}(2460)^-$ candidates reconstructed in generic MC samples. General properties of the MLP used for this case are similar to those of the architecture employed for the $D^*_{s0}(2317)^-$ event classification. Although, the $D_{s1}(2460)^-$ decay scheme contains an additional intermediate state, D_s^{*-}, and an additional photon radiated by D_s^{*-}. Therefore, the following parameters are additionally included in the MVA input layer: $p^*(D_s^{*-})$, $P_{\chi^2}(D_s^{*-})$, $\chi^2(D_s^{*-})$ and $E(\gamma)$, which consequently triggers the increase of the number of nodes in the only hidden layer from 6 to 9. We then repeat training, validation and application of the classification algorithm for $D_{s1}(2460)^-$ candidates. Similarly to the $D^*_{s0}(2317)^-$ case, a higher FoM is reached using the MLP selection compared to the simple cut-based selection: 11.69 vs. 6.33. Although, unlike for the $D^*_{s0}(2317)^-$ event selection, the number of selected true $D_{s1}(2460)^-$ candidates is increased by 30%: from 1,086 $\pm$ 35 to 1,412 $\pm$ 40.

We then proceed with the method earlier employed for the simple event selection to acquire peaking background parameters in both ΔM distributions to make simultaneous fit possible (see Figs. C.26 to C.30 in App. C.3). Fit values acquired by separating different topologies using truth-matching are summarised in Table 6.9. After fixing peaking background parameters to the updated values, we run the SF

Topology type	μ [MeV]	σ [MeV]	N
Simultaneous fit results			
True $D^*_{s0}(2317)^-$ signal	349.4 ± 0.2	5.43 ± 0.19	3,862 $\pm$ 148
Feed-down background	344.7 (fixed)	13.2 (fixed)	1.765$\cdot N_2$
True $D_{s1}(2460)^-$ signal	346.9 ± 0.3	5.95 ± 0.33	1,563 $\pm$ 76
Feed-up background	351.9 (fixed)	14.8 (fixed)	0.148$\cdot N_1$
$D_{s1}(2460)^-$ broken signal	350.8 (fixed)	20.6 (fixed)	0.256$\cdot N_2$
Results estimated by applying truth-matching requirements			
True $D^*_{s0}(2317)^-$ signal	348.9 ± 0.1	6.09 ± 0.09	4,185 $\pm$ 68
Feed-down background	344.7 ± 0.7	13.2 ± 0.7	2,491 $\pm$ 174
True $D_{s1}(2460)^-$ signal	346.7 ± 0.2	6.08 ± 0.16	1,412 $\pm$ 40
Feed-up background	351.9 ± 1.5	15.3 ± 3.5	621$\pm$ 85
$D_{s1}(2460)^-$ broken signal	350.8 ± 5.7	20.6 ± 14.5	362 $\pm$ 188

Table 6.9: Simultaneous fit results and results estimated by applying truth-matching conditions in generic MC for events classified with the MLP event classifier.

over events reconstructed in generic MC and acquire the result depicted in Fig. 6.19. Final values of simultaneous fit parameters are listed in Table 6.9. We conclude that the SF procedure is stable and delivers results that are consistent with values estimated by applying truth-matching conditions within 2σ.

Eventually, the MLP-based classification is applied to data to discriminate events reconstructed in both decay channels. Results of the simultaneous fit to distributions of events selected with the MLP share similar features with those selected with the standard cut-based procedure. Assessing the overall performance of the MLP, we report that a better signal purity is reached for both decay channels, while the $D^*_{s0}(2317)^-$ and $D_{s1}(2460)^-$ signal yields have increased by 10% and 40%, respec-

Topology type	μ [MeV]	σ [MeV]	N
True $D^*_{s0}(2317)^-$ signal	350.0 ± 0.5	6.63 ± 0.53	686 $\pm$ 62
Feed-down background	351.9 (fixed)	13.2 (fixed)	1.765$\cdot N_2$
True $D_{s1}(2460)^-$ signal	346.2 ± 1.7	6.18 ± 1.52	102 $\pm$ 26
Feed-up background	344.7 (fixed)	14.8 (fixed)	0.148$\cdot N_1$
$D_{s1}(2460)^-$ broken signal	350.8 (fixed)	20.6 (fixed)	0.256$\cdot N_2$

Table 6.10: Simultaneous fit results for events classified with the MLP on data.

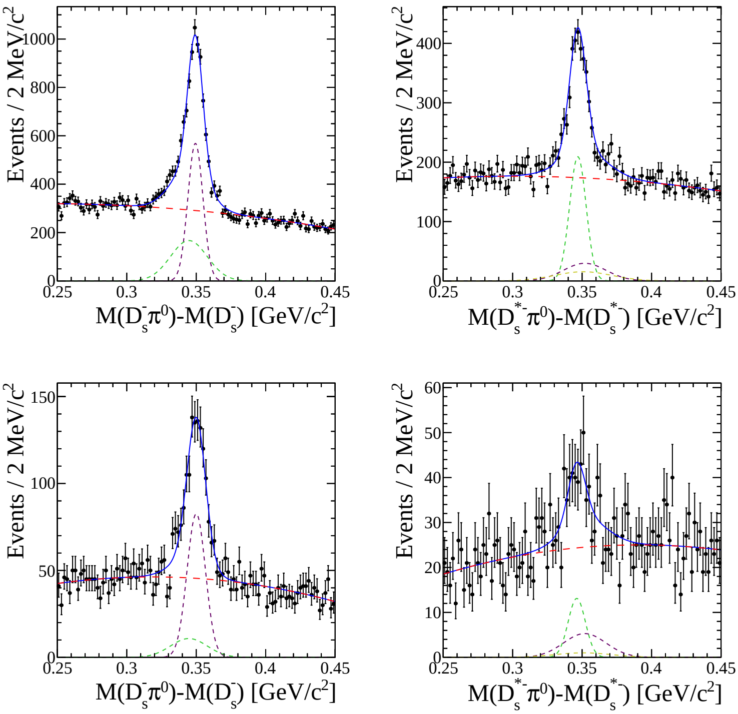

Figure 6.19: Simultaneous fit results in generic MC for events classified with the MLP: [left] $\Delta M(D_s^- \pi^0)$ distribution, [right] $\Delta M(D_s^{*-} \pi^0)$ distribution; [top] in generic MC and [bottom] on data. In the left column of plots, the purple line represents true $D_{s0}^*(2317)^-$ contribution, the green line - $D_{s1}(2460)^-$ reflection. Similarly, in the right column of plots the green line represents true $D_{s1}(2460)^-$ contribution, the purple line - $D_{s0}^*(2317)$ reflection, the yellow line - $D_{s1}(2460)^-$ broken signal. Final values of the simultaneous fit parameter are summarised in Table 6.9 and Table 6.10.

tively. The developed MVA selection preserves 52.4% of true $D_{s0}^*(2317)^-$ candidates and 62.0% of correctly reconstructed $D_{s1}(2460)^-$ signal events, while the background rejection is estimated to be 96.3% and 95.7%, respectively. These results bring us to the conclusion that, as expected, MVA show a better classification efficiency and allows increasing the signal yield, while rejecting background more effectively. Hence, it is reasonable to follow this approach, when moving to the final goal of this analysis – search for resonances in the $D_s^+ D_{s0}^*(2317)^-$ and $D_s^+ D_{s1}(2460)^-$ systems.

6.8 Study of MVA-selected $\mathbf{D_s^+ D_{sJ}^{(*)-}}$ events on data

The developed multi-variable analysis is eventually applied to select $D_s^+ D_{s0}^*(2317)^-$ and $D_s^+ D_{s1}(2460)^-$ events on data. To improve the efficiency of $D_s^+ D_{sJ}^{(*)-}$ candidate classification, the MLP is further supplemented with kinematic and vertex variables of the primary D_s^+ meson. In consequence, this necessitates the increase of the number of nodes in the network architecture. All other MLP settings are invariably inherited from the previous section. Optimisation of the MLP response selection criterion with the aforementioned FoM metric appears to be inefficient due to the low number of truth-matched $D_s^+ D_{sJ}^{(*)-}$ events in generic MC. Therefore, a threshold value is determined manually, relying on the linear classifier distribution for signal and background events (see Fig. C.8 in App. C.2). A value of 0.2 is used for this purpose. Additionally, we provide plots depicting correlation matrices and results of the convergence test (see Figs. C.6 and C.7 in App. C.2).

The $D_s^+ D_{s0}^*(2317)^-$ and $D_s^+ D_{s1}(2460)^-$ invariant mass distributions for events that pass MLP selection on data are depicted in Fig. 6.20. Both distributions appear to be PHSP-like, no sign of a resonant structure is observed. We therefore perform a fit to these distributions with the 7^{th} order Bernstein polynomial, which was earlier used to approximate the same distributions in generic MC. The scaled-down distribution of events selected in generic MC illustrated in Fig. 6.20 is in reasonable agreement with the fit shape, illustrating the validity of the PHSP approximation.

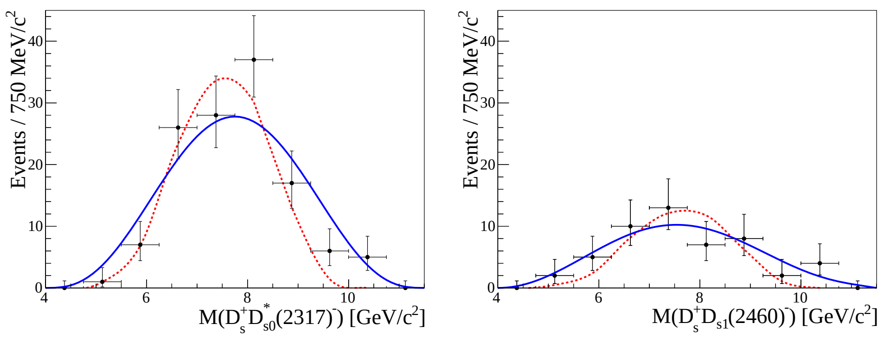

Figure 6.20: The [left] $D_s^+ D_{s0}^*(2317)^-$ and [right] $D_s^+ D_{s1}(2460)^-$ invariant mass distributions in generic MC (red dotted line) and data (black points). The fit to data is performed using the 7^{th} order Bernstein polynomial and is depicted with a blue continuous line.

6.9 Measurements of resonance properties

The $\Delta M(D_s^-\pi^0)$ and $\Delta M(D_s^{*-}\pi^0)$ distributions in $e^+e^- \to D_s^+ D_{s0}^*(2317)^-$ and $e^+e^- \to D_s^+ D_{s1}(2460)^-$ inclusive processes, respectively, are shown in Fig. 6.19. The result of the simultaneous fit to these distribution is summarised Table 6.10.

We find that the mass difference for the $D_{s0}^*(2317)^-$ meson is quantified as 350.0 $\pm$ 0.5 (stat.) $\pm$ 0.1 (syst.) MeV/c^2. For comparison, the PDG world average reports 349.4 $\pm$ 0.5 MeV/c^2. For the $D_{s1}(2460)^-$ meson, we have found 346.2 $\pm$ 1.7 (stat.) $\pm$ 1.4 (syst.) MeV/c^2, while the value reported by the PDG is 347.3 $\pm$ 0.7 MeV/c^2. Both results are also in reasonable agreement with the former Belle study [202], which quotes $\Delta M(D_s^-\pi^0)$ = 348.7 $\pm$ 0.5 (stat.) $\pm$ 0.7 (syst.) MeV/c^2 and $\Delta M(D_s^{*-}\pi^0)$ = 344.1 $\pm$ 1.3 (stat.) $\pm$ 1.1 (syst.) MeV/c^2. Evaluating systematic errors for these measurements is not trivial, since we are not measuring a mass but a mass difference. Therefore, most systematics cancel each other. We follow a conservative approach, which considers the PDF systematics only, estimated by varying fitting parameters by $\pm 1\sigma$. When evaluated in this way, the systematic uncertainty on $\Delta M(D_s^-\pi^0)$ is significantly improved compared to the earlier Belle analysis [202], while the error on $\Delta M(D_s^{*-}\pi^0)$ is compatible.

Resolution measured for $\Delta M(D_s^-\pi^0)$ and $\Delta M(D_s^{*-}\pi^0)$ distributions in data are 6.63 $\pm$ 0.53 MeV/c^2 and 6.18 $\pm$ 1.52 MeV/c^2, respectively. For comparison, a former Belle analysis in the continuum performed on 86.9 fb^{-1}, where only one $c\bar{s}$-meson was involved, delivered 7.6 $\pm$ 0.5 MeV/c^2 and 5.8 $\pm$ 1.3 MeV/c^2, respectively [202]. This indicates a clear improvement of the mass resolution in the reported analysis. Meanwhile, the resolution of mass difference distributions in generic MC are 5.43 $\pm$ 0.19 MeV/c^2 and 5.95 $\pm$ 0.33 MeV/c^2, respectively, which confirms good data-MC agreement.

We therefore set upper limits on intrinsic widths of the $D_{s0}^*(2317)^-$ and $D_{s1}(2460)^-$ mesons by performing a likelihood scan. A likelihood value is calculated for a simultaneous fit to $\Delta M(D_s^-\pi^0)$ and $\Delta M(D_s^{*-}\pi^0)$ distributions performed with a slightly modified model. It features the convolution of the Gaussian PDF describing the scanned signal component, parameters of which are fixed to values acquired in generic MC, with the Breit-Wigner function, which accounts for the intrinsic width of the resonance. The intrinsic width parameter is fixed for each individual fit to a discrete value in the scan range. Parameters of all other fit model components are also fixed to values acquired in generic MC, while the only fluctuating parameter is the signal yield of the meson, which width is being scanned. Using the resulting set of likelihood values, the exponentiated difference to the maximum likelihood value reached across the scanned range is calculated and plotted, as shown in Fig. 6.21. The UL at a fixed confidence level (CL) is calculated by integrating the area under the likelihood curve and searching for the $[0, \Gamma^{\text{UL}}]$ interval, which contains the corresponding fraction of the total area. Result of the likelihood scans are quantifies as following:

$$\begin{aligned} \Gamma(D_{s0}^{*}(2317)^{-}) &< 4.07 \text{ MeV at 95\% CL} \\ \Gamma(D_{s1}(2460)^{-}) &< 13.4 \text{ MeV at 95\% CL} \end{aligned} \tag{6.6}$$

Commenting on likelihood lineshapes illustrates Fig. 6.21, the difference between the $D_{s0}^{*}(2317)^{-}$ and $D_{s1}(2460)^{-}$ cases can be explained by the different degree of the data-MC agreement between the two. While resolutions of $D_{s1}(2460)^{-}$ mass in generic MC and data are numerically close, these values feature larger difference between measured means for $D_{s0}^{*}(2317)^{-}$. This explains the behaviour, when a fit is favouring the non-zero intrinsic width of $D_{s0}^{*}(2317)^{-}$ for the Voigt convolution. Width UL values reported in Eq. 6.6 clearly illustrated the lack of statistics, as they are – to different extent – not competitive to world-best measurements expressed as: $\Gamma(D_{s0}^{*}(2317)^{-})$ < 3.8 MeV and $\Gamma(D_{s1}(2460)^{-})$ < 3.5 MeV at 95% CL [104].

Finally, using the acquired $D_{s0}^{*}(2317)^{-}$ and $D_{s1}(2460)^{-}$ yields, we also calculate the ratio of production rates of these two mesons in the continuum, weighted with the corresponding branching fractions:

$$\begin{aligned} &\frac{\mathcal{B}(D_{s1}(2460)^{-} \to D_{s}^{*-}\pi^{0})}{\mathcal{B}(D_{s0}^{*}(2317)^{-} \to D_{s}^{-}\pi^{0})} \times \frac{\sigma(D_{s1}(2460)^{-})}{\sigma(D_{s0}^{*}(2317)^{-})} \\ &\qquad = 0.26 \pm 0.07(\text{stat}) \pm 0.03(\text{syst}), \end{aligned} \tag{6.7}$$

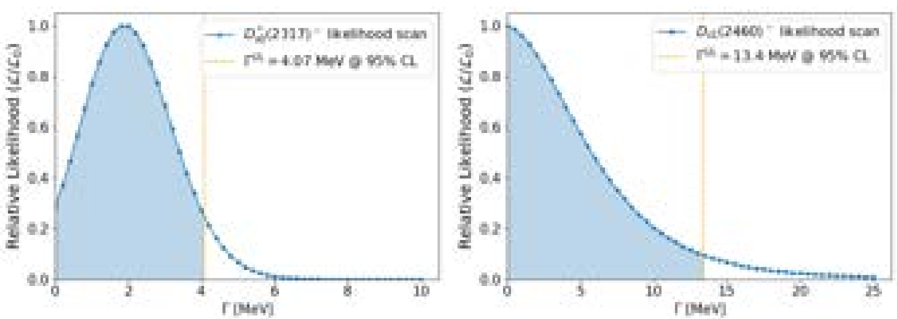

Figure 6.21: The [left] $D_{s0}^{*}(2317)^{-}$ and [right] $D_{s1}(2460)^{-}$ width UL likelihood scan. The right limit of the $[0, \Gamma^{\text{UL}}]$ interval is illustrated with a vertical dashed line and quantified in the legend.

Charged tracks	From secondary D_s^- K^+	K^-	$\pi^\pm$	From primary D_s^+ K^+	K^-	$\pi^\pm$
SVD1	1.40	1.37	0.69	1.42	1.61	0.73
SVD2	1.57	1.34	0.84	1.56	1.56	0.86
Weighted	1.53	1.35	0.81	1.53	1.57	0.83
Final uncertainty for all tracks: 3.21%						

Table 6.11: Systematic uncertainties for the charged track identification.

where the statistical uncertainty is obtained by error propagation, while the systematic uncertainty results from adding in quadrature systematic uncertainties associated with each decay channel, as reported in Table 6.13.

The result reported in Eq. 6.7 is in agreement with the former Belle publication [202]. However, according to simple arguments based on production cross-sections of 1^+ and 0^+ states, one would expect the ratio to be three, $i.e.$ 10 times larger than the experimental measurements [226]. This prediction is motivated by the following considerations. The first term in Eq. 4, related to branching fractions should be equal to unity [226]. As per the second term, according to the Breit-Wigner theory for cross-section calculations, if phase-space differences are neglected, each cross-section should be weighted with a factor $2J + 1$, where $J = 0$ for the $D_{s0}^*(2317)^-$ and $J = 1$ for the $D_{s1}(2460)^-$. Thus, our measured cross-section ratio is approximately factor 10 lower than predicted and is inconsistent with a chiral multiplet.

6.10 Systematic uncertainties

In this section, systematic uncertainties of cross-section UL measurements are estimated. Expected sources of systematic uncertainties are described individually and calculated below.

The PID group studied systematic uncertainties for charged track identification in an inclusive D^* sample [227], which are used for the reported analysis. Importantly, the SVD underwent significant upgrades during the experiment, leading to discrepancies in systematic uncertainties between the old SVD1 and new SVD2 (see Table 6.11). To account for this, we apply weights of 0.227 and 0.773 to reflect fractions of data accumulated with each SVD generation. We then calculate the square root of weighted systematic errors for individual tracks summed in quadrature to obtain the final systematic uncertainty for the charged track identification: 3.21%.

The systematic uncertainty for the charged track reconstruction has been earlier studied for partially reconstructed $D^{*+} \to D^0(\to K_s^0(\to \pi^+\pi^-)\pi^+\pi^-)\pi$ decays with high-p_T tracks ($p_T > 200$ MeV/c) [228]. Eventually, the systematic uncertainty for each track is estimated to be 0.35%. Considering the correlation between reconstructed tracks, their respective uncertainties are linearly added [229]. This yields the final systematic uncertainty for 6 charged tracks equal to 2.1%.

The total reconstruction efficiency is the product of two values: $\varepsilon^{\text{tot}} = \varepsilon^{\text{pre}} \cdot \varepsilon^{\text{post}}$. They arise from a two-step selection: event pre-selection performed in signal MC by applying selection criteria described in Sec. 6.3.2, and the post-selection performed in generic MC by using an MLP-based approach – each denoted as ε^{pre} and $\varepsilon^{\text{post}}$, respectively. The later, in particular, includes kinematic variables, such as p^*, which feature more reliable distributions in generic MC. The independence of all variables involved in the total efficiency calculation was carefully checked. Hence, the factorisation of ε^{tot} is a good approximation. The final efficiency are quantified as: $(4.23 \pm 0.34) \cdot 10^{-3}$ and $(2.08 \pm 0.47) \cdot 10^{-3}$, for the decays involving $D_{s0}^*(2317)^-$ and $D_{s1}(2460)^-$, respectively.

Following the idea of Poissonian treatment of error measurements, the systematic error associated with the absolute MC statistics can be evaluated as:

$$\Delta\varepsilon = \sqrt{\frac{\varepsilon(1-\varepsilon)}{N}} \tag{6.8}$$

where ε is the reconstruction efficiency (ε^{pre} in our case), and N is the total number of simulated signal Monte-Carlo events. Eq. 6.8 yields relative errors for the $e^+e^- \to D_s^+ D_{s0}^*(2317)^-$ and $e^+e^- \to D_s^+ D_{s1}(2460)^-$ inclusive decay channels of 1.86% and 2.42%, respectively, for one million MC signal events generated per sample.

The relative error of secondary decays branching fractions is calculated as:

$$\delta = \frac{\sum_{ij} \varepsilon_{ij}(\Delta Br_i Br_j + Br_i \Delta Br_j)}{\sum_{ij}(\varepsilon_{ij} Br_i Br_j)} \tag{6.9}$$

where Br_i and Br_j are branching fractions of the considered decay modes of primary and secondary $D_s^{\pm}$ mesons, ΔBr_i and ΔBr_j are their respective uncertainties and ε_{ij} is the reconstruction efficiency of those modes. As such, uncertainties of secondary decays' branching fractions are 5.83% and 5.62% for decay channels involving $D_{s0}^*(2317)^-$ and $D_{s1}(2460)^-$, respectively.

Systematic uncertainties associated with the background modelling in $D_s^+ D_{sJ}^{(*)-}$ invariant mass distributions is estimated by varying the order of the Bernstein polynomial utilised to perform the fit by +1 or -1. We do not consider higher/lower orders because such fit functions clearly either do not approximate invariant mass

Meson	ε_{MC}	$\varepsilon_{\text{data}}$	$\eta = \frac{\varepsilon_{\text{MC}}}{\varepsilon_{\text{data}}}$	δ [%]
π^0	0.883±0.011	0.877±0.025	1.007±0.014	3.1%
ϕ	0.885±0.008	0.942±0.009	0.939±0.014	1.4%
$K^*(892)$	0.757±0.020	0.781±0.029	1.020±0.035	3.5%
D_s^-	0.836±0.009	0.915±0.019	0.914±0.027	2.7%
D_s^{*-}	0.824±0.013	0.780±0.043	1.056±0.055	5.5%

Table 6.12: Correction factors for the mass selection imposed on intermediate resonances and the corresponding systematic uncertainties.

distributions under study well enough, or overfit them. The fit goodness (FCN) is then recorded for each fit, and the quadrature sum of its deviations from the goodness of the optimal fit – 7^{th} order Bernstein polynomial – is taken as the systematic error of background modelling. It takes values of 1.0% and 1.2% for the considered decay channels.

As explained in Sec. 6.3.2, a tight mass selection is imposed on intermediate mesons to eliminate background and, at the same time, to preserve the highest reconstruction efficiency possible. A dedicated investigation confirms that no peaking background is observed for invariant mass distributions of intermediate resonances. Although, a discrepancy between signal MC and data is always present, which can be explained by modelling imperfection. To preserve consistency between signal MC and data, a correction factor to the mass resolution is introduced (see Table 6.12). It is calculated as $\eta = \varepsilon_{\text{MC}}/\varepsilon_{\text{data}}$ (see 4$^{\text{th}}$ column in Table 6.12), where ε_{MC} and $\varepsilon_{\text{data}}$ are mass selection efficiencies estimated in signal MC and data, and each ε is calculated as a ratio of the number of signal events falling into the assigned signal region of a particular secondary meson over the total number of signal events. These values are given in 2$^{\text{nd}}$ and 3$^{\text{rd}}$ columns of Table 6.12. Systematic uncertainties related to these correction factors are calculated for all the secondary mesons to which a mass selection is applied. These individual errors are further added to the total systematic uncertainty in quadrature.

Commenting on results reported in Table 6.12, the reason for the discrepancy in D_s^- invariant mass resolution (see Tables C.8 and C.19 in App. C.2) can be explained by the way how signal MC was generated: the considered decay channels are equally weighted in signal MC, which is not the case for generic MC and data. This is the reason why a wider contribution in the D_s^- invariant mass distribution (see Figs. C.16 and C.25 in App. C.2) appears to be more significant on data and smears the weighted width. Additional smearing to the D_s^- invariant mass is introduced

Contribution	Value for a decay channel including $D_{s0}^{*}(2317)^{-}$ [%]	$D_{s1}(2460)^{-}$ [%]
Charged tracks identification	3.21	3.21
Track reconstruction	2.10	2.10
MC statistics	1.82	2.42
Integrated luminosity	1.40	1.40
π^0 reconstruction	2.00	2.00
γ reconstruction	-	2.30
Secondary BF	5.83	5.62
Background fit PDF order	1.03	1.23
Mass cuts on secondary particles	5.58	7.80
TOTAL	9.50	11.22

Table 6.13: Summary of systematic uncertainties for decay channels including $D_{s0}^{*}(2317)^{-}$ and $D_{s1}(2460)^{-}$.

by the imperfection of low-momentum tracks reconstruction, which exhibits in the form of a heavy left tail in the distribution depicted in Fig. C.25 in App. C.2. These factors collectively lead to the discrepancy of the mass resolution between MC and data quantified in Table 6.12.

There are several other contributions that are commonly included in the total systematic uncertainty. As such, they are precisely-estimated for the Belle environment and can be taken for granted. In particular, the systematic uncertainty for the total luminosity used for the study of data is estimated to be 1.4% [230]. The γ detection efficiency is 2% per each photon (there is only one photon in the $D_s^+ D_{s1}(2460)^-$ inclusive decay channel, which is radiated by D_s^{*-}). The error of π^0 reconstruction efficiency is 2.3% according to a study of the $\tau \to \pi\pi^0\nu_\tau$ control sample [231].

As previously mentioned, many tests are performed to the signal MC generation model, each with different masses and beam energy settings. Therefore, the uncertainty related to the model is not included in the total systematic uncertainty. Theoretically, we know too little to nothing about this decay chain, so it makes little sense to account for systematic uncertainties associated with the used MC model by using another imperfect model.

Systematic errors calculated for all the contributing sources are summarised in Table 6.13. The square root of the quadrature sum of all contributions is calculated to acquire the total systematic uncertainty. The final values are 9.50% and 11.22% for decay channels involving $D_{s0}^{*}(2317)^{-}$ and $D_{s1}(2460)^{-}$, respectively.

6.11 Cross-section upper limit calculations

As discussed in the introduction (see Sec. 6.2), one of the main targets for the current analysis is to confirm the exotic states reported by LHCb [166, 188]. No significant signal is observed in $D_s^+ D_{sJ}^{(*)-}$ systems in our analysis, as illustrated by Fig. 6.20. However, upper limits on cross-sections of the corresponding processes can be set. These are reported in this section. Reminding of the considerations elaborated on in Sec. 6.1, the current analysis – considering mass thresholds and combined quantum numbers - has access to search for $X(4274)$ and $X(4685)$ in the $D_s^+ D_{s0}^*(2317)^-$ system, and for $X(4500)$, $X(4630)$ and $X(4700)$ in $D_s^+ D_{s1}(2460)^-$. We therefore calculate cross-section upper limits for these X states using the values reported by Ref. [188], which are summarised in Table 6.14.

Contribution	J^P	M_0 [MeV]	Γ_0 [MeV]	Significance [$\times\sigma$]
$X(4274)$	1^+	$4295 \pm 4^{+4}_{-6}$	$53 \pm 5 \pm 5$	18 (18)
$X(4685)$	1^+	$4684 \pm 7^{+13}_{-16}$	$126 \pm 15^{+37}_{-41}$	15 (15)
$X(4630)$	1^-	$4626 \pm 16^{+18}_{-110}$	$174 \pm 27^{+134}_{-73}$	5.5 (5.7)
$X(4500)$	0^+	$4474 \pm 3 \pm 3$	$77 \pm 6 \pm^{+10}_{-8}$	20 (20)
$X(4700)$	0^+	$4694 \pm 4^{+16}_{-3}$	$87 \pm 8^{+16}_{-6}$	17 (18)

Table 6.14: Results reported by Ref. [188] on properties of X states observed in the $J/\psi\phi$ system. Only the resonances accessible in the scope of the current analysis are listed. The reported global (local) significance is given in the last column.

Two approaches are considered for the upper limit calculation on the signal yield, which is essential for determining the upper limit on the product of the Born cross-section and branching fractions: the asymptotic and Feldman-Cousins methods.

6.11.1 Asymptotic method

According to the asymptotic method[5], to estimate the UL on the number of signal events at 90% CL the following equation should be solved:

$$\frac{\int_0^{N^{90\%}} \mathcal{L}(x)dx}{\int_0^{+\infty} \mathcal{L}(x)dx} = 0.9, \tag{6.10}$$

where $\mathcal{L}(x)$ is the maximised likelihood for data and $N^{90\%}$ is the yield at 90% CL.

[5]Similarly to the width UL calculation described in Sec. 6.9

Here, we shortly describe the practical implementation of the asymptotic method. Firstly, a null fit is performed to a $D_s^+ D_{sJ}^{(*)-}$ invariant mass distribution with a model that includes a relativistic Breit-Wigner and a Bernstein polynomial. Parameters of the Bernstein polynomial are floating in the full range of [0,1][6], while the mean value, width and degrees of freedom[7] of relativistic Breit-Wigner used to describe the signal component are fixed to values taken from Ref. [188] (see Table 6.14). The optimal fit to the $D_s^+ D_{sJ}^{(*)-}$ invariant mass distribution is performed with the number of events in the Breit-Wigner (N_{sig}) floating. The fit yields the maximum likelihood value, noted as $\mathcal{L}_0$, which describes the highest fit goodness that can be achieved with the given model.

A likelihood scan is performed by carrying out a sequence of fits with the parameter N_{sig} set to integer values in the scan interval – [1, 10] for the example given below. For each iteration, the FCN value of the optimal fit is recorded. The acquired $\mathcal{L}(N_{\text{sig}})$ evolution is then rescaled as following:

$$\Delta L = e^{\mathcal{L}(N_{\text{sig}})-\mathcal{L}_0} \tag{6.11}$$

At this stage, systematic uncertainties must be incorporated. We do that by performing the convolution of the existing ΔL function with a Gaussian, which has a width proportional to the value of the systematic uncertainty. This effectively contributes to the existing ΔL function with the following adding:

$$\Delta(\Delta L) = \frac{\Delta\mathcal{L}_j \cdot \mathcal{L}_j}{\sqrt{2\pi\varepsilon_{\text{syst}} N_j^{\text{sig}}}} \cdot e^{-\frac{1}{2}\left(\frac{\Delta N_j^{\text{sig}}}{\varepsilon_{\text{syst}} N_j^{\text{sig}}}\right)^2} \tag{6.12}$$

where N_j^{sig} is the j-th fitted yield ($j = \overline{1, 10}$), $\Delta N_j^{\text{sig}} = N_j^{\text{sig}} - N_{j-1}^{\text{sig}}$ is the fitted yield increment, $\mathcal{L}_j$ is the fit goodness reached with the fixed value N_j^{sig}, $\Delta\mathcal{L}_j = \mathcal{L}_j - \mathcal{L}_{j-1}$ is likelihood increment and $\varepsilon_{\text{syst}}$ the total systematic error, as calculated in Sec. 6.10.

The updated $\Delta\mathcal{L}(N_{\text{sig}})$ scatter plot obtained in this way (*e.g.* see Fig. 6.22) is then numerically integrated across [0,10] and [0,$N^{90\%}$] intervals to determine the endpoint value at which the desired ratio is reached (see Eq. 6.10). The determined $N^{90\%}$ value is considered to be the upper limit on the fitted yield at 90% confidence level. We therefore follow this approach to numerically estimate ULs on the number of fitted events for each of the X resonances listed in Table 6.14.

[6]Parameters of the Bernstein polynomial are mathematically constrained in the [0,1] interval.
[7]These are defined by the assigned quantum numbers.

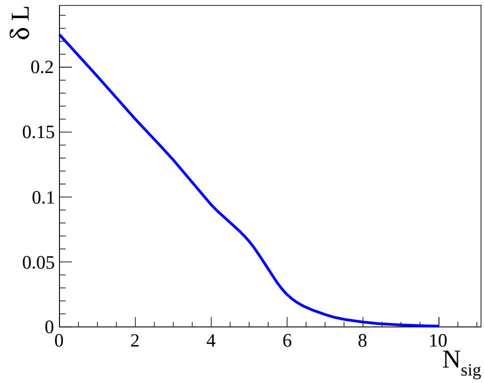

Figure 6.22: Example of the likelihood scan for $X(4700)$.

In order to include systematic uncertainties associated with parameters fixed to values reported by Ref. [188], we repeat UL calculations with these parameters, namely mass mean and width, individually varied by $\pm1\sigma$ from respective central values. Deviations from original UL values are then added in quadrature to estimate an additional contribution to the final systematic error. It appears to be negligible for all states ULs are set for (below 0.003%). Final N^{UL} values are reported in Table 6.15.

6.11.2 Feldman-Cousins method

A widely used Feldman-Cousins method provides reliable upper limit estimates on the number of signal events, especially for cases, where statistics is limited (which is relevant for the current analysis). The most straightforward way to perform UL calculations using the FC method is to exploit a *TFeldmanCousins()* class available in ROOT. It requires only two values as input: the number of observed events and expected background events (the values already estimated for the asymptotic method). The FC method shows stable performance with these given values, and provides trustworthy results (see Table 6.15). The problem with using the *TFeldmanCousins()* class is that it does not allow accounting for systematic uncertainties.

We therefore develop a manual approach based on the counting model to incorporate systematic uncertainties. The event distribution model is configured as a first step - the convolution of the Poisson and Gaussian functions. The numbers of observed and expected background events are calculated following the way described for the asymptotic method. Lastly, the *StandardHypoTestInvDemo()* ROOT method is used to estimate an UL based on the p-value scan with the following scan parameters, which reproduce the original FC method, as explained in Ref. [232]:

- Frequentist (Neumann) calculator;
- Two-sided profile likelihood test statistics;
- CLs is disabled [8];
- 10k toy MC samples generated (pseudo experiments).

A manual implementation of the counting model allows enabling or disabling systematic uncertainties in the UL calculator by just changing the respective flag. We first compare results of the developed counting model with results acquired with the standard *TFeldmanCousins()* class (see Table 6.15, no systematic uncertainties for both methods). We found these two sets of results being in very good agreement, which proves the validity of the developed manual counting model.

We then proceed with including systematic errors in the upper limit calculation. But first, an additional contribution derived from parameters of the considered X states has to be introduced, exactly as it is done for the asymptotic method (see Sec. 6.11.1). In contrast to the asymptotic method, these contributions appear to be more significant, ranging from 2.4% to 5.5%. Global systematic uncertainties (see Sec. 6.10), the statistical error of background estimate, and the aforementioned "LHCb systematics" are added in quadrature to deliver total uncertainty (calculated for each state, individually). These values are reported in Table 6.15.

Unfortunately, when complete systematic uncertainties are included in the counting model, it does not perform as expected, and many behaviour artifacts are observed. We therefore conclude that this approach derives unphysical results and decided to proceed differently. Namely, ULs are estimated for each state with three different parameters of the expected background: the central value and central value plus/minus the error (b, $b + \Delta b$ and $b - \Delta b$). The most conservative UL value is assigned for each case. Final results are reported in Table 6.15.

6.11.3 Comparison of the two methods

Comparing the methods described above, we conclude that the manual implementation of the FC-like counting model appears to be the most trustworthy. In contrast, the asymptotic method seems insensitive to changes in low-multiplicity counts. Although, the FC method (both implemented with a standard class and with

[8] The scan is performed over the p_{s+b} value, not the p_{s+b}/p_b ratio (as for the CLs method), where p_{s+b} is the quantified p-value for the signal and background assumptions, and p_b is the p-value with background assumption only

Mode	Tot. err. [%]	N^{UL} with a method Asymptotic	FC	CM	$\sigma^{UL} \times \mathcal{B}(X \to D_s D_{sJ}^{(*)})$ [fb]
$e^+e^- \to X(4274)A$	13.3	4.77	2.42	2.45	86.6
$e^+e^- \to X(4685)A$	14.1	4.78	1.91	2.04	71.9
$e^+e^- \to X(4630)A$	18.3	4.94	1.95	2.05	161.0
$e^+e^- \to X(4500)A$	18.0	4.81	2.32	2.34	183.5
$e^+e^- \to X(4700)A$	18.7	4.92	2.16	2.18	171.2

Table 6.15: Results of N^{UL} and $\sigma^{UL} \times \mathcal{B}(X \to D_s D_{sJ}^{(*)})$ calculation for the considered processes performed with different methods.

a counting model) does not allow incorporating systematic uncertainties directly, and an alternative approach to their treatment is required. Such an approach has been found, and eventually systematic uncertainties are considered for both methods. Finally, we chose the counting model for the calculation of final results.

As such, Born cross-section ULs can be estimated as:

$$\sigma^{\text{UL}} = \frac{N^{\text{UL}} \times |1 - \Pi|^2}{\mathcal{L} \times \Sigma_{ij} \varepsilon^*_{ij} \mathcal{B}_i \mathcal{B}_j \times (1+\delta)_{\text{ISR}}}, \tag{6.13}$$

where N^{UL} is the UL on the yield estimated with the counting model described above; $|1 - \Pi|^2$ is the vacuum-polarisation correction factor[9]; $\mathcal{L}$ is the total integrated luminosity [230]; $\varepsilon^*_{ij} = \varepsilon_{ij}/\eta^i \eta^j \eta^{\pi^0} \eta^{D_s}$ or $\varepsilon_{ij}/\eta^i \eta^j \eta^{\pi^0} \eta^{D_s} \eta^{D^*_s}$ is the reconstruction efficiency corrected for the data/MC discrepancy as described in Sec. 6.10 for a decay channel involving $D^*_{s0}(2317)^-$ or $D_{s1}(2460)^-$, respectively; $\mathcal{B}_i$ and $\mathcal{B}_j$ are branching fractions of primary and secondary $D_s^\pm$ mesons; and $(1+\delta)_{\text{ISR}}$ is the ISR correction factor. The radiative and vacuum-polarisation correction factors strongly depend on the CM energy of the reconstructed data sample. Since the reported analysis struggles with low event multiplicity, slicing the sample into separate energy points to account for individual correction factors would make the background parametrisation and further Born cross-section calculation challenging, if not impossible. We therefore apply these correction factors relying on values calculated at the CM energy of the $\Upsilon(4S)$ resonance: $(1+\delta)_{\text{ISR}} = 0.657$ and $|1-\Pi|^2 = 0.930$, as per Ref. [235]. It is a reasonable approximation, considering that the $\Upsilon(4S)$ collisions make up about 80% of the total Belle data sample.

[9] $\Pi(q)$ is the vacuum-polarisation function, depending on the transfer momentum [233, 234]

Chapter 7

Summary and Outlook

7.1 Study of indirect SR in the PXD

Minimising background contamination and its online monitoring are crucial for reliable data taking and longevity of the PXD. To reflect changes in the beam pipe design, the Photon Monitor has been revised as described in this thesis.

In brief,

- We have studied patterns of the indirect SR radiation contamination across various runs with different beam conditions, particularly β_Y^* and beam currents, and compared them to those before LS1.

- To account for the observed evolution of the photon radiation pattern, we have updated definitions of reference and measurement areas in L1 of the PXD to target regions most affected by the indirect SR.

- The photon rate and photon fraction PVs calculated across these new areas were tested using Phase 3 of Run 2 data and compared to those defined previously. The test demonstrated a clear improvement in online photon radiation monitoring.

- An analysis of Phase 3 of Run 2 data for selected “good” runs was performed to visualise the correlation between photon contamination and beam currents. This illustrated a clear upward trend in the photon fraction PV, which – with the new area definitions – occasionally exceeds the currently set limit.

The observed evolution of the photon fraction underscores the importance of online monitoring for the indirect SR. To this end, updated PVs will be communicated to the BCG shifter in the SuperKEKB CR for real-time monitoring. The localized pattern of the photon contamination also raises concerns about the potentially harmful impact of the concentrated radiation on the PXD hardware, which deserves to be studied separately. Earlier efforts by the SuperKEKB team to adjust the beam orbit partially mitigated the localized contamination by smearing it more evenly across L1 modules. Although similar countermeasures have not been implemented since machine operations resumed after LS1, they could be reconsidered, if stability of the machine operation improves in future runs.

7.2 Search for resonant structures with $c\bar{c}s\bar{s}$ quark content

In this work, we have, for the first time, meticulously carried out a search for resonant states with $c\bar{c}s\bar{s}$ quark content in the $e^+e^- \to D_s^+ D_{s0}^*(2317)^-$ and $e^+e^- \to D_s^+ D_{s1}(2460)^-$ inclusive processes in the continuum. Although no signal evidence was found in the decay modes under examination, results reported in this thesis, namely cross-section upper-limits and other sideline results discussed below, are of significant relevance, as they provide a solid foundation for further discussion and exploration by offering crucial insights into properties of heavy-light systems.

The only feasible Belle reference for the current analysis is the search for exotic $c\bar{c}s\bar{s}$ candidates in an ISR process reported in Refs. [196, 197]. It delivers cross-section measurements that are of the same order of magnitude as those estimated in this study, $i.e.$ in the $[120 - 240]$ fb range. The LHCb experiment has significantly impacted the search for $X_{c\bar{c}s\bar{s}}$ states through charged B meson decays by performing two consecutive searches for exotic candidates in the $B^- \to J/\psi \phi K^-$ decay channel in a highly competitive dataset. In view of these results, it is crucial to obtain confirmation of the states observed by LHCb from other experiments in different production mechanisms, not only in B decays. The Belle experiment and its upgrade, Belle II, therefore offer unique opportunities for searching for $X_{c\bar{c}s\bar{s}}$ states via ISR and in the continuum. The size of the Belle II dataset is expected to match the one of Belle by mid-2026. The cross-section upper-limits reported in this thesis highlights the importance of the data sample size. Hence, revisiting the analysis, when a substantially larger Belle II data set is available might be feasible.

Precise mass splitting measurements

We have also performed a fit to distributions of the $D_{s0}^*(2317)^-$ and $D_{s1}(2460)^-$ mass differences to their primary decay products. As discussed in the Introduction (see Chapter 5), $D_{s0}^*(2317)^-$ and $D_{s1}(2460)^-$ are considered to be the first chiral partners of the same heavy-light system. The spontaneous breaking of the chiral symmetry in the QCD leads to a mass term that elevates the (0^+, 1^+) above the (0^-, 1^-) doublet by an amount equal to ΔM [226]. Chiral invariance implies that ΔM satisfies the Goldberger-Treiman relation, $i.e.$ $\Delta M = g_\pi f_\pi$. The value of g_π represents the pure pionic coupling of a constituent chiral quark, such as the constant in the Georgi-Manohar model [236]. The well-known and simpler constituent-quark model of a nucleon would predict the constant $g_{NN\pi} = 3g_\pi$. The nucleon mass is the analog of ΔM for the nucleon system (m_N). It satisfies the standard Goldberger-Treiman relation, providing $m_N = g_{NN\pi} f_\pi$. Consequently, $\Delta M = m_N/3$ in the chiral limit, and its theoretical value should be 345 MeV/c^2.

To test this theory, several analyses have been employed. The summary of published results is illustrated in Fig. 7.1. Former analyses on the measurement of $\Delta M(D_s^-\pi^0)$ were performed more than 20 years ago. Due to large estimated systematic errors, the three results shown in Fig. 7.1 [top] are considered compatible within 1σ. Meanwhile, the current analysis yields a mass resolution estimate with the 10 times lower systematic uncertainty than earlier studies: $\Delta M(D_s^-\pi^0)$ = 350.0 $\pm$ 0.5 $\pm$ 0.1 MeV/c^2. The mass difference measured in the present work confirms the significant difference from the theoretical expectation by more than 7σ and is compatible with the previous Belle measurement [202]. We also provide a similar summary for mass splitting measurements of $D_{s1}(2460)^-$ (see Fig. 7.1 [bottom]), where the result reported in this thesis – $\Delta M(D_s^{*-}\pi^0)$ = 346.2 $\pm$ 1.7 $\pm$ 1.4 MeV/c^2 – enter with the statistical and systematic errors comparable to those for earlier measurements.

It is worth noting that both mass splitting measurements have been estimated in decay channels that include an additional D_s^+ meson in comparison to earlier studies. Despite our efforts to compensate it by developing an MLP-based event selection, this naturally decreases the reconstruction efficiency, which in turn smears the measurement making it less competitive. In contrast, this analysis makes use of the full Belle data sample – 10 times larger than the one used for the former Belle analysis. Notwithstanding these inherent trade-offs, we found good agreement within 1σ with the former Belle measurement [202] and the PDG average. It is also interesting to note that the ΔM value evaluated in the $D_{s1}(2460)^-$ analysis, and that of the $D_{s0}^*(2317)^-$ analysis are identical within the error. No tension with the chiral symmetry breaking theory is observed.

Width measurements

Measurement of the $D_{s0}^*(2317)^-$ and $D_{s1}(2460)^-$ widths remain crucial to disclose their nature. In this analysis, we revisited the measurement of the mass resolution for $D_{s0}^*(2317)^-$ and $D_{s1}(2460)^-$, and found 6.63 $\pm$ 0.53 MeV/c^2 and 6.18 $\pm$ 1.52 MeV/c^2, respectively. Meanwhile, the earlier Belle measurement from Ref. [202] quotes 7.6 $\pm$ 0.5 MeV/c^2 and 5.8 $\pm$ 1.3 MeV/c^2, respectively. This result motivated us to look into the the measurement of the $D_{s0}^*(2317)^-$ and $D_{s1}(2460)^-$ width ULs. Unfortunately, the likelihood scan performed to set new limits showed low sensitivity due to large statistical uncertainties and marginal data-MC agreement. The obtained results are quantified as $\Gamma(D_{s0}^*(2317)^-) < 4.07$ MeV and $\Gamma(D_{s1}(2460)^-) < 13.4$ MeV, which are not competitive with the current world-best measurement reporting UL values of 3.8 and 3.5 MeV, respectively [223]. Here, just like for mass splitting measurements, an inclusive $D_{sJ}^{(*)-}$ analysis performed with the full Belle II data set would be capable of substantially improving current standing width upper-limits. The projected Belle II data set of 50 ab^{-1} could potentially allow to reach a sensitivity below

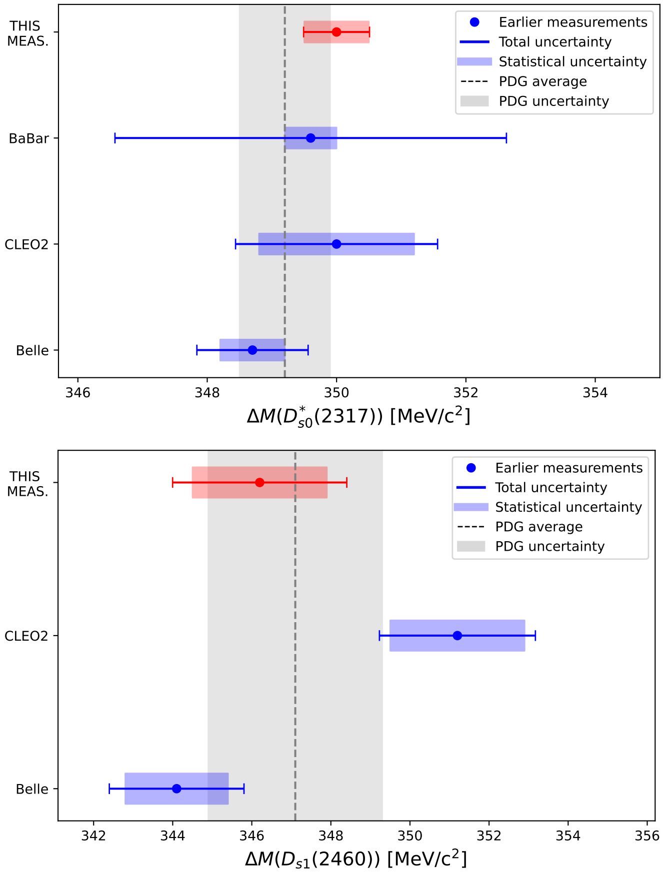

Figure 7.1: Comparison of PDG average, earlier experimental measurements (BaBar, Belle and CLEO2) and results obtained in the current analysis (THIS MEAS) for the $D^*_{s0}(2317)^-$ [top] and $D_{s1}(2460)^-$ [bottom] mass splitting measurements.

$\mathcal{O}(1)$ MeV for the $D^*_{s0}(2317)^-$ width measurement, which would be a significant step towards disclosing its ambiguous nature.

Measurement of the production ratio

As an additional input to the theory, we measured the ratio of the $D_{s1}(2460)^-/D^*_{s0}(2317)^-$ yield normalized to their reconstruction efficiencies, which delivers an unexpected result (see Eq. 6.7). Whether $D_{s0}^{*}(2317)^{-}$ and $D_{s1}(2460)^{-}$ are conventional or exotic resonances remains an open question. However, experimental measurements suggest that either a similar mechanism is deflating masses of both mesons from those predicted for the canonical 0^{+} and 1^{+} cs mesons, or both states belong to the same family of exotics.

In summary, we have experimentally observed that chiral dynamical properties of the $D_{s0}^{*}(2317)^{-}$ and $D_{s1}(2460)^{-}$ resonant states tend to those of heavy-quark particles. With larger Belle II datasets becoming available soon, new opportunities arise for measuring $D_{sJ}^{(*)-}$ properties. An inclusive analysis of $e^{+}e^{-} \to D_{s}^{+}\pi^{0}$ in the continuum remains the golden channel to measure the width of the $D_{s0}^{*}(2317)^{-}$ at $e^{+}e^{-}$ colliders, or at least to provide a new precise upper limit to better constraint the plethora of theoretical models. Meanwhile, a potential inclusive analysis of $e^{+}e^{-} \to D_{s}^{-(*)}D_{s}^{+}\pi^{0}$ with higher statistics will enable further search for resonant states with the double cs quark content. The acquired results in terms of background suppression and improved mass resolution pose the base for further studies and precise measurements. The search for states with $c\bar{c}s\bar{s}$ quark content reported in this thesis delivers several curious conclusions and ignites further interest in the field.

Appendix A

Appendix to the Belle II experiment overview.

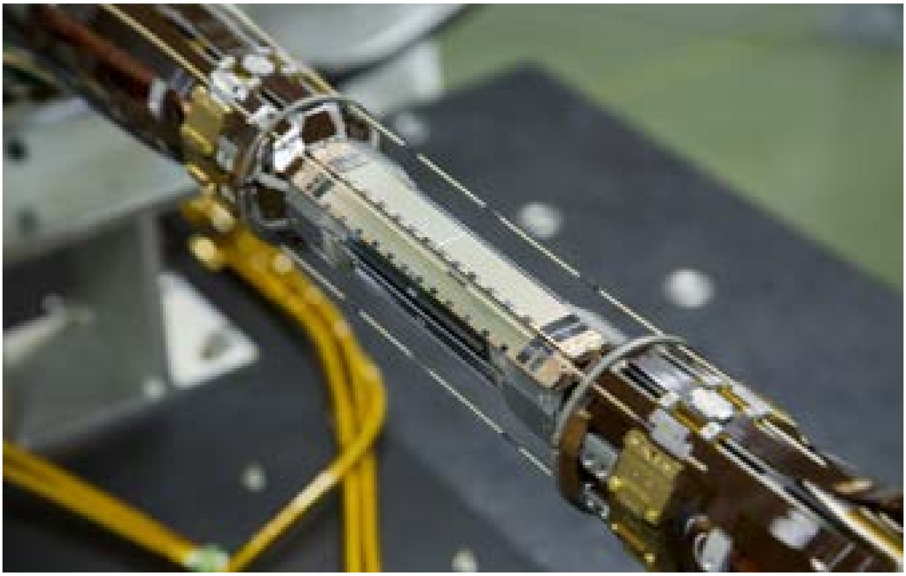

Figure A.1: Picture of the Belle II PXD taken during the assembly process [33].

Figure A.2: Picture of the Belle II detector taken in February 2023 during the undergoing LS1. The partially disassembled state reveals detector components that are usually hidden behind the detector shielding. In particular, the QCS magnet, the ARICH and the KLM are visible.

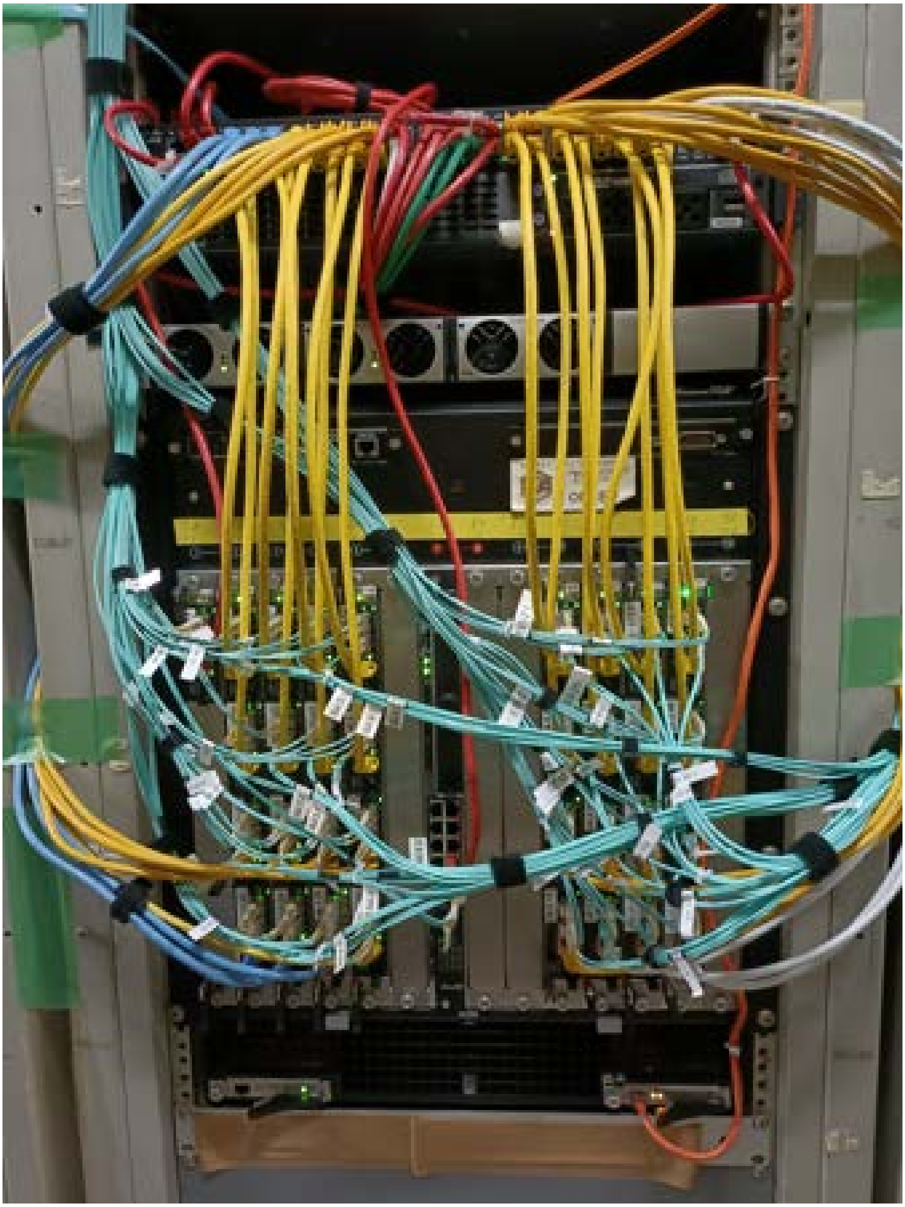

Figure A.3: Photograph of the ONSEN data reduction system.

Appendix B

Appendix to beam-induced background in the PXD

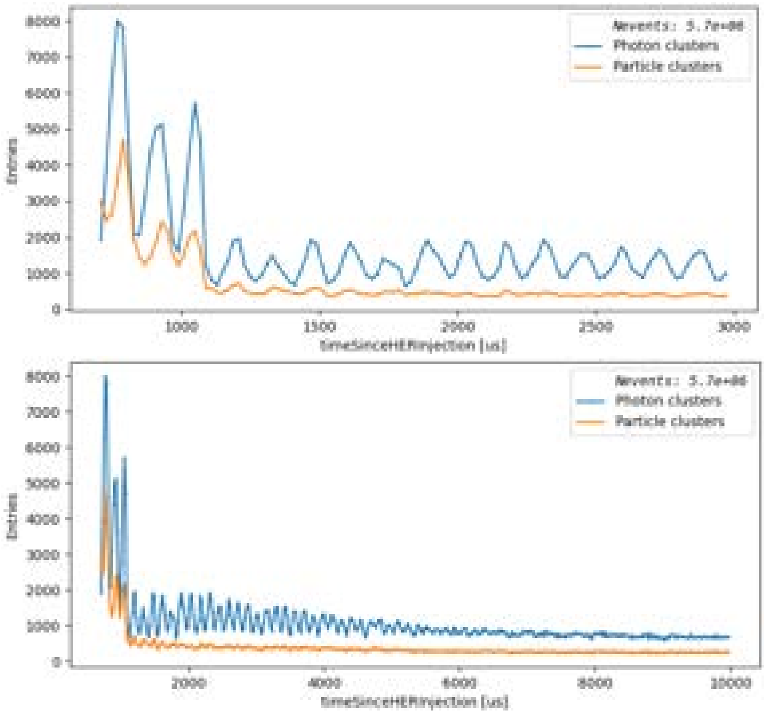

Figure B.1: Number of photon and particle clusters versus time since the last HER injection in Experiment 30 Run 3425 with PXD2.

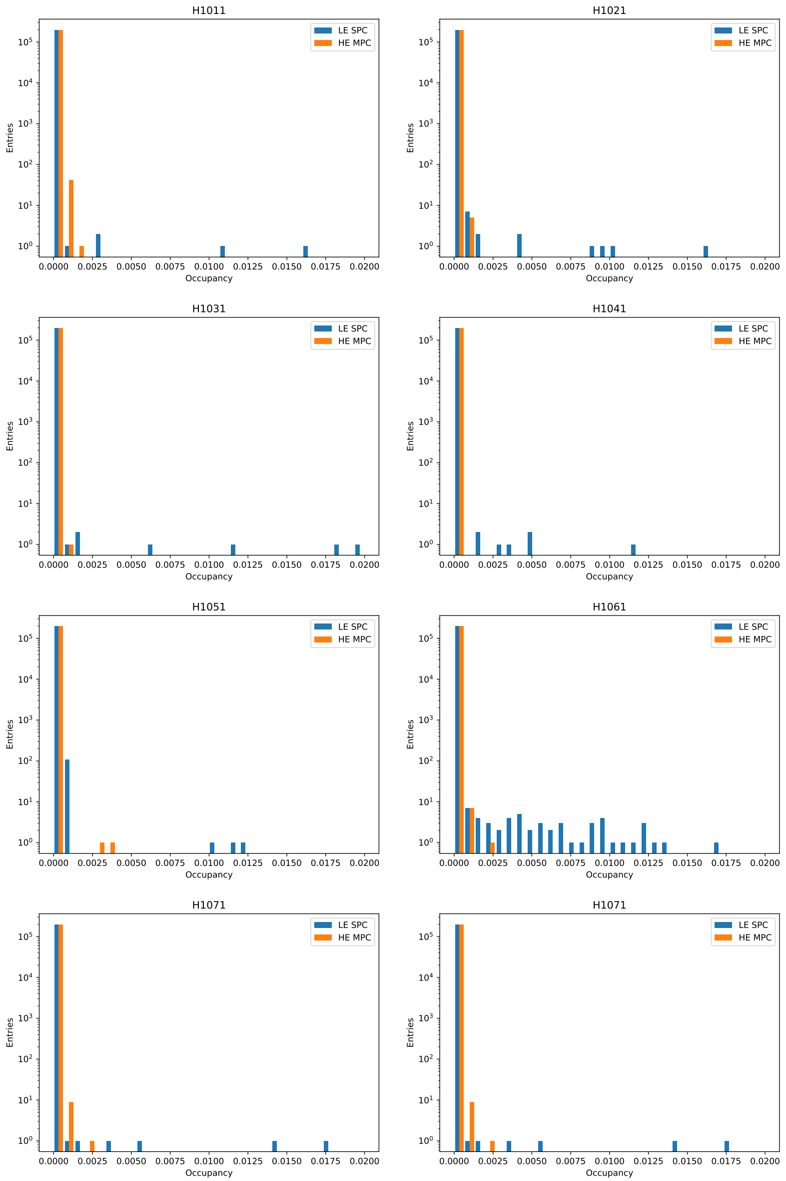

Figure B.2: LE SPC and HE MPC occupancy distribution in each BWD module of L1 in Exp30 Run2486 with PXD2.

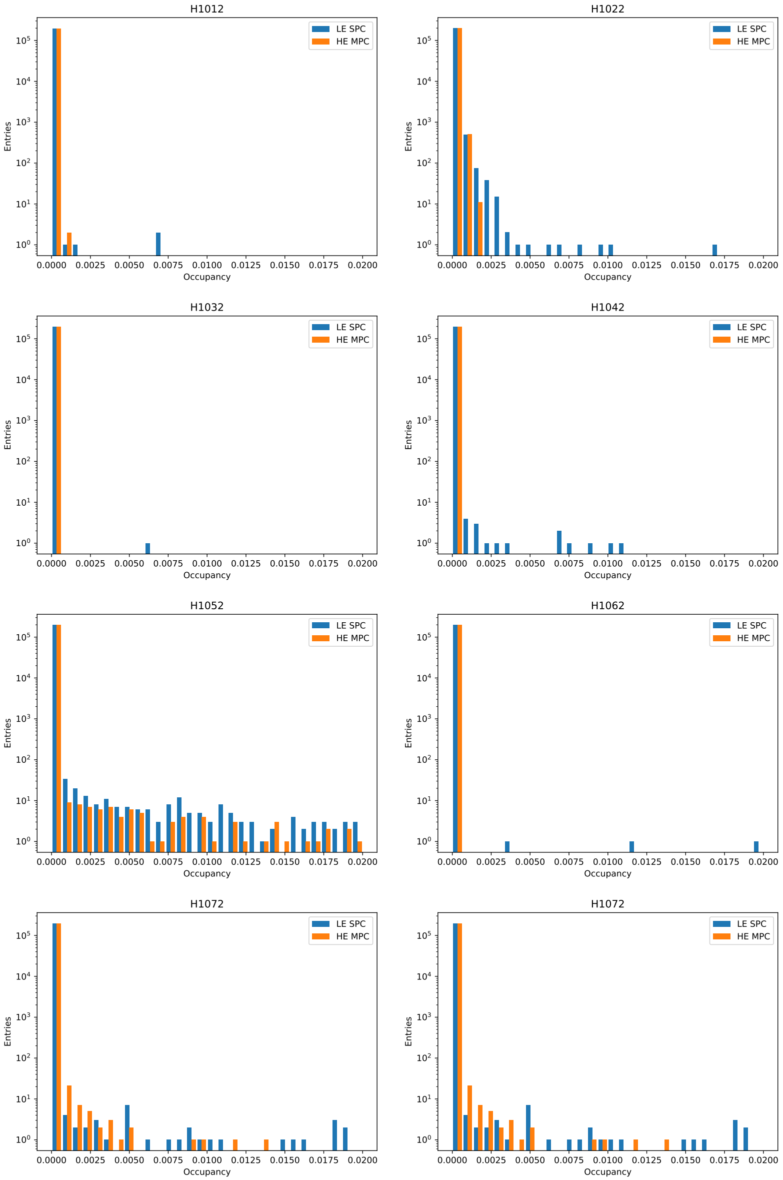

Figure B.3: LE SPC and HE MPC occupancy distribution in each FWD module of L1 in Exp30 Run2486 with PXD2.

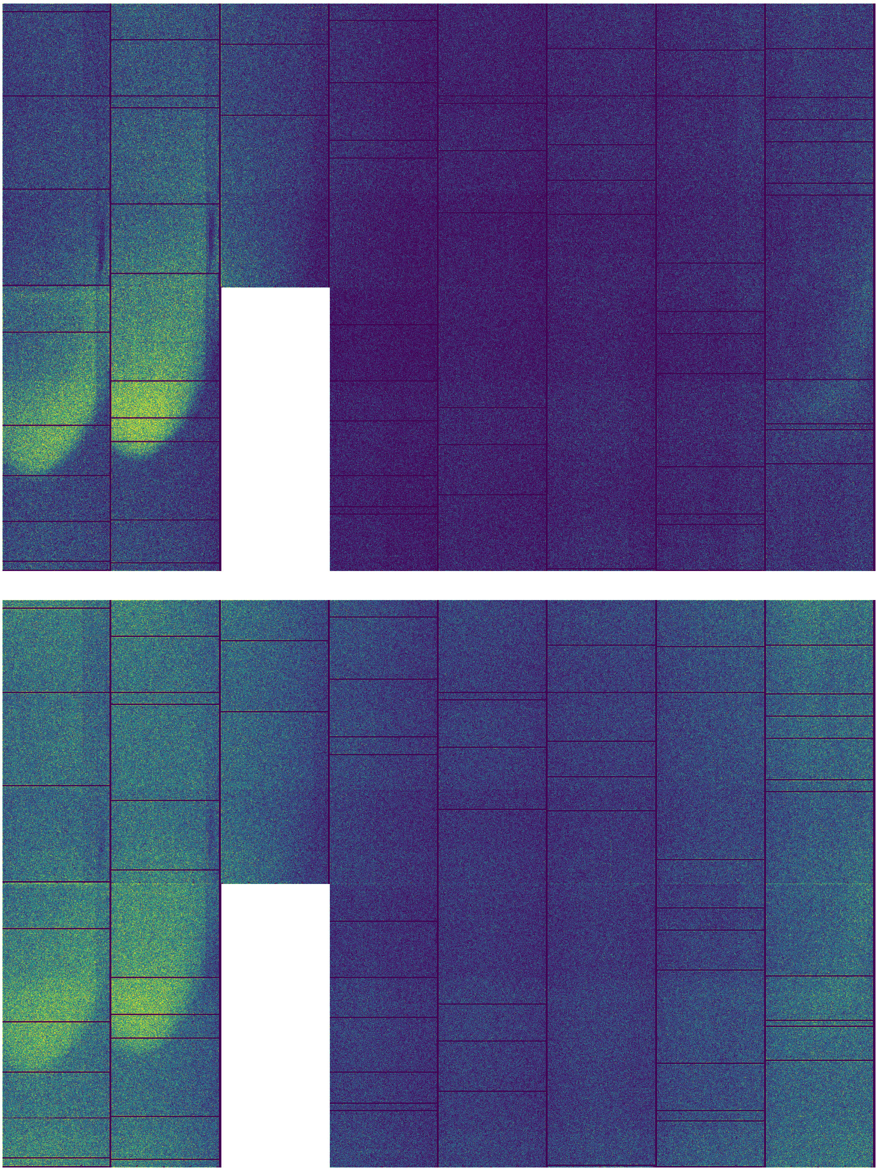

Figure B.4: Map of [top] HE SPC and [bottom] HE DPC in the Experiment 12 Run 2154 with PXD1.

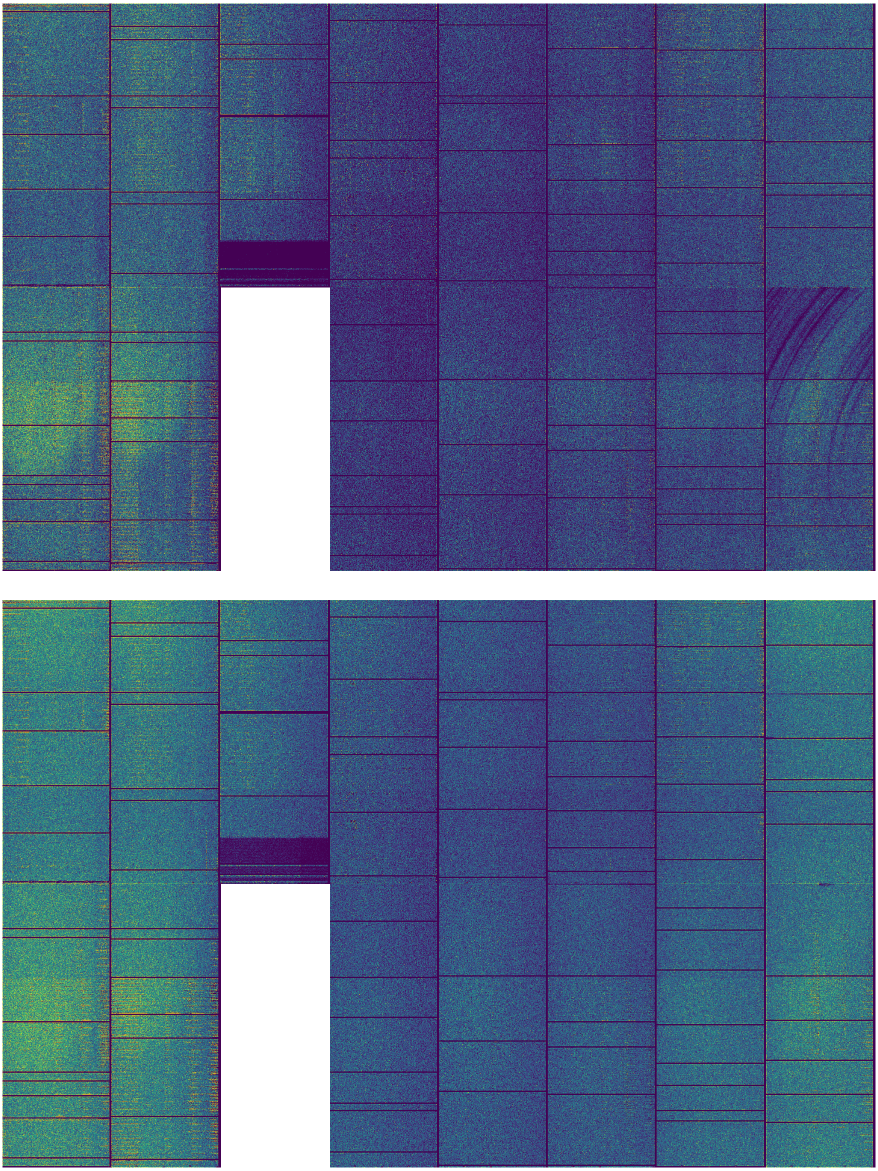

Figure B.5: Map of [top] HE SPC and [bottom] HE DPC in the Experiment 26 Run 1774 with PXD2.

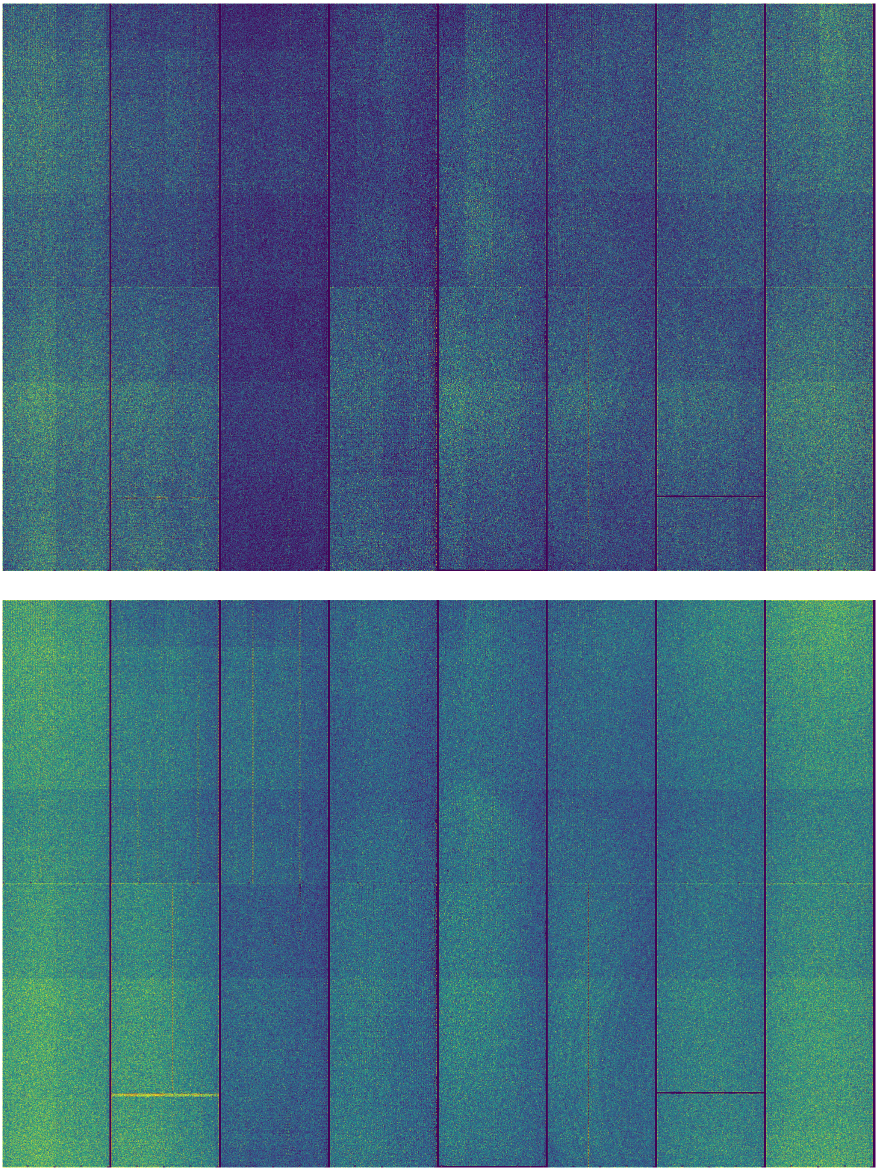

Figure B.6: Map of [top] HE SPC and [bottom] HE DPC in the Experiment 30 Run 2486 with PXD2.

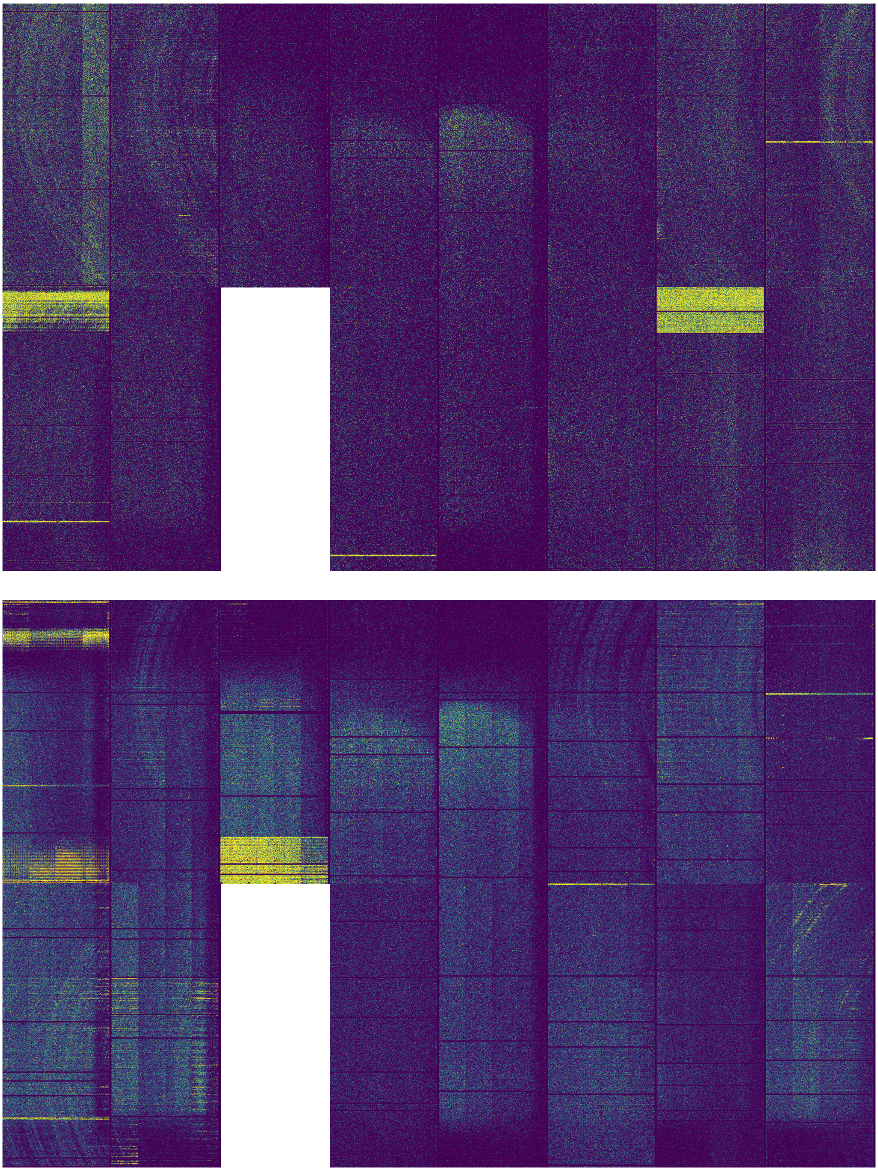

Figure B.7: Map of LE DPC [top] in the Experiment 12 Run 2153 and [bottom] in the Experiment 26 Run 1774 with PXD1.

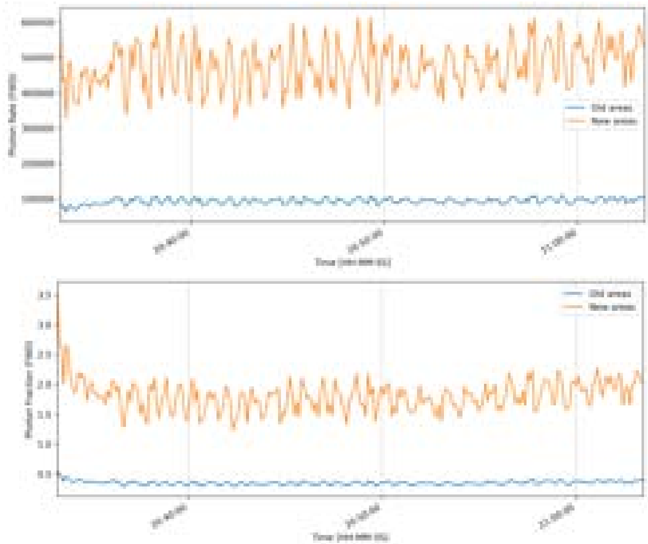

Figure B.8: [top] Photon rate and [bottom] photon fraction calculated by the Photon Monitor using old versus new area definitions in FWD modules.

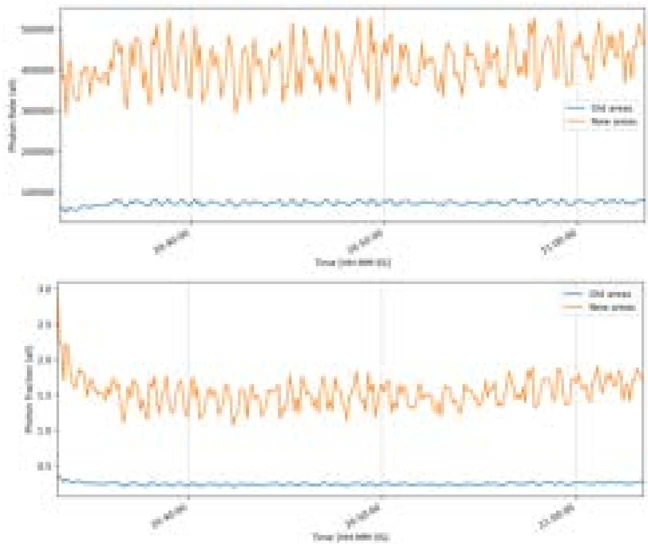

Figure B.9: [top] Photon rate and [bottom] photon fraction calculated by the Photon Monitor using old versus new area definitions in all modules combined.

Appendix C

Appendix to search for exotic states with the $c\bar{c}s\bar{s}$ quark content

C.1 Definition of selection criteria

Spatial variables employed for selection of charged tracks

The Kalman filter is one of the most widely used algorithms for the reconstruction of charged particle tracks in high energy physics. It is a recursive least-squares estimation method that extends the classical χ^2 fitting by incorporating correlations between successive measurements and iteratively updating track parameters and their uncertainties as new hits are included.

In the Belle experiment, the Kalman filter is used to reconstruct trajectories of charged particles through tracking detectors, including the vertex detector and central drift chamber. As charged particles move in a uniform magnetic field, their trajectories follow helices rather than straight lines. To apply the Kalman filter – which requires linear equations of motion – the helical trajectory is linearized around a reference surface. This is achieved using a five-parameter helix model that locally approximates the curved path.

The five helix parameters used to describe the spatial and kinematic properties of charged tracks are:

- **dr** – the distance of closest approach (DCA) to the interaction point in the transverse r–φ plane;
- **dz** – the displacement of the track from the IP along the beam (or r–z) direction;

- $\boldsymbol{\varphi_0}$ – the azimuthal angle of the track momentum at the point of closest approach;
- $\mathbf{tan}\boldsymbol{\lambda}$ – the tangent of the dip angle λ, which describes the slope of the track relative to the transverse plane;
- $\mathbf{q/p_T}$ – the inverse transverse momentum multiplied by the particle's charge, which characterizes the curvature of the track in the magnetic field.

These parameters are used both in the Kalman filtering process and in the selection of well-reconstructed tracks. In particular, spatial consistency with the primary interaction point is ensured by requiring $dr < 1.5$ cm and $|dz| < 3.0$ cm for all selected tracks. These requirements suppress tracks originating from beam background, secondary interactions, or long-lived particles such as K_S^0 or Λ decays.

Helicity angle

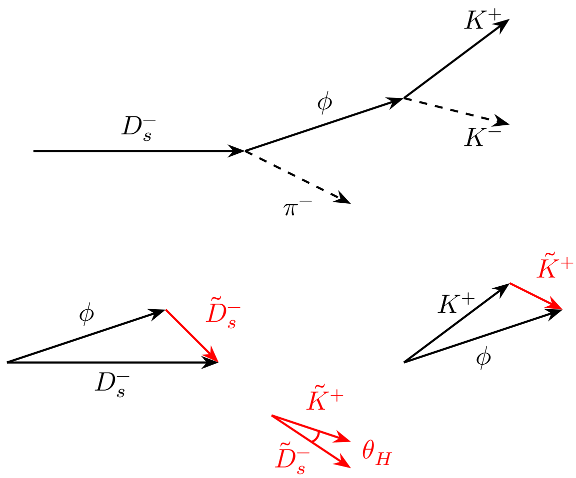

Figure C.1: Schematic illustration of the helicity angle definition. Black vectors represent momenta of intermediate particles in the lab system, while red vectors – in the system of ϕ. The identical approach is applied for a scheme that includes K^* instead of ϕ.

Fox-Wolfram momentum

The Fox-Wolfram momentum is a set of event-shape variables introduced by Geoffrey C. Fox and Stephen Wolfram in a paper dedicated to event shapes in hadronic e^+e^- collisions in 1978 [237]. These variable have proven over time to be extremely capable of distinguishing jet-like and spherical event topologies to separate $B\bar{B}$ from continuum events.

Momenta are defined as:

$$H_\ell = \frac{4\pi}{2\ell+1} \sum_{m=-\ell}^{\ell} \left| \sum_i Y_\ell^m(\varphi_i, \theta_i) \frac{|\vec{p}_i|}{\sqrt{s}} \right|^2, \tag{C.1}$$

where:

- Y_ℓ^m are spherical harmonics;
- $|\vec{p}_i|$ is the magnitude of the momentum of an i-th particle (or jet);
- $\sqrt{s}$ is the total centre-of-mass energy of an event;
- θ_i, φ_i are the polar and azimuthal angles of a particle in spherical coordinates.

In practical analyses, a more commonly used form expresses momenta in terms of Legendre polynomials $P_\ell(\cos\theta_{ij})$, where θ_{ij} is the angle between i^{th} and j^{th} particles:

$$H_\ell = \sum_{i,j} \frac{|\vec{p}_i||\vec{p}_j|}{E_{\text{vis}}^2} P_\ell(\cos\theta_{ij}), \tag{C.2}$$

where $E_{\text{vis}} = \sum_i |\vec{p}_i|$ is the total visible energy in an event.

Normalized momenta are defined as $R_\ell = H_\ell/H_0$. Among these, the second momentum R_2 is particularly effective at separating spherical $B\bar{B}$ events from the jet-like continuum background. In the present analysis, a requirement on R_2 is tested to reject $B\bar{B}$ events and enhance signal purity.

Scaled momentum

$$x_p = \frac{p^*(D_s^+ D_{sJ}^{(*)-})}{\sqrt{s - M^2(D_s^+ D_{sJ}^{(*)-})}}. \tag{C.3}$$

Chi-squared probability

P_{χ^2} is calculated as the upper-tail probability of the chi-squared cumulative distribution function (CDF). It is commonly defined as:

$$P_{\chi^2} = \text{Prob}(\chi^2_\nu \geq \chi^2_{\text{obs}}), \tag{C.4}$$

where

- χ^2_{obs} is the observed chi-squared statistic;
- ν (or ndf) is the number of degrees of freedom;
- P_{χ^2} represents the probability that a chi-squared distributed variable with ν degrees of freedom exceeds the observed value.

This probability is computed using the (lower) incomplete gamma function:

$$P_{\chi^2} = 1 - \frac{\gamma\left(\frac{\nu}{2}, \frac{\chi^2_{\text{obs}}}{2}\right)}{\Gamma\left(\frac{\nu}{2}\right)}, \tag{C.5}$$

where

- $\gamma(s, x)$ is the lower incomplete gamma function;
- $\Gamma(s)$ is the complete gamma function.

A small P_{χ^2} value indicates that observed data are unlikely under the null hypothesis, potentially suggesting a poor fit.

C.2 Supplementary plots

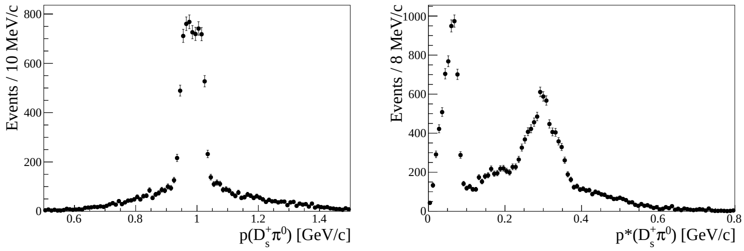

Figure C.2: $D_{s0}(2317)^-$ momentum distribution in signal MC in the [left] lab and [right] CM systems.

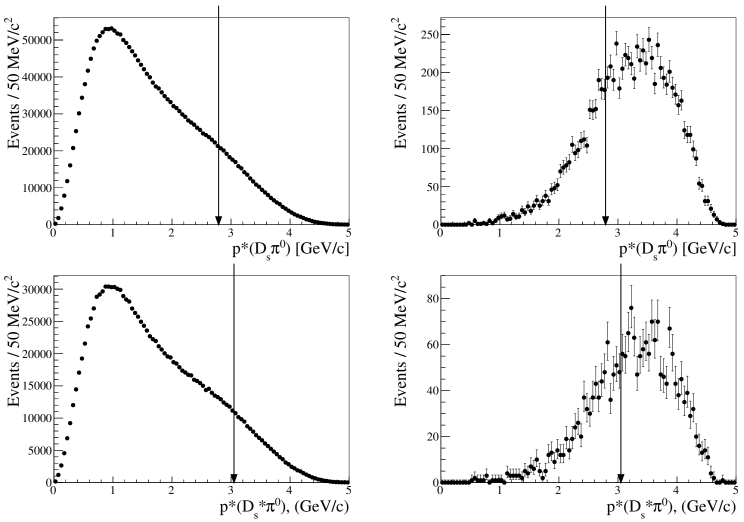

Figure C.3: Top row: $p^*(D_s\pi^0)$ distribution for [left] mismatched and [right] matched $D_{s0}^*(2317)^-$ candidates. Bottom row: $p^*(D_s^*\pi^0)$ distribution for [left] mismatched and [right] matched $D_{s1}(2460)^-$ candidates (all in generic MC). In each plot, an arrow indicates the optimised value for the given selection criterion.

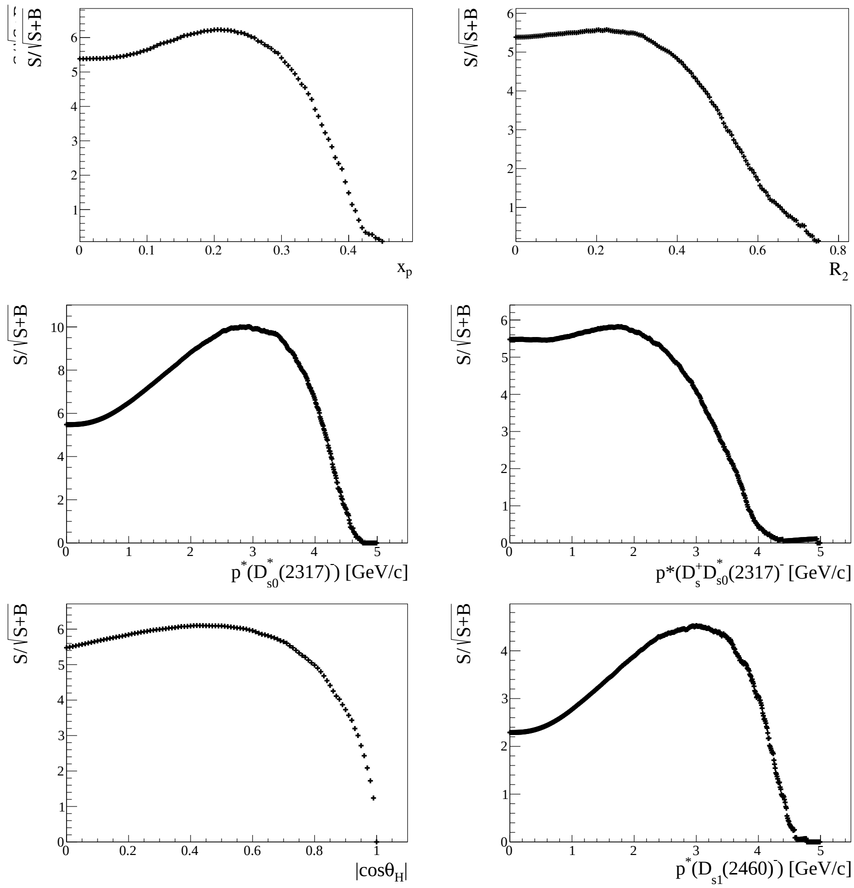

Figure C.4: Selection optimisation for the competing selection criteria: [top-left] x_p, [top-right] R_2, [centre-left] $p^*(D_{s0}(2317))$ and [centre-right] $p^*(D_s^+ D_{s0}^*(2317)^-)$. Optimisation of the $|cos\theta_H|$ and $p^*(D_{s1}(2460)^-)$ selection criteria in generic MC.

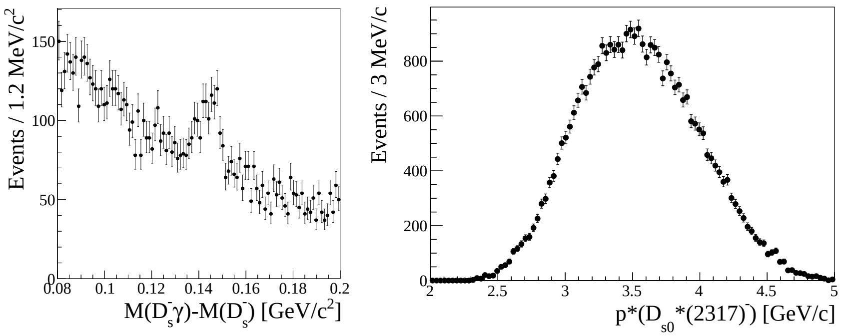

Figure C.5: [left] D_s^* invariant mass distribution in data samples. [right] Momentum distribution in c.m.s. for MVA-selected $D_{s0}^*(2317)^-$ candidates in generic MC.

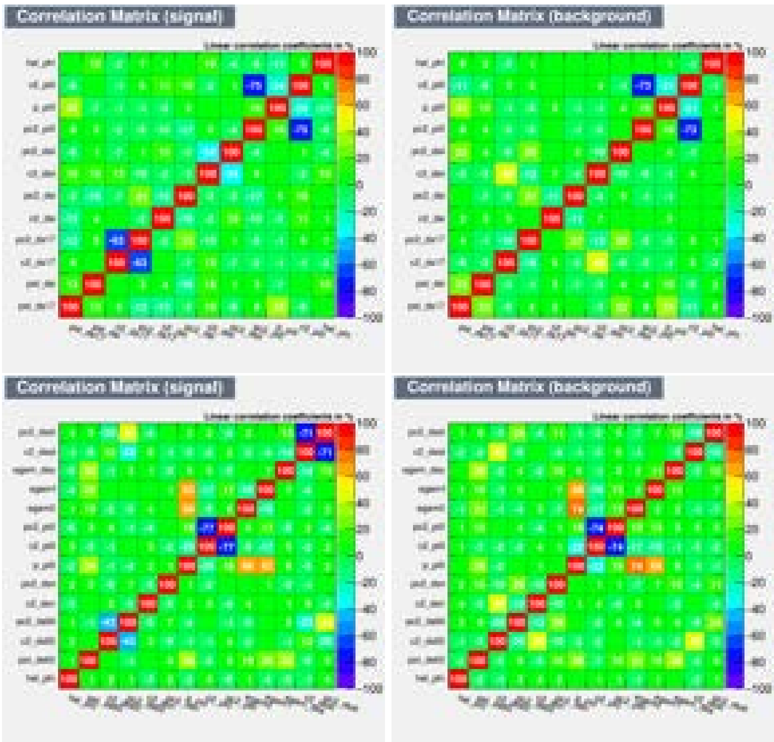

Figure C.6: Correlation matrix for [left column] signal and [right column] background [top row] $D_s^+ D_{s0}^*(2317)^-$ and [bottom row] $D_s^+ D_{s1}(2460)^-$ events.

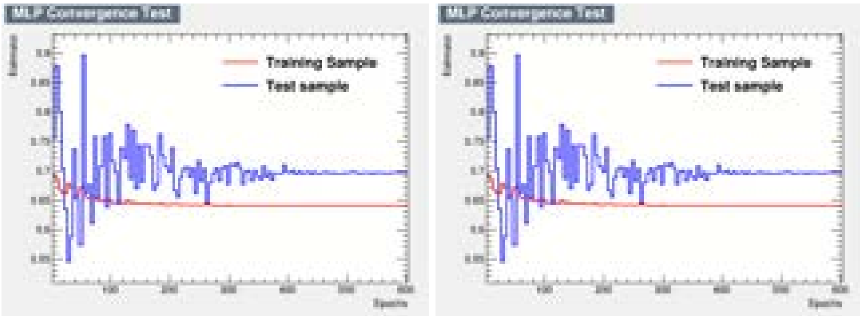

Figure C.7: MLP convergence test for [left] $D_s^+ D_{s0}^*(2317)^-$ and [right] $D_s^+ D_{s1}(2460)^-$ events classification with the MLP.

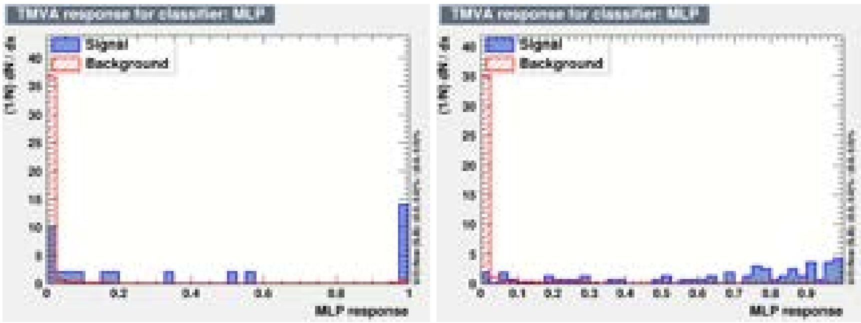

Figure C.8: MLP classifier response for [top-left] $D_s^+ D_{s0}^*(2317)^-$ and [right] $D_s^+ D_{s1}(2460)^-$ event candidates.

C.3 Fits to intermediate resonances

Parameter	Value
Bifurcated Gaussian	
μ	1019.6 ± 0.1 MeV/c^2
σ_{G1}	3.69 ± 0.60 MeV/c^2
σ_{G2}	1.59 ± 0.19 MeV/c^2
N_{sig}	2405 ± 146
Chebyshev polynomial	
a_0	0.052 ± 0.113
N_{bkg}	476 ± 137

Table C.1: Parameters of the fit to the K^-K^+ invariant mass distribution in signal MC.

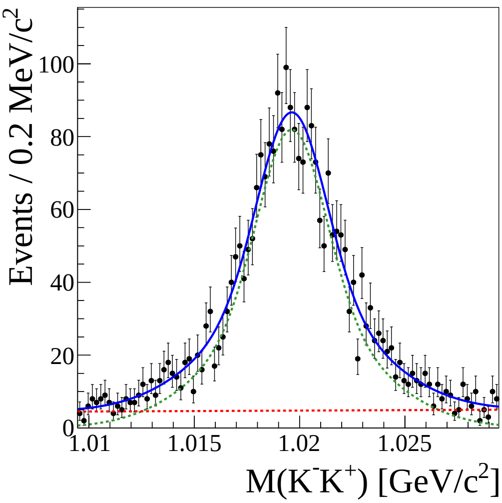

Figure C.9: Fit to the $M(K^-K^+)$ distribution in signal MC. The solid blue curve represents the Bifurcated Gaussian + Chebyshev polynomial fit function. The Bifurcated Gaussian component (dashed green) indicates the matched signal, while the first-order Chebyshev polynomial (dashed red) represents remaining mismatched combinations.

Parameter	Value
Double-sided Crystal Ball	
μ	$(7.20 \pm 1.59) \times 10^{-5}$ MeV/c^2
σ	0.554 ± 0.195 MeV/c^2
α_L	1.52 ± 0.09
n_L	1.67 ± 0.20
α_R	1.27 ± 0.11
n_R	2.02 ± 0.47
N_{sig}	3113 ± 80
Chebyshev polynomial	
a_0	1.039 ± 0.001
N_{bkg}	100 ± 59

Table C.2: Parameters of the fit to the $M_{\text{res}} = M(\phi_{\text{rec}}) - M(\phi_{\text{gen}})$ residual distribution in signal MC.

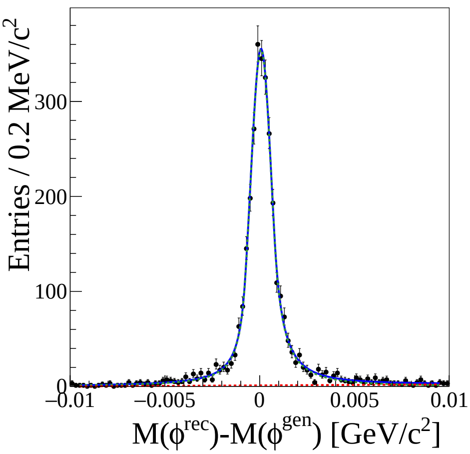

Figure C.10: Fit to the $M_{\text{res}} = M(\phi_{\text{rec}}) - M(\phi_{\text{gen}})$ residual distribution in signal MC. The solid blue curve represents the double-sided Crystal Ball + Chebyshev polynomial fit function. The double-sided Crystal Ball component (dashed green) indicates the matched signal, while the first-order Chebyshev polynomial (dashed red) represents remaining mismatched combinations.

Parameter	Value
Breit-Wigner	
μ	891.4 ± 0.6 MeV/c^2
σ	46.7 ± 2.1 MeV/c^2
N_{sig}	3117 ± 101
Chebyshev polynomial	
a_0	0.256 ± 0.121
N_{bkg}	575 ± 87

Table C.3: Parameters of the fit to the $K^-\pi^+$ invariant mass distribution in signal MC.

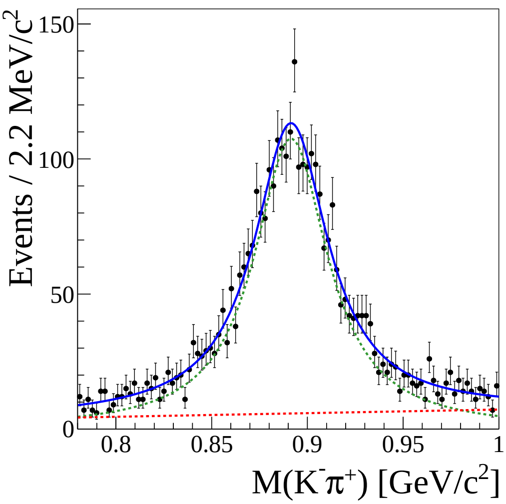

Figure C.11: Fit to the $M(K^-\pi^+)$ distribution in signal MC. The solid blue curve represents the Breit-Wigner + Chebyshev polynomial fit function. The Breit-Wigner component (dashed green) indicates the matched signal component, while the first-order Chebyshev polynomial (dashed red) represents remaining mismatched combinations.

Parameter	Value
	Gaussian
μ	134.4 ± 0.1 MeV/c^2
σ	4.48 ± 0.1 MeV/c^2
N_{sig}	5370 ± 158
	Chebyshev polynomial
a_0	0.010 ± 0.018
a_1	-0.165 ± 0.027
N_{bkg}	9913 ± 171

Table C.4: Parameters of the fit to the $\gamma\gamma$ invariant mass distribution in signal MC.

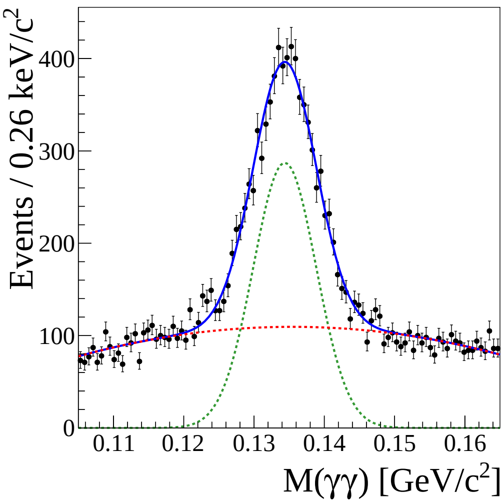

Figure C.12: Fit to the $M(\gamma\gamma)$ distribution in signal MC. The solid blue curve represents the Gaussian + Chebyshev polynomial fit function. The Gaussian component (dashed green) indicates the matched signal component, while the second-order Chebyshev polynomial (dashed red) represents remaining mismatched combinations.

Parameter	Value
Bifurcated Gaussian	
μ	1967.4 ± 0.1 MeV/c^2
σ_{G1}	7.68 ± 0.73 MeV/c^2
σ_{G2}	2.85 ± 0.10 MeV/c^2
ratio	0.171 ± 0.031
N_{sig}	3106 ± 57
Chebyshev polynomial	
a_0	-0.291 ± 0.434
N_{bkg}	30 ± 13
σ_{fin}	3.67 ± 0.20 MeV/c^2

Table C.5: Parameters of the fit to the $\phi\pi^+$ invariant mass distribution in signal MC. The parameter σ_{fin} is the invariant mass resolution estimated as a weighted sum of Gaussian widths.

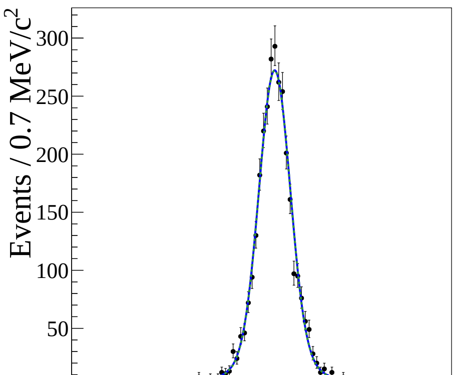

Figure C.13: Fit to the $M(\phi\pi^+)$ distribution in signal MC. The solid blue curve represents the Bifurcated Gaussian + Chebyshev polynomial fit function. Bifurcated Gaussian component (dashed green) indicates the matched signal component, while the second-order Chebyshev polynomial (dashed red) represents remaining mismatched combinations.

Parameter	Value
	Gaussian
μ	1967.0 ± 0.9 MeV/c^2
σ	7.88 ± 0.62 MeV/c^2
N_{sig}	134 ± 12
	Chebyshev polynomial
a_0	-1.647 ± 1.420
N_{bkg}	11 ± 6

Table C.6: Parameters of the fit to the $\phi\pi^+\pi^0$ invariant mass distribution in signal MC.

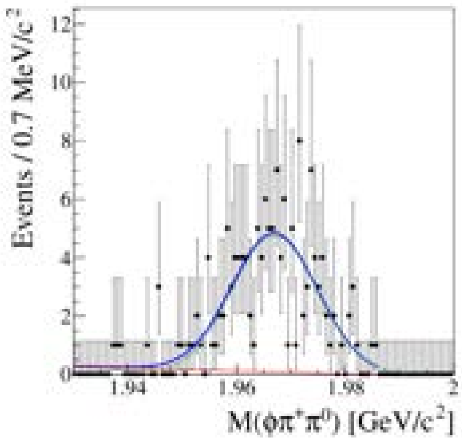

Figure C.14: Fit to the $M(\phi\pi^+\pi^0)$ distribution in signal MC. The solid blue curve represents the Gaussian + Chebyshev polynomial fit function. Gaussian component (dashed green) indicates the matched signal component, while the second-order Chebyshev polynomial (dashed red) represents remaining mismatched combinations.

Parameter	Value
Bifurcated Gaussian	
μ	1967.4 ± 0.1 MeV/c^2
σ_{G1}	3.19 ± 0.09 MeV/c^2
σ_{G2}	9.06 ± 0.95 MeV/c^2
ratio	0.855 ± 0.024
N_{sig}	2616 ± 53
Chebyshev polynomial	
a_0	0.298 ± 0.426
N_{bkg}	29 ± 14
σ_{fin}	4.04 ± 0.21 MeV/c^2

Table C.7: Parameters of the fit to the $\phi\pi^+\pi^0$ invariant mass distribution in signal MC. The parameter σ_{fin} is the invariant mass resolution estimated as a weighted sum of Gaussian widths.

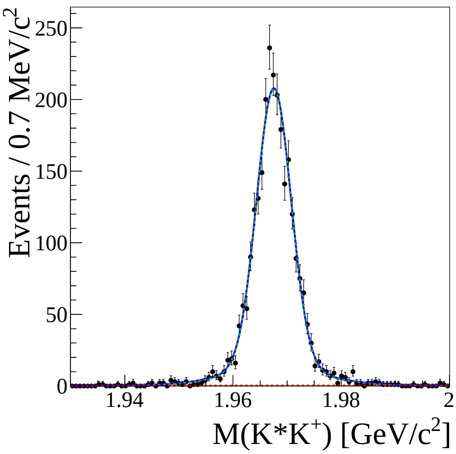

Figure C.15: Parameters of the fit to the $M(\phi\pi^+\pi^0)$ distribution in signal MC. The solid blue curve represents the Bifurcated Gaussian + Chebyshev polynomial fit function. The Bifurcated Gaussian component (dashed green) indicates the matched signal component, while the second-order Chebyshev polynomial (dashed red) represents remaining mismatched combinations.

Parameter	Value
Bifurcated Gaussian	
μ	1967.5 ± 0.0 MeV/c^2
σ_{G1}	3.02 ± 0.07 MeV/c^2
σ_{G2}	8.29 ± 0.53 MeV/c^2
ratio	0.825 ± 0.020
N_{sig}	5858 ± 78
Chebyshev polynomial	
a_0	-0.195 ± 0.267
N_{bkg}	69 ± 19
σ_{fin}	3.94 ± 0.15 MeV/c^2

Table C.8: Parameters of the fit to the invariant mass of the D_s^+ candidates distribution reconstructed into $\phi\pi^+$, $\phi\pi^+\pi^0$ and K^*K^+ in signal MC.

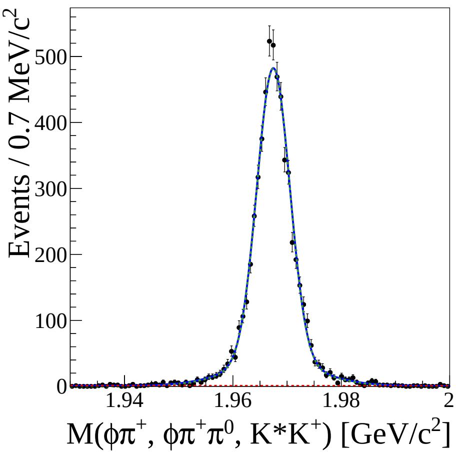

Figure C.16: Fit to the $M(\phi\pi^+, \phi\pi^+\pi^0, K^*K^+)$ distribution in signal MC. The solid blue curve represents the Bifurcated Gaussian + Chebyshev polynomial fit function. The Bifurcated Gaussian component (dashed green) indicates the matched signal component, while the second-order Chebyshev polynomial (dashed red) represents remaining mismatched combinations.

Parameter	Value
Double Gaussian	
μ	2112.4 ± 0.2 MeV/c^2
σ	4.92 ± 0.29 MeV/c^2
μ_{BS}	2108.3 ± 1.9 MeV/c^2
σ_{BS}	17.95 ± 2.92 MeV/c^2
N_{sig}	1675 ± 135
N_{BS}	1145 ± 151
Second-order Chebyshev polynomial	
a_0	-0.390 ± 0.041
a_1	-0.302 ± 0.044
N_{bkg}	3212 ± 179

Table C.9: Parameters of the fit to the $\phi\pi^+\pi^0$ invariant mass distribution in signal MC. The parameter σ_{fin} is the invariant mass resolution estimated as a weighted sum of Gaussian widths.

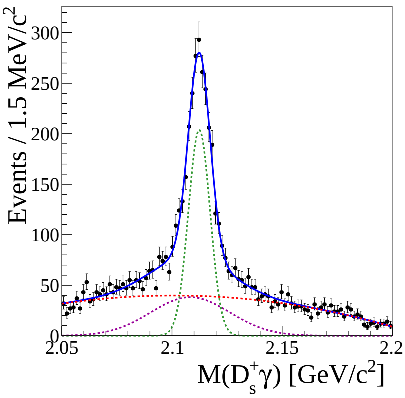

Figure C.17: Fit to the $M(D_s^+\gamma)$ distribution in signal MC. The solid blue curve represents the Double Gaussian + Chebyshev polynomial fit function. The narrow Gaussian component (dashed green) indicates the matched signal component, a wide Gaussian (dashed purple) – broken signal component, while the second-order Chebyshev polynomial (dashed red) represents remaining mismatched combinations.

Fixed Parameters

Parameter	Value
Broken signal	
μ^{BS}	345.9 MeV/c^2
σ^{BS}	14.3 MeV/c^2
f^{BS}	0.437

Floating Parameters

Parameter	Value
$D^*_{s0}(2317)$ signal	
μ	349.0 ± 0.1 MeV/c^2
σ	4.95 ± 0.07 MeV/c^2
N_{sig}	3806 ± 64
$D_{s1}(2460)$ signal	
μ	347.6 ± 0.1 MeV/c^2
σ	4.13 ± 0.11 MeV/c^2
N_{sig}	1615 ± 36
Background (Chebyshev polynomials)	
a_1^{2317}	-0.514 ± 0.040
a_1^{2460}	-0.643 ± 0.046
N_{bkg}^{2317}	1640 ± 44
N_{bkg}^{2460}	1106 ± 39

Table C.10: Parameters of the simultaneous fit to the $\Delta M(D_s^- \pi^0)$ and the $\Delta M(D_s^{*-} \pi^0)$ distributions in signal MC.

Fixed Parameters (left)

Parameter	Value
Th	4.2861 GeV/c^2

Floating Parameters (left)

Parameter	Value
Relativistic Breit-Wigner	
μ	4.2868 ± 0.0001 GeV/c^2
σ	0.1135 ± 0.005 MeV/c^2
γ	67 ± 10 keV
N_{sig}	3132 ± 63
Threshold function	
A	-1606 ± 79
B	152230 ± 14200
C	$(-5.83 \pm 0.89) \times 10^6$
N_{bkg}	1586 ± 49

Fixed Parameters (right)

Parameter	Value
T_h	4.4278 GeV

Floating Parameters (right)

Parameter	Value
Relativistic Breit-Wigner	
μ	4.4297 ± 0.0001 GeV/c^2
Γ	0.166 ± 0.020 MeV/c^2
γ_V	0.118 ± 0.055 MeV/c^2
N_{sig}	1580 ± 83
Threshold function	
A	-1553 ± 151
B	154440 ± 31900
C	$(-6.68 \pm 2.03) \times 10^6$
N_{bkg}	1337 ± 81

Table C.11: Parameters of the fit to: [left] the $D_s^+ D_{s0}^*(2317)^-$ and [right] the $D_s^+ D_{s1}(2460)^-$ invariant mass distributions in signal MC. The signal component is described with a Voigt PDF, while the background is approximated with a threshold function defined in the equation given below.

$$f(x) = \begin{cases} 0, & x < \text{Th} \\ (x - \text{Th})^2 \cdot \exp\left[A(x - \text{Th}) + B(x - \text{Th})^2 + C(x - \text{Th})^3\right], & x \geq \text{Th} \end{cases}$$

Parameter	Value
Double Gaussian	
μ_1	123.2 ± 0.6 MeV/c^2
μ_2	134.6 ± 0.1 MeV/c^2
σ_1	4.40 ± 0.44 MeV/c^2
σ_2	4.66 ± 0.05 MeV/c^2
Fraction	0.927 ± 0.010
N_{sig}	$105{,}350 \pm 911$
Chebyshev polynomial (2$^{\text{nd}}$ order)	
a_1	0.0857 ± 0.0045
a_2	-0.0367 ± 0.0047
N_{bkg}	$283{,}520 \pm 1{,}000$
Weighted σ	4.46 ± 0.08 MeV/c^2

Table C.12: Parameters of the fit to the π^0 invariant mass distributions on generic MC (cut-based selection).

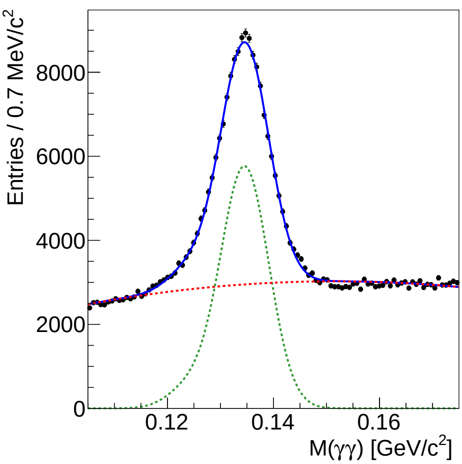

Figure C.18: Fit to the π^0 invariant mass distributions on generic MC. The solid blue curve represents the total fitting model that consists of the double Gaussian describing the signal component (dashed green) and the 2$^{\text{nd}}$ order Chebychev polynomial (dashed red) used to approximate combinatorial background.

Parameter	Value
Double Gaussian	
μ_{narrow}	1966.2 ± 0.1 MeV/c^2
μ_{wide}	1965.3 ± 0.3 MeV/c^2
σ_{narrow}	3.53 ± 0.10 MeV/c^2
σ_{wide}	8.17 ± 0.55 MeV/c^2
Fraction	0.341 ± 0.037
N_{sig}	$16,456 \pm 177$
Chebyshev polynomial (0$^{\text{th}}$ order)	
a_0	-0.092 ± 0.011
N_{bkg}	$25{,}624 \pm 202$
Weighted σ	5.11 ± 0.25 MeV/c^2

Table C.13: Parameters of the fit to the D_s^- invariant mass distributions on generic MC (cut-based selection).

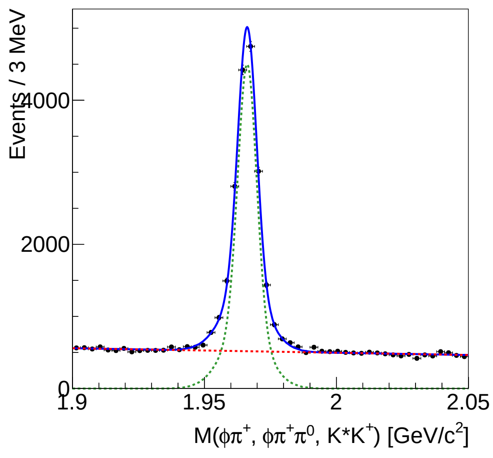

Figure C.19: Fit to the D_s^- invariant mass distributions on generic MC. The solid blue curve represents the total fitting model that consists of a double Gaussian describing the signal component (dashed green) and the 1$^{\text{st}}$ order Chebychev polynomial (dashed red) used to approximate combinatorial background.

Parameter	Value
Gaussian (signal)	
μ	348.9 ± 1.0 MeV/c^2
σ	6.21 ± 0.09 MeV/c^2
N_{sig}	4509 ± 70
Chebyshev polynomial (1$^{\text{st}}$ order)	
a_1	-2.392 ± 0.146
N_{bkg}	642 ± 52

Table C.14: Parameters of the fit to the $D_s^- \pi^0$ invariant mass distributions in generic MC for matched $D_{s0}^*(2317)^-$ candidates (cut-based selection).

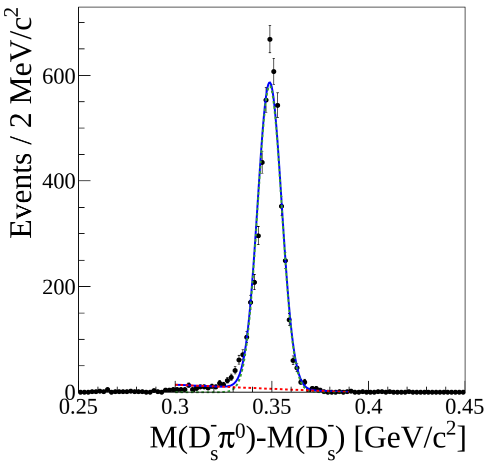

Figure C.20: Fit to the $D_s^- \pi^0$ invariant mass distributions in generic MC for matched $D_{s0}^*(2317)^-$ candidates. The solid blue curve represents the total fitting model that consists of the 1$^{\text{st}}$ order Chebychev polynomial and the Gaussian fit function.

Parameter	Value
Gaussian (feed-down)	
$\mu^{\text{feed-down}}$	345.2 ± 0.8 MeV/c^2
$\sigma^{\text{feed-down}}$	13.9 ± 0.8 MeV/c^2
$N^{\text{feed-down}}$	3117 ± 235
Chebyshev polynomial (2$^{\text{nd}}$ order)	
a_1	-0.216 ± 0.008
a_2	0.0307 ± 0.010
N_{bkg}	51224 ± 321

Table C.15: Parameters of the fit to the $D_s^- \pi^0$ invariant mass distributions in generic MC for mismatched $D_{s0}^*(2317)^-$ candidates (cut-based selection).

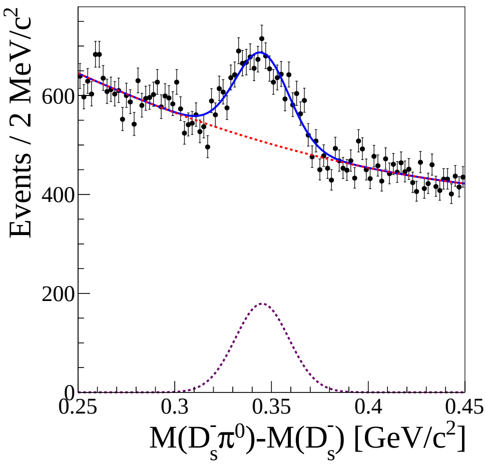

Figure C.21: Fit to the $D_{s0}^*(2317)^-$ invariant mass distribution in generic MC. The solid blue curve represents the total fitting model that consists of the Gaussian describing the $D_{s1}(2460)^-$ reflection component (dashed purple) and the 2$^{\text{nd}}$ order Chebychev polynomial (dashed red) used to approximate combinatorial background.

Parameter	Value
Gaussian (signal)	
μ	346.9 ± 2.0 MeV/c^2
σ	6.0 ± 0.2 MeV/c^2
N_{sig}	1086 ± 35
Chebyshev polynomial (1$^{\text{st}}$ order)	
a_1	-1.97 ± 0.65
N_{bkg}	195 ± 34

Table C.16: Parameters of the fit to the $D_s^{*-}\pi^0$ invariant mass distributions in generic MC for matched $D_{s1}(2460)^-$ candidates (cut-based selection).

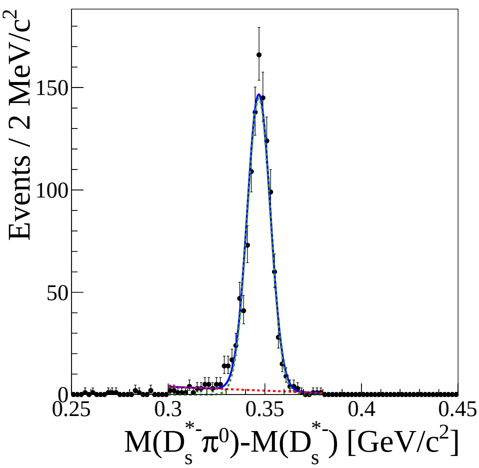

Figure C.22: Fit to the $D_s^{*-}\pi^0$ invariant mass distributions in generic MC for matched $D_{s1}(2460)^-$ candidates. The solid blue curve represents the total fitting model that consists of the 1$^{\text{st}}$ order Chebychev polynomial and the Gaussian fit function.

Parameter	Value
Gaussian (feed-up)	
$\mu^{\text{feed-up}}$	351.3 ± 1.3 MeV/c^2
$\sigma^{\text{feed-up}}$	17.1 ± 1.5 MeV/c^2
$N_{\text{feed-up}}$	733 ± 91
Chebyshev Polynomial (2$^{\text{nd}}$ order)	
a_1	-0.164 ± 0.032
a_2	0.050 ± 0.052
$N_{\text{pol\_bkg}}$	3181 ± 97

Table C.17: Parameters of the fit to the $D_s^{*-}\pi^0$ invariant mass distributions in generic MC for mismatched $D_{s1}(2460)^-$ candidates that are not coming from $D_{s1}(2460)^-$ decays (cut-based selection).

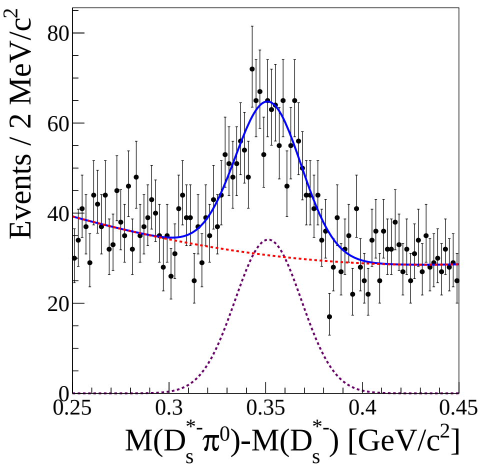

Figure C.23: Fit to the $D_{s1}(2460)^-$ invariant mass distribution in generic MC for mismatched $D_{s1}(2460)^-$ candidates that are not coming from $D_{s1}(2460)^-$ decays. The solid blue curve represents the total fitting model that consists of the Gaussian describing the $D_{s0}^*(2317)^-$ reflection component (dashed purple) and the 2$^{\text{nd}}$ order Chebychev polynomial (dashed red) used to approximate combinatorial background.

Fixed Parameters

Parameter	Value
a_1	-0.164
a_2	0.050

Floating Parameters

Parameter	Value
Gaussian (broken signal)	
μ^{BS}	351.8 ± 5.1 MeV/c^2
σ^{BS}	27.0 ± 6.6 MeV/c^2
N^{BS}	628 ± 184
Chebyshev Polynomial (2$^{\mathrm{nd}}$ order)	
$N_{\mathrm{pol\_bkg}}$	$11,499 \pm 216$

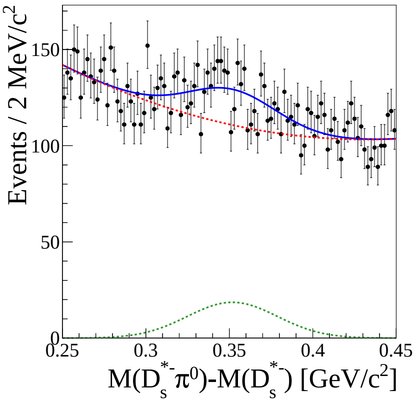

Table C.18: Parameters of the fit to the $D_s^{*-}\pi^0$ invariant mass distributions in generic MC for "broken signal" events (cut-based selection). To ensure stability of the fitting procedure, parameters of the polynomial are fixed to those estimate by the fit in Fig. C.23

Figure C.24: Fit to the $D_{s1}(2460)^-$ invariant mass distribution in generic MC for mismatched $D_{s1}(2460)^-$ candidates that are coming from $D_{s1}(2460)^-$ decays (cut-based selection). The solid blue curve represents the total fitting model that consists of the Gaussian describing the BS component (dashed green) and the 2$^{\mathrm{nd}}$ order Chebychev polynomial (dashed red) used to approximate combinatorial background.

Parameter	Value
Double Gaussian	
μ_1	1966.3 ± 0.3 MeV/c^2
μ_2	1962.4 ± 1.5 MeV/c^2
σ_1	4.13 ± 0.33 MeV/c^2
σ_2	9.88 ± 2.01 MeV/c^2
Fraction	0.368 ± 0.087
N_{sig}	$2{,}144 \pm 94$
Chebyshev polynomial (0$^{\text{th}}$ order)	
a_0	-0.116 ± 0.021
N_{bkg}	$7{,}369 \pm 119$
Weighted σ	6.24 ± 0.94 MeV/c^2

Table C.19: Parameters of the fit to the D_s^- invariant mass distributions in data.

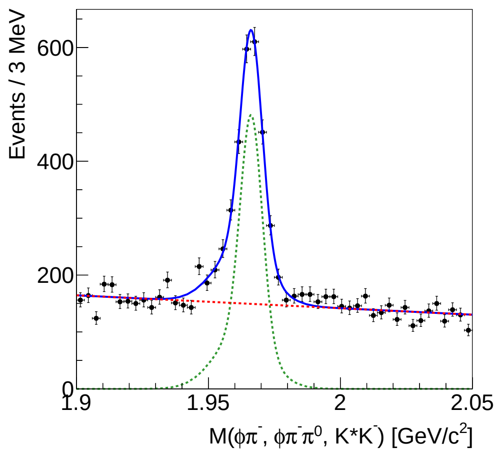

Figure C.25: Fit to the D_s^- invariant mass distributions in data. The solid blue curve represents the total fitting model that consists of the double Gaussian describing the signal component (dashed green) and the 1$^{\text{st}}$ order Chebychev polynomial (dashed red) used to approximate combinatorial background.

Parameter	Value
Gaussian (signal)	
μ	348.9 ± 0.1 MeV/c^2
σ	6.09 ± 0.09 MeV/c^2
N_{sig}	$4,185 \pm 68$
Chebyshev polynomial (1$^{\text{st}}$ order)	
a_1	-1.952 ± 0.393
N_{bkg}	732 ± 69

Table C.20: Parameters of the fit to the $D_s^- \pi^0$ invariant mass distributions in generic MC for matched $D_{s0}^*(2317)^-$ candidates.

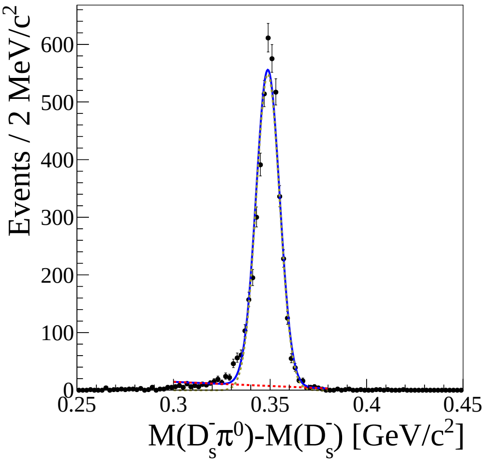

Figure C.26: Fit to the $D_s^- \pi^0$ invariant mass distributions in generic MC for matched $D_{s0}^*(2317)^-$ candidates (MVA selection). The solid blue curve represents the total fitting model that consists of the 1$^{\text{st}}$ order Chebychev polynomial and the Gaussian fit function.

Parameter	Value
Gaussian (feed-down)	
$\mu^{\text{feed-down}}$	344.7 ± 0.7 MeV/c^2
$\sigma^{\text{feed-down}}$	13.2 ± 0.7 MeV/c^2
$N_{\text{feed-down}}$	$2,491 \pm 174$
Chebyshev polynomial (2$^{\text{nd}}$ order)	
a_1	-0.182 ± 0.010
a_2	-0.025 ± 0.014
N_{bkg}	$27,824 \pm 236$

Table C.21: Parameters of the fit to the $D_s^-\pi^0$ invariant mass distributions in generic MC for mismatched $D_{s0}^*(2317)^-$ candidates (MVA selection).

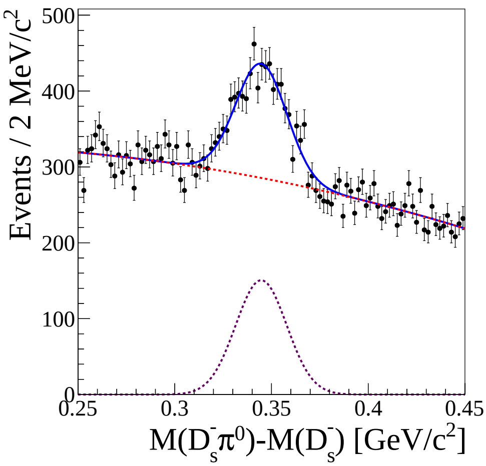

Figure C.27: Fit to the $D_{s0}^*(2317)^-$ invariant mass distribution in generic MC (MVA selection). The solid blue curve represents the total fitting model that consists of the Gaussian describing the $D_{s1}(2460)^-$ reflection component (dashed purple) and the 2$^{\text{nd}}$ order Chebychev polynomial (dashed red) used to approximate combinatorial background.

Parameter	Value
Gaussian (signal)	
μ	346.7 ± 0.2 MeV/c^2
σ	6.08 ± 0.16 MeV/c^2
N_{sig}	$1,412 \pm 40$
Chebyshev polynomial (1st order)	
a_1	-2.049 ± 0.574
N_{bkg}	248 ± 38

Table C.22: Parameters of the fit to the $D_s^{*-}\pi^0$ invariant mass distributions in generic MC for matched $D_{s1}(2460)^-$ candidates (MVA selection).

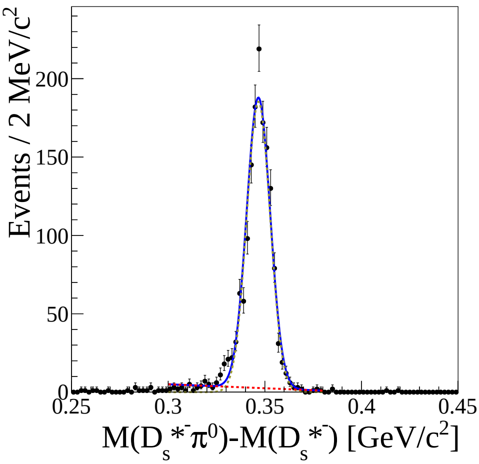

Figure C.28: Fit to the $D_s^{*-}\pi^0$ invariant mass distributions in generic MC for matched $D_{s1}(2460)^-$ candidates. The solid blue curve represents the total fitting model that consists of the 1st order Chebychev polynomial and the Gaussian fit function.

Parameter	Value
Gaussian (feed-up)	
$\mu^{\text{feed-down}}$	351.9 ± 1.5 MeV/c^2
$\sigma^{\text{feed-down}}$	14.75 ± 3.84 MeV/c^2
$N_{\text{feed-down}}$	621 ± 86
Chebyshev polynomial (2$^{\text{nd}}$ order)	
a_1	0.061 ± 0.023
a_2	-0.094 ± 0.033
N_{bkg}	$5,741 \pm 112$

Table C.23: Parameters of the fit to the $D_s^{*-}\pi^0$ invariant mass distributions in generic MC for mismatched $D_{s1}(2460)^-$ candidates that are not coming from $D_{s1}(2460)^-$ decays (MVA selection).

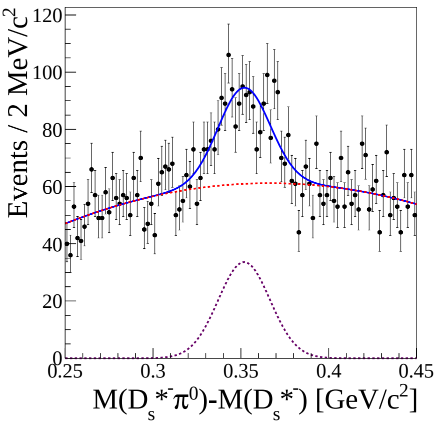

Figure C.29: Fit to the $D_{s1}(2460)^-$ invariant mass distribution in generic MC for mismatched $D_{s1}(2460)^-$ candidates that are not coming from $D_{s1}(2460)^-$ decays. The solid blue curve represents the total fitting model that consists of the Gaussian describing the $D_{s0}^*(2317)^-$ reflection component (dashed purple) and the 2$^{\text{nd}}$ order Chebychev polynomial (dashed red) used to approximate combinatorial background.

Parameter	Value
Gaussian (broken signal)	
μ	350.8 ± 5.8 MeV/c^2
σ	20.6 ± 14.5 MeV/c^2
N_{BS}	362 ± 188
Chebyshev polynomial (1$^{\text{st}}$ order)	
a_1	-0.121 ± 0.017
N_{bkg}	$11,241 \pm 218$

Table C.24: Parameters of the fit to the $D_s^{*-}\pi^0$ invariant mass distributions in generic MC for "broken signal" events (MVA selection). To ensure stability of the fitting procedure, parameters of the polynomial are fixed to those estimate by the fit in Fig. C.23

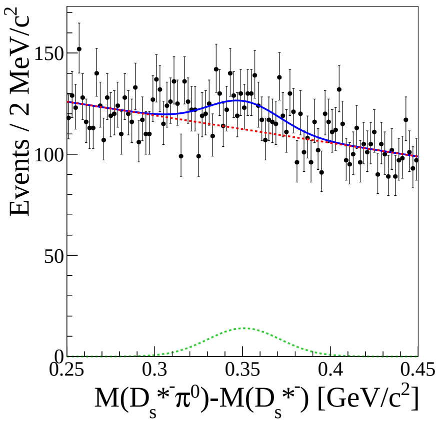

Figure C.30: Fit to the $D_{s1}(2460)^-$ invariant mass distribution in generic MC for mismatched $D_{s1}(2460)^-$ candidates that are coming from $D_{s1}(2460)^-$ decays. The solid blue curve represents the total fitting model that consists of the Gaussian describing the BS component (dashed green) and the 2$^{\text{nd}}$ order Chebychev polynomial (dashed red) used to approximate combinatorial background.

C.4 $\mathbf{D_s^+ D_{s0}^*(2317)^-}$ *+ anything* decay file

```
JetSetPar PARJ(41)=0.32
JetSetPar PARJ(42)=0.62
#
Alias MyDsp Dsprt
Alias MyDs+ D_s+
Alias MyDs- D_s-
Alias MyDs2317+ D_s0*+
Alias MyDs2317- D_s0*-
Alias MyPhi phi
Alias MyKst0 K*0
Alias BarMyKst0 anti-K*0
#
Decay vpho
1.0 MyDsp                        PHSP;
Enddecay
#
Decay MyDsp
0.500 MyDs+ MyDs2317-            PHSP;
0.500 MyDs- MyDs2317+            PHSP;
Enddecay
#
Decay MyDs+ 0.3333 MyPhi pi+      SVS;
0.3333 MyPhi pi+ pi0             PHSP;
0.3333 BarMyKst0 K+               SVS;
Enddecay
#
Decay MyDs-
0.3333 MyPhi pi-                  SVS;
0.3333 MyPhi pi- pi0             PHSP;
0.3333 MyKst0 K-                  SVS;
Enddecay
#
Decay BarMyKst0
1.000 K- pi+                      VSS;
Enddecay
#
Decay MyKst0
1.000 K+ pi-                      VSS;
```

```
Enddecay
# Decay MyDs2317+
1.0000 MyDs+ pi0                                   PHSP;
Enddecay
#
Decay MyDs2317-
1.0000 MyDs- pi0                                   PHSP;
Enddecay
#
Decay MyPhi
1.000 K- K+                                         VSS;
Enddecay
#
Decay pi0
1.0000 gamma gamma                                 PHSP;
Enddecay
#
End
```

C.5 $\mathbf{D_s^+ D_{s1}(2460)^-}$ + *anything* decay file

```
#
JetSetPar PARJ(41)=0.32
JetSetPar PARJ(42)=0.62
#
Alias MyDsp Dsprt
Alias MyDs+ D_s+
Alias MyDs- D_s-
Alias MyDs2460+ D'_s1+
Alias MyDs2460- D'_s1-
Alias MyDs_st+ D_s*+
Alias MyDs_st- D_s*-
Alias MyPhi phi
Alias MyKst0 K*0
Alias BarMyKst0 anti-K*0
#
Decay vpho
1.0 MyDsp                                          PHSP;
```

```
Enddecay
#
Decay MyDsp
0.500 MyDs2460+ MyDs-                    SVS;
0.500 MyDs2460- MyDs+                    SVS;
Enddecay
#
Decay MyDs2460+
1.000 MyDs_st+ pi0                       PHSP;
Enddecay
#
Decay MyDs2460-
1.000 MyDs_st- pi0                       PHSP;
Enddecay
#
Decay MyDs_st+
1.000 MyDs+ gamma                   VSP_PWAVE;
Enddecay
#
Decay MyDs_st-
1.000 MyDs- gamma                   VSP_PWAVE;
Enddecay
#
Decay MyDs+
0.3333 MyPhi pi+                          SVS;
0.3333 MyPhi pi+ pi0                     PHSP;
0.3333 BarMyKst0 K+                       SVS;
Enddecay
#
Decay MyDs-
0.3333 MyPhi pi-                          SVS;
0.3333 MyPhi pi- pi0                     PHSP;
0.3333 MyKst0 K-                          SVS;
Enddecay
#
Decay BarMyKst0
1.000 K- pi+                              VSS;
Enddecay
#
Decay MyKst0
```

```
1.000 K+ pi-                                VSS;
Enddecay
#
Decay MyPhi
1.000 K- K+                                 VSS;
Enddecay
#
Decay pi0
1.0000 gamma gamma                          PHSP;
Enddecay
#
End
```

References

[1] C. N. Yang and R. L. Mills. "Conservation of Isotopic Spin and Isotopic Gauge Invariance." *Phys. Rev.* 96, 191–195 (1954).

[2] Sheldon L. Glashow. "Partial-symmetries of weak interactions." *Nuclear Physics* 22 4, 579–588 (1961).

[3] Steven Weinberg. "A Model of Leptons." *Phys. Rev. Lett.* 19, 1264–1266 (1967).

[4] F. Englert and R. Brout. "Broken Symmetry and the Mass of Gauge Vector Mesons." *Phys. Rev. Lett.* 13, 321–323 (1964).

[5] Peter W. Higgs. "Broken Symmetries and the Masses of Gauge Bosons." *Phys. Rev. Lett.* 13, 508–509 (1964).

[6] "Search for elastic muon-neutrino electron scattering." *Physics Letters B* 46 1, 121–124 (1973).

[7] G. Aad and other. "Observation of a new particle in the search for the Standard Model Higgs boson with the ATLAS detector at the LHC." *Physics Letters B* 716 1, 1–29 (2012).

[8] Nima Arkani–Hamed, Savas Dimopoulos, and Gia Dvali. "The hierarchy problem and new dimensions at a millimeter." *Physics Letters B* 429 3, 263–272 (1998).

[9] Keith R. Dienes, Emilian Dudas, and Tony Gherghetta. "Grand unification at intermediate mass scales through extra dimensions." *Nucl. Phys. B* 537, 47–108 (1999).

[10] Lisa Randall and Raman Sundrum. "Large Mass Hierarchy from a Small Extra Dimension." *Phys. Rev. Lett.* 83, 3370–3373 (1999).

[11] Ralph Blumenhagen et al. "TOWARD REALISTIC INTERSECTING D-BRANE MODELS." *Annual Review of Nuclear and Particle Science* 55 Volume 55, 2005, 71–139 (2005).

[12] C. D. Froggatt and Holger Bech Nielsen. "Hierarchy of Quark Masses, Cabibbo Angles and CP Violation." *Nucl. Phys. B* 147, 277–298 (1979).

[13] Paul Langacker. "The standard model and beyond." 2010. ISBN: 978-1-4200-7906-7.

[14] R. D. Peccei and Helen R. Quinn. "CP Conservation in the Presence of Pseudoparticles." *Phys. Rev. Lett.* 38, 1440–1443 (1977).

[15] Steven Weinberg. "A New Light Boson?" *Phys. Rev. Lett.* 40, 223–226 (1978).

[16] F. Wilczek. "Problem of Strong P and T Invariance in the Presence of Instantons." *Phys. Rev. Lett.* 40, 279–282 (1978).

[17] Csaba Csáki, Christophe Grojean, and John Terning. "Alternatives to an elementary Higgs." *Rev. Mod. Phys.* 88, 045001 (2016).

[18] Nima Arkani-Hamed et al. "The Littlest Higgs." *Journal of High Energy Physics* 2002 07, 034 (2002).

[19] Z. Chacko, Hock-Seng Goh, and Roni Harnik. "Natural Electroweak Breaking from a Mirror Symmetry." *Phys. Rev. Lett.* 96, 231802 (2006).

[20] Carlo Rovelli. "Zakopane lectures on loop gravity." 2011. arXiv:1102.3660.

[21] Thomas Appelquist, Alan Chodos, and Peter G. O. Freund, eds. "Modern Kaluza-Klein Theories." Available at Internet Archive: `https://archive.org/details/modernkaluzaklei0000unse`. Menlo Park, CA: Addison-Wesley, 1987. ISBN: 0-201-09829-7.

[22] Jihn E. Kim and H.P. Nilles. "The μ-problem and the strong CP-problem." *Physics Letters B* 138 1, 150–154 (1984).

[23] Julius Wess and Jonathan Bagger. "Supersymmetry and Supergravity." 2nd ed. Princeton, NJ: Princeton University Press, 1992. ISBN: 978-0691025308.

[24] John Terning. "Modern Supersymmetry: Dynamics and Duality." Oxford: Clarendon Press, 2006. ISBN: 978-0198567639.

[25] Michael B. Green, John H. Schwarz, and Edward Witten. "Superstring Theory: 25th Anniversary Edition." Cambridge Monographs on Mathematical Physics. Cambridge University Press, 2012.

[26] Joseph Polchinski. "String Theory." Cambridge Monographs on Mathematical Physics. Cambridge University Press, 1998.

[27] K. Becker, M. Becker, and J. H. Schwarz. "String theory and M-theory: A modern introduction." Cambridge University Press, Dec. 2006. ISBN: 978-0-511-25486-4, 978-0-521-86069-7, 978-0-511-81608-6.

[28] Luis E. Ibanez and Angel M. Uranga. "String theory and particle physics: An introduction to string phenomenology." Cambridge University Press, Feb. 2012. ISBN: 978-0-521-51752-2, 978-1-139-22742-1.

[29] Howard Georgi and Sheldon L. Glashow. "Unity of All Elementary-Particle Forces." *Physical Review Letters* 32, 438–441 (1974).

[30] T. Abe et al. "Belle II Technical Design Report." 2010. arXiv:1011.0352 [physics.ins-det].

[31] F. Abudinén et al. "Precise Measurement of the D^0 and D^+ Lifetimes at Belle II." *Phys. Rev. Lett.* 127, 211801 (2021).

[32] P. Ahlburg et al. "The new and complete Belle II DEPFET pixel detector: Commissioning and previous operational experience." *Nuclear Instruments and Methods in Physics Research Section A: Accelerators, Spectrometers, Detectors and Associated Equipment* 1068, 169763 (2024).

[33] Hua Ye. "Commissioning of the Belle II Pixel Vertex Detector." *PoS* EPS-HEP2019, 122 (2020).

[34] Stefan Rummel and Ladislav Andricek. "The DEPFET active pixel sensor for vertexing at ILC and Super KEKB." *Nuclear Instruments and Methods in Physics Research Section A: Accelerators, Spectrometers, Detectors and Associated Equipment* 623 1, 189–191, 1st International Conference on Technology and Instrumentation in Particle Physics (2010).

[35] Hans Krüger. "Front-end electronics for DEPFET pixel detectors at SuperBelle (BELLE II)." *Nuclear Instruments and Methods in Physics Research Section A: Accelerators, Spectrometers, Detectors and Associated Equipment* 617 1, 337–341, 11th Pisa Meeting on Advanced Detectors (2010).

[36] J Knopf et al. "A 256 channel 8-Bit current digitizer ASIC for the Belle-II PXD." *Journal of Instrumentation* 6 01, C01085 (2011).

[37] M Lemarenko et al. "Test results of the Data Handling Processor for the DEPFET Pixel Vertex Detector." *Journal of Instrumentation* 8 01, C01032 (2013).

[38] S. Ramo. "Currents Induced by Electron Motion." *Proceedings of the I.R.E.* 27, 584–585 (1939).

[39] M.J. French et al. "Design and results from the APV25, a deep sub-micron CMOS front-end chip for the CMS tracker." *Nuclear Instruments and Methods in Physics Research Section A: Accelerators, Spectrometers, Detectors and Associated Equipment* 466 2, 359–365, 4th Int. Symp. on Development and Application of Semiconductor Tracking Detectors (2001).

[40] N. Taniguchi. "Central Drift Chamber for Belle-II." *Journal of Instrumentation* 12 06, C06014 (2017).

[41] Valerio Bertacchi et al. "Track finding at Belle II." *Computer Physics Communications* 259, 107610 (2021).

[42] Kazuki Kojima. "The operation and performance of the TOP detector at the Belle II experiment." *PoS* EPS-HEP2021, 803 (2022).

[43] M Yonenaga et al. "Performance evaluation of the aerogel RICH counter for the Belle II spectrometer using early beam collision data." *Progress of Theoretical and Experimental Physics* 2020 9, 093H01 (2020).

[44] J. Fast. "The Belle II imaging Time-of-Propagation (iTOP) detector." *Nuclear Instruments and Methods in Physics Research Section A: Accelerators, Spectrometers, Detectors and Associated Equipment* 876, 145–148, The 9th international workshop on Ring Imaging Cherenkov Detectors (RICH2016) (2017).

[45] Blair N. Ratcliff. "Imaging rings in Ring Imaging Cherenkov counters." *Nuclear Instruments and Methods in Physics Research Section A: Accelerators, Spectrometers, Detectors and Associated Equipment* 502 1, 211–221, Experimental Techniques of Cherenkov Light Imaging. Proceedings of the Fourth International Workshop on Ring Imaging Cherenkov Detectors (2003).

[46] Dmitri Kotchetkov et al. "Front-end electronic readout system for the Belle II imaging Time-Of-Propagation detector." *Nuclear Instruments and Methods in Physics Research Section A: Accelerators, Spectrometers, Detectors and Associated Equipment* 941, 162342 (2019).

[47] R. Pestotnik et al. "Aerogel RICH for forward PID at Belle II." *Nuclear Instruments and Methods in Physics Research Section A: Accelerators, Spectrometers, Detectors and Associated Equipment* 732, 371–374, Vienna Conference on Instrumentation 2013 (2013).

[48] M Yamaga et al. "RPC systems for BELLE detector at KEKB." *Nuclear Instruments and Methods in Physics Research Section A: Accelerators, Spectrometers, Detectors and Associated Equipment* 456 1, 109–112, Proceedings of the 5th Int. Workshop on Resistive Plate Chambers and Related Detectors (2000).

[49] M Nakao et al. "Data acquisition system for Belle II." *Journal of Instrumentation* 5 12, C12004 (2010).

[50] Yoshihito Iwasaki et al. "Level 1 Trigger System for the Belle II Experiment." *IEEE Transactions on Nuclear Science* 58 4, 1807–1815 (2011).

[51] M Nakao. "Timing distribution for the Belle II data acquisition system." *Journal of Instrumentation* 7 01, C01028 (2012).

[52] Dehui Sun et al. "Belle2Link: A Global Data Readout and Transmission for Belle II Experiment at KEK." *Physics Procedia* 37, 1933–1939, Proceedings of the 2nd International Conference on Technology and Instrumentation in Particle Physics (TIPP 2011) (2012).

[53] T. Higuchi et al. "Development of a PCI Based Data Acquisition Platform for High Intensity Accelerator Experiments." 2003. arXiv:0305088 hep-ex.

[54] E Kou et al. "The Belle II Physics Book." *Progress of Theoretical and Experimental Physics* 2019 12, 123C01 (2019).

[55] Matthew Barrett et al. "The Belle II Online–Offline Data Operations System." *Computing and Software for Big Science* 5 1, 1 (2021).

[56] Rene Brun and Fons Rademakers. "ROOT — An object oriented data analysis framework." *Nucl. Instrum. Meth. A* 389 1-2, 81–86 (1997).

[57] Dmytro Levit et al. "FPGA Based Data Read-Out System of the Belle II Pixel Detector." *IEEE Transactions on Nuclear Science* 62 3, 1033–1039 (2015).

[58] Stefan Huber et al. "Performance of the Data-Handling Hub Readout System for the Belle II Pixel Detector." *IEEE Transactions on Nuclear Science* 68 8, 1961–1967 (2021).

[59] X. Inc. "Aurora 8B/10B Protocol Specification." Accessed: 2025-10-21. Xilinx. 2014.

[60] M. Schnell. "Development of an FPGA-based Data Reduction System for the Belle II DEPFET Pixel Detector." PhD thesis. Rheinische Friedrich-Wilhelms-Universität Bonn, 2015.

[61] S. Reiter. "Implementation, Operation and Monitoring of the Data Acquisition System of the Belle II Pixel Detector during Physics Data Taking in 2019 — 2022." PhD thesis. Justus-Liebig-Universität Gießen, 2024.

[62] Björn Spruck et al. "The Belle II Pixel Detector Data Acquisition and Reduction System." *IEEE Transactions on Nuclear Science* 60 5, 3709–3713 (2013).

[63] D Münchow et al. "The data acquisition system of the Belle II Pixel Detector." *Journal of Instrumentation* 9 08, C08009 (2014).

[64] Thomas Geßler et al. "The ONSEN Data Reduction System for the Belle II Pixel Detector." *IEEE Transactions on Nuclear Science* 62 3, 1149–1154 (2015).

[65] W Kühn et al. "FPGA based compute nodes for high level triggering in PANDA." *Journal of Physics: Conference Series* 119 2, 022027 (2008).

[66] J. Zhao et al. "A general xTCA compliant and FPGA based data processing building blocks for trigger and data acquisition system." *2014 19th IEEE-NPSS Real Time Conference.* 2014, pp. 1–4.

[67] PICMG. "PICMG 3.0 R3.0, AdvancedTCA Base Specification." Technical specification. PICMG. 2008.

[68] Intel, Hewlett-Packard, NEC, et al. "Intelligent Platform Management Interface Specification v1.5. Version 1.1." Technical specification. IPMI Consortium. 2002.

[69] PICMG. "AMC.0 R2.0, AdvancedMC Mezzanine Module Specification. Version 2.0." Technical specification. PICMG. 2006.

[70] PICMG. "MTCA.0 R1.0, MicroTCA Specification." Technical specification. PICMG. 2006.

[71] Xilinx, Inc. "DS100: Virtex-5 Family Overview. Version 5.1." Accessed: 2025-10-23. Xilinx, Inc. 2015.

[72] Xilinx, Inc. "UG190: Virtex-5 FPGA User Guide. Version 5.4." Accessed: 2025-10-23. Xilinx, Inc. 2012.

[73] A. Natochii et al. "Measured and projected beam backgrounds in the Belle II experiment at the SuperKEKB collider." *Nuclear Instruments and Methods in Physics Research Section A: Accelerators, Spectrometers, Detectors and Associated Equipment* 1055, 168550 (2023).

[74] Hiroyuki Nakayama et al. "Small-Beta Collimation at SuperKEKB to Stop Beam-Gas Scattered Particles and to Avoid Transverse Mode Coupling Instability." *Conf. Proc. C* 1205201, 1104–1106 (2012).

[75] N. Ohuchi et al. "SuperKEKB beam final focus superconducting magnet system." *Nuclear Instruments and Methods in Physics Research Section A: Accelerators, Spectrometers, Detectors and Associated Equipment* 1021, 165930 (2022).

[76] J. Schueler et al. "Application of recoil-imaging time projection chambers to directional neutron background measurements in the SuperKEKB accelerator tunnel." *Nuclear Instruments and Methods in Physics Research Section A: Accelerators, Spectrometers, Detectors and Associated Equipment* 1040, 167291 (2022).

[77] Yukiyoshi Ohnishi and otehr. "Accelerator design at SuperKEKB." *Progress of Theoretical and Experimental Physics* 2013 3, 03A011 (2013).

[78] T. Ishibashi et al. "Movable collimator system for SuperKEKB." *Phys. Rev. Accel. Beams* 23, 053501 (2020).

[79] A. Natochii et al. "Improved simulation of beam backgrounds and collimation at SuperKEKB." *Phys. Rev. Accel. Beams* 24, 081001 (2021).

[80] M. Iwasaki et al. "Beam Background and MDI Design for SuperKEKB/Belle-II." *Conf. Proc. C* 1205201, 1825–1827 (2012).

[81] Emy Mulyani et al. "First measurements of the vertical beam size with an X-ray beam size monitor in SuperKEKB rings." *Nuclear Instruments and Methods in Physics Research Section A: Accelerators, Spectrometers, Detectors and Associated Equipment* 919, 1–15 (2019).

[82] E. Kovalenko. "On-line luminosity measurements at Belle II." *Journal of Instrumentation* 15 06, C06067 (2020).

[83] Y. Suetsugu, K. Shibata, and M. Shirai. "Design study of distributed pumping system using multilayer NEG strips for particle accelerators." *Nuclear Instruments and Methods in Physics Research Section A: Accelerators, Spectrometers, Detectors and Associated Equipment* 597 2, 153–159 (2008).

[84] S. Bacher et al. "Performance of the diamond-based beam-loss monitor system of Belle II." *Nuclear Instruments and Methods in Physics Research Section A: Accelerators, Spectrometers, Detectors and Associated Equipment* 997, 165157 (2021).

[85] M. Gabriel, F. Simon, H. Windel, et al. "A time resolved study of injection backgrounds during the first commissioning phase of SuperKEKB." *The European Physical Journal C* 81 11, 972 (2021).

[86] I. Jaegle et al. "Compact, directional neutron detectors capable of high-resolution nuclear recoil imaging." *Nuclear Instruments and Methods in Physics Research Section A: Accelerators, Spectrometers, Detectors and Associated Equipment* 945, 162296 (2019).

[87] S. R. de Jong. "Study of Thermal Neutron Flux from SuperKEKB in the Belle II Commissioning Detector." BELLE2-PTHESIS-2018-002. Ph.D. thesis. Victoria, BC: University of Victoria, 2017.

[88] H. Ikeda et al. "Beam Loss Monitor at SuperKEKB." *Proceedings of the International Beam Instrumentation Conference (IBIC'14).* TUPD22. 2014, pp. 459–462.

[89] M. Y. Han and Y. Nambu. "Three-Triplet Model with Double SU(3) Symmetry." *Phys. Rev.* 139, B1006–B1010 (1965).

[90] Thomas G. Trippe et al. "Review of particle properties." *Rev. Mod. Phys.* 48, S1–S245 (1976).

[91] T. Barnes and E. S. Swanson. "Kaon–Nucleon Scattering Amplitudes and Z^* Enhancements from Quark Born Diagrams." Phys. Rev. C, forthcoming (1992).

[92] L. Montanet et al. "Review of Particle Properties." *Phys. Rev. D* 50, 1173–1814 (1994).

[93] T. Nakano and others (LEPS Collaboration). "Evidence for a narrow $S = +1$ baryon resonance." 2003. arXiv:0301020 [hep-ex].

[94] Dmitri Diakonov, Victor Petrov, and Maxim Polyakov. "Exotic anti-decuplet of baryons: prediction from chiral solitons." *Zeitschrift für Physik A Hadrons and Nuclei* 359 3, 305–314 (1997).

[95] W-M Yao et al. "Review of Particle Physics." *Journal of Physics G: Nuclear and Particle Physics* 33 1, 1 (2006).

[96] M. Battaglieri et al. "Search for Θ^+ (1540) pentaquark in high-statistics measurement of $\gamma p \to \bar{K}^0 K^+ n$ at CLAS." 2006. arXiv:0510061 [hep-ex].

[97] McKinnon et al. "Search for the Θ^+ Pentaquark in the Reaction $\gamma d \to pK^- K^+ n$." *Phys. Rev. Lett.* 96, 212001 (2006).

[98] V. Kubarovsky et al. "Search for Θ^{++} pentaquarks in the exclusive reaction $\gamma p \to K^+ K^- p$." 2006. arXiv:0605001 [hep-ex].

[99] J. J. Aubert et al. "Experimental Observation of a Heavy Particle J." *Phys. Rev. Lett.* 33, 1404–1406 (1974).

[100] J. -E. Augustin et al. "Discovery of a Narrow Resonance in e^+e^- Annihilation." *Phys. Rev. Lett.* 33, 1406–1408 (1974).

[101] G. S. Abrams et al. "Discovery of a Second Narrow Resonance in e^+e^- Annihilation." *Phys. Rev. Lett.* 33, 1453–1455 (1974).

[102] E. Eichten et al. "Spectrum of Charmed Quark-Antiquark Bound States." *Phys. Rev. Lett.* 34, 369–372 (1975).

[103] Stanley F. Radford and Wayne W. Repko. "Potential model calculations and predictions for heavy quarkonium." *Physical Review D* 75 7 (2007).

[104] S. Navas et al. "Review of particle physics." *Phys. Rev. D* 110 3, 030001 (2024).

[105] R. L. Jaffe. "Perhaps a Stable Dihyperon." *Phys. Rev. Lett.* 38, 195–198 (1977).

[106] L. Maiani et al. "Diquark-antidiquark states with hidden or open charm and the nature of $X(3872)$." *Phys. Rev. D* 71, 014028 (2005).

[107] K. Terasaki. "Charmed scalar mesons and related." 2004. arXiv:hep-ph/0405146.

[108] A. V. Manohar and M. B. Wise. "Heavy Quark Physics." Vol. 10. Cambridge Monographs on Particle Physics, Nuclear Physics and Cosmology. Cambridge University Press, 2000, pp. 1–191.

[109] Angelo Esposito et al. "Four-quark hadrons: An updated review." *International Journal of Modern Physics A* 30 04n05, 1530002 (2015).

[110] Richard F. Lebed, Ryan E. Mitchell, and Eric S. Swanson. "Heavy-quark QCD exotica." *Progress in Particle and Nuclear Physics* 93, 143–194 (2017).

[111] S. Dubynskiy and M.B. Voloshin. "Hadro-charmonium." *Physics Letters B* 666 4, 344–346 (2008).

[112] S. Dubynskiy, A. Gorsky, and M.B. Voloshin. "Holographic hadro-quarkonium." *Physics Letters B* 671 1, 82–86 (2009).

[113] Nathan Isgur and Jack Paton. "A flux tube model for hadrons." *Physics Letters B* 124 3, 247–251 (1983).

[114] D. Horn and J. Mandula. "Model of mesons with constituent gluons." *Phys. Rev. D* 17, 898–908 (1978).

[115] Stephen Godfrey and Nathan Isgur. "Mesons in a relativized quark model with chromodynamics." *Phys. Rev. D* 32, 189–231 (1985).

[116] Philip R. Page, Eric S. Swanson, and Adam P. Szczepaniak. "Hybrid meson decay phenomenology." *Phys. Rev. D* 59, 034016 (1999).

[117] V. Crede and C.A. Meyer. "The experimental status of glueballs." *Progress in Particle and Nuclear Physics* 63 1, 74–116 (2009).

[118] Myron Bander et al. "Exotic Mesons and e^+e^- Annihilation." *Phys. Rev. Lett.* 36, 695–697 (1976).

[119] A. De Rújula, Howard Georgi, and S. L. Glashow. "Molecular Charmonium: A New Spectroscopy?" *Phys. Rev. Lett.* 38, 317–321 (1977).

[120] Aneesh V. Manohar and Mark B. Wise. "Exotic QQqq states in QCD." *Nuclear Physics B* 399 1, 17–33 (1993).

[121] Nils A. Törnqvist. "From the deuteron to deusons, an analysis of deuteronlike meson-meson bound states." *Zeitschrift für Physik C Particles and Fields* 61 3, 525–537 (1994).

[122] Freeman J. Dyson and Nguyen-Huu Xuong. "$Y = 2$ States in SU(6) Theory." *Phys. Rev. Lett.* 13, 815–817 (1964).

[123] R. J. Eden et al. "The Analytic S-Matrix." Cambridge: Cambridge University Press, 1966.

[124] Samuel H. Blitz and Richard F. Lebed. "Tetraquark cusp effects from diquark pair production." *Phys. Rev. D* 91, 094025 (2015).

[125] D. V. Bugg. "An explanation of Belle states Zb(10610) and Zb(10650)." *Europhysics Letters* 96 1, 11002 (2011).

[126] E. S. Swanson. "Cusps and exotic charmonia." *International Journal of Modern Physics E* 25 07, 1642010 (2016).

[127] E. Oset and A. Ramos. "Cusps and poles in the $J/\psi N$ scattering amplitude." *Phys. Rev. D* 91, 051504 (2015).

[128] L.D. Landau. "On analytic properties of vertex parts in quantum field theory." *Nuclear Physics* 13 1, 181–192 (1959).

[129] S. Coleman and R. E. Norton. "Singularities in the physical region." *Il Nuovo Cimento (1955–1965)* 38 1, 438–442 (1965).

[130] Christoph Schmid. "Final-State Interactions and the Simulation of Resonances." *Phys. Rev.* 154, 1363–1375 (1967).

[131] Adam P. Szczepaniak. "Dalitz plot distributions in presence of triangle singularities." *Physics Letters B* 757, 61–64 (2016).

[132] Xiao-Hai Liu, Makoto Oka, and Qiang Zhao. "Searching for observable effects induced by anomalous triangle singularities." *Physics Letters B* 753, 297–302 (2016).

[133] "Amplitude analysis and the nature of the Zc(3900)." *Physics Letters B* 772, 200–209 (2017).

[134] Adam P. Szczepaniak. "Triangle singularities and XYZ quarkonium peaks." *Physics Letters B* 747, 410–416 (2015).

[135] R. Aaij et al. "Evidence for the decay X(3872)→ψ(2S)γ." *Nuclear Physics B* 886, 665–680 (2014).

[136] A. V. Berezhnoy and A. K. Likhoded. "Processes $e^+e^- \to cccc$ and $e^+e^- \to J/\psi + gg$ at $\sqrt{s} = 10.59$ GeV." *Physics of Atomic Nuclei* 67 4, 757–761 (2004).

[137] Pakhlov et al. "Production of New Charmoniumlike States in $e^+e^- \to J/\psi D^{(*)}\overline{D}^{(*)}$ at $\sqrt{s} \approx 10.6$ GeV." *Phys. Rev. Lett.* 100, 202001 (2008).

[138] K. Abe et al. "Observation of a Charmoniumlike State Produced in Association with a J/ψ in e^+e^- Annihilation at $\sqrt{s} \approx 10.6$ GeV." *Phys. Rev. Lett.* 98, 082001 (2007).

[139] S.-K. Choi et al. "Observation of a Narrow Charmoniumlike State in Exclusive $B^\pm \to K^\pm\pi^+\pi^- J/\psi$ Decays." *Phys. Rev. Lett.* 91, 262001 (2003).

[140] K. Abe et al. "Observation of Large *CP* Violation in the Neutral *B* Meson System." *Phys. Rev. Lett.* 87, 091802 (2001).

[141] R. Aaij et al. "Determination of the $X(3872)$ Meson Quantum Numbers." *Phys. Rev. Lett.* 110, 222001 (2013).

[142] Stephen Lars Olsen, Tomasz Skwarnicki, and Daria Zieminska. "Nonstandard heavy mesons and baryons: Experimental evidence." *Rev. Mod. Phys.* 90, 015003 (2018).

[143] A. Esposito, A. Pilloni, and A.D. Polosa. "Multiquark resonances." *Physics Reports* 668, 1–97, Multiquark Resonances (2017).

[144] R. Aaij et al. "Study of the lineshape of the $\chi_{c1}(3872)$ state." *Phys. Rev. D* 102, 092005 (2020).

[145] H. Hirata et al. "Study of the lineshape of $X(3872)$ using B decays to $D^0\overline{D}^{*0}K$." *Phys. Rev. D* 107, 112011 (2023).

[146] BESIII Collaboration et al. "A coupled-channel analysis of the $X(3872)$ lineshape with BESIII data." 2023. arXiv:2309.01502 [hep-ex].

[147] C. Hanhart et al. "Reconciling the $X(3872)$ with the near-threshold enhancement in the $D^0\overline{D}^{*0}$ final state." *Phys. Rev. D* 76, 034007 (2007).

[148] S.-K. Choi et al. "Observation of a Near-Threshold $\omega J/\psi$ Mass Enhancement in Exclusive $B \to K\omega J/\psi$ Decays." *Phys. Rev. Lett.* 94, 182002 (2005).

[149] B. Aubert et al. "Observation of $Y(3940) \to J/\psi\omega$ in $B \to J/\psi\omega K$ at BABAR." *Phys. Rev. Lett.* 101, 082001 (2008).

[150] P. del Amo Sanchez et al. "Evidence for the decay $X(3872) \to J/\psi\omega$." *Phys. Rev. D* 82, 011101 (2010).

[151] S. Uehara et al. "Observation of a Charmoniumlike Enhancement in the $\gamma\gamma \to \omega J/\psi$ Process." *Phys. Rev. Lett.* 104, 092001 (2010).

[152] J. P. Lees et al. "Study of $X(3915) \to J/\psi\omega$ in two-photon collisions." *Phys. Rev. D* 86, 072002 (2012).

[153] C. Patrignani. "Review of Particle Physics." *Chinese Physics C* 40 10, 100001 (2016).

[154] Feng-Kun Guo and Ulf-G. Meißner. "Where is the $\chi_{c0}(2P)$?" *Phys. Rev. D* 86, 091501 (2012).

[155] Stephen Lars Olsen. "Is the $X(3915)$ the $\chi_{c0}(2P)$?" *Phys. Rev. D* 91, 057501 (2015).

[156] Hui Wang, Youchang Yang, and Jialun Ping. "Strong decays of $\chi_{cJ}(2P)$ and $\chi_{cJ}(3P)$." *The European Physical Journal A* 50 4, 76 (2014).

[157] Estia J. Eichten, Kenneth Lane, and Chris Quigg. "Charmonium levels near threshold and the narrow state $X(3872) \to \pi^+\pi^- J/\psi$." *Phys. Rev. D* 69, 094019 (2004).

[158] Bai-Qing Li and Kuang-Ta Chao. "Higher charmonia and X, Y, Z states with screened potential." *Physical Review D* 79 9, 094004 (2009).

[159] Jugoro Iizuka. "A Systematics and Phenomenology of Meson Family*." *Progress of Theoretical Physics Supplement* 37-38, 21–34 (1966).

[160] S. Okubo. "ϕ-meson and unitary symmetry model." *Physics Letters* 5 2, 165–168 (1963).

[161] George Zweig. "An SU(3) Model for Strong Interaction Symmetry and Its Breaking." Tech. rep. CERN-TH-401. CERN, 1964.

[162] Xin Li and M. B. Voloshin. "$X(3915)$ as a $D_s\overline{D}_s$ bound state." *Phys. Rev. D* 91, 114014 (2015).

[163] Richard F. Lebed and Antonio D. Polosa. "$\chi_{c0}(3915)$ as the lightest $c\bar{c}s\bar{s}$ state." *Phys. Rev. D* 93, 094024 (2016).

[164] R. Aaij et al. "Amplitude analysis of the $B^+ \to D^+D^-K^+$ decay." *Phys. Rev. D* 102, 112003 (2020).

[165] R. Aaij et al. "Observation of a Resonant Structure near the $D_s^+D_s^-$ Threshold in the $B^+ \to D_s^+D_s^-K^+$ Decay." *Phys. Rev. Lett.* 131, 071901 (2023).

[166] R. Aaij et al. "Observation of $J/\psi\phi$ Structures Consistent with Exotic States from Amplitude Analysis of $B^+ \to J/\psi\phi K^+$ Decays." *Phys. Rev. Lett.* 118, 022003 (2017).

[167] T. Aaltonen et al. "Evidence for a Narrow Near-Threshold Structure in the $J/\psi\phi$ Mass Spectrum in $B^+ \to J/\psi\phi K^+$ Decays." *Phys. Rev. Lett.* 102, 242002 (2009).

[168] R. Aaij et al. "Observation of New Resonances Decaying to $J/\psi K^+$ and $J/\psi\phi$." *Physical Review Letters* 127 8 (2021).

[169] Serguei Chatrchyan et al. "Observation of a Peaking Structure in the $J/\psi\phi$ Mass Spectrum from $B^\pm \to J/\psi\phi K^\pm$ Decays." *Phys. Lett. B* 734, 261–281 (2014).

[170] Victor Mukhamedovich Abazov et al. "Inclusive Production of the X(4140) State in $p\overline{p}$ Collisions at D0." *Phys. Rev. Lett.* 115 23, 232001 (2015).

[171] V. V. Anisovich et al. "Exotic mesons with hidden charm as diquark–antidiquark states." *International Journal of Modern Physics A* 30 32, 1550186 (2015).

[172] N. V. Drenska, R. Faccini, and A. D. Polosa. “Exotic hadrons with hidden charm and strangeness.” *Phys. Rev. D* 79, 077502 (2009).

[173] Fl Stancu. “Can $Y(4140)$ be a tetraquark?” *Journal of Physics G: Nuclear and Particle Physics* 37 7, 075017 (2010).

[174] Zhi-Gang Wang and Ye-Fan Tian. “Tetraquark state candidates: Y(4140), Y(4274) and X(4350).” *International Journal of Modern Physics A* 30 01, 1550004 (2015).

[175] Raphael M. Albuquerque, Mirian E. Bracco, and Marina Nielsen. “A QCD sum rule calculation for the $Y(4140)$ narrow structure.” *Physics Letters B* 678 2, 186–190 (2009).

[176] Tanja Branz, Thomas Gutsche, and Valery E. Lyubovitskij. “Hadronic molecule structure of the $Y(3940)$ and $Y(4140)$.” *Phys. Rev. D* 80, 054019 (2009).

[177] Xiaozhao Chen et al. “Mass of $Y(4140)$ in Bethe-Salpeter equation for quarks.” 2015. arXiv:1512.06483 [hep-ph].

[178] Gui-Jun Ding. “Possible molecular states of $D_s^*\bar{D}_s^*$ system and Y(4140).” *The European Physical Journal C* 64 2, 297 (2009).

[179] Marek Karliner and Jonathan L. Rosner. “Exotic resonances due to η exchange.” *Nuclear Physics A* 954, 365–370, Recent Progress in Strangeness and Charm Hadronic and Nuclear Physics (2016).

[180] Xiang Liu and Hong-Wei Ke. “Line shape of the radiative open-charm decay of $Y(4140)$ and $Y(3930)$.” *Phys. Rev. D* 80, 034009 (2009).

[181] Xiang Liu and Shi-Lin Zhu. “$Y(4143)$ is probably a molecular partner of $Y(3930)$.” *Phys. Rev. D* 80, 017502 (2009).

[182] R. Molina and E. Oset. “$Y(3940)$, $Z(3930)$, and the $X(4160)$ as dynamically generated resonances from the vector-vector interaction.” *Phys. Rev. D* 80, 114013 (2009).

[183] Zhi-Gang Wang, Zhi-Cheng Liu, and Xiao-Hong Zhang. “Analysis of the Y(4140) and related molecular states with QCD sum rules.” *The European Physical Journal C* 64 3, 373–386 (2009).

[184] Jian-Rong Zhang and Ming-Qiu Huang. “Molecular states from QCD sum rules: a view on $Y(4140)$.” *Journal of Physics G: Nuclear and Particle Physics* 37 2, 025005 (2010).

[185] Namit Mahajan. “$Y(4140)$: Possible options.” *Physics Letters B* 679 3, 228–230 (2009).

[186] Xiang Liu. "The hidden charm decay of Y(4140) by the rescattering mechanism." *Physics Letters B* 680 2, 137–140 (2009).

[187] E. S. Swanson. "Z_b and Z_c exotic states as coupled channel cusps." *Phys. Rev. D* 91, 034009 (2015).

[188] R. Aaij et al. "Amplitude analysis of $B^+ \to J/\psi\phi K^+$ decays." *Phys. Rev. D* 95, 012002 (2017).

[189] T. Aaltonen et al. "Observation of the $Y(4140)$ Structure in the $J/\psi\phi$ Mass Spectrum in $B^\pm \to J/\psi\phi K^\pm$ Decays." *Mod. Phys. Lett. A* 32 26, 1750139 (2017).

[190] Victor Mukhamedovich Abazov et al. "Search for the $X(4140)$ state in $B^+ \to J/\psi\phi K^+$ decays with the D0 Detector." *Phys. Rev. D* 89 1, 012004 (2014).

[191] T. Barnes, S. Godfrey, and E. S. Swanson. "Higher charmonia." *Phys. Rev. D* 72, 054026 (2005).

[192] Hua-Xing Chen et al. "The hidden-charm pentaquark and tetraquark states." *Physics Reports* 639, 1–121, The hidden-charm pentaquark and tetraquark states (2016).

[193] Bai-Qing Li, Ce Meng, and Kuang-Ta Chao. "Coupled-channel and screening effects in charmonium spectrum." *Phys. Rev. D* 80, 014012 (2009).

[194] Qi-Fang Lü and Yu-Bing Dong. "$X(4140)$, $X(4274)$, $X(4500)$, and $X(4700)$ in the relativized quark model." *Phys. Rev. D* 94, 074007 (2016).

[195] Pablo G. Ortega et al. "Canonical description of the new LHCb resonances." *Phys. Rev. D* 94, 114018 (2016).

[196] S. Jia et al. "Evidence for a vector charmoniumlike state in $e^+e^- \to D_s^+ D_{s2}^*(2573)^- +$ c.c.." *Phys. Rev. D* 101, 091101 (2020).

[197] S. Jia et al. "Observation of a vector charmoniumlike state in $e^+e^- \to D_s^+ D_{s1}(2536)^- +$ c.c.." *Phys. Rev. D* 100, 111103 (2019).

[198] J. P. Lees and other. "Study of the reaction $e^+e^- \to \psi(2S)\pi^+\pi^-$ via initial-state radiation at BaBar." *Phys. Rev. D* 89, 111103 (2014).

[199] X. L. Wang et al. "Measurement of $e^+e^- \to \pi^+\pi^-\psi(2S)$ via initial state radiation at Belle." *Phys. Rev. D* 91, 112007 (2015).

[200] M. Karliner and J. L. Rosner. "Exotic resonances due to η exchange." *Nucl. Phys. A* 954, 365–370 (2016).

[201] B. Aubert et al. "Observation of a Narrow Meson State Decaying to $D_s^+\pi^0$ at a Mass of 2.32 GeV$/c^2$." *Phys. Rev. Lett.* 90, 242001 (2003).

[202] Y. Mikami et al. “Measurements of the D_{sJ} Resonance Properties.” *Phys. Rev. Lett.* 92, 012002 (2004).

[203] D. Besson et al. “Observation of a narrow resonance of mass 2.46 GeV$/c^2$ decaying to $D_s^{*+}\pi^0$ and confirmation of the $D^*_{\mathrm{sJ}}(2317)$ state.” *Phys. Rev. D* 68, 032002 (2003).

[204] D. Ebert, R.N. Faustov, and V.O. Galkin. “Masses of heavy tetraquarks in the relativistic quark model.” *Physics Letters B* 634 2, 214–219 (2006).

[205] C. P. Shen et al. “Evidence for a New Resonance and Search for the $Y(4140)$ in the $\gamma\gamma \to \phi J/\psi$ Process.” *Phys. Rev. Lett.* 104, 112004 (2010).

[206] L. Maiani, A. D. Polosa, and V. Riquer. “Interpretation of axial resonances in $J/\psi - \phi$ at the LHCb.” *Phys. Rev. D* 94, 054026 (2016).

[207] Elisabetta Prencipe. “Search for four- and six-quark exotic states with c- and s- quarks.” DFG Research Grant n. 324081743. 2015.

[208] J. M. Link et al. “Measurement of masses and widths of excited charm mesons D_2^* and evidence for broad states.” *Phys. Lett. B* 586, 11–20 (2004).

[209] James P. Alexander et al. “Production and decay of the D(s1)+ (2536).” *Phys. Lett. B* 303, 377–384 (1993).

[210] M. A. Nowak, M. Rho, and I. Zahed. “Chiral effective action with heavy-quark symmetry.” *Phys. Rev. D* 48, 4370–4374 (1993).

[211] M. Di Pierro and E. Eichten. “Excited heavy-light systems and hadronic transitions.” *Phys. Rev. D* 64, 114004 (2001).

[212] Luka Leskovec et al. “Positive parity D_s mesons.” 2016. arXiv:1511.04140.

[213] Daniel Mohler et al. “$D^*_{s0}(2317)$ Meson and D-Meson-Kaon Scattering from Lattice QCD.” *Phys. Rev. Lett.* 111, 222001 (2013).

[214] Marina Nielsen. “$D^+_{sJ}(2317) \to D^+_s\pi^0$ decay width.” *Physics Letters B* 634 1, 35–38 (2006).

[215] P. Colangelo and F. De Fazio. “Understanding $D_{sJ}(2317)$.” *Physics Letters B* 570 3, 180–184 (2003).

[216] Stephen Godfrey. “Testing the nature of the $D^*_{s0}(2317)^+$ and $D_{sJ}(2463)^+$ states using radiative transitions.” *Physics Letters B* 568 3, 254–260 (2003).

[217] Amand Faessler et al. “Strong and radiative decays of the $D^*_{s0}(2317)$ meson in the DK-molecule picture.” *Phys. Rev. D* 76, 014005 (2007).

[218] Matthias F.M. Lutz and Madeleine Soyeur. “Radiative and isospin-violating decays of Ds-mesons in the hadrogenesis conjecture.” *Nuclear Physics A* 813 1, 14–95 (2008).

[219] Liuming Liu et al. “Interactions of charmed mesons with light pseudoscalar mesons from lattice QCD and implications on the nature of the $D^*_{s0}(2317)$.” *Phys. Rev. D* 87, 014508 (2013).

[220] Hai-Yang Cheng and Wei-Shu Hou. “B decays as spectroscope for charmed four-quark states.” *Physics Letters B* 566 3, 193–200 (2003).

[221] M. Cleven et al. “Strong and radiative decays of the $D^*_{s0}(2317)$ and $D_{s1}(2460)$.” *Eur. Phys. J. A* 50, 149 (2014).

[222] Prof. Christoph Hanhart. “Private communication.” 2024.

[223] B. Aubert et al. “Study of the $D^*_{sJ}(2317)^+$ and $D_{sJ}(2460)^+$ mesons in inclusive $c\bar{c}$ production near $\sqrt{s} = 10.6$ GeV.” *Phys. Rev. D* 74, 032007 (2006).

[224] S.-K. Choi et al. “Bounds on the width, mass difference and other properties of $X(3872) \to \pi^+\pi^- J/\psi$ decays.” *Physical Review D* 84 5 (2011).

[225] B. Aubert et al. “Study of $B \to D^{(*)+}_{sJ}\overline{D}^{(*)}$ Decays.” *Phys. Rev. Lett.* 93, 181801 (2004).

[226] William A. Bardeen, Estia J. Eichten, and Christopher T. Hill. “Chiral multiplets of heavy-light mesons.” *Phys. Rev. D* 68, 054024 (2003).

[227] N. Dash. “Systematic uncertainty for the K^0_S reconstruction efficiency.” Belle Note 1472, dated December 5, 2017. Dec. 2017.

[228] B. Bhuyan. “High p_T tracking efficiency using partially reconstructed D^* decays.” Belle Note 1165, dated December 16, 2010. Dec. 2010.

[229] Belle Collaboration. “Systematics — Belle II Wiki.” Access restricted, accessed on April 9, 2025. 2024.

[230] Belle Collaboration. “Integrated Luminosity Summary for Belle Runs.” Access restricted, accessed on April 9, 2025. 2024.

[231] S. Ryu et al. “Measurements of branching fractions of τ lepton decays with one or more K^0_S.” *Phys. Rev. D* 89, 072009 (2014).

[232] Gary J. Feldman and Robert D. Cousins. “Unified approach to the classical statistical analysis of small signals.” *Phys. Rev. D* 57, 3873–3889 (1998).

[233] S. Actis et al. “Quest for precision in hadronic cross sections at low energy: Monte Carlo tools vs. experimental data.” *Eur. Phys. J. C* 66, 585–686 (2010).

[234] Xiang-Kun Dong et al. “Hadronic cross section of e^+e^- annihilation at bottomonium energy region *.” *Chinese Physics C* 44 8, 083001 (2020).

[235] S. Jia et al. “Search for $(1S, 2S) \to Z_c^+ Z_c^{(\prime)-}$ and $e^+e^- \to Z_c^+ Z_c^{(\prime)-}$ at $\sqrt{s} = 10.52$, 10.58, and 10.867 GeV.” *Phys. Rev. D* 97, 112004 (2018).

[236] Howard Georgi. “Generalized dimensional analysis.” *Physics Letters B* 298 1-2, 187–189 (1993).

[237] Geoffrey C. Fox and Stephen Wolfram. “Event shapes in e+e− annihilation.” *Nuclear Physics B* 149 3, 413–496 (1979).